

# **BUCKLING OF GRADED COATINGS**

## **A CONTINUUM MODEL**

**Fazil Erdogan  
and  
Tz-Cheng Chiu**

**Lehigh University  
Bethlehem, PA 18015**

**October 2000**

**AIR FORCE OFFICE OF SCIENTIFIC RESEARCH  
GRANT F49620-98-1-0028**

**DISTRIBUTION STATEMENT A  
Approved for Public Release  
Distribution Unlimited**

**20010419 101**

## DTIC CONVERSATION RECORD FOR DISTRIBUTION STATEMENT REQUEST

DTIC Personnel Making Call <i>JACK RIKE</i>	Date <i>17 April 02</i>	Time <i>1425</i>
Authorizing Official <i>F. Erdogan</i>	Phone	
Agency <i>LEHIGH Univ. MECH. Engineering &amp; Mechanics</i>		
Title		
Internet Document URL (if applicable)		
<b>Distribution Statement</b> (Please check one box)		
<input checked="" type="checkbox"/> <b>DISTRIBUTION STATEMENT A:</b> Approved for public release. Distribution is unlimited.		
<input type="checkbox"/> <b>DISTRIBUTION STATEMENT B:</b> Distribution authorized to U.S. Government Agencies only.		
<input type="checkbox"/> <b>DISTRIBUTION STATEMENT C:</b> Distribution authorized to U.S. Government Agencies and their contractors.		
<input type="checkbox"/> <b>DISTRIBUTION STATEMENT D:</b> Distribution authorized to U.S. Department of Defense (DoD) and U.S DoD contractors only.		
<input type="checkbox"/> <b>DISTRIBUTION STATEMENT E:</b> Distribution authorized to U.S. Department of Defense (DoD) components only.		
<input type="checkbox"/> <b>DISTRIBUTION STATEMENT F:</b> Further dissemination only as directed by the controlling DoD office indicated below or by higher authority.		
<input type="checkbox"/> <b>DISTRIBUTION STATEMENT X:</b> Distribution authorized to U.S. Government agencies and private individuals or enterprises eligible to obtain export-controlled technical data in accordance with DoD Directive 5230.25, Withholding of Unclassified Technical Data from Public Disclosure, 6 Nov 84.		
<b>Reason for the above identified distribution statement</b> (in accordance with DoD Directive 5230.24)		
<hr/> <hr/> <hr/> <hr/>		
Controlling Office	Date of Distribution Statement Determination	
AQ Number (For DTIC-OCA Use Only)		
<hr/> <hr/> <hr/> <hr/>		

# **BUCKLING OF GRADED COATINGS**

## **A CONTINUUM MODEL**

**Fazil Erdogan  
and  
Tz-Cheng Chiu**

**Lehigh University  
Bethlehem, PA 18015**

**October 2000**

**AIR FORCE OFFICE OF SCIENTIFIC RESEARCH  
GRANT F49620-98-1-0028**

## Abstract

Requirements for the protection of hot section components in many high temperature applications such as earth-to-orbit winged planes and advanced turbine systems have led to the application of thermal barrier coatings (TBCs) that utilize ceramic coatings on metal substrates. An alternative concept to homogeneous ceramic coatings is the functionally graded materials (FGM) in which the composition of the coating is intentionally graded to improve the bonding strength and to reduce the magnitude of the residual and thermal stresses. A widely observed failure mode in such layered systems is known to be interface cracking that leads to spallation fracture. In most cases, the final stage of the failure process for a thin coating appears to be due to buckling instability under thermally or mechanically induced compressive stress. The debonding and spallation problems are also observed in other layered material systems such as surface coatings in electronic devices and fiber reinforced composite laminates. In the case of TBCs, stress concentrations due to interface asperities and voids and relatively low toughness of interfaces eventually lead to the formation of interface cracks or generally highly weakened interfacial zones. Buckling instability may then occur under sufficiently high compressive stresses.

The objective of this study is to develop a solution to the buckling instability problem by using continuum elasticity rather than a structural mechanics approach. The emphasis in the solution will be on the investigation of the effect of material inhomogeneity in graded coatings on the instability load, the postbuckling behavior, and fracture mechanics parameters such as the stress intensity factors and strain energy release rate. In plane strain and axisymmetric problems for an interface crack, the linear elastic small deformation theory gives only a trivial solution and does not produce instability regardless of the relative dimensions and the load amplitude. In this analysis, a nonlinear continuum theory is employed to examine the interface crack problem. First by using a perturbation

technique, the plane strain problem of a graded coating bonded to a homogeneous substrate containing an interface crack is reduced to an eigenvalue problem and the instability load is evaluated analytically. It is assumed that the applied load is a uniform in-plane compressive strain away from the crack region. The analytical solution of the instability problem permits the study of the effect of material inhomogeneity upon the inception of buckling and establishes benchmark results for the numerical solutions of related problems.

To study the postbuckling behavior and to calculate the stress intensity factors and strain energy release rate a geometrically nonlinear finite element procedure with enriched crack-tip element is developed. Both plane strain and axisymmetric interface crack problems in TBCs with either homogeneous or graded coating are then considered by using the finite element procedure. It is assumed that the applied load is a uniform temperature drop. Comparison of the results with that obtained from the plate approximation shows that because of the higher constraints the plate theory predicts greater instability strains and lower strain energy release rates. It is also observed that compared with a homogeneous coating the graded coating gives lower strain energy release rate because of the lower thermal residual stress and higher bending stiffness. The failure of the coating may be examined either by comparing the calculated strain energy release rate with the mode dependent material toughness or by using a maximum stress-based rupture theory in the debonded part of the coating.

# Chapter 1

## Introduction

### 1.1 Introduction

In order to meet the demanding performance requirements established by emerging technologies such as the aerospace plane, high performance engine, and microelectronics, it is often necessary that components perform multiple functions or exhibit characteristics not attainable by any single engineering material currently available. Examples include the blades in gas turbine engines which require high heat and corrosion resistance as well as low heat conductivity and high mechanical toughness. Similarly, in machine tools, gears, and bearings high toughness and high wear resistance are required in the same components. In these cases, considerable efforts have been devoted to develop processing composites in which dissimilar materials are combined to take advantage of favorable properties of each material. The composites are usually particulate, fiber or filament reinforced, or layered in structure. Many of the laminated materials, thin films, and coatings fall into the latter category.

One of the applications of layered composites under extensive development during the last few decades is using ceramic coatings to protect metallic components from high temperature and corrosive environments. These ceramic coatings, commonly referred to as thermal barrier coatings (TBCs), can lower the surface temperature of metallic components such as combustor heat shields, blades, and vanes in land-based and aero gas turbines operating with exhaust-gas and smoke-gas at temperatures around 1300°C. Lowering the temperature of such components not only prolongs their life but also saves a considerable amount of the energy required for their internal cooling. Thus, the TBC technology is considered by many as a viable near-term solution for the development of more efficient aircraft engines and stationary gas turbines.

A state-of-the-art TBC system used in aircraft engines typically consists of an 125-250  $\mu\text{m}$  thick thermally insulating ceramic layer, and a 50-125  $\mu\text{m}$  thick metallic bond coat between the ceramic layer and the metal component.  $\text{Y}_2\text{O}_3$  partially stabilized  $\text{ZrO}_2$  (PSZ) is most commonly used as the ceramic layer because of its low thermal conductivity and relatively high coefficient of thermal expansion for a ceramic. The role of metallic bond coat (e.g., NiCrAlY) is to provide a good ceramic-metal bond and protect the substrate from high temperature oxidation since the transport of oxygen through the PSZ layers is relatively fast at typical turbine operating temperatures. The protection of the metallic substrate from oxidation is achieved by forming a thermally grown oxide (TGO) layer (mainly  $\text{Al}_2\text{O}_3$ ) at high temperature along the ceramic/bond coat interface as the oxygen diffusion barrier.

A common feature of layered composites such as TBCs is that they consist of bonded dissimilar homogeneous materials. Because of the discontinuities in material properties across the interface, generally higher thermal and mechanical stresses would develop in the bonded structure. Consequently, the composite becomes very susceptible to cracking and debonding. A novel concept which is used to overcome the shortcomings of discontinuous material properties is to introduce an interfacial region with graded thermomechanical properties [1-5]. This is achieved by varying volume fractions of the constituents between zero and one hundred percent, thereby obtaining a continuous through-thickness material property and possibly microstructure variation. These inhomogeneous particulate composites with varying volume fractions are referred to as Functionally Graded Materials (FGMs). By using FGMs, it is possible to obtain both smoother stress distribution [6] and higher bonding strength [7]. For example, in the TBC application it was shown in [6] that by replacing the homogeneous ceramic coating with a graded metal/ceramic layer, the stress singularity at the point of intersection of the free end and interface between the

homogeneous coating and the substrate disappears and stress distribution becomes considerably smoother.

The synthesis of FGMs can be achieved through various techniques such as plasma spraying [8], chemical and physical vapor deposition [9], centrifugal casting [10] and combustion sintering [11]. By controlling both composition profile and microstructure, the concept of FGMs could provide great flexibility in material design and their potential for applications appears to be nearly unlimited. Besides the thermal barrier coatings on high temperature components, other current and potential applications of the concept of FGM includes wear-resistant coatings on load transfer components, armors or shields with improved impact resistance, and thermoelectric cells.

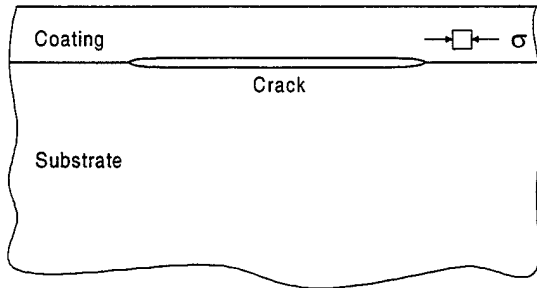
Aside from the fabricated FGMs, there are also other materials in which physical properties vary continuously across the interfacial region or through the thickness as a natural consequence of material processing. For example, in many diffusion bonded materials the atomic composition of the two species vary continuously across the nominal interface resulting in a region with graded properties. In soil mechanics, because of the change in overburden pressure, the stiffness of the medium in macro scale varies in depth direction. There are also geological structures such as shale-sandstone interfacial zones which are naturally inhomogeneous. Other examples for natural FGMs are such biological materials as bones and sea shells.

One major technical issue involved in developing the next generation of protective coatings is to assess the structural reliability of these coatings. Therefore, it is important to identify the relevant failure mechanisms, develop the necessary models, and perform the appropriate failure analysis. A major mode of failure in thermal barrier and a variety of other coatings is known to be cracking that leads to spallation. From the mechanics perspective the modes of failure may depend on the stress state in the coating. Usually residual tensile stresses tend to induce coating fracture normal to the interfaces. For

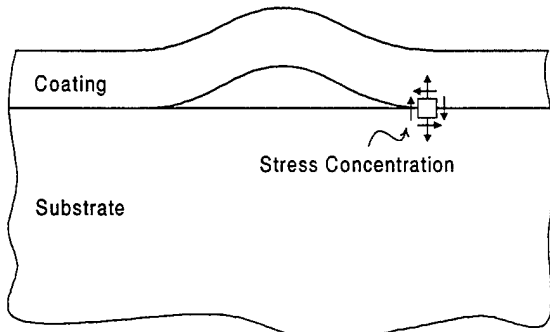
example, surface cracking usually occurs during the heating process and/or when the coating is under in-plane tensile loading. These cracks tend to branch into T-shaped and propagate along or parallel to the interface. Consequently, the coating may either peel off directly or spall off due to the connection of these T-shaped cracks. On the other hand, in the presence of interface cracks the residual compressive stresses induced by, for example, thermal expansion mismatch upon cooling during thermal cycling and/or bond coat oxidation provide the driving force for coating to blister and eventually spall off. These alternative failure processes exhibit very different dependences on the mechanical properties of the coatings and interfaces, and should be considered separately. While the fracture associated with tensile stresses is equally important, the focus of this study will be on the spallation associated with residual compressive stresses.

## 1.2 Spallation of Coatings

In the presence of an interface crack and in-plane compressive stress the final stage of the spallation appears to be through the buckling mechanism. From Figure 1.1 it may be seen that for flat plates the interface crack does not change the stress state without buckling because the prior normal and shear stresses at the interface are zero and the in-plane compression is unchanged and hence, there is no driving force. However, the driving force for crack growth at the interface arises when elastic buckling of the coating initiates. Buckling of the coating occurs when the in-plane compression in the coating exceeds a critical value. Propagation of the interface crack would take place once the crack driving force exceeds the fracture toughness of the material element within the vicinity of the crack tip. The spallation may also be caused by a brittle rupture mechanism due to bending.



(a) Crack without buckling



(b) Crack with buckling

Figure 1.1 A schematic showing (a) an interface crack without coating buckling and (b) the stress concentration that accompanies coating buckling.

A prerequisite for the buckling mechanism associated with compressive stresses is the preexisting separation along or parallel to the interface. For example, an interface crack in a Rene-41/PSZ TBC system [12] requires a length of about 20 times coating thickness for buckling to occur after 800°C cooling. It had been suggested that the requisite separation may occur by localized void coalescence [13] at elevated temperatures. However, the source of inhomogeneous void formation and coalescence is still ambiguous. One likely source of void formation, analogous to void nucleation at grain boundaries during creep, is the presence of out-of-plane tensile stresses at the interface [14]. For example, the relatively large local tensions that develop in the presence of boundary waviness, especially in the presence of interface sliding, may exceed the critical void nucleation stress and permit the formation of stable voids. Another likely mechanism for crack initiation also involves interface asperities. Usually the bond coat-top coat interface is uneven with

local peaks and valleys rather than flat, especially in the case of thermal spraying process for the purpose of better bonding between bond coat and top coat. Oxidation preference is another source for interface asperities. For example, it is observed in the Pt-Al bond coat/electron beam physical vapor deposition (EBPVD) PSZ top coat TBC system that a thermally grown oxide (TGO) layer has wedge-like intrusions into the bond coat grain boundaries (bond coat thickness  $\sim 30 \mu\text{m}$ , grain size  $\sim 75$  to  $100 \mu\text{m}$ ) [15]. Regardless of the oxidation mechanism stresses would develop during the oxidation of curved surfaces and the sign (tension or compression) of the stresses is strongly mechanism and curvature sensitive [16]. In most cases the stress magnitude increases rapidly as the radius of curvature of the surface decreases. Furthermore, it has been shown that large tensile stress concentrations exist at the peak or the valley of asperities [13]. Hence, when the asperities satisfy certain size requirements, localized brittle cracking may occur. These cracks or voids may further connect with each other to form a large separation along or near the interface.

One major player in the spallation of TBCs is the thermally grown oxide. Earlier experimental results [17-19] showed that under thermal cycling TBC spalled off during the cool-down period. Furthermore, the spallation occurred either at the bond coat-TGO interface, in TGO layer, at the TBC-TGO interface, or in the TBC layer and near the TBC-TGO interface. Intuitively, the TGO layer may be attributed as the weak cleavage plane for crack growth. Still, to understand the influence of TGO on the spallation of TBCs a more detailed investigation on the mechanisms of oxide growth and its material properties is required.

Usually the oxide layer of thickness less than  $1 \mu\text{m}$  grows from bond coat during the TBC deposition process, and it continues to grow during the heat treatment ( $\sim 1000^\circ\text{C}$ ) and during service stage ( $900$ - $1300^\circ\text{C}$  for turbine vane and blade). Many high temperature isothermal and thermal cycling oxidation experiments have been performed for various

TBC systems [17-22]. By using X-ray diffraction (XRD) these experiments had identified that the major oxide constituent is rhombohedral  $\alpha$ -Al<sub>2</sub>O<sub>3</sub>. Some other minor oxide phases, including Cr<sub>2</sub>O<sub>3</sub>, CoO, NiO, and various kinds of Co(Cr,Al)<sub>2</sub>O<sub>4</sub> or Ni(Cr,Al)<sub>2</sub>O<sub>4</sub> spinels, were also detected for the case of MCrAlY (M being a metal) bond coat. It was observed from the fractograph of the surface of oxide scale after the spallation of top coat occurred that columnar Al<sub>2</sub>O<sub>3</sub> grains prevail as a subscale in contact with the bond coat and that NiO and Ni(Cr,Al)<sub>2</sub>O<sub>4</sub> grows on the surface of the rather uniform Al<sub>2</sub>O<sub>3</sub> [18-20,23]. Furthermore, such forms of oxide were observed on the spalling plane in the experiments. Consequently, it may be conjectured that these minor oxide phases would, first weaken the bonding strength of the interface and, second by work as interface asperities that enhance the crack initiation.

From the location and microstructure of oxide layer one may presume that the mechanism of oxide growth is via the inward diffusion of oxygen through the ceramic top coat and the outward diffusion of cation (mainly Al<sup>3+</sup>) toward the bond coat surface. Furthermore, investigations of self diffusion in Al<sub>2</sub>O<sub>3</sub> [24] have shown that oxygen transport along grain boundaries is considerably faster than within the grains. For aluminum in Al<sub>2</sub>O<sub>3</sub>, diffusion through both paths are roughly equally fast and about the same as that for oxygen transport at grain boundaries. As a result the new aluminum oxide tends to form at the columnar grain boundaries of the existing Al<sub>2</sub>O<sub>3</sub>.

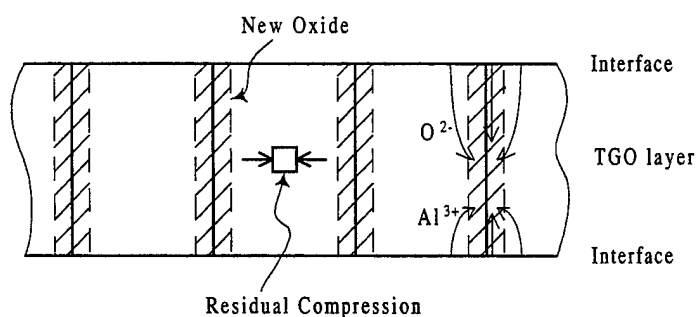


Figure 1.2 Residual compression induced by internal oxide formation.

Oxide scales on, for example [25], FeCrAl alloys often show pronounced lateral growth which is again explained by the fresh oxide formation at grain boundaries. Consequently, residual stresses are likely to occur for such oxide structure (Figure 1.2). A consequence of the residual stress would be local sliding and debonding when the stress exceeds a critical value [13]. Note that the compressive residual stress is not likely to be uniform, but rather vary with position through the TGO layer such that the spatial variation is dictated by the relative rates of oxygen and aluminum diffusion to internal grain boundaries. Thickening of the oxide coating would, in this instance, occur by diffusive creep, involving a compression induced flux of aluminum and oxygen ions from the grain boundary to the bond coat-TGO interface and/or TGO-top coat interface.

Because of the extended exposure to elevated temperature the TBC system may undergo significant stress relaxation. It is well known that most polycrystalline brittle materials are not amenable to plastic deformation by dislocation motion. Instead, for  $\text{Al}_2\text{O}_3$  in excess 1000°C, the primary mode of deformation involves diffusion. For columnar type microstructure subjected to biaxial compression, all of the grain boundaries are under essentially the same stress and atom transport occur from these boundaries onto the bond coat-TGO and TGO-top coat interfaces. The deformation rate is limited by the motion of the slowest diffusing species, along either the grain boundaries or the interfaces. The macroscopic deformation due to this diffusion mechanism may be characterized by Coble creep [25] which is essentially governed by linear viscoelastic constitutive laws. Note that usually the oxidation process occurs at temperatures that permit limited stress relaxation. At higher temperature the relaxation becomes more prevalent compared with the oxidation process. The stress effects are thus more likely to obtain at lower oxidation temperatures.

Aside from the intrinsic residual stresses resulting from the oxidation process, the differences between the thermal expansion coefficients of the metal substrate, bond coat,

oxide scale, and top coat also lead to the development of residual stress during cooling down from the elevated temperature in the thermal-cycling process. Usually the thermal expansion coefficients are much smaller for ceramic TBC and TGO compared with metallic bond coat and substrate. It is also known that except from the compressive intrinsic stress in the TGO layer arisen from oxidation process, the TBC system is under nearly stress-free condition at elevated temperature. Consequently, during the cool down process in-plane residual compressive stresses are developed in the top coat and TGO layer. The residual compressive stresses may lead to interface separation and eventually the spallation of coating from the substrate.

One may observe that compressive residual stresses would still be developed in the top coat during the cool-down process and thus the spallation may occur even without the existence of TGO layer. However, due to the fact that compared to other materials used in the TBC system the thermal expansion coefficient is the smallest and the stiffness is the highest for aluminum oxide (e.g. Table 1.1 [26]), the magnitude of the residual stresses in the TGO layer would be very high. The higher (in magnitude) residual stresses associated with oxide may accelerate the crack initiation and propagation and thus lead to earlier spallation.

By introducing the concept of FGM replacing the homogeneous ceramic top coat, the in-plane thermal residual stresses would reduce significantly. However, the advantage of FGM coating might be compromised once the metallic particle in the FGM oxidizes. In an earlier experiment [27] it was observed that, again, spallation occurred in the FGM coating upon the cooling down stage after extended exposure to elevated temperature. Metallographic and XRD analysis indicated that most of the metallic phase in the spalled region was oxidized. One may imagine that during service an unfavorable oxide layer is "inserted" into the graded material transition region. A concept to overcome this is to add an extra oxygen barrier graded layer such that the alternative TBC system contains multi-

FGM layers (thermal barrier/oxygen barrier FGM layer and oxygen barrier/metallic bond coat FGM layer) above the structural components [27].

Table 1.1 Material properties of a thermal barrier coating system at 22, 566, and 1149°C [26].

	Young's Modulus (GPa)	Poisson's Ratio	Coefficient of Thermal Expansion ( $\times 10^{-6}^{\circ}\text{C}^{-1}$ )
Substrate (Ni-based Superalloy)	175.8	0.25	13.91
	150.4	0.2566	15.36
	94.1	0.3224	19.52
Bond Coat (NiCrAlY)	137.9	0.27	15.16
	121.4	0.27	15.37
	93.8	0.27	17.48
TGO ( $\text{Al}_2\text{O}_3$ )	386	0.257	6
	349	0.257	8
	311	0.257	8.9
TBC ( $\text{ZrO}_2$ -8wt.% $\text{Y}_2\text{O}_3$ )	27.6	0.25	10.01
	6.9	0.25	11.01
	1.84	0.25	12.41

### 1.3 Literature Survey

Debonding or spallation induced by in-plane compressive stress is considered to be one of the dominant modes of failure in thin films and coatings used, for example, in microelectronics and optical applications as well as in wear, corrosion, and heat resistant coatings. In many composite laminates delaminations are also being frequently observed due to either manufacturing processes or low-velocity lateral impact. Many analytical and experimental investigations have been performed to clarify the influence of embedded cracks/delaminations on the compressive strength of coatings and composite laminates [28-38]. Surveys and reviews of such studies have been given, e.g., by Garg [39], Abrate [40], and Hutchinson and Suo [41]. Most of these investigations have utilized structural mechanics theories such as those for beams, plates, and shells, and, therefore, employed

approximations on the coating thickness/debonding length ratio, the boundary conditions enforced at the edges of debonding, and the deformed shape of the coating. Such analyses provide estimates of the critical debonding size as well as other practical information. However, solutions using a more exact theory are preferable because they provide more accurate results and give a basis for assessing the accuracy of those simplified models.

Various studies have been carried out on the instability problem of embedded cracks within the context of continuum mechanics. By using exact equilibrium equations Keer, Nemat-Nasser, and Oranratnachai [42] estimated the buckling loads for a half space or layer containing an array of coplanar equally spaced cracks. This study was done for a class of hypoelastic materials for which the Jaumann rate of the Kirchhoff stress relates to the deformation rate tensor by an isotropic linear relation similar to Hooke's law. Wang *et al.* [43] studied the local buckling stability problem of a half space containing a through-the-thickness crack subjected to in-plane compression by solving the stability equation of linear elasticity theory and using singular integral equation technique. The plane strain stability problem of a layer bonded to a half space with an interface crack was also investigated by Wang and Takao [44]. Using a similar approach, Madenci and coworkers [45-50] examined the local buckling and imperfection problems of a layer or half-space containing a penny shaped crack subjected to mechanical or thermal loading.

Because of the nonlinear nature of the problem, finite element methods have been used extensively in investigating the general problems of buckling and delamination growth. By using a geometrically nonlinear finite element code based on structural mechanics Nilsson and Giannakopoulos [51] analyzed buckling induced delamination growth of an initial circular delamination for composite laminates loaded in in-plane compression. Based on the method given by Storåkers and Andersson [52], in this analysis the strain energy release rates were extracted from the calculated plate resultants. Nilsson and coworkers [53-56] further extended the same finite element procedure to account for crack-tip

fracture mode separation by reducing the loading at the crack tip in a nonlinear plate to that of a linear beam. The stress intensity factor were then identified by two-dimensional split beam solution by Suo and Hutchinson [57] and Suo [58]. By using a three-dimensional finite element formulation with modified crack closure method [59] for extracting fracture mechanics parameters Whitcomb [60-62] considered various relevant factors in the analysis of delamination buckling and growth including the influence of crack tip mode dependence, general contours, and contact at delamination buckling. As for the studies involving TBCs, Nusier and Newaz [63] investigated the thermal buckling problem of a stepped disk specimen with an interface crack at the bond coat-top coat interface by using a two-dimensional nonlinear finite element procedure with a virtual crack extension method [64] for fracture mechanics parameter read-out.

Although many crack problems involving thermal or mechanical loading have been studied extensively for FGMs (e.g., [65-67] for problems involving interface cracking and [68-70] for problems with cracks perpendicular to the interface), very limited studies have been done for the spallation problem associated with in-plane compressive stresses. The only work that the author is aware of was done by Bao and Cai [71] who studied the delamination cracking problem in functionally graded coating/substrate system and examined the effect of various factors including coating gradation, location of the crack, and the thickness ration of the coating/substrate system by following the split beam approach [58].

#### 1.4 Overview

The main objectives of this study of the interface crack problem in a functionally graded coating/homogeneous substrate material system subjected to thermally or mechanically induced in-plane compressive stresses may be summarized as

- To develop a fracture model

- To determine the load/crack length relation at instability
- To obtain the solution of the crack problem
- To examine the effect of material inhomogeneity on the crack problem.

In Chapter 2 the problem of a FGM coating bonded to a semi-infinite homogeneous substrate containing an interface crack subjected to fixed-grip compression parallel to the free surface is formulated within the context of kinematically nonlinear plane elasticity. By using a perturbation technique the nonlinear equilibrium equations are reduced to a pair of linear partial differential equations, in which the compressive strain appears as unknown constant coefficient, with the displacement perturbations as unknown functions. These equations may further be reduced to a pair of homogeneous Cauchy-type singular integral equations by means of applying Fourier transformation, introducing a new set of unknown functions (i.e., the derivative of crack opening displacements), and substituting the boundary and continuity conditions. The resulting eigenvalue problem is then solved numerically as described in Chapter 3. The compressive strain at buckling instability and the phase angle are obtained from the lowest eigenvalue and corresponding eigenvector of the homogeneous equations. By following the same procedure, the buckling instability problem of a FGM layer bonded to a semi-infinite homogeneous substrate with a highly weakened interfacial zone, which contains a series of short cracks and is modeled by a large crack that covers the weakened zone with crack surface bridging, is also considered in Chapters 2 and 3.

Note that the perturbation technique described in Chapter 2 can only provide the information at the inception of elastic instability and would not be suitable to determine the stresses and displacements beyond the instability point. This is done by performing the related nonlinear postbuckling analysis in Chapter 4. In this study it is assumed that locally the constitutive equations are linear and the problem is solved by using a geometrically nonlinear finite element program. Enriched crack tip elements are used to calculate the

stress intensity factors and strain energy release rate directly. At each value of compressive load the equilibrium is determined by using the principle of virtual work. An incremental-iterative procedure is used for solving the related nonlinear equations.

In Chapter 5 the results for stability and postbuckling analysis are given for some specific material properties. Effect of coating/substrate thickness ratio and the initial curvature of the specimen on the fracture mechanics parameters are studied by using finite element method. A more realistic axisymmetric top coat/TGO/bond coat/substrate specimen with an interface crack under temperature drop is also considered. The top coat can be either homogeneous ceramics or metal/ceramics FGM. These results are then compared with solutions based on structural mechanics theory.

Chapter 6 gives the conclusions drawn from this study. Directions for future research are also discussed.

## Chapter 2

### Buckling of FGM Coating - Analytical Procedure

#### 2.1 Governing Equations

As shown in Appendix A, the equilibrium equations and boundary conditions of finite deformation theory of elasticity, without body forces, may be expressed as

$$\sigma_{ij,j} + (\sigma_{jk}u_{i,k})_{,j} = 0, \quad (2.1)$$

$$(\sigma_{ij} + \sigma_{jk}u_{i,k})n_j = T_i, \quad (2.2)$$

respectively, where  $u_i$ ,  $\sigma_{ij}$ ,  $T_i$ , and  $n_i$  are the components of the displacement, second Piola-Kirchhoff stress, applied traction, and unit normal vector, respectively. Note that (2.1) and (2.2) are referenced to a fixed Cartesian coordinate system under the Lagrangian description of deformation. The Green-Lagrange strains are given by

$$\epsilon_{ij} = \frac{1}{2}(u_{i,j} + u_{j,i} + u_{k,i}u_{k,j}). \quad (2.3)$$

Note that (2.1), (2.2), and (2.3) correspond to (A21), (A15), and (A9), respectively, except that the left sub- and superscripts used in Appendix A are omitted here for simplicity. A set of linearized governing equations for the buckling analysis may be developed under the adjacent equilibrium concept. Assume that a critical original equilibrium configuration, denoted by (0), exists (at bifurcation point). The displacements, stresses, tractions, and strains for an adjacent (buckled) configuration may be expressed as

$$u_i = u_i^{(0)} + u_i^*, \quad (2.4a)$$

$$\sigma_{ij} = \sigma_{ij}^{(0)} + \sigma_{ij}^*, \quad (2.4b)$$

$$T_i = T_i^{(0)} + T_i^*, \quad (2.4c)$$

$$\epsilon_{ij} = \epsilon_{ij}^{(0)} + \epsilon_{ij}^*, \quad (2.4d)$$

respectively, where quantity with asterisk denotes a small deviation from its critical original configuration. Substituting (2.4) into (2.1), we have

$$\sigma_{ij,j}^{(0)} + (\sigma_{jk}^{(0)} u_{i,k}^{(0)})_{,j} + \sigma_{ij,j}^* + (\sigma_{jk}^{(0)} u_{i,k}^*)_{,j} + (\sigma_{jk}^* u_{i,k}^{(0)})_{,j} + (\sigma_{jk}^* u_{i,k}^*)_{,j} = 0. \quad (2.5)$$

By using the equilibrium of the original configuration and by neglecting higher order terms, (2.5) may be reduced to

$$[(\delta_{ik} + u_{i,k}^{(0)})\sigma_{jk}^* + \sigma_{jk}^{(0)} u_{i,k}^*]_{,j} = 0, \quad (2.6)$$

where  $\delta_{ik}$  denotes the Kronecker delta. Similarly, by substituting (2.4) into (2.2) and (2.3) and neglecting higher order terms, we may obtain

$$[(\delta_{ik} + u_{i,k}^{(0)})\sigma_{jk}^* + \sigma_{jk}^{(0)} u_{i,k}^*]n_j = T_i^*, \quad (2.7)$$

$$\epsilon_{ij}^* = \frac{1}{2}[(\delta_{ik} + u_{k,i}^{(0)})u_{k,j}^* + (\delta_{jk} + u_{k,j}^{(0)})u_{k,i}^*]. \quad (2.8)$$

Assuming that the displacement derivatives in the original configuration are small, i.e.,  $u_{i,k}^{(0)} \ll 1$ , Equations (2.6)-(2.8) may further be reduced to

$$\sigma_{ij,j}^* + (\sigma_{jk}^{(0)} u_{i,k}^*)_{,j} = 0, \quad (2.9)$$

$$(\sigma_{ij}^* + \sigma_{jk}^{(0)} u_{i,k}^*)n_j = T_i^*, \quad (2.10)$$

$$\epsilon_{ij}^* = \frac{1}{2}(u_{i,j}^* + u_{j,i}^*). \quad (2.11)$$

Equations (2.9)-(2.11) may then be used for studying the buckling instability problems.

## 2.2 Formulation of the Crack Problem

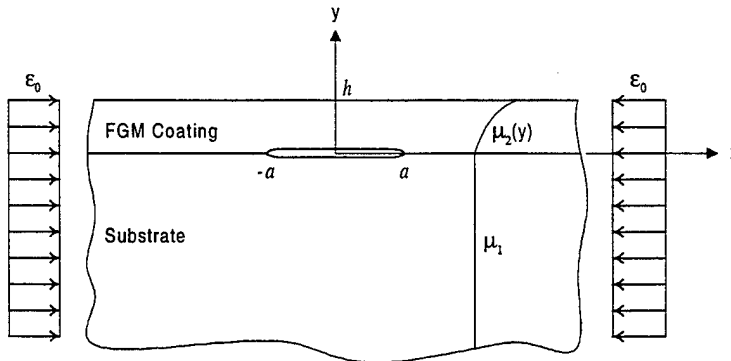


Figure 2.1 Functionally graded coating bonded to a homogeneous substrate with an interface crack subjected to uniform compressive strain.

The plane strain problem described in Figure 2.1 for a layered system subjected to a uniform compressive strain  $\epsilon_0$  is considered. The medium consists of a FGM coating of thickness  $h$  bonded to a semi-infinite substrate containing an interface crack of length  $2a$ . The compressive strain  $\epsilon_0$  represents the magnitude of the external load. It is assumed that the substrate is homogeneous with elastic constants  $\mu_1, \kappa_1$ , the coating is inhomogeneous with elastic parameters  $\mu_2, \kappa_2$ , and  $\mu_2$  is approximated by

$$\mu_2(y) = \mu_1 e^{\gamma y} \quad (2.12)$$

where  $\mu_i$  is the shear modulus,  $\kappa_i = 3 - 4\nu_i$  for plane strain,  $\nu_i$  being the Poisson's ratio. The subscripts,  $i = 1$  and  $2$ , denote the substrate and coating, respectively. It may be seen that at the original equilibrium configuration we have

$$\begin{aligned} \epsilon_{ixx}^{(0)} &= -\epsilon_0, \\ \sigma_{iyy}^{(0)} &= 0, \quad i = 1, 2. \\ \sigma_{ixy}^{(0)} &= 0, \end{aligned} \quad (2.13)$$

From the generalized Hooke's law for the plane elasticity problem given by

$$\begin{aligned}\sigma_{xx} &= \left(\frac{\kappa+1}{\kappa-1}\right)\mu\epsilon_{xx} + \left(\frac{3-\kappa}{\kappa-1}\right)\mu\epsilon_{yy}, \\ \sigma_{yy} &= \left(\frac{3-\kappa}{\kappa-1}\right)\mu\epsilon_{xx} + \left(\frac{\kappa+1}{\kappa-1}\right)\mu\epsilon_{yy}, \\ \sigma_{xy} &= \mu\epsilon_{xy},\end{aligned}\tag{2.14}$$

and using (2.13) we may obtain

$$\begin{aligned}\epsilon_{iyy}^{(0)} &= \left(\frac{3-\kappa_i}{\kappa_i+1}\right)\epsilon_0, \\ \sigma_{ixx}^{(0)} &= -\frac{8\mu_i\epsilon_0}{\kappa_i+1}, \\ i &= 1, 2.\end{aligned}\tag{2.15}$$

Substituting (2.13) and (2.15) into (2.9), we have

$$\frac{\partial\sigma_{ixx}^*}{\partial x} + \frac{\partial\sigma_{ixy}^*}{\partial y} - \left(\frac{8\mu_i\epsilon_0}{\kappa_i+1}\right)\frac{\partial^2 u_i^*}{\partial x^2} = 0,\tag{2.16a}$$

$$\frac{\partial\sigma_{ixy}^*}{\partial x} + \frac{\partial\sigma_{iyy}^*}{\partial y} - \left(\frac{8\mu_i\epsilon_0}{\kappa_i+1}\right)\frac{\partial^2 v_i^*}{\partial x^2} = 0,\tag{2.16b}$$

where  $i = 1, 2$ . From the Hooke's law the  $\sigma_{ij}^* - \epsilon_{ij}^*$  relations may be expressed as

$$\begin{aligned}\sigma_{xx}^* &= \left(\frac{\kappa+1}{\kappa-1}\right)\mu\epsilon_{xx}^* + \left(\frac{3-\kappa}{\kappa-1}\right)\mu\epsilon_{yy}^*, \\ \sigma_{yy}^* &= \left(\frac{3-\kappa}{\kappa-1}\right)\mu\epsilon_{xx}^* + \left(\frac{\kappa+1}{\kappa-1}\right)\mu\epsilon_{yy}^*, \\ \sigma_{xy}^* &= \mu\epsilon_{xy}^*.\end{aligned}\tag{2.17}$$

In previous studies it was shown that the influence of the variation in Poisson's ratio in the crack problem is rather insignificant and  $\kappa$  may be assumed to be constant throughout the medium. Thus, by substituting (2.11) and (2.17) into (2.16), we find the governing equations for the stability problem as follows:

$$(\kappa + 1) \frac{\partial^2 u_i^*}{\partial x^2} + (\kappa - 1) \frac{\partial^2 u_i^*}{\partial y^2} + 2 \frac{\partial^2 v_i^*}{\partial x \partial y} + \gamma_i (\kappa - 1) \left( \frac{\partial u_i^*}{\partial y} + \frac{\partial v_i^*}{\partial x} \right) - 8 \left( \frac{\kappa - 1}{\kappa + 1} \right) \epsilon_0 \frac{\partial^2 u_i^*}{\partial x^2} = 0, \quad (2.18a)$$

$$(\kappa - 1) \frac{\partial^2 v_i^*}{\partial x^2} + (\kappa + 1) \frac{\partial^2 v_i^*}{\partial y^2} + 2 \frac{\partial^2 u_i^*}{\partial x \partial y} + \gamma_i (3 - \kappa) \frac{\partial u_i^*}{\partial x} + \gamma_i (\kappa + 1) \frac{\partial v_i^*}{\partial y} - 8 \left( \frac{\kappa - 1}{\kappa + 1} \right) \epsilon_0 \frac{\partial^2 v_i^*}{\partial x^2} = 0, \quad (2.18b)$$

where  $i = 1, 2$ , and  $\gamma_1 = 0$  for the homogeneous substrate,  $\gamma_2 = \gamma$  for the FGM coating. From Equations (2.10), (2.13), and (2.15) the boundary conditions may be expressed in the general form as

$$\sigma_{kij}^* n_j = T_{ki}^*, \quad k = 1, 2, \quad (2.19)$$

where  $n_j = n_y$  along  $y = h$  and  $n_j = -n_y$  along  $y = 0$  for the FGM coating;  $n_j = n_y$  along  $y = 0$  for the homogeneous substrate. From Equation (2.19) the boundary and continuity conditions for the medium can be written explicitly as follows:

$$\sigma_{2yy}^*(x, h) = 0, \quad \sigma_{2xy}^*(x, h) = 0, \quad -\infty < x < \infty, \quad (2.20a,b)$$

$$\sigma_{1yy}^*(x, -0) = \sigma_{2yy}^*(x, +0), \quad \sigma_{1xy}^*(x, -0) = \sigma_{2xy}^*(x, +0), \quad -\infty < x < \infty, \quad (2.20c,d)$$

$$\sigma_{1yy}^*(x, -0) = 0, \quad \sigma_{1xy}^*(x, -0) = 0, \quad -a < x < a, \quad (2.20e,f)$$

$$u_1^*(x, -0) = u_2^*(x, +0), \quad v_1^*(x, -0) = v_2^*(x, +0), \quad |x| > a. \quad (2.20g,h)$$

Therefore, the buckling instability problem may be characterized by Equations (2.18) and (2.20). To solve Equation (2.18), first we define the Fourier transforms of the two displacement deviation components,  $u_i^*$  and  $v_i^*$ , respectively, as

$$U_i(\alpha, y) = \int_{-\infty}^{\infty} u_i^*(x, y) e^{-i\alpha x} dx, \quad i = 1, 2. \quad (2.21)$$

$$V_i(\alpha, y) = \int_{-\infty}^{\infty} v_i^*(x, y) e^{-i\alpha x} dx,$$

By definition,  $u_i^*$  and  $v_i^*$  may be expressed in terms of  $U_i$  and  $V_i$ , respectively as

$$\begin{aligned} u_i^*(x, y) &= \frac{1}{2\pi} \int_{-\infty}^{\infty} U_i(\alpha, y) e^{i\alpha x} d\alpha, \\ v_i^*(x, y) &= \frac{1}{2\pi} \int_{-\infty}^{\infty} V_i(\alpha, y) e^{i\alpha x} d\alpha, \end{aligned} \quad i = 1, 2. \quad (2.22)$$

For the inhomogeneous layer 2, by substituting (2.21) into (2.18), it may be shown that

$$\begin{aligned} - \left[ (\kappa + 1) - 8 \left( \frac{\kappa - 1}{\kappa + 1} \right) \epsilon_0 \right] \alpha^2 U_2 + (\kappa - 1) \frac{d^2 U_2}{dy^2} + 2i\alpha \frac{dV_2}{dy} \\ + \gamma(\kappa - 1) \frac{dU_2}{dy} + \gamma(\kappa - 1)i\alpha V_2 = 0 \end{aligned} \quad (2.23a)$$

$$\begin{aligned} - \left[ (\kappa - 1) - 8 \left( \frac{\kappa - 1}{\kappa + 1} \right) \epsilon_0 \right] \alpha^2 V_2 + (\kappa + 1) \frac{d^2 V_2}{dy^2} + 2i\alpha \frac{dU_2}{dy} \\ + \gamma(3 - \kappa)i\alpha U_2 + \gamma(\kappa + 1) \frac{dV_2}{dy} = 0 \end{aligned} \quad (2.23b)$$

Solving Equation (2.23) we obtain that

$$\begin{aligned} U_2(\alpha, y) &= \sum_{k=1}^4 C_k(\alpha) e^{n_k y}, \\ V_2(\alpha, y) &= \sum_{k=1}^4 m_k(\alpha) C_k(\alpha) e^{n_k y}, \end{aligned} \quad 0 < y < h, \quad (2.24)$$

where  $C_1, \dots, C_4$  are unknown functions of  $\alpha$ ,  $n_1, \dots, n_4$  are the roots of the characteristic equation

$$\begin{aligned} n^4 + 2\gamma n^3 + \left\{ \gamma^2 - 2\alpha^2 \left[ 1 - \frac{8\kappa\epsilon_0}{(\kappa+1)^2} \right] \right\} n^2 - 2\alpha^2 \gamma \left[ 1 - \frac{8\kappa\epsilon_0}{(\kappa+1)^2} \right] n \\ + \left( \frac{3-\kappa}{\kappa+1} \right) \alpha^2 \gamma^2 + \left\{ 1 + \frac{16\epsilon_0}{(\kappa+1)^2} \left[ 4 \left( \frac{\kappa-1}{\kappa+1} \right) \epsilon_0 - \kappa \right] \right\} \alpha^4 = 0, \end{aligned} \quad (2.25)$$

and  $m_1, \dots, m_4$  are given by

$$m_k(\alpha) = \frac{-i\alpha[2n_k + \gamma(3 - \kappa)]}{(\kappa + 1)n_k^2 + \gamma(\kappa + 1)n_k - \left[(\kappa - 1) - 8\left(\frac{\kappa - 1}{\kappa + 1}\right)\epsilon_0\right]\alpha^2}, \quad k = 1, \dots, 4. \quad (2.26)$$

Solving (2.26) we find

$$n_1 = -\frac{\gamma}{2} - \sqrt{\frac{\gamma^2}{4} + \alpha^2 \left[1 - \frac{8\kappa\epsilon_0}{(\kappa + 1)^2}\right] + \alpha \sqrt{\alpha^2 \frac{(8\epsilon_0)^2}{(\kappa + 1)^4} - \gamma^2 \left(\frac{3 - \kappa}{\kappa + 1}\right)}}, \quad (2.27a)$$

$$n_2 = -\frac{\gamma}{2} - \sqrt{\frac{\gamma^2}{4} + \alpha^2 \left[1 - \frac{8\kappa\epsilon_0}{(\kappa + 1)^2}\right] - \alpha \sqrt{\alpha^2 \frac{(8\epsilon_0)^2}{(\kappa + 1)^4} - \gamma^2 \left(\frac{3 - \kappa}{\kappa + 1}\right)}}, \quad (2.27b)$$

$$n_3 = -\frac{\gamma}{2} + \sqrt{\frac{\gamma^2}{4} + \alpha^2 \left[1 - \frac{8\kappa\epsilon_0}{(\kappa + 1)^2}\right] + \alpha \sqrt{\alpha^2 \frac{(8\epsilon_0)^2}{(\kappa + 1)^4} - \gamma^2 \left(\frac{3 - \kappa}{\kappa + 1}\right)}}, \quad (2.27c)$$

$$n_4 = -\frac{\gamma}{2} + \sqrt{\frac{\gamma^2}{4} + \alpha^2 \left[1 - \frac{8\kappa\epsilon_0}{(\kappa + 1)^2}\right] - \alpha \sqrt{\alpha^2 \frac{(8\epsilon_0)^2}{(\kappa + 1)^4} - \gamma^2 \left(\frac{3 - \kappa}{\kappa + 1}\right)}}. \quad (2.27d)$$

Similarly, for the homogeneous medium 1,  $-\infty < y < 0$ , the solution of (2.18) with  $\gamma_1 = 0$  may be obtained by letting  $\gamma = 0$  in (2.23) and (2.25)-(2.27). The transformed displacement perturbations may then be expressed as follows:

$$U_1(\alpha, y) = \sum_1^4 A_k(\alpha) e^{\lambda_k y}, \quad -\infty < y < 0, \quad (2.28)$$

$$V_1(\alpha, y) = \sum_1^4 r_k(\alpha) A_k(\alpha) e^{\lambda_k y},$$

where  $A_1, \dots, A_4$  are unknown functions of  $\alpha$ ,  $\lambda_1, \dots, \lambda_4$  may be expressed as

$$\begin{aligned}
\lambda_1 &= \sqrt{1 - \frac{8\epsilon_0}{\kappa + 1} |\alpha|}, \\
\lambda_2 &= \sqrt{1 - \frac{8(\kappa - 1)\epsilon_0}{(\kappa + 1)^2} |\alpha|}, \\
\lambda_3 &= -\sqrt{1 - \frac{8\epsilon_0}{\kappa + 1} |\alpha|}, \\
\lambda_4 &= -\sqrt{1 - \frac{8(\kappa - 1)\epsilon_0}{(\kappa + 1)^2} |\alpha|},
\end{aligned} \tag{2.29}$$

and  $r_1, \dots, r_4$  are given by

$$\begin{aligned}
r_1(\alpha) &= -i\frac{\alpha}{\lambda_1}, \\
r_2(\alpha) &= -i\frac{\lambda_2}{\alpha}, \\
r_3(\alpha) &= -i\frac{\alpha}{\lambda_3}, \\
r_4(\alpha) &= -i\frac{\lambda_4}{\alpha}.
\end{aligned} \tag{2.30}$$

However, the boundedness condition of  $u_1^*$  and  $v_1^*$  as  $y$  goes to  $-\infty$  requires that

$$A_3 = A_4 = 0. \tag{2.31}$$

By substituting (2.22), (2.24), (2.26) and (2.27) into (2.11) and (2.17) we may obtain the stress perturbation components for the inhomogeneous coating 2 ( $0 < y < h$ ) as follows:

$$\sigma_{2xx}^*(x, y) = \frac{\mu_2}{2\pi} \int_{-\infty}^{\infty} \sum_{k=1}^4 \left[ i\alpha \left( \frac{\kappa+1}{\kappa-1} \right) + m_k n_k \left( \frac{3-\kappa}{\kappa-1} \right) \right] C_k e^{n_k y} e^{i\alpha x} d\alpha, \tag{2.32a}$$

$$\sigma_{2yy}^*(x, y) = \frac{\mu_2}{2\pi} \int_{-\infty}^{\infty} \sum_{k=1}^4 \left[ i\alpha \left( \frac{3-\kappa}{\kappa-1} \right) + m_k n_k \left( \frac{\kappa+1}{\kappa-1} \right) \right] C_k e^{n_k y} e^{i\alpha x} d\alpha, \tag{2.32b}$$

$$\sigma_{2xy}^*(x, y) = \frac{\mu_2}{2\pi} \int_{-\infty}^{\infty} \sum_{k=1}^4 (n_k + i\alpha m_k) C_k e^{n_k y} e^{i\alpha x} d\alpha. \quad (2.32c)$$

Similarly, from (2.11), (2.17), (2.22), (2.28)-(2.31) the stress perturbation components for the homogeneous substrate 1 ( $-\infty < y < 0$ ) are given by

$$\begin{aligned} \sigma_{1xx}^*(x, y) = & \frac{\mu_1}{2\pi} \int_{-\infty}^{\infty} \left\{ 2A_1 e^{\lambda_1 y} \right. \\ & \left. + \left[ \frac{\kappa+1}{\kappa-1} - \left( \frac{3-\kappa}{\kappa-1} \right) \left( \frac{\lambda_2}{\alpha} \right)^2 \right] A_2 e^{\lambda_2 y} \right\} i\alpha e^{i\alpha x} d\alpha, \end{aligned} \quad (2.33a)$$

$$\sigma_{1yy}^*(x, y) = - \frac{\mu_1}{2\pi} \int_{-\infty}^{\infty} \left\{ 2A_1 e^{\lambda_1 y} + \left[ 1 + \left( \frac{\lambda_1}{\alpha} \right)^2 \right] A_2 e^{\lambda_2 y} \right\} i\alpha e^{i\alpha x} d\alpha, \quad (2.33b)$$

$$\sigma_{1xy}^*(x, y) = \frac{\mu_1}{2\pi} \int_{-\infty}^{\infty} \left[ \left( \lambda_1 + \frac{\alpha^2}{\lambda_1} \right) A_1 e^{\lambda_1 y} + 2\lambda_2 A_2 e^{\lambda_2 y} \right] e^{i\alpha x} d\alpha. \quad (2.33c)$$

To solve the unknowns  $C_1, \dots, C_4$  and  $A_1, A_2$  the homogeneous equations (2.20a-d) may be used to eliminate four of the six unknowns and the mixed boundary conditions (2.20e-h) would give a pair of dual integral equations to determine the remaining two.

### 2.3 The Integral Equations

We define the density functions as follows:

$$\begin{aligned} \frac{\partial}{\partial x} [v_2^*(x, +0) - v_1^*(x, -0)] &= f_1(x), \\ &\quad -\infty < x < \infty. \end{aligned} \quad (2.34)$$

$$\frac{\partial}{\partial x} [u_2^*(x, +0) - u_1^*(x, -0)] = f_2(x),$$

It may be seen that (2.20g,h) would be satisfied if we require

$$f_i(x) = 0, \quad |x| > a, \quad i = 1, 2, \quad (2.35)$$

$$\int_{-a}^a f_i(x)dx = 0, \quad i = 1, 2. \quad (2.36)$$

Note that (2.36) is also known as the single-valuedness condition. Physically it means that the displacements are single-valued for the uncracked portion along  $y = 0$ . By taking Fourier transform of (2.34) we have

$$i\alpha[V_2(\alpha, +0) - V_1(\alpha, -0)] = F_1(\alpha) \quad (2.37a)$$

$$i\alpha[U_2(\alpha, +0) - U_1(\alpha, -0)] = F_2(\alpha) \quad (2.37b)$$

where by definition and from (2.35)  $F_1$  and  $F_2$  are given by

$$\begin{aligned} F_1(\alpha) &= \int_{-a}^a f_1(x)e^{-i\alpha x}dx, \\ F_2(\alpha) &= \int_{-a}^a f_2(x)e^{-i\alpha x}dx. \end{aligned} \quad (2.38)$$

By substituting (2.32) and (2.33) into the homogeneous equations (2.20a-d) we obtain

$$\sum_{k=1}^4 \left[ i\alpha \left( \frac{3-\kappa}{\kappa-1} \right) + m_k n_k \left( \frac{\kappa+1}{\kappa-1} \right) \right] e^{n_k h} C_k = 0, \quad (2.39)$$

$$\sum_{k=1}^4 (n_k + i\alpha m_k) e^{n_k h} C_k = 0, \quad (2.40)$$

$$2i\alpha A_1 + i\alpha \left[ 1 + \left( \frac{\lambda_1}{\alpha} \right)^2 \right] A_2 + \sum_{k=1}^4 \left[ i\alpha \left( \frac{3-\kappa}{\kappa-1} \right) + m_k n_k \left( \frac{\kappa+1}{\kappa-1} \right) \right] C_k = 0, \quad (2.41)$$

$$\left( \lambda_1 + \frac{\alpha^2}{\lambda_1} \right) A_1 + 2\lambda_2 A_2 - \sum_{k=1}^4 (n_k + i\alpha m_k) C_k = 0. \quad (2.42)$$

Substituting the appropriate expressions for  $U$ 's and  $V$ 's into Equation (2.37) we have

$$-\left( \frac{\alpha^2}{\lambda_1} \right) A_1 - \lambda_2 A_2 + \sum_{k=1}^4 i\alpha m_k C_k = F_1, \quad (2.43)$$

$$-i\alpha(A_1 + A_2 - C_1 - C_2 - C_3 - C_4) = F_2, \quad (2.44)$$

It is seen that all the unknown functions  $A_1(\alpha)$ ,  $A_2(\alpha)$  and  $C_1(\alpha), \dots, C_4(\alpha)$  may be determined in terms of linear combinations of  $F_1(\alpha)$  and  $F_2(\alpha)$  by using (2.39)-(2.44). The detailed expression of  $A_1$ ,  $A_2$  and  $C_1, \dots, C_4$  in terms of  $F_1$  and  $F_2$  are given in Appendix B.

By substituting (2.33b,c) into (2.20e,f) the boundary conditions on the crack surface may be expressed as follows:

$$\lim_{y \rightarrow -0} -\frac{\mu_1}{2\pi} \int_{-\infty}^{\infty} \left\{ 2A_1 e^{\lambda_1 y} + \left[ 1 + \left( \frac{\lambda_1}{\alpha} \right)^2 \right] A_2 e^{\lambda_2 y} \right\} i\alpha e^{i\alpha x} d\alpha = 0, \quad -a < x < a, \quad (2.45)$$

$$\lim_{y \rightarrow -0} \frac{\mu_1}{2\pi} \int_{-\infty}^{\infty} \left[ \left( \lambda_1 + \frac{\alpha^2}{\lambda_1} \right) A_1 e^{\lambda_1 y} + 2\lambda_2 A_2 e^{\lambda_2 y} \right] e^{i\alpha x} d\alpha = 0, \quad -a < x < a. \quad (2.46)$$

From Appendix B the expression of  $A_1$  and  $A_2$  in terms of  $F_1$  and  $F_2$  are given by

$$A_1 = -\left( \frac{d_{22}}{d_{11}d_{22} - d_{21}d_{12}} \right) \frac{F_1}{|\alpha|} - \left( \frac{d_{12}}{d_{11}d_{22} - d_{21}d_{12}} \right) \frac{F_2}{i\alpha}, \quad (B27)$$

$$A_2 = \left( \frac{d_{21}}{d_{11}d_{22} - d_{21}d_{12}} \right) \frac{F_1}{|\alpha|} + \left( \frac{d_{11}}{d_{11}d_{22} - d_{21}d_{12}} \right) \frac{F_2}{i\alpha}, \quad (B28)$$

where  $d_{ij}(\alpha)$ ,  $i, j = 1, 2$ , are given in Appendix B. Now substituting (2.38), (B27), and (B28) into (2.45) and (2.46) and then changing the order of integrations, we may write the integral equations with the density functions  $f_1$  and  $f_2$  as unknowns as follows:

$$\frac{\mu_1}{\pi} \int_{-a}^a \sum_{j=1}^2 K_{ij}(x, t) f_j(t) dt = 0, \quad i = 1, 2, \quad -a < x < a \quad (2.47)$$

where the kernels  $K_{ij}$  are given by

$$K_{11} = \lim_{y \rightarrow -0} \frac{1}{2} \int_{-\infty}^{\infty} \frac{i\alpha}{|\alpha|} [D_{111}(\alpha) e^{\lambda_1 y} + D_{112}(\alpha) e^{\lambda_2 y}] e^{i\alpha(x-t)} d\alpha, \quad (2.48)$$

$$K_{12} = \lim_{y \rightarrow -0} \frac{1}{2} \int_{-\infty}^{\infty} [D_{121}(\alpha) e^{\lambda_1 y} + D_{122}(\alpha) e^{\lambda_2 y}] e^{i\alpha(x-t)} d\alpha, \quad (2.49)$$

$$K_{21} = \lim_{y \rightarrow -0} \frac{1}{2} \int_{-\infty}^{\infty} [D_{211}(\alpha) e^{\lambda_1 y} + D_{212}(\alpha) e^{\lambda_2 y}] e^{i\alpha(x-t)} d\alpha, \quad (2.50)$$

$$K_{22} = \lim_{y \rightarrow -0} \frac{1}{2} \int_{-\infty}^{\infty} \frac{i\alpha}{|\alpha|} [D_{221}(\alpha) e^{\lambda_1 y} + D_{222}(\alpha) e^{\lambda_2 y}] e^{i\alpha(x-t)} d\alpha, \quad (2.51)$$

in which  $D_{ijk}(\alpha)$ ,  $i, j, k = 1, 2$ , are given in Appendix B. It is observed that the integrands in (2.48)-(2.51) are continuous functions of  $\alpha$  and vanish at  $\alpha = 0$ . Therefore, any singularities the kernels  $K_{ij}$  may have must come from the asymptotic behavior of the integrands as  $|\alpha|$  approaches infinity. The details of the asymptotic expansions of the integrands in the kernels (2.48)-(2.51) are given in Appendix C. The leading terms of asymptotic expansions of  $D_{ijk}$  for  $|\alpha|$  goes to infinity are shown to be (Appendix C)

$$D_{111}^{\infty} = \frac{2\lambda_1^*}{1 - \lambda_1^{*2}}, \quad (2.52a)$$

$$D_{112}^{\infty} = - \frac{(1 + \lambda_1^{*2})^2}{2\lambda_2^*(1 - \lambda_1^{*2})}, \quad (2.52b)$$

$$D_{121}^{\infty} = - \frac{1 + \lambda_1^{*2}}{1 - \lambda_1^{*2}}, \quad (2.52c)$$

$$D_{122}^{\infty} = \frac{1 + \lambda_1^{*2}}{1 - \lambda_1^{*2}}, \quad (2.52d)$$

$$D_{211}^{\infty} = - \frac{1 + \lambda_1^{*2}}{1 - \lambda_1^{*2}}, \quad (2.52e)$$

$$D_{212}^{\infty} = \frac{1 + \lambda_1^{*2}}{1 - \lambda_1^{*2}}, \quad (2.52f)$$

$$D_{221}^{\infty} = - \frac{(1 + \lambda_1^{*2})^2}{2\lambda_1^*(1 - \lambda_1^{*2})}, \quad (2.52g)$$

$$D_{222}^{\infty} = \frac{2\lambda_2^*}{1 - \lambda_1^{*2}}, \quad (2.52h)$$

where

$$\lambda_1^* = \frac{\lambda_1}{|\alpha|}, \quad \lambda_2^* = \frac{\lambda_2}{|\alpha|}. \quad (B6,7)$$

In evaluating the kernels  $K_{ij}$  (Equations (2.48)-(2.51)) we separate the asymptotic leading terms (2.52) and evaluate them independently. For the case of  $K_{11}$  we may write

$$K_{11}^{\infty} = \lim_{y \rightarrow -0} \frac{1}{2} \int_{-\infty}^{\infty} \frac{i\alpha}{|\alpha|} [D_{111}^{\infty} e^{\lambda_1^* |\alpha| y} + D_{112}^{\infty} e^{\lambda_2^* |\alpha| y}] e^{i\alpha(x-t)} d\alpha. \quad (2.53)$$

Separating the infinite integral (2.53) into two parts,  $-\infty$  to 0 and 0 to  $\infty$ , and making a change of variable for the part from  $-\infty$  to 0 by letting  $\varphi = -\alpha$ , after some simplifications we obtain

$$K_{11}^{\infty} = \lim_{y \rightarrow -0} \int_0^{\infty} [D_{111}^{\infty} e^{\lambda_1^* \alpha y} + D_{112}^{\infty} e^{\lambda_2^* \alpha y}] \sin \alpha(t-x) d\alpha. \quad (2.54)$$

By using the relation

$$\begin{aligned} \lim_{y \rightarrow -0} \int_0^{\infty} e^{\alpha \lambda_i^* y} \sin \alpha(t-x) d\alpha &= \lim_{y \rightarrow -0} \frac{t-x}{(\lambda_i^* y)^2 + (t-x)^2} \\ &= \frac{1}{t-x}, \quad i = 1, 2, \end{aligned} \quad (2.55)$$

Equation (2.54) may be further simplified as

$$K_{11}^{\infty} = \frac{D_{111}^{\infty} + D_{112}^{\infty}}{t-x}, \quad (2.56)$$

which is a Cauchy kernel. After the separation of the asymptotic leading terms (2.52a,b) which gives the Cauchy kernel the remainder of the integrand in  $K_{11}$  is headed by a term no higher than  $\frac{1}{\alpha}$  as  $|\alpha| \rightarrow \infty$  as indicated in Appendix C. It is analytic everywhere and

we may eliminate the limiting process by substituting  $y = 0$  directly under the integral. This then gives the Fredholm kernel  $k_{11}(x, t)$  as follows

$$k_{11}(x, t) = \frac{1}{2} \int_{-\infty}^{\infty} \frac{i\alpha}{|\alpha|} [D_{111}(\alpha) - D_{111}^{\infty} + D_{112}(\alpha) - D_{112}^{\infty}] e^{i\alpha(x-t)} d\alpha. \quad (2.57)$$

Likewise, for the case of  $K_{22}$  we have a Cauchy kernel (from the asymptotic leading terms)

$$K_{22}^{\infty} = \frac{D_{221}^{\infty} + D_{222}^{\infty}}{t - x}, \quad (2.58)$$

with a Fredholm kernel (for the remainder of  $K_{22}$ ) expressed by

$$k_{22}(x, t) = \frac{1}{2} \int_{-\infty}^{\infty} \frac{i\alpha}{|\alpha|} [D_{221}(\alpha) - D_{221}^{\infty} + D_{222}(\alpha) - D_{222}^{\infty}] e^{i\alpha(x-t)} d\alpha. \quad (2.59)$$

However, from (2.52c-f)  $D_{121}^{\infty} + D_{122}^{\infty} = D_{211}^{\infty} + D_{212}^{\infty} = 0$ , the Cauchy kernels do not exist for the case of  $K_{12}$  and  $K_{21}$  and by substituting  $y = 0$  directly under the integrals in (2.49) and (2.50) the Fredholm kernels  $k_{12}$  and  $k_{21}$  can be expressed by

$$k_{12}(x, t) = \frac{1}{2} \int_{-\infty}^{\infty} [D_{121}(\alpha) + D_{122}(\alpha)] e^{i\alpha(x-t)} d\alpha, \quad (2.60)$$

$$k_{21}(x, t) = \frac{1}{2} \int_{-\infty}^{\infty} [D_{211}(\alpha) + D_{212}(\alpha)] e^{i\alpha(x-t)} d\alpha. \quad (2.61)$$

It is observed that  $D_{ij1} - D_{ij1}^{\infty} + D_{ij2} - D_{ij2}^{\infty}$ ,  $i, j = 1, 2$ , are real and are even functions of  $\alpha$  (see Equation (2.52) and Appendix B). Thus (2.57), (2.59), (2.60), and (2.61) may be simplified as

$$k_{11}(x, t) = \int_0^{\infty} [D_{111}(\alpha) - D_{111}^{\infty} + D_{112}(\alpha) - D_{112}^{\infty}] \sin\alpha(t - x) d\alpha, \quad (2.62)$$

$$k_{12}(x, t) = \int_0^{\infty} [D_{121}(\alpha) - D_{121}^{\infty} + D_{122}(\alpha) - D_{122}^{\infty}] \cos\alpha(t - x) d\alpha, \quad (2.63)$$

$$k_{21}(x, t) = \int_0^\infty [D_{211}(\alpha) - D_{211}^\infty + D_{212}(\alpha) - D_{212}^\infty] \cos \alpha (t - x) d\alpha, \quad (2.64)$$

$$k_{22}(x, t) = \int_0^\infty [D_{221}(\alpha) - D_{221}^\infty + D_{222}(\alpha) - D_{222}^\infty] \sin \alpha (t - x) d\alpha, \quad (2.65)$$

respectively.

From the discussion above, it can be seen that the singular behavior of the kernels come solely from  $K_{11}$  and  $K_{22}$  and thus Equation (2.47) may be expressed by a system of singular integral equations (SIEs) as follows:

$$\frac{\mu_1}{\pi} \int_{-a}^a \sum_{j=1}^2 \left[ (D_{ij1}^\infty + D_{ij2}^\infty) \left( \frac{\delta_{ij}}{t-x} \right) + k_{ij}(x, t) \right] f_j(t) dt = 0, \quad (2.66)$$

$$i = 1, 2, \quad -a < x < a.$$

With the single-valuedness condition (2.36) the SIEs will then be solved for the unknown density functions  $f_1$  and  $f_2$ . It is interesting to note that Equations (2.36) and (2.62) are homogeneous. This implies that for nontrivial solution of  $f_1$  and  $f_2$ , a corresponding critical value of  $\epsilon_0$  would be obtained. Physically, this value  $(\epsilon_0)_{\text{cr}}$  represents the critical compressive strain at which buckling occurs.

## 2.4 The Problem of a Weakened Interface

Besides a single large separation at the coating/substrate interface as described in Section 2.2, a highly weakened interfacial zone may exist in the TBC systems. The weakened interfacial region consists of a series of small cracks with "weak" unbroken ligaments between them as shown in Figure 2.2(a). Mathematically we may consider the unbroken ligaments between  $x = -a$  and  $a$  acting as springs. Thus, the problem of a series of cracks may be modeled as a single crack of length  $2a$  with springs connecting the crack surfaces as shown in Figure 2.2(b). The problem under consideration is the buckling instability of a graded coating bonded to a homogeneous substrate containing a weakened

interface under uniform compressive strain  $\epsilon_0$ . Note that the problem of interest in this section is basically the same as the one described in Section 2.2 (Figure 2.1) except that crack surface tractions are not zero.

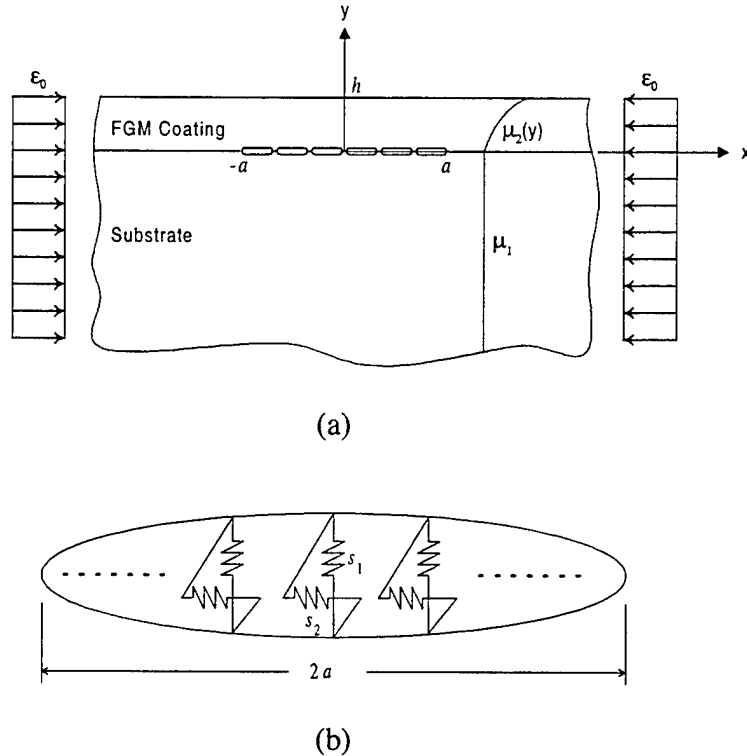


Figure 2.2 (a) Functionally graded coating bonded to a homogeneous substrate with a weakened interface subjected to uniform compressive strain. (b) Crack with surface spring model used for the weakened interface.

Following the same derivation as in Section 2.2 the stability problem for the coating with a weakened interface may be described by (2.18) with the boundary conditions (2.20a-d,g,h). However, the crack surface stress boundary conditions (2.20e,f) have to be replaced by the ones considering the spring bridging effect. We assume that for very small value of bridging stresses the stresses are proportional to the crack opening displacements. Thus, the crack surface stress boundary conditions may be expressed as

$$\sigma_{1yy}^*(x, -0) = s_1 [v_2(x, +0) - v_1(x, -0)], \quad -a < x < a, \quad (2.67a)$$

$$\sigma_{1xy}^*(x, -0) = s_2 [u_2(x, +0) - u_1(x, -0)], \quad -a < x < a, \quad (2.67b)$$

where  $s_1$  and  $s_2$  are the "spring constants". From the continuity condition (2.20g,h) we may write the crack opening displacements in terms of the density functions  $f_1$  and  $f_2$  defined by (2.34) as

$$v_2(x, +0) - v_1(x, -0) = \int_{-a}^x f_1(t) dt, \quad -a < x < a, \quad (2.68a)$$

$$u_2(x, +0) - u_1(x, -0) = \int_{-a}^x f_2(t) dt, \quad -a < x < a. \quad (2.68b)$$

Following the same procedure described in Section 2.3 the stability problem for the weakened interface may then be expressed as

$$\frac{\mu_1}{\pi} \int_{-a}^a \sum_{j=1}^2 \left[ (D_{ij1}^\infty + D_{ij2}^\infty) \left( \frac{\delta_{ij}}{t-x} \right) + k_{ij}(x, t) \right] f_j(t) dt - s_i \int_{-a}^x f_i(t) dt = 0, \quad (2.69)$$

$$i = 1, 2, \quad -a < x < a.$$

with the single-valuedness conditions (2.36). The homogeneous integral equations (2.69) and (2.36) will be solved to determine the buckling strain  $(\epsilon_0)_{\text{cr}}$ .

## Chapter 3

### Solution of Singular Integral Equations and Numerical Procedure

#### 3.1 Solution of the Integral Equations

To solve the integral equations (2.36), (2.66), and (2.69), first the following normalized quantities are defined

$$s = \frac{t}{a}, \quad r = \frac{x}{a}, \quad (3.1)$$

$$f_i^*(s) = f_i(t), \quad k_{ij}^*(r, s) = a k_{ij}(x, t), \quad i, j = 1, 2.$$

Equations (2.36), (2.66), and (2.69) are given, respectively, by

$$\int_{-1}^1 f_i^*(s) ds = 0, \quad i = 1, 2, \quad (3.2)$$

$$\frac{\mu_1}{\pi} \int_{-1}^1 \sum_{j=1}^2 \left[ (D_{ij1}^\infty + D_{ij2}^\infty) \left( \frac{\delta_{ij}}{s-r} \right) + k_{ij}^*(r, s) \right] f_j^*(s) ds = 0, \quad (3.3a,b)$$

$$i = 1, 2, \quad -1 < r < 1,$$

$$\frac{\mu_1}{\pi} \int_{-1}^1 \sum_{j=1}^2 \left[ (D_{ij1}^\infty + D_{ij2}^\infty) \left( \frac{\delta_{ij}}{s-r} \right) + k_{ij}^*(r, s) \right] f_j^*(s) ds - a s_i \int_{-1}^r f_i^*(s) ds = 0, \quad (3.4)$$

$$i = 1, 2, \quad -1 < r < 1.$$

##### 3.1.1 The Infinite Integral

In order to evaluate the Fredholm kernels  $k_{ij}^*(r, s)$  for various values of the inhomogeneity parameter  $\gamma h$  and normalized crack length  $a/h$ , we define

$$\eta = \frac{|\alpha|}{|\gamma|}, \quad (3.5)$$

giving

$$k_{11}^*(r, s) = (|\gamma| h) \left(\frac{a}{h}\right) \int_0^\infty B_{11}(\eta) \sin \left[ (|\gamma| h) \left(\frac{a}{h}\right) (s-r) \eta \right] d\eta, \quad (3.6)$$

$$k_{12}^*(r, s) = (|\gamma| h) \left(\frac{a}{h}\right) \int_0^\infty B_{12}(\eta) \cos \left[ (|\gamma| h) \left(\frac{a}{h}\right) (s-r) \eta \right] d\eta, \quad (3.7)$$

$$k_{21}^*(r, s) = (|\gamma| h) \left(\frac{a}{h}\right) \int_0^\infty B_{21}(\eta) \cos \left[ (|\gamma| h) \left(\frac{a}{h}\right) (s-r) \eta \right] d\eta, \quad (3.8)$$

$$k_{22}^*(r, s) = (|\gamma| h) \left(\frac{a}{h}\right) \int_0^\infty B_{22}(\eta) \sin \left[ (|\gamma| h) \left(\frac{a}{h}\right) (s-r) \eta \right] d\eta, \quad (3.9)$$

where from (2.62)-(2.65)

$$B_{ij}(\eta) = D_{ij1}(\alpha) - D_{ij1}^\infty + D_{ij2}(\alpha) - D_{ij2}^\infty, \quad i, j = 1, 2. \quad (3.10)$$

Note that  $\eta = 1/\xi$  where  $\xi$  is the expansion parameter used in the asymptotic analysis in Appendix C.

The kernel  $k_{11}^*$  is evaluated in such a way that the zero to infinity integral is broken into three integrals, i.e.

$$\begin{aligned} k_{11}^*(r, s) &= (|\gamma| h) \left(\frac{a}{h}\right) \left\{ \int_0^A \left[ B_{11}(\eta) - \frac{B_{111}}{\eta} \right] \sin \left[ (|\gamma| h) \left(\frac{a}{h}\right) (s-r) \eta \right] d\eta \right. \\ &\quad + \int_A^\infty \left[ B_{11}(\eta) - \frac{B_{111}}{\eta} \right] \sin \left[ (|\gamma| h) \left(\frac{a}{h}\right) (s-r) \eta \right] d\eta \\ &\quad \left. + B_{111} \int_0^\infty \left(\frac{1}{\eta}\right) \sin \left[ (|\gamma| h) \left(\frac{a}{h}\right) (s-r) \eta \right] d\eta \right\}. \end{aligned} \quad (3.11)$$

The integrand of the first integral in (3.11) is bounded everywhere and integrated numerically; The third integral may be evaluated analytically and can be expressed as

$$\int_0^\infty \left(\frac{1}{\eta}\right) \sin \left[ (|\gamma| h) \left(\frac{a}{h}\right) (s-r) \eta \right] d\eta = \frac{\pi}{2} \frac{\left| (|\gamma| h) \left(\frac{a}{h}\right) (s-r) \right|}{(|\gamma| h) \left(\frac{a}{h}\right) (s-r)}. \quad (3.12)$$

Because both  $a$  and  $h$  are greater than zero, Equation (3.12) may be simplified as

$$\int_0^\infty \left( \frac{1}{\eta} \right) \sin \left[ (|\gamma| h) \left( \frac{a}{h} \right) (s-r) \eta \right] d\eta = \frac{\pi}{2} \frac{|s-r|}{s-r}; \quad (3.13)$$

The second integral may be written as

$$\begin{aligned} & \int_A^\infty \left[ B_{11}(\eta) - \frac{B_{111}}{\eta} \right] \sin \left[ (|\gamma| h) \left( \frac{a}{h} \right) (s-r) \eta \right] d\eta \\ &= \int_A^\infty \sum_{j=2}^{10} \left( \frac{B_{11j}}{\eta^j} \right) \sin \left[ (|\gamma| h) \left( \frac{a}{h} \right) (s-r) \eta \right] d\eta \\ &+ \int_A^\infty \left[ B_{11}(\eta) - \sum_{j=1}^{10} \left( \frac{B_{11j}}{\eta^j} \right) \right] \sin \left[ (|\gamma| h) \left( \frac{a}{h} \right) (s-r) \eta \right] d\eta, \end{aligned} \quad (3.14)$$

where  $\sum_{j=1}^{10} \left( \frac{B_{11j}}{\eta^j} \right)$  is the 10-term asymptotic expansions of  $B_{11}$  for large values of  $\eta$  and

the expressions for  $B_{11j}$ ,  $j = 1, 2$ , are given in Appendix C. It may be seen that the asymptotic leading term of  $B_{11}(\eta) - \sum_{j=1}^{10} \left( \frac{B_{11j}}{\eta^j} \right)$  is of order  $1/\eta^{11}$  and, therefore, we have

$$\int_A^\infty \left[ B_{11}(\eta) - \sum_{j=1}^{10} \left( \frac{B_{11j}}{\eta^j} \right) \right] \sin \left[ (|\gamma| h) \left( \frac{a}{h} \right) (s-r) \eta \right] d\eta \sim O\left(\frac{1}{A^{10}}\right). \quad (3.15)$$

By choosing a large value for  $A$  in (3.15) such that  $1/A^{10}$  is small to any order that we desire, we may then neglect the second integral on the r. h. s. of (3.14) and express the Fredholm kernel  $k_{11}^*$  as

$$\begin{aligned} k_{11}^*(r, s) &= (|\gamma| h) \left( \frac{a}{h} \right) \left\{ \int_0^A \left[ B_{11}(\eta) - \frac{B_{111}}{\eta} \right] \sin \left[ (|\gamma| h) \left( \frac{a}{h} \right) (s-r) \eta \right] d\eta \right. \\ &+ \sum_{j=2}^{10} B_{11j} \int_A^\infty \left( \frac{1}{\eta^j} \right) \sin \left[ (|\gamma| h) \left( \frac{a}{h} \right) (s-r) \eta \right] d\eta \\ &\left. + \frac{\pi}{2} \frac{|s-r|}{s-r} B_{111} \right\}. \end{aligned} \quad (3.16)$$

In Equation (3.16), only the first term is to be integrated numerically; The second term, which is expressed as a summation of integrals, may be determined in closed form. The closed form expressions for these integrals are shown in Appendix D; The last term is a

sign function and is discontinuous at  $s = r$ . From a previous study [72] it is shown that not separating this term from the numerically evaluated integral would lead to erroneous results, thereby inhibiting convergence of the final solution.

We may use the same procedure used for  $k_{11}^*$  to evaluate  $k_{22}^*$ . The result may be expressed as

$$k_{22}^*(r, s) = (|\gamma| h) \left( \frac{a}{h} \right) \left\{ \int_0^A \left[ B_{22}(\eta) - \frac{B_{221}}{\eta} \right] \sin \left[ (|\gamma| h) \left( \frac{a}{h} \right) (s - r) \eta \right] d\eta \right. \\ \left. + \sum_{j=2}^{10} B_{22j} \int_A^\infty \left( \frac{1}{\eta^j} \right) \sin \left[ (|\gamma| h) \left( \frac{a}{h} \right) (s - r) \eta \right] d\eta \right. \\ \left. + \frac{\pi}{2} \frac{|s - r|}{s - r} B_{221} \right\}, \quad (3.17)$$

where the first term will be integrated numerically and the second term has closed form expression.

Having described the way to evaluate  $k_{11}^*$  and  $k_{22}^*$ , we now do the same for  $k_{12}^*$  and  $k_{21}^*$ . The kernel  $k_{12}^*(r, s)$  may be rewritten as

$$k_{12}^*(r, s) = (|\gamma| h) \left( \frac{a}{h} \right) \left\{ \int_0^A B_{12}(\eta) \cos \left[ (|\gamma| h) \left( \frac{a}{h} \right) (s - r) \eta \right] d\eta \right. \\ \left. + \int_A^\infty \left[ B_{12}(\eta) - \frac{B_{121}}{\eta} \right] \cos \left[ (|\gamma| h) \left( \frac{a}{h} \right) (s - r) \eta \right] d\eta \right. \\ \left. + B_{121} \int_A^\infty \left( \frac{1}{\eta} \right) \cos \left[ (|\gamma| h) \left( \frac{a}{h} \right) (s - r) \eta \right] d\eta \right\}. \quad (3.18)$$

The integrand of the first term in Equation (3.18) is bounded everywhere within the limits of integration; The second integral in (3.18) may be rewritten as

$$\begin{aligned}
& \int_A^\infty \left[ B_{12}(\eta) - \frac{B_{121}}{\eta} \right] \cos \left[ (|\gamma| h) \left( \frac{a}{h} \right) (s - r) \eta \right] d\eta \\
&= \int_A^\infty \sum_{j=2}^{10} \left( \frac{B_{12j}}{\eta^j} \right) \cos \left[ (|\gamma| h) \left( \frac{a}{h} \right) (s - r) \eta \right] d\eta \\
&+ \int_A^\infty \left[ B_{12}(\eta) - \sum_{j=1}^{10} \left( \frac{B_{12j}}{\eta^j} \right) \right] \cos \left[ (|\gamma| h) \left( \frac{a}{h} \right) (s - r) \eta \right] d\eta,
\end{aligned} \tag{3.19}$$

where  $\sum_{j=1}^{10} \left( \frac{B_{12j}}{\eta^j} \right)$  is the 10-term asymptotic expansions of  $B_{12}$  for large values of  $\eta$  and the expressions for  $B_{12j}$ ,  $j = 1, 2$ , are given in Appendix C. The cosine integrals in the first term on the r. h. s. of (3.19) can be expressed in closed form (Appendix D). Following the same argument used in the case of  $k_{11}^*$ , the second integral in (3.19) may be neglected if a sufficiently large value of  $A$  is chosen. The third integral in (3.18) has a closed form expression as follows:

$$\int_A^\infty \left( \frac{1}{\eta} \right) \cos \left[ (|\gamma| h) \left( \frac{a}{h} \right) (s - r) \eta \right] d\eta = - \text{Ci} \left[ (|\gamma| h) \left( \frac{a}{h} \right) |s - r| A \right], \tag{3.20}$$

where  $\text{Ci}$ , the cosine integral, is defined by

$$\text{Ci}(x) = \gamma_0 + \ln x + \int_0^x \frac{\cos t - 1}{t} dt, \quad x > 0, \tag{3.21}$$

in which  $\gamma_0 = 0.57721566490$ , is the Euler's constant. The reason that the integral (3.20) is separated from  $k_{12}^*$  is similar to why the sign function is separated from the kernel  $k_{11}^*$ . It is because the logarithmic term in  $\text{Ci} \left[ (|\gamma| h) \left( \frac{a}{h} \right) |s - r| A \right]$  could not be properly approximated by numerical quadrature when integrated. As will be described in Section 3.1.3, this term will be integrated in closed form.

From the above discussions  $k_{12}^*$  may be expressed as

$$\begin{aligned}
k_{12}^*(r, s) = & (|\gamma| h) \left( \frac{a}{h} \right) \left\{ \int_0^A B_{12}(\eta) \cos \left[ (|\gamma| h) \left( \frac{a}{h} \right) (s - r) \eta \right] d\eta \right. \\
& + \sum_{j=2}^{10} B_{12j} \int_A^\infty \left( \frac{1}{\eta^j} \right) \cos \left[ (|\gamma| h) \left( \frac{a}{h} \right) (s - r) \eta \right] d\eta \\
& - B_{121} \gamma_0 - B_{121} \ln \left[ (|\gamma| h) \left( \frac{a}{h} \right) |s - r| A \right] \\
& \left. - B_{121} \int_0^{(|\gamma| h) \left( \frac{a}{h} \right) (s - r) A} \frac{\cos t - 1}{t} dt \right\}.
\end{aligned} \tag{3.22}$$

Following the same argument as in  $k_{12}^*$  we may write  $k_{21}^*$  as

$$\begin{aligned}
k_{21}^*(r, s) = & (|\gamma| h) \left( \frac{a}{h} \right) \left\{ \int_0^A B_{21}(\eta) \cos \left[ (|\gamma| h) \left( \frac{a}{h} \right) (s - r) \eta \right] d\eta \right. \\
& + \sum_{j=2}^{10} B_{21j} \int_A^\infty \left( \frac{1}{\eta^j} \right) \cos \left[ (|\gamma| h) \left( \frac{a}{h} \right) (s - r) \eta \right] d\eta \\
& - B_{211} \gamma_0 - B_{211} \ln \left[ (|\gamma| h) \left( \frac{a}{h} \right) |s - r| A \right] \\
& \left. - B_{211} \int_0^{(|\gamma| h) \left( \frac{a}{h} \right) (s - r) A} \frac{\cos t - 1}{t} dt \right\}.
\end{aligned} \tag{3.23}$$

It is interesting to note that, although not shown explicitly,  $k_{12}^*(r, s)$  and  $k_{21}^*(r, s)$  differ only by a sign, as is the case for problems that possesses symmetry with respect to the  $y$ -axis.

### 3.1.2 Nature of the Stress Singularity

It is known in fracture mechanics that the stress field near the crack tip possesses a leading term that is proportional to  $r^{-p}$ , where  $r$  is a small distance measured from the crack tip and  $p$  is the power of singularity which is a measure of the unboundedness of the stress field. It may be seen that if  $p$  is larger than one, the displacement field would be unbounded at the crack tip, which is unacceptable; on the other hand, if  $p$  is smaller than zero,  $r^{-p}$  maintains a positive power and the stress vanishes as  $r$  approaches zero and there is no stress singularity at the crack tip. Therefore, the value of  $p$  should be between zero and one. In this case the stress at the crack tip is unbounded but still integrable.

From the derivation of the singular integral equation in the previous chapter and the discussion earlier in this chapter, it can be seen that the terms in (3.3) and (3.4) that involve Fredholm kernels are bounded and analytic everywhere. The only contribution to the singular behavior is from the Cauchy kernel. Therefore, only the terms (in (3.3) and (3.4)) containing Cauchy kernels are considered in examining the singularities of the unknown density functions  $f_1^*(s)$  and  $f_2^*(s)$ .

First we consider the singular integral equation (3.3a). By moving the nonsingular contributions to the right hand side, the equation can be expressed as

$$\frac{1}{\pi} \int_{-1}^1 \frac{f_1^*(s)}{(s-r)} ds = \Psi(r), \quad (3.24)$$

where  $\Psi(r)$  represents all the bounded terms. To study the behavior of  $f_1^*(s)$  near crack tips  $s = 1$  and  $-1$ , we assume that

$$f_1^*(s) = \frac{g_1(s)}{(1+s)^{p_1}(1-s)^{p_2}}, \quad (3.25)$$

where  $g_1(s)$  satisfies the Hölder condition on  $-1 \leq s \leq 1$ . Also, because  $f_1^*(s)$  is of the same order as stress, the singularities  $p_1$  and  $p_2$  should satisfy the condition  $0 < \operatorname{Re}(p_1, p_2) < 1$ . Defining that

$$F_1(z) = \frac{1}{\pi} \int_{-1}^1 \frac{f_1^*(s)}{(s-z)} ds, \quad (3.26)$$

and substituting (3.26) into (3.25), we obtain

$$F_1(z) = \frac{1}{\pi} \int_{-1}^1 \frac{g_1(s)}{(1+s)^{p_1}(1-s)^{p_2}(s-z)} ds. \quad (3.27)$$

By following Muskhelishvili [73] the asymptotic behavior of (3.27) near the end points 1 and  $-1$  can be expressed as

$$F_1(z) = \frac{g_1(-1)e^{i\pi p_1}}{2^{p_2}(1+z)^{p_1}\sin(\pi p_1)} - \frac{g_1(1)e^{-i\pi p_2}}{2^{p_1}(1-z)^{p_2}\sin(\pi p_2)} + F_0(z), \quad (3.28)$$

where  $F_0(z)$  has singularity less than  $p_1, p_2$ . Using the Plemelj formula, we obtain

$$\frac{1}{\pi} \int_{-1}^1 \frac{f_1^*(s)}{(s-r)} ds = \frac{1}{2} [F_1^+(r) + F_1^-(r)]. \quad (3.29)$$

From (3.28) and (3.29) it then follows that

$$\frac{1}{\pi} \int_{-1}^1 \frac{f_1^*(s)}{(s-r)} ds = \frac{g_1(-1)\cot(\pi p_1)}{2^{p_2}(1+r)^{p_1}} - \frac{g_1(1)\cot(\pi p_2)}{2^{p_1}(1-r)^{p_2}} + F_0(r). \quad (3.30)$$

Substituting (3.30) into (3.24) we have

$$\frac{g_1(-1)\cot(\pi p_1)}{2^{p_2}(1+r)^{p_1}} - \frac{g_1(1)\cot(\pi p_2)}{2^{p_1}(1-r)^{p_2}} + F_0(r) = \Psi(r). \quad (3.31)$$

Now multiplying both sides of (3.31) by  $(r+1)^{p_1}$  and taking limit as  $r \rightarrow -1$ , we obtain

$$\frac{g_1(-1)\cot(\pi p_1)}{2^{p_2}} = 0, \quad (3.32)$$

or

$$\cot(\pi p_1) = 0. \quad (3.33)$$

Similarly, multiplying both sides of (3.31) by  $(r-1)^{p_2}$  and taking limit as  $r \rightarrow 1$ , we have

$$\cot(\pi p_2) = 0. \quad (3.34)$$

The only acceptable roots of (3.33) and (3.34) that satisfy  $0 < \operatorname{Re}(p_1, p_2) < 1$  are  $p_1 = p_2 = 1/2$ . By following the same procedure for other integral equations ((3.3b), (3.4)), we can conclude that the density function  $f_2^*(s)$  also has square root singularities at  $s = \pm 1$ . In conclusion, we define

$$f_i^*(s) = \frac{g_i(s)}{\sqrt{1-s^2}}, \quad -1 < s < 1, \quad i = 1, 2, \quad (3.35)$$

where  $g_i(s)$ ,  $i = 1, 2$ , satisfies the Hölder condition on the closed interval of  $(-1, 1)$  and  $g_i(-1) \neq 0, g_i(1) \neq 0$ ,  $i = 1, 2$ .

### 3.1.3 Converting to Linear System

Because the integral equations (3.2) and (3.3) can not be solved in closed form, a series expansion approach is used for solving the density functions. It may be seen that  $g_i(s)$  in (3.35) is a bounded function. Hence, we may write  $g_i$  in a series of orthogonal polynomials as follows:

$$g_i(s) = \sum_{j=0}^{\infty} C_{ij}^* T_j(s), \quad i = 1, 2, \quad (3.36)$$

where  $T_n(s)$  ( $n = 0, 1, \dots$ ) is the Chebyshev polynomial of the first kind and  $C_{ij}^*$  are unknown constants. Substituting (3.35) and (3.36) into the single-valuedness condition (3.2) we have

$$\sum_{j=0}^{\infty} C_{ij}^* \int_{-1}^1 \frac{T_j(s) ds}{\sqrt{1-s^2}} = 0, \quad i = 1, 2. \quad (3.37)$$

Since the Chebyshev polynomials satisfy the following relation:

$$\frac{1}{\pi} \int_{-1}^1 \frac{T_j(s) ds}{\sqrt{1-s^2}} = \begin{cases} 1, & j = 0, \\ 0, & j > 0, \end{cases} \quad (3.38)$$

we observe from Equation (3.37) that

$$C_{i0}^* = 0, \quad i = 1, 2. \quad (3.39)$$

Because this study is to determine the buckling instability point, which corresponds to the onset of the first buckling mode, we may assume that the deformation is symmetric with respect to the  $y$ -axis. It is such that  $u_j^*$  and  $v_j^*$  ( $j = 1, 2$ ) are odd and even functions of  $x$ , respectively. Furthermore, from (2.34) it may be seen that the density functions  $f_1$  and  $f_2$  are odd and even functions of  $x$ , respectively. Since we have

$$T_n(-s) = (-1)^n T_n(s), \quad n = 0, 1, 2, \dots, \quad (3.40)$$

from (3.1), (3.35)-(3.36) it may be seen that

$$C_{1(2n)}^* = C_{2(2n-1)}^* = 0, \quad n = 1, 2, 3, \dots \quad (3.41)$$

Thus, we may rewrite (3.36) as

$$g_1(s) = \sum_{j=1}^{\infty} C_{1j} T_{2j-1}(s), \quad (3.42a)$$

$$g_2(s) = \sum_{j=1}^{\infty} C_{2j} T_{2j}(s). \quad (3.42b)$$

By substituting (3.35) and (3.42), the singular integral equation (3.3) may be rewritten as

$$\begin{aligned} & \frac{\mu_1}{\pi} \int_{-1}^1 \sum_{k=1}^{\infty} \frac{C_{1k} T_{2k-1}(s)}{\sqrt{1-s^2}} \left[ \frac{D_{111}^{\infty} + D_{112}^{\infty}}{s-r} + k_{11}^*(r, s) \right] ds \\ & + \frac{\mu_1}{\pi} \int_{-1}^1 \sum_{k=1}^{\infty} \frac{C_{2k} T_{2k}(s)}{\sqrt{1-s^2}} k_{12}^*(r, s) ds = 0, \quad -1 < r < 1. \end{aligned} \quad (3.43a)$$

$$\begin{aligned} & \frac{\mu_1}{\pi} \int_{-1}^1 \sum_{k=1}^{\infty} \frac{C_{2k} T_{2k}(s)}{\sqrt{1-s^2}} \left[ \frac{D_{221}^{\infty} + D_{222}^{\infty}}{s-r} + k_{22}^*(r, s) \right] ds \\ & + \frac{\mu_1}{\pi} \int_{-1}^1 \sum_{k=1}^{\infty} \frac{C_{1k} T_{2k-1}(s)}{\sqrt{1-s^2}} k_{21}^*(r, s) ds = 0, \quad -1 < r < 1. \end{aligned} \quad (3.43b)$$

By using

$$\frac{1}{\pi} \int_{-1}^1 \frac{T_j(s) ds}{(s-r)\sqrt{1-s^2}} = \begin{cases} 0, & j = 0, \quad |r| < 1, \\ U_{j-1}(r), & j > 0, \quad |r| < 1, \\ -\frac{\left(r - \frac{|r|}{r} \sqrt{r^2 - 1}\right)^j}{\left(\frac{|r|}{r} \sqrt{r^2 - 1}\right)}, & j \geq 0, \quad |r| > 1, \end{cases} \quad (3.44)$$

the singular integral equations (3.43) are regularized and can be expressed as

$$\begin{aligned} & \mu_1 (D_{111}^{\infty} + D_{112}^{\infty}) \sum_{k=1}^{\infty} C_{1k} U_{2k-2}(r) + \frac{\mu_1}{\pi} \sum_{k=1}^{\infty} C_{1k} \int_{-1}^1 \frac{T_{2k-1}(s)}{\sqrt{1-s^2}} k_{11}^*(r, s) ds \\ & + \frac{\mu_1}{\pi} \sum_{k=1}^{\infty} C_{2k} \int_{-1}^1 \frac{T_{2k}(s)}{\sqrt{1-s^2}} k_{12}^*(r, s) ds = 0, \quad -1 < r < 1. \end{aligned} \quad (3.45a)$$

$$\begin{aligned} & \mu_1(D_{221}^\infty + D_{222}^\infty) \sum_{k=1}^{\infty} C_{2k} U_{2k-1}(r) + \frac{\mu_1}{\pi} \sum_{k=1}^{\infty} C_{2k} \int_{-1}^1 \frac{T_{2k}(s)}{\sqrt{1-s^2}} k_{22}^*(r, s) ds \\ & + \frac{\mu_1}{\pi} \sum_{k=1}^{\infty} C_{1k} \int_{-1}^1 \frac{T_{2k-1}(s)}{\sqrt{1-s^2}} k_{21}^*(r, s) ds = 0, \quad -1 < r < 1. \end{aligned} \quad (3.45b)$$

where  $U_n(s)$  ( $n = 0, 1, \dots$ ) is the Chebyshev polynomial of the second kind. The approach used for evaluating the Fredholm kernels  $k_{ij}^*(r, s)$  has been discussed in Section 3.1.1. Note that in these kernels we separate the sign and logarithm functions which would introduce irregularities from the numerically evaluated integrals. The contribution of these functions in (3.45) can be expressed in closed form. Thus for the sign and logarithmic functions, we have

$$\int_{-1}^1 \frac{T_j(s)}{\sqrt{1-s^2}} \frac{|s-r|}{s-r} ds = \frac{2}{j} U_{j-1}(r) \sqrt{1-r^2}, \quad j \geq 1, \quad (3.46)$$

$$\begin{aligned} \int_{-1}^1 \frac{T_j(s)}{\sqrt{1-s^2}} \ln \left[ (|\gamma| h) \left( \frac{a}{h} \right) |s-r| A \right] ds &= \int_{-1}^1 \frac{T_j(s)}{\sqrt{1-s^2}} \ln |s-r| ds \\ &+ \ln \left[ (|\gamma| h) \left( \frac{a}{h} \right) A \right] \int_{-1}^1 \frac{T_j(s)}{\sqrt{1-s^2}} ds. \end{aligned} \quad (3.47)$$

By observing that

$$\int_{-1}^1 \frac{T_j(s)}{\sqrt{1-s^2}} \ln |s-r| ds = - \frac{\pi}{j} T_j(r), \quad j \geq 1, \quad (3.48)$$

from (3.38) and (3.47), we obtain

$$\int_{-1}^1 \frac{T_j(s)}{\sqrt{1-s^2}} \ln \left[ (|\gamma| h) \left( \frac{a}{h} \right) |s-r| A \right] ds = - \frac{\pi}{j} T_j(r), \quad j \geq 1. \quad (3.49)$$

By substituting (3.16), (3.17), (3.22), (3.23), (3.46), and (3.49) into (3.45) and truncating the series at  $k = n$ , Equation (3.45) may be rewritten as follows:

$$\begin{aligned}
& \mu_1 \sum_{k=1}^n C_{1k} \left[ (D_{111}^\infty + D_{112}^\infty) U_{2k-2}(r) + (|\gamma| h) \left( \frac{a}{h} \right) B_{111} \sqrt{1-r^2} \frac{U_{2k-2}(r)}{2k-1} \right] \\
& + \mu_1 (|\gamma| h) \left( \frac{a}{h} \right) \sum_{k=1}^n C_{1k} \frac{1}{\pi} \int_{-1}^1 \frac{T_{2k-1}(s)}{\sqrt{1-s^2}} \hat{k}_{11}(r, s) ds \\
& + \mu_1 (|\gamma| h) \left( \frac{a}{h} \right) B_{121} \sum_{k=1}^n C_{2k} \frac{T_{2k}(r)}{2k} \\
& + \mu_1 (|\gamma| h) \left( \frac{a}{h} \right) \sum_{k=1}^n C_{2k} \frac{1}{\pi} \int_{-1}^1 \frac{T_{2k}(s)}{\sqrt{1-s^2}} \hat{k}_{12}(r, s) ds = 0, \\
& \quad -1 < r < 1,
\end{aligned} \tag{3.50a}$$

$$\begin{aligned}
& \mu_1 \sum_{k=1}^n C_{2k} \left[ (D_{221}^\infty + D_{222}^\infty) U_{2k-1}(r) + (|\gamma| h) \left( \frac{a}{h} \right) B_{221} \sqrt{1-r^2} \frac{U_{2k-1}(r)}{2k} \right] \\
& + \mu_1 (|\gamma| h) \left( \frac{a}{h} \right) \sum_{k=1}^n C_{2k} \frac{1}{\pi} \int_{-1}^1 \frac{T_{2k}(s)}{\sqrt{1-s^2}} \hat{k}_{22}(r, s) ds \\
& + \mu_1 (|\gamma| h) \left( \frac{a}{h} \right) B_{211} \sum_{k=1}^n C_{1k} \frac{T_{2k-1}(r)}{2k-1} \\
& + \mu_1 (|\gamma| h) \left( \frac{a}{h} \right) \sum_{k=1}^n C_{1k} \frac{1}{\pi} \int_{-1}^1 \frac{T_{2k-1}(s)}{\sqrt{1-s^2}} \hat{k}_{21}(r, s) ds = 0, \\
& \quad -1 < r < 1,
\end{aligned} \tag{3.50b}$$

where

$$\begin{aligned}
\hat{k}_{11}(r, s) &= \int_0^A \left[ B_{11}(\eta) - \frac{B_{111}}{\eta} \right] \sin \left[ (|\gamma| h) \left( \frac{a}{h} \right) (s-r) \eta \right] d\eta \\
&+ \sum_{j=2}^{10} B_{11j} \int_A^\infty \left( \frac{1}{\eta^j} \right) \sin \left[ (|\gamma| h) \left( \frac{a}{h} \right) (s-r) \eta \right] d\eta,
\end{aligned} \tag{3.51}$$

$$\begin{aligned}
\hat{k}_{12}(r, s) &= \int_0^A B_{12}(\eta) \cos \left[ (|\gamma| h) \left( \frac{a}{h} \right) (s-r) \eta \right] d\eta \\
&+ \sum_{j=2}^{10} B_{12j} \int_A^\infty \left( \frac{1}{\eta^j} \right) \cos \left[ (|\gamma| h) \left( \frac{a}{h} \right) (s-r) \eta \right] d\eta \\
&- B_{121} \left[ \gamma_0 + \int_0^{(|\gamma| h) \left( \frac{a}{h} \right) (s-r) A} \frac{\cos t - 1}{t} dt \right],
\end{aligned} \tag{3.52}$$

$$\begin{aligned}
\hat{k}_{21}(r, s) = & \int_0^A B_{21}(\eta) \cos \left[ (|\gamma| h) \left( \frac{a}{h} \right) (s - r) \eta \right] d\eta \\
& + \sum_{j=2}^{10} B_{21j} \int_A^\infty \left( \frac{1}{\eta^j} \right) \cos \left[ (|\gamma| h) \left( \frac{a}{h} \right) (s - r) \eta \right] d\eta \\
& - B_{211} \left[ \gamma_0 + \int_0^{(|\gamma| h) \left( \frac{a}{h} \right) (s - r) A} \frac{\cos t - 1}{t} dt \right], \tag{3.53}
\end{aligned}$$

$$\begin{aligned}
\hat{k}_{22}(r, s) = & \int_0^A \left[ B_{22}(\eta) - \frac{B_{221}}{\eta} \right] \sin \left[ (|\gamma| h) \left( \frac{a}{h} \right) (s - r) \eta \right] d\eta \\
& + \sum_{j=2}^{10} B_{22j} \int_A^\infty \left( \frac{1}{\eta^j} \right) \sin \left[ (|\gamma| h) \left( \frac{a}{h} \right) (s - r) \eta \right] d\eta. \tag{3.54}
\end{aligned}$$

It may be seen that the unknowns in the linear system (3.50) are  $C_{1k}$  and  $C_{2k}$ ,  $k = 1, \dots, n$ . To solve this linear system, we use a collocation technique to reduce (3.50) to a system of linear algebraic equations in the unknowns  $C_{1k}$  and  $C_{2k}$  given by

$$\begin{aligned}
& \mu_1 \sum_{k=1}^n C_{1k} \left[ (D_{111}^\infty + D_{112}^\infty) U_{2k-2}(r_m) + (|\gamma| h) \left( \frac{a}{h} \right) B_{111} \sqrt{1 - r_m^2} \frac{U_{2k-2}(r_m)}{2k-1} \right] \\
& + \mu_1 (|\gamma| h) \left( \frac{a}{h} \right) \sum_{k=1}^n C_{1k} \frac{1}{\pi} \int_{-1}^1 \frac{T_{2k-1}(s)}{\sqrt{1-s^2}} \hat{k}_{11}(r_m, s) ds \\
& + \mu_1 (|\gamma| h) \left( \frac{a}{h} \right) B_{121} \sum_{k=1}^n C_{2k} \frac{T_{2k}(r_m)}{2k} \\
& + \mu_1 (|\gamma| h) \left( \frac{a}{h} \right) \sum_{k=1}^n C_{2k} \frac{1}{\pi} \int_{-1}^1 \frac{T_{2k}(s)}{\sqrt{1-s^2}} \hat{k}_{12}(r_m, s) ds = 0, \tag{3.55a} \\
& m = 1, \dots, n,
\end{aligned}$$

$$\begin{aligned}
& \mu_1 \sum_{k=1}^n C_{2k} \left[ (D_{221}^\infty + D_{222}^\infty) U_{2k-1}(r_m) + (|\gamma| h) \left( \frac{a}{h} \right) B_{221} \sqrt{1 - r_m^2} \frac{U_{2k-1}(r_m)}{2k} \right] \\
& + \mu_1 (|\gamma| h) \left( \frac{a}{h} \right) \sum_{k=1}^n C_{2k} \frac{1}{\pi} \int_{-1}^1 \frac{T_{2k}(s)}{\sqrt{1-s^2}} \hat{k}_{22}(r_m, s) ds \\
& + \mu_1 (|\gamma| h) \left( \frac{a}{h} \right) B_{211} \sum_{k=1}^n C_{1k} \frac{T_{2k-1}(r_m)}{2k-1} \\
& + \mu_1 (|\gamma| h) \left( \frac{a}{h} \right) \sum_{k=1}^n C_{1k} \frac{1}{\pi} \int_{-1}^1 \frac{T_{2k-1}(s)}{\sqrt{1-s^2}} \hat{k}_{21}(r_m, s) ds = 0, \tag{3.55b} \\
& m = 1, \dots, n,
\end{aligned}$$

where  $\hat{k}_{ij}$ ,  $i, j = 1, 2$ , are given by (3.51)-(3.54) and the collocation points  $r_m$  are chosen as

$$r_m = \cos \frac{(2m-1)\pi}{2n}, \quad m = 1, \dots, n. \quad (3.56)$$

Note that although there is no restriction on the choice of the collocation points, usually the roots  $r_m$  of Chebyshev polynomials (3.56) are chosen. These seem to give better convergence in numerical analysis.

It may be seen that the system of linear algebraic equations (3.55) are homogeneous. For nontrivial solutions of  $C_{1k}$  and  $C_{2k}$ ,  $k = 1, \dots, n$ , the determinant of the matrix formed by the coefficients of  $C_{1k}$  and  $C_{2k}$  in (3.55) must be zero. From this condition, the critical compressive strain  $(\epsilon_0)_{\text{cr}}$  corresponding to the buckling instability point may be obtained. Furthermore, the crack opening shape at instability may be obtained from the corresponding  $C_{1k}$ 's and  $C_{2k}$ 's. Note that from the nature of the eigenvalue problem it may be seen that the exact values of  $C_{1k}$ 's and  $C_{2k}$ 's are not available. Instead, the eigenvectors are determined within a multiplicative arbitrary constant.

### 3.1.4 Crack Opening Shape

From (2.68), (3.1), (3.35), and (3.42) we may express the crack opening displacement component in the  $y$ - and  $x$ -direction, respectively, as

$$v_2(x, +0) - v_1(x, -0) = a \sum_{k=1}^n C_{1k} \int_{-1}^r \frac{T_{2k-1}(s)}{\sqrt{1-s^2}} ds, \quad (3.57a)$$

$$r = \frac{x}{a}, \quad -1 < r < 1,$$

$$u_2(x, +0) - u_1(x, -0) = a \sum_{k=1}^n C_{2k} \int_{-1}^r \frac{T_{2k}(s)}{\sqrt{1-s^2}} ds, \quad (3.57b)$$

$$r = \frac{x}{a}, \quad -1 < r < 1.$$

The integral in (3.57) can be expressed in closed form as

$$\int_{-1}^r \frac{T_j(s)}{\sqrt{1-s^2}} ds = -\frac{1}{j} U_{j-1}(r) \sqrt{1-r^2}, \quad j \geq 1. \quad (3.58)$$

By substituting (3.58) into (3.57) we may then express the normalized crack opening displacement components as

$$\frac{v_2(x, +0) - v_1(x, -0)}{a} = - \sum_{k=1}^n C_{1k} \frac{U_{2k-2}(x/a)}{2k-1} \sqrt{1-(x/a)^2}, \quad (3.59a)$$

$$\frac{u_2(x, +0) - u_1(x, -0)}{a} = - \sum_{k=1}^n C_{2k} \frac{U_{2k-1}(x/a)}{2k} \sqrt{1-(x/a)^2}. \quad (3.59b)$$

Again, In the perturbation analysis the exact values of  $C_{1k}$ 's and  $C_{2k}$ 's can not be obtained, but only their relation as a "vector". Therefore, Equation (3.59) gives only the crack opening shape, rather than the real opening displacement.

### 3.1.5 Stress Intensity Factors

Note that because  $\sigma_{1yy}^{(0)} = \sigma_{1xy}^{(0)} = 0$  (Equation (2.13)), we have  $\sigma_{1yy} = \sigma_{1yy}^*$  and  $\sigma_{1xy} = \sigma_{1xy}^*$ . The mode I and II stress intensity factors for the crack geometry given in Figure 2.1 can then be defined and evaluated as follows:

$$K_I(-a) = \lim_{x \rightarrow -a} \sqrt{2\pi(-a-x)} \sigma_{1yy}^*(x, 0), \quad (3.60)$$

$$K_I(a) = \lim_{x \rightarrow a} \sqrt{2\pi(x-a)} \sigma_{1yy}^*(x, 0), \quad (3.61)$$

$$K_{II}(-a) = \lim_{x \rightarrow -a} \sqrt{2\pi(-a-x)} \sigma_{1xy}^*(x, 0), \quad (3.62)$$

$$K_{II}(a) = \lim_{x \rightarrow a} \sqrt{2\pi(x-a)} \sigma_{1xy}^*(x, 0), \quad (3.63)$$

where  $x$  lies outside the crack. Recognizing that while the stresses inside the crack give us the system of singular integral equations, these equations also provide the stress

expressions outside of the crack at  $y = 0$ , provided the density functions are known. Therefore, we can write

$$\sigma_{1yy}^*(x, 0) = \frac{\mu_1}{\pi} \int_{-a}^a \sum_{j=1}^2 \left[ (D_{1j1}^\infty + D_{1j2}^\infty) \left( \frac{\delta_{1j}}{t-x} \right) + k_{1j}(x, t) \right] f_j(t) dt, \quad (3.64)$$

$$\sigma_{2yy}^*(x, 0) = \frac{\mu_1}{\pi} \int_{-a}^a \sum_{j=1}^2 \left[ (D_{2j1}^\infty + D_{2j2}^\infty) \left( \frac{\delta_{2j}}{t-x} \right) + k_{2j}(x, t) \right] f_j(t) dt, \quad (3.65)$$

or, in terms of the normalized quantities (3.1),

$$\sigma_{1yy}^*(x, 0) = \frac{\mu_1}{\pi} \int_{-1}^1 \sum_{j=1}^2 \left[ (D_{1j1}^\infty + D_{1j2}^\infty) \left( \frac{\delta_{1j}}{s-r} \right) + k_{1j}^*(r, s) \right] f_j^*(s) ds, \quad (3.66)$$

$$\sigma_{2yy}^*(x, 0) = \frac{\mu_1}{\pi} \int_{-1}^1 \sum_{j=1}^2 \left[ (D_{2j1}^\infty + D_{2j2}^\infty) \left( \frac{\delta_{2j}}{s-r} \right) + k_{2j}^*(r, s) \right] f_j^*(s) ds. \quad (3.67)$$

By substituting (3.66) into (3.60), we have

$$K_I(-a) = \lim_{r \rightarrow -1} \sqrt{2\pi a(-1-r)} \left\{ \frac{\mu_1(D_{111}^\infty + D_{112}^\infty)}{\pi} \int_{-1}^1 \frac{f_1^*(s)}{(s-r)} ds \right. \\ \left. + \frac{\mu_1}{\pi} \int_{-1}^1 \sum_{j=1}^2 k_{1j}^*(r, s) f_j^*(s) ds \right\}. \quad (3.68)$$

Recalling that the density functions are of the form of Equation (3.35) and  $k_{ij}^*(r, s)$ ,  $i, j = 1, 2$ , are bounded in  $|s| < 1$ , Equation (3.68) can be simplified as

$$K_I(-a) = \lim_{r \rightarrow -1} \mu_1(D_{111}^\infty + D_{112}^\infty) \sqrt{\frac{2a}{\pi}(-1-r)} \int_{-1}^1 \frac{f_1^*(s)}{(s-r)} ds. \quad (3.69)$$

Following the discussion in Section 3.1.2 regarding the behavior of Cauchy integral and from Equations (3.26) and (3.28) with that  $p_1 = p_2 = 1/2$ , we have

$$\frac{1}{\pi} \int_{-1}^1 \frac{f_1^*(s)}{(s-r)} ds = \frac{g_1(-1)e^{i\pi/2}}{\sqrt{2}(1+r)^{1/2}} - \frac{g_1(1)e^{-i\pi/2}}{\sqrt{2}(1-r)^{1/2}} + F_0(r), \quad |r| > 1, \quad (3.70)$$

where  $F_0$  is a bounded function. Substituting (3.70) back to (3.69), we obtain

$$K_I(-a) = \mu_1(D_{111}^\infty + D_{112}^\infty)\sqrt{\pi a} g_1(-1). \quad (3.71)$$

By substituting (3.42a) with  $n$ -term truncation into (3.71), the mode I stress intensity factor at  $x = -a$  can be expressed as

$$K_I(-a) = -\mu_1(D_{111}^\infty + D_{112}^\infty)\sqrt{\pi a} \sum_{j=1}^n C_{1j}, \quad (3.72)$$

where  $D_{111}^\infty$  and  $D_{112}^\infty$  are given in (2.52). Similarly, from (3.61), (3.66), and (3.70) we may express mode I stress intensity factor at  $x = a$  as

$$K_I(a) = -\mu_1(D_{111}^\infty + D_{112}^\infty)\sqrt{\pi a} g_1(1), \quad (3.73)$$

or

$$K_I(a) = -\mu_1(D_{111}^\infty + D_{112}^\infty)\sqrt{\pi a} \sum_{j=1}^n C_{1j}. \quad (3.74)$$

By following the same process, the mode II stress intensity factors at the crack tips are given as follows:

$$K_{II}(-a) = \mu_1(D_{221}^\infty + D_{222}^\infty)\sqrt{\pi a} \sum_{j=1}^n C_{2j}, \quad (3.75)$$

$$K_{II}(a) = -\mu_1(D_{221}^\infty + D_{222}^\infty)\sqrt{\pi a} \sum_{j=1}^n C_{2j}. \quad (3.76)$$

It may be seen from the symmetry of the geometry and loading (Figure 2.1) that the mode I stress intensity factors would be the same at both crack tips; and the mode II stress intensity factors would be opposite in sign. This observation agrees with Equations (3.72) and (3.74)-(3.76). Note that since we can not obtain the exact values of  $C_{1k}$ 's and  $C_{2k}$ 's from the perturbation analysis but only their relative magnitudes, the values of stress intensity factors are not available. However, the phase angle which describes the mode

II/mode I ratio of stress intensity factors at the inception of buckling instability can be obtained as follows:

$$\psi(a) = \tan^{-1} \left( \frac{K_{\text{II}}(a)}{K_{\text{I}}(a)} \right) = \tan^{-1} \left( \lambda_2^* \sum_{j=1}^n C_{2j} \Big/ \lambda_1^* \sum_{j=1}^n C_{1j} \right), \quad (3.77)$$

where  $\lambda_1^*$  and  $\lambda_2^*$  are given in (B6) and (B7).

### 3.2 On the Problem of the Weakened Interface

The problem of the weakened interface may be described by (3.1), (3.2), and (3.4). It may be seen that compared with (3.3), only one extra term exists in the singular integral equation (3.4). Thus we may use the same solution technique with minor modifications to the system of linear equations. Again, we express the density functions  $f_1^*$  and  $f_2^*$  by (3.35) and (3.42). The last integral in (3.4) may be written as:

$$\begin{aligned} as_1 \int_{-1}^r f_1^*(s) ds &= as_1 \sum_{k=1}^n C_{1k} \int_{-1}^r \frac{T_{2k-1}(s)}{\sqrt{1-s^2}} ds, \quad \text{for } i = 1; \\ as_2 \int_{-1}^r f_2^*(s) ds &= as_2 \sum_{k=1}^n C_{2k} \int_{-1}^r \frac{T_{2k}(s)}{\sqrt{1-s^2}} ds, \quad \text{for } i = 2. \end{aligned} \quad (3.77)$$

By substituting (3.58) into (3.77), adding them into (3.50), and using the same collocation scheme we obtain the system of linear algebraic equations for the unknowns  $C_{1k}$  and  $C_{2k}$  as follows:

$$\begin{aligned}
& \mu_1 \sum_{k=1}^n C_{1k} \left[ (D_{111}^\infty + D_{112}^\infty) U_{2k-2}(r_m) + (|\gamma| h) \left( \frac{a}{h} \right) B_{111} \sqrt{1-r_m^2} \frac{U_{2k-2}(r_m)}{2k-1} \right] \\
& + \mu_1 (|\gamma| h) \left( \frac{a}{h} \right) \sum_{k=1}^n C_{1k} \frac{1}{\pi} \int_{-1}^1 \frac{T_{2k-1}(s)}{\sqrt{1-s^2}} \hat{k}_{11}(r_m, s) ds \\
& + \mu_1 (|\gamma| h) \left( \frac{a}{h} \right) B_{121} \sum_{k=1}^n C_{2k} \frac{T_{2k}(r_m)}{2k} \\
& + \mu_1 (|\gamma| h) \left( \frac{a}{h} \right) \sum_{k=1}^n C_{2k} \frac{1}{\pi} \int_{-1}^1 \frac{T_{2k}(s)}{\sqrt{1-s^2}} \hat{k}_{12}(r_m, s) ds \\
& + a s_1 \sum_{k=1}^n C_{1k} \frac{U_{2k-2}(r_m)}{2k-1} \sqrt{1-r_m^2} = 0, \quad m = 1, \dots, n,
\end{aligned} \tag{3.78a}$$

$$\begin{aligned}
& \mu_1 \sum_{k=1}^n C_{2k} \left[ (D_{221}^\infty + D_{222}^\infty) U_{2k-1}(r_m) + (|\gamma| h) \left( \frac{a}{h} \right) B_{221} \sqrt{1-r_m^2} \frac{U_{2k-1}(r_m)}{2k} \right] \\
& + \mu_1 (|\gamma| h) \left( \frac{a}{h} \right) \sum_{k=1}^n C_{2k} \frac{1}{\pi} \int_{-1}^1 \frac{T_{2k}(s)}{\sqrt{1-s^2}} \hat{k}_{22}(r_m, s) ds \\
& + \mu_1 (|\gamma| h) \left( \frac{a}{h} \right) B_{211} \sum_{k=1}^n C_{1k} \frac{T_{2k-1}(r_m)}{2k-1} \\
& + \mu_1 (|\gamma| h) \left( \frac{a}{h} \right) \sum_{k=1}^n C_{1k} \frac{1}{\pi} \int_{-1}^1 \frac{T_{2k-1}(s)}{\sqrt{1-s^2}} \hat{k}_{21}(r_m, s) ds \\
& + a s_2 \sum_{k=1}^n C_{2k} \frac{U_{2k-1}(r_m)}{2k} \sqrt{1-r_m^2} = 0, \quad m = 1, \dots, n,
\end{aligned} \tag{3.78b}$$

where  $\hat{k}_{ij}$ ,  $i, j = 1, 2$ , are given in (3.51)-(3.54) and the collocation points  $r_m$  are chosen as (3.56). Again, it can be seen that (3.78) is a system of homogeneous equations. The eigenvalues obtained from (3.78) correspond to the buckling instability point and the eigenvectors give the corresponding buckling mode shape.

### 3.3 On the Numerical Procedures

In Section 3.1.3 we obtained a system of linear algebraic equation (3.55) (Equation (3.78) for the weakened interface problem). It may be seen that in the system of equations the coefficients of the unknowns involve some integrals that can not be evaluated analytically. Thus, we have to employ numerical integration technique to evaluate these

integrals. Two types of integrals, namely, the outer integrals involving the Chebyshev polynomials and the integrals from zero to  $A$  in the kernels  $\hat{k}_{ij}$ 's (Equations (3.51)-(3.54)), are evaluated numerically by using Gaussian quadratures.

### 3.3.1 Integrals Involving the Chebyshev Polynomials

From (3.55) and (3.78) we may see that the integrals involving the Chebyshev polynomials may be expressed as

$$\int_{-1}^1 \frac{T_n(s)}{\sqrt{1-s^2}} \hat{k}_{ij}(r_m, s) ds, \quad i, j = 1, 2, \quad n > 0. \quad (3.79)$$

A commonly used technique for evaluating (3.79) is the Gauss-Chebyshev integration formula [74]. Yet there are still certain restrictions when applying Gauss-Chebyshev formula to compute (3.79) [72]. Therefore, the approach that we choose for evaluating (3.79) is to regularize the integrand and then to use the Gaussian quadratures for integration. This is achieved first by making a change of variables as follows:

$$\begin{aligned} s &= \cos \theta, \\ T_n(s) &= \cos(n \cos^{-1} s) = \cos(n\theta), \end{aligned} \quad (3.80)$$

giving

$$\int_{-1}^1 \frac{T_n(s)}{\sqrt{1-s^2}} \hat{k}_{ij}(r_m, s) ds = \int_0^\pi \cos(n\theta) \hat{k}_{ij}(\cos \theta - r_m) d\theta, \quad i, j = 1, 2, \quad (3.81)$$

where from (3.51)-(3.54) it can be seen that  $\hat{k}_{ij}(r, s) = \hat{k}_{ij}(s - r)$ . For better convergence of the numerical calculation, the integral from  $\theta = 0$  to  $\pi$  is broken into two integrals from  $\theta = 0$  to  $\cos^{-1} r_m$  and from  $\theta = \cos^{-1} r_m$  to  $\pi$ , and are then computed by using Gaussian quadratures.

### 3.3.2 Convergence of the Approximation

In Section 3.1.3 the singular integral equations are converted into a linear system of size  $2n$  by  $2n$ , where  $n$  is the number of terms in the summation that make up the density functions which are the unknowns in the singular integral equations.  $n$  is also the number of collocations points that we chose to form the system of linear equations. Theoretically, as the value of  $n$  increases, the accuracy of series approximation of the unknown density functions would be higher. Nevertheless, the numerical computation required for the higher order approximations increases in a quadratic fashion. Therefore, in order to obtain a satisfactory solution without spending too much computing time, it is important to examine the relation between the calculated solution and the number of terms  $n$  used in the approximation. To do that, we start a pilot case for the problem described in Figure 2.1 by taking for the value of the material constants, Poisson's ratio,  $\nu = 0.3$ , the inhomogeneity parameter of the FGM coating,  $\gamma h = -2.3026$  ( $\mu_2(h)/\mu_1 = 0.1$ ), and  $h/a = 0.3$ . The computed critical or instability strain  $(\epsilon_0)_{\text{cr}}$  as a function of  $n$  is given in Table 3.1. It can be seen from Table 3.1 that by using 8 approximation terms and collocation points, the results agree with higher order approximations up to 3 significant digits. Therefore, we will use  $n = 8$  in our analysis unless otherwise stated.

Table 3.1 Effect of the number of approximation terms on the instability point and phase angle for the problem described in Figure 2.1 with  $\gamma h = -2.3026$ ,  $\nu = 0.3$ , and  $h/a = 0.3$ .

Approximation terms $n$	Instability load $(\epsilon_0)_{\text{cr}}$	Phase angle $\psi$ (degree)
2	0.04027	-37.82
4	0.03672	-42.15
8	0.03671	-42.36
16	0.03671	-42.37
32	0.03671	-42.39

## Chapter 4

### Postbuckling Analysis

#### 4.1 Introduction

Although the buckling instability problem can be solved analytically by using a perturbation technique and the bifurcation point may be obtained as described in the previous chapter, the solution for the problem of FGM coating/homogeneous substrate containing an interface crack under compressive loading described in Figure 2.1 cannot be obtained beyond the inception of buckling by using the perturbation technique. Moreover, the fracture mechanics parameters for the crack problem, e.g., stress intensity factors, are nonzero only for the postbuckling state. Therefore, a nonlinear, postbuckling analysis which studies the full displacement field is required to complete the fracture analysis. In the present chapter this is done by using a finite element method. The finite element procedure developed for solving the postbuckling problem is based on a general displacement-based finite element code FRAC2D [75] in which special enriched crack-tip elements are used to calculate the fracture mechanics parameters.

Because nonlinear behavior is involved in the postbuckling of layered material containing an interface crack, an incremental-iterative finite element approach is used. Nonlinearities come into play because displacements (but not strains) and rotations are large. However, it is assumed that the displacements are small around the crack tip and that linear elastic fracture mechanics may be employed to investigate the behavior near the interface crack tip. The finite element analysis uses special enriched elements for the crack tip region as well as a geometrically nonlinear formulation for the rest of the coating/substrate composite to investigate the interface crack behavior simultaneously with the postbuckling deformation. The derivation of the finite element approach for the

geometrically nonlinear problem, the formulation for the special enriched elements, and the implementation of the material inhomogeneity are described in the following sections.

#### 4.2 Formulation of the Nonlinear Problem

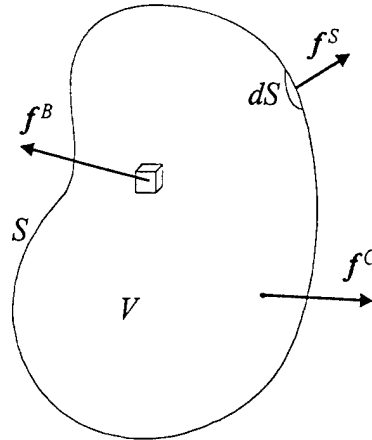


Figure 4.1 A general elastic medium under loading.

Consider an arbitrary elastic medium subjected to external loading as shown in Figure 4.1. By using the principle of virtual displacement [76], we may express the equilibrium equation with respect to the configuration of the medium at time  $t$  in terms of the following variational form

$$\int_{^tV} {}^t\tau_{ij} \delta_t e_{ij} d^tV = {}^tR, \quad (4.1)$$

where  ${}^tV$  is the volume of the medium at time  $t$ ,  ${}^t\tau_{ij}$  is the Cartesian component of the Cauchy stress tensor,  $\delta_t e_{ij}$  is the virtual strain corresponding to virtual displacements  $\delta u_i$  and  $\delta u_j$ , and  $\delta_t e_{ij}$  is given by

$$\delta_t e_{ij} = \frac{1}{2} \left[ \frac{\partial(\delta u_i)}{\partial {}^t x_j} + \frac{\partial(\delta u_j)}{\partial {}^t x_i} \right], \quad (4.2)$$

${}^t x_i$  being the Cartesian coordinates of material point at time  $t$ , and the external virtual work  ${}^t R$  is given by

$${}^t R = \int_{tV} {}^t f_i^B \delta u_i d^t V + \int_{tS} {}^t f_i^S \delta u_i^S d^t S + {}^t f_i^C \delta u_i^C, \quad (4.3)$$

where  ${}^t f_i^B$ ,  ${}^t f_i^S$ , and  ${}^t f_i^C$  are the Cartesian components of the applied body force, distributed surface traction, and concentrated external loading, respectively, at time  $t$ ,  $\delta u_i^S$  and  $\delta u_i^C$  are  $\delta u_i$  evaluated, respectively on the surface  ${}^t S$  and at the point where  ${}^t f_i^C$  is applied. Note that in this analysis, the motion of the medium is relative to a fixed Cartesian coordinate system. Also note that the postbuckling problem under consideration is static and consequently, time-independent. The terminology "time  $t$ " is used only to denote the deformed configuration which differs from the original, undeformed configuration. No inertia terms are included.

The coordinates of an arbitrary point  $P$  in the body at time 0 are  ${}^0 x_1$ ,  ${}^0 x_2$ ,  ${}^0 x_3$ ; at time  $t$  they are  ${}^t x_1$ ,  ${}^t x_2$ ,  ${}^t x_3$ , where the left superscript refer to the configuration of the medium, and therefore, we have

$${}^t x_i = {}^0 x_i + {}^t u_i, \quad i = 1, 2, 3. \quad (4.4)$$

The notation scheme for coordinates and displacements is also used for other quantities (stress, body force, surface traction, etc.). In addition to that, a left subscript denotes the configuration with respect to which the quantity is measured. For example,  ${}^0 f^B$  denotes the body force at time  $t$ , but measured in configuration 0. The exception is that if the quantity under consideration in the same configuration in which it is also measured, the left subscript may not be used, e.g.,  ${}^t f^B = {}^t f^B$ .

An inherent shortcoming in the general application of (4.1) is that the configuration of the medium at time  $t$  is unknown. To overcome this difficulty we may rewrite (4.1) such that the quantities of interest are measured with respect to configuration 0 (the Lagrangian formulation) and the integral can be evaluated over the original, undeformed domain. For the Lagrangian formulation the general stain tensor we used is the Green-Lagrange strain tensor which is given as follows:

$${}^t_0\epsilon_{ij} = \frac{1}{2}({}^t_0u_{i,j} + {}^t_0u_{j,i} + {}^t_0u_{k,i} {}^t_0u_{k,j}). \quad (4.5)$$

Note that while a differentiation is involved, the left subscript indicates the configuration in which the coordinate is measured, for example,  ${}^t_0x_{i,j} = \frac{\partial {}^t x_i}{\partial {}^0 x_j}$ . The corresponding stress tensors we used for the Green-Lagrange strain tensor  ${}^t_0\epsilon_{ij}$  is the second Piola-Kirchhoff stress tensor  ${}^t_0\sigma_{ij}$ . As shown in Appendix A, the relation between Cauchy stress and the second Piola-Kirchhoff stress is given by

$${}^t\tau_{mn} = \left( \frac{d^0 V}{d^t V} \right) {}^t_0 x_{m,i} {}^t_0 x_{n,j} {}^t_0 \sigma_{ij}. \quad (4.6)$$

Given that [77]

$$\delta_t e_{mn} = {}^t_0 x_{i,m} {}^t_0 x_{j,n} \delta_0^t \epsilon_{ij}, \quad (4.7)$$

and from (4.6) we may write

$$\int_{tV} {}^t\tau_{ij} \delta_t e_{ij} d^t V = \int_0 V {}^t_0 \sigma_{ij} \delta_0^t \epsilon_{ij} d^0 V. \quad (4.8)$$

By assuming that the external virtual work  ${}^t R$  defined by (4.3) is deformation-independent and can be specified at undeformed configuration,  ${}^t R$  can be expressed as

$${}^t R = \int_0 V {}^t_0 f_i^B \delta u_i d^0 V + \int_0 S {}^t_0 f_i^S \delta u_i^S d^0 S + {}^t_0 f_i^C \delta u_i^C. \quad (4.9)$$

Therefore, we may rewrite Equation (4.1) as follows:

$$\int_0 V {}^t_0 \sigma_{ij} \delta_0^t \epsilon_{ij} d^0 V = {}^t R, \quad (4.10)$$

where  ${}^t R$  is given in (4.9).

Since in general the medium may undergo large displacements and large strains and therefore the kinematic relation (4.5) can not be linearized, Equation (4.10) can not be solved directly. Nevertheless, we may employ an incremental-iterative method to solve (4.10). That is, instead of applying full amount of the external loadings, a series of loading

increments are applied until the summation of the increments reaches the full amount. For each loading increment, an approximate solution can be obtained by referring all variables to a previously calculated known equilibrium configuration and linearizing the resulting equations for the increment. The solution is then improved by iterations.

To derive the governing equations for the incremental-iterative approach, first we consider the equilibrium at time  $t + \Delta t$ . Similar to (4.10), we may write

$$\int_{\partial V} {}^{t+\Delta t} \sigma_{ij} \delta {}^{t+\Delta t} \epsilon_{ij} d^0 V = {}^{t+\Delta t} R, \quad (4.11)$$

where

$${}^{t+\Delta t} u_i = {}^t u_i^{(*)} + u_i, \quad i = 1, 2, 3, \quad (4.12)$$

$${}^{t+\Delta t} \sigma_{ij} = {}^0 \sigma_{ij}^{(*)} + {}_0 \sigma_{ij}, \quad i, j = 1, 2, 3, \quad (4.13)$$

$${}^{t+\Delta t} \epsilon_{ij} = {}^0 \epsilon_{ij}^{(*)} + {}_0 \epsilon_{ij}, \quad i, j = 1, 2, 3, \quad (4.14)$$

in which we assume that  ${}^t u_i^{(*)}$ ,  ${}^t \sigma_{ij}^{(*)}$ , and  ${}^t \epsilon_{ij}^{(*)}$  are known quantities obtained solving (4.10); and  $u_i$ ,  ${}_0 \sigma_{ij}$ , and  ${}_0 \epsilon_{ij}$  are the incremental displacement, stress, and strain, respectively. For generality we also assume that the values of  ${}^t u_i^{(*)}$ ,  ${}^t \sigma_{ij}^{(*)}$ , and  ${}^t \epsilon_{ij}^{(*)}$  are not the "exact" solutions from (4.10) but with small errors. The "error" which represents the difference between the external virtual work ( ${}^t R$ ) and the internal virtual work (l. h. s. of Equation (4.10)) evaluated with the approximate solutions is defined by

$${}^t E^{(*)} = {}^{t+\Delta t} E^{(0)} = {}^t R - \int_{\partial V} {}^0 \sigma_{ij}^{(*)} \delta {}^t \epsilon_{ij}^{(*)} d^0 V. \quad (4.15)$$

In Equation (4.15)  ${}^{t+\Delta t} E^{(0)}$  represents the "intrinsic error" to be taken into account in the analysis at time  $t + \Delta t$ . Note that there is, again, no time history involved in the analysis and the terminologies "time  $t$ " and "time  $t + \Delta t$ " are only used to denote two successive incremental steps. By substituting (4.5) and (4.12) into (4.14) we may express the incremental strain  ${}_0 \epsilon_{ij}$  as

$${}_0\epsilon_{ij} = {}_0e_{ij} + {}_0\eta_{ij}, \quad (4.16)$$

where  ${}_0e_{ij}$  and  ${}_0\eta_{ij}$  represent the linear and nonlinear part of  ${}_0\epsilon_{ij}$ , respectively, and are given by

$${}_0e_{ij} = \frac{1}{2}({}_0u_{i,j} + {}_0u_{j,i} + {}_0^tu_{k,i}^{(*)} {}_0u_{k,j} + {}_0u_{k,i} {}_0^tu_{k,j}^{(*)}), \quad (4.17)$$

$${}_0\eta_{ij} = \frac{1}{2} {}_0u_{k,i} {}_0u_{k,j}. \quad (4.18)$$

The virtual strain  $\delta {}_0^{t+\Delta t}\epsilon_{ij}$  can then be written as

$$\delta {}_0^{t+\Delta t}\epsilon_{ij} = \delta {}_0\epsilon_{ij} = \delta {}_0e_{ij} + \delta {}_0\eta_{ij}, \quad i, j = 1, 2, 3. \quad (4.19)$$

By substituting (4.13) and (4.19) into (4.11), we have the governing equation as

$$\int_{\text{o}V} {}_0\sigma_{ij} \delta {}_0\epsilon_{ij} d^0V + \int_{\text{o}V} {}_0^t\sigma_{ij}^{(*)} \delta {}_0\eta_{ij} d^0V = {}^{t+\Delta t}R - \int_{\text{o}V} {}_0^t\sigma_{ij}^{(*)} \delta {}_0e_{ij} d^0V. \quad (4.20)$$

It may be seen from (4.17) that

$$\int_{\text{o}V} {}_0^t\sigma_{ij}^{(*)} \delta {}_0e_{ij} d^0V = \int_{\text{o}V} {}_0^t\sigma_{ij}^{(*)} \delta {}_0^t\epsilon_{ij}^{(*)} d^0V. \quad (4.21)$$

By substituting (4.15) and (4.21) into (4.20) we have

$$\int_{\text{o}V} {}_0\sigma_{ij} \delta {}_0\epsilon_{ij} d^0V + \int_{\text{o}V} {}_0^t\sigma_{ij}^{(*)} \delta {}_0\eta_{ij} d^0V = ({}^{t+\Delta t}R - {}^tR) + {}^{t+\Delta t}E^{(0)}. \quad (4.22)$$

To linearize (4.22) we approximate the virtual strain increment and constitutive equations by the following relations

$$\delta {}_0\epsilon_{ij} \cong \delta {}_0e_{ij}, \quad i, j = 1, 2, 3, \quad (4.23)$$

$${}_0\sigma_{ij} \cong {}_0C_{ijkl} {}_0e_{kl} + {}_0C_{Tij}\Delta T, \quad i, j = 1, 2, 3, \quad (4.24)$$

giving

$$\begin{aligned} & \int_{\Omega} {}_0 C_{ijkl} {}_0 e_{kl} \delta_0 e_{ij} d^0 V + \int_{\Omega} {}_0^t \sigma_{ij}^{(*)} \delta_0 \eta_{ij} d^0 V \\ &= ({}^{t+\Delta t} R - {}^t R) + {}^{t+\Delta t} E^{(0)} - \int_{\Omega} {}_0 C_{Tij} \Delta T \delta_0 e_{ij} d^0 V, \end{aligned} \quad (4.25)$$

where  ${}_0 C_{ijkl}$  and  ${}_0 C_{Tij}$  are functions of  ${}^0 x_i$  ( $i = 1, 2, 3$ ) for linear elastic inhomogeneous materials,  ${}^{t+\Delta t} R - {}^t R$  corresponds to the incremental external loading,  $\Delta T$  is the temperature change in the medium from time  $t$  to  $t + \Delta t$ , and  $\Delta T$  is assumed to be a known function of  $({}^0 x_1, {}^0 x_2, {}^0 x_3)$ . The linearized governing equation (4.25) is then solved by using finite element technique. Details of the finite element analysis will be discussed later. Assuming that the displacement, strain, and stress approximations have been calculated, we may then examine the difference between the external virtual work ( ${}^{t+\Delta t} R$ ) and internal virtual work (l. h. s. of Equation (4.11)). Denoting the calculated values with a superscript (1) in anticipation that an iteration will in general be necessary, the "error" due to linearization is

$${}^{t+\Delta t} E^{(1)} = {}^{t+\Delta t} R - \int_{\Omega} {}^{t+\Delta t} {}_0 \sigma_{ij}^{(1)} \delta {}^{t+\Delta t} {}_0 \epsilon_{ij}^{(1)} d^0 V. \quad (4.26)$$

The "error" described in (4.26) represents the "out-of-balance virtual work" resulting from linearization of (4.22). Also it may be seen that (4.26) has the same form as (4.15). In order to further reduce the "out-of-balance virtual work" we need to perform an iteration in which the following equation is solved until the difference between the external and internal virtual work is negligible within a certain convergence measure:

$$\begin{aligned} & \int_{\Omega} {}_0 C_{ijkl} {}_0 e_{kl}^{(n)} \delta_0 e_{ij}^{(n)} d^0 V + \int_{\Omega} {}_0^t \sigma_{ij}^{(n-1)} \delta_0 \eta_{ij}^{(n)} d^0 V \\ &= {}^{t+\Delta t} E^{(n-1)}, \quad n = 2, 3, \dots, \end{aligned} \quad (4.27)$$

where

$${}^{t+\Delta t}E^{(n)} = {}^{t+\Delta t}R - \int_{\Omega} {}^{t+\Delta t}{}_0\sigma_{ij}^{(n)} \delta {}^{t+\Delta t}{}_0\epsilon_{ij}^{(n)} d^0V, \quad (4.28)$$

and the incremental strain corrections  ${}_0e_{kl}^{(n)}$  and  ${}_0\eta_{ij}^{(n)}$  correspond to the displacement correction  $u_i^{(n)}$  which are given by

$${}_0e_{ij}^{(n)} = \frac{1}{2} \left[ {}_0u_{i,j}^{(n)} + {}_0u_{j,i}^{(n)} + {}^{t+\Delta t}{}_0u_{k,i}^{(n-1)} {}_0u_{k,j}^{(n)} + {}_0u_{k,i}^{(n)} {}^{t+\Delta t}{}_0u_{k,j}^{(n-1)} \right], \quad (4.29)$$

$${}_0\eta_{ij}^{(n)} = \frac{1}{2} {}_0u_{k,i}^{(n)} {}_0u_{k,j}^{(n)}. \quad (4.30)$$

The displacements are then updated for each iteration as

$${}^{t+\Delta t}u_i^{(n)} = {}^{t+\Delta t}u_i^{(n-1)} + u_i^{(n)}, \quad i = 1, 2, 3. \quad (4.31)$$

Observing the resemblance between the governing equations for the incremental part (Equation (4.25)) and the iterative part (Equation (4.27)) of the analysis, we may further reduce the governing equations for the incremental-iterative approach to a single equation given by

$$\begin{aligned} & \int_{\Omega} {}_0C_{ijkl} {}_0e_{kl}^{(n)} \delta {}_0e_{ij}^{(n)} d^0V + \int_{\Omega} {}^{t+\Delta t}{}_0\sigma_{ij}^{(n-1)} \delta {}_0\eta_{ij}^{(n)} d^0V \\ &= \delta_{n1} \left[ ({}^{t+\Delta t}R - {}^tR) - \int_{\Omega} {}_0C_{Tij} \Delta T \delta {}_0e_{ij}^{(1)} d^0V \right] \\ & \quad + {}^{t+\Delta t}E^{(n-1)}, \quad n = 1, 2, 3, \dots, \end{aligned} \quad (4.32)$$

where  $\delta_{n1}$  is the Kronecker delta and

$${}^{t+\Delta t}u_i^{(0)} = {}^t u_i^{(*)}, \quad {}^{t+\Delta t}{}_0\sigma_{ij}^{(0)} = {}^t {}_0\sigma_{ij}^{(*)}, \quad {}^{t+\Delta t}{}_0\epsilon_{ij}^{(0)} = {}^t {}_0\epsilon_{ij}^{(*)}, \quad i, j = 1, 2, 3, \quad (4.33)$$

$${}_0e_{ij}^{(1)} = {}_0e_{ij}, \quad {}_0\eta_{ij}^{(1)} = {}_0\eta_{ij}, \quad i, j = 1, 2, 3. \quad (4.34)$$

The finite element implementation of the governing equation (4.32) is described in the following section.

### 4.3 Finite Element Procedure for the Nonlinear Problem

To derive the governing equations for the displacement-based isoparametric continuum finite elements, we consider only the incremental-iterative nodal-point displacements  $a_r^{(n)}$  as degrees of freedom. By substituting

$$\begin{aligned} {}_0 e_{ij}^{(n)} &= \frac{\partial {}_0 e_{ij}^{(n)}}{\partial a_r^{(n)}} a_r^{(n)}, \quad \delta {}_0 e_{ij}^{(n)} = \frac{\partial {}_0 e_{ij}^{(n)}}{\partial a_r^{(n)}} \delta a_r^{(n)}, \\ \delta {}_0 \eta_{ij}^{(n)} &= \frac{\partial^2 {}_0 \eta_{ij}^{(n)}}{\partial a_r^{(n)} \partial a_s^{(n)}} a_s^{(n)} \delta a_r^{(n)}, \end{aligned} \quad (4.35)$$

into (4.32), from principle of virtual work we obtain

$$\begin{aligned} &\left[ \int_{^0V} {}_0 C_{ijkl} \frac{\partial {}_0 e_{kl}^{(n)}}{\partial a_s^{(n)}} \frac{\partial {}_0 e_{ij}^{(n)}}{\partial a_r^{(n)}} d^0 V + \int_{^0V} {}^{t+\Delta t} {}_0 \sigma_{ij}^{(n-1)} \frac{\partial^2 {}_0 \eta_{ij}^{(n)}}{\partial a_r^{(n)} \partial a_s^{(n)}} d^0 V \right] a_s^{(n)} \\ &= \delta_{n1} \left[ ({}^{t+\Delta t} R_r - {}^t R_r) - \int_{^0V} {}_0 C_{Tij} \Delta T \frac{\partial {}_0 e_{ij}^{(1)}}{\partial a_r^{(1)}} d^0 V \right] + {}^{t+\Delta t} E_r^{(n-1)}, \quad (4.36) \\ &\quad r = 1, 2, \dots, M, \end{aligned}$$

where  $M$  is the total number of degrees of freedom in the finite element analysis and

$${}^t R_r = \int_{^0V} {}^t {}_0 f_i^B \frac{\partial u_i^{(n)}}{\partial a_r^{(n)}} d^0 V + \int_{^0S} {}^t {}_0 f_i^S \frac{\partial u_i^{(n)}}{\partial a_r^{(n)}} d^0 S + {}^t {}_0 f_i^C \frac{\partial u_i^{(n)}}{\partial a_r^{(n)}}, \quad (4.37)$$

$${}^{t+\Delta t} R_r = \int_{^0V} {}^{t+\Delta t} {}_0 f_i^B \frac{\partial u_i^{(n)}}{\partial a_r^{(n)}} d^0 V + \int_{^0S} {}^{t+\Delta t} {}_0 f_i^S \frac{\partial u_i^{(n)}}{\partial a_r^{(n)}} d^0 S + {}^{t+\Delta t} {}_0 f_i^C \frac{\partial u_i^{(n)}}{\partial a_r^{(n)}}, \quad (4.38)$$

$${}^{t+\Delta t} E_r^{(n)} = \begin{cases} {}^{t+\Delta t} R_r - \int_{^0V} {}^{t+\Delta t} {}_0 \sigma_{ij}^{(n)} \frac{\partial {}_0 e_{ij}^{(n)}}{\partial a_r^{(n)}} d^0 V, & n \neq 0, \\ {}^t R_r - \int_{^0V} {}^{t+\Delta t} {}_0 \sigma_{ij}^{(0)} \frac{\partial {}^{t+\Delta t} {}_0 \epsilon_{ij}^{(0)}}{\partial a_r^{(0)}} d^0 V, & n = 0. \end{cases} \quad (4.39)$$

It may be seen that Equation (4.36) represents a system of equations for the unknown nodal displacements.

For axisymmetric or plane problems we may replace the degrees of freedom  $a_r$  for the general problem by incremental nodal point  $x$ - and  $y$ -displacement  $u_1^k$  and  $u_2^k$  where  $k$  denotes the node number in the element. Following typical finite element formulation, we may write (4.36) in a matrix form for a single finite element with  $M$  nodal points as follows:

$$\left( {}^{t+\Delta t}{}_0\mathbf{K}_L^{(n-1)} + {}^{t+\Delta t}{}_0\mathbf{K}_{NL}^{(n-1)} \right) \widehat{\mathbf{U}}^{(n)} = \delta_{n1} {}^{t+\Delta t}{}_0\mathbf{F}_r + {}^{t+\Delta t}{}_0\mathbf{E}_r^{(n-1)}, \quad n = 1, 2, \dots, \quad (4.40)$$

where  $\widehat{\mathbf{U}}^{(n)}$  is the vector of increments in the nodal point displacements,  ${}^{t+\Delta t}{}_0\mathbf{K}_L^{(n)}$  and  ${}^{t+\Delta t}{}_0\mathbf{K}_{NL}^{(n)}$  are the linear and nonlinear strain incremental stiffness matrices at time  $t + \Delta t$ ,  ${}^{t+\Delta t}{}_0\mathbf{F}_r$  is the vector of increments in the equivalent loads applied at nodal points, and  ${}^{t+\Delta t}{}_0\mathbf{E}_r^{(n)}$  is the vector of "out of balance" loads applied at nodal points. These vectors and matrices are given by

$$\widehat{\mathbf{U}}^{(n)\top} = \left\{ u_1^{1(n)}, u_2^{1(n)}, u_1^{2(n)}, u_2^{2(n)}, \dots, u_1^{M(n)}, u_2^{M(n)} \right\}, \quad (4.41)$$

$${}^{t+\Delta t}{}_0\mathbf{K}_L^{(n)} = \int_{\Omega V} {}^{t+\Delta t}{}_0\mathbf{B}_L^{(n)\top} \mathbf{C} {}^{t+\Delta t}{}_0\mathbf{B}_L^{(n)} d^0V, \quad (4.42)$$

$${}^{t+\Delta t}{}_0\mathbf{K}_{NL}^{(n)} = \int_{\Omega V} \mathbf{B}_{NL}^{\top} {}^{t+\Delta t}{}_0\mathbf{S}^{(n)} \mathbf{B}_{NL} d^0V, \quad (4.43)$$

$${}^{t+\Delta t}{}_0\mathbf{F}_r = {}^{t+\Delta t}\mathbf{R}_r - {}^t\mathbf{R}_r - \int_{\Omega V} {}^t\mathbf{B}_L^{(*)\top} {}_0\widehat{\mathbf{S}}_T d^0V, \quad (4.44)$$

$${}^{t+\Delta t}{}_0\mathbf{E}_r^{(n)} = \begin{cases} {}^{t+\Delta t}\mathbf{R}_r - \int_{\Omega V} {}^{t+\Delta t}{}_0\mathbf{B}_L^{(n)\top} {}^{t+\Delta t}{}_0\widehat{\mathbf{S}}^{(n)} d^0V, & n \neq 0, \\ {}^t\mathbf{R}_r - \int_{\Omega V} {}^t\mathbf{B}_L^{(*)\top} {}_0\widehat{\mathbf{S}}^{(*)} d^0V, & n = 0, \end{cases} \quad (4.45)$$

$${}^{t+\Delta t}\mathbf{R}_r = \int_{\Omega V} \mathbf{N}^T {}^{t+\Delta t}{}_0\mathbf{f}^B d^0V + \int_{\Omega S} \mathbf{N}^{S^T} {}^{t+\Delta t}{}_0\mathbf{f}^S d^0S + \mathbf{N}^{C^T} {}^{t+\Delta t}{}_0\mathbf{f}^C, \quad (4.46)$$

$${}^t\mathbf{R}_r = \int_{\Omega V} \mathbf{N}^T {}^t{}_0\mathbf{f}^B d^0V + \int_{\Omega S} \mathbf{N}^{S^T} {}^t{}_0\mathbf{f}^S d^0S + \mathbf{N}^{C^T} {}^t{}_0\mathbf{f}^C, \quad (4.47)$$

where  ${}^{t+\Delta t}{}_0\mathbf{B}_L^{(n)}$  and  $\mathbf{B}_{NL}$  are the linear and nonlinear strain-displacement transformation matrices, respectively,  $\mathbf{C}$  is the constitutive relation for the medium,  ${}^{t+\Delta t}{}_0\mathbf{S}^{(n)}$  and  ${}^{t+\Delta t}{}_0\widehat{\mathbf{S}}^{(n)}$  are the stress matrix and vector, respectively,  ${}_0\widehat{\mathbf{S}}_T$  is the thermal stress vector that results from the temperature change,  ${}^{t+\Delta t}\mathbf{R}_r$  is the externally applied nodal point load at time  $t + \Delta t$ ,  $\mathbf{N}$ ,  $\mathbf{N}^S$ ,  $\mathbf{N}^C$  are the volume-, surface-, and point-displacement interpolation matrices, and  ${}^{t+\Delta t}{}_0\mathbf{f}^C$ ,  ${}^{t+\Delta t}{}_0\mathbf{f}^S$ , and  ${}^{t+\Delta t}{}_0\mathbf{f}^B$  are the vectors of concentrated, surface, and body forces applied at time  $t + \Delta t$ . Note that in (4.45) the superscript (\*) indicates that the values used for calculating the corresponding matrices are taken from the final results given by the iterations at a certain increment. The matrices and vectors used in (4.42)-(4.45) are given in Appendix E for two-dimensional axisymmetric, plane strain, and plane stress problems. Note that we use the approximated kinematic relation (4.23) and (E6) to compute the the incremental strain vector and to update the total strain vector as follows:

$${}_0\widehat{\boldsymbol{\epsilon}}^{(n)} = {}^t{}_0\mathbf{B}_L^{(n)}\widehat{\mathbf{U}}^{(n)}, \quad (4.48)$$

$${}^{t+\Delta t}{}_0\widehat{\boldsymbol{\epsilon}}^{(n)} = {}_0\widehat{\boldsymbol{\epsilon}}^{(n)} + {}^{t+\Delta t}{}_0\widehat{\boldsymbol{\epsilon}}^{(n-1)}. \quad (4.49)$$

For the two-dimensional problem under consideration the surface and line integrals replacing the volume and surface integrals defined in (4.42)-(4.47) are evaluated by using Gaussian integrations. For example, the incremental linear stiffness matrix  ${}^{t+\Delta t}{}_0\mathbf{K}_L^{(n)}$  in (4.42) may be expressed as

$${}^{t+\Delta t}{}_0\mathbf{K}_L^{(n)} = \sum_{i=1}^m \sum_{j=1}^m w_i w_j \det(\mathbf{J})_{ij} \left({}^{t+\Delta t}{}_0\mathbf{B}_L^{(n)}\right)_{ij}^T \left(\mathbf{C}\right)_{ij} \left({}^{t+\Delta t}{}_0\mathbf{B}^{(n)}\right)_{ij}, \quad (4.50)$$

where  $w_i$  is the Gaussian weight on a local coordinates,  $\det(\mathbf{J})$  is the determinant of the Jacobian transforming local to global coordinates, the subscripts  $i$  and  $j$  here designate (the global coordinates of) the Gaussian integration points and refer to the fact that the parent quantities are evaluated at these points.

#### 4.4 Fracture Mechanics Parameters and Crack-tip Enriched Finite Elements

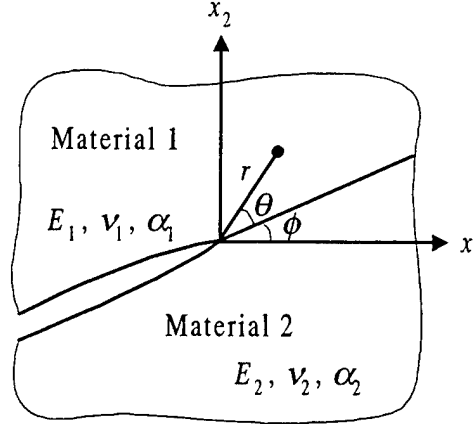


Figure 4.2 Crack at bimaterial interface between two isotropic materials.

For the interface crack problems in the layered material systems we assume, without loss in generality, that locally near the crack tip the displacements are small and that the linear elastic fracture mechanics may be used to describe the behavior around the crack tip. The asymptotic displacement expressions for an interface crack between two dissimilar isotropic materials (Figure 4.2) are given by [78]

$$\begin{aligned} {}^t u_{1j} &= f_{1j} {}^t K_I + g_{1j} {}^t K_{II}, \\ &\quad j = 1, 2, \\ {}^t u_{2j} &= f_{2j} {}^t K_I + g_{2j} {}^t K_{II}, \end{aligned} \quad (4.51)$$

where the subscript  $j$  denotes the material number,  $f_{ij}$  and  $g_{ij}$  are shown in Appendix F,  ${}^t K_I$  and  ${}^t K_{II}$  are the modes I and II stress intensity factors and they are defined such that

$${}^t K_I + i {}^t K_{II} = \lim_{r \rightarrow 0} \sqrt{2\pi} r^{1/2-i\epsilon} ({}^t \sigma_{\theta\theta} + i {}^t \sigma_{r\theta}), \quad (4.52)$$

where the bimaterial constant  $\epsilon$  is given by

$$\epsilon = \frac{1}{2\pi} \ln \left[ \left( \frac{\kappa_1}{\mu_1} + \frac{1}{\mu_2} \right) / \left( \frac{\kappa_2}{\mu_2} + \frac{1}{\mu_1} \right) \right]. \quad (4.53)$$

The phase angle which may be used to describe the relative ratio of mode II/mode I contributions is defined as

$$\psi = \tan^{-1} \left( \frac{{}^t K_{\text{II}}}{{}^t K_{\text{I}}} \right). \quad (4.54)$$

The strain energy release rate for the crack is given by

$$G = \frac{1}{2 \cosh^2(\pi\epsilon)} \left( \frac{1}{\bar{E}_1} + \frac{1}{\bar{E}_2} \right) \left( {}^t K_{\text{I}}^2 + {}^t K_{\text{II}}^2 \right), \quad (4.55)$$

where

$$\bar{E}_i = \begin{cases} E_i, & \text{for plane stress problems,} \\ \frac{E_i}{1 - \nu_i^2}, & \text{for plane strain and axisymmetric problems.} \end{cases} \quad (4.56)$$

The enriched element method, first introduced by Benzley [79] to treat crack problems in isotropic elastic media, includes the effects of the singularity (see (4.51) and (4.52)) in the element by "enriching" the conventional finite element displacement formulations with terms that give the proper singularity at the singular node. It may be seen that the displacements within the enriched elements can be expressed in terms of the nodal displacements  $u_{1j}^k$  and  $u_{2j}^k$  and stress intensity factors  ${}^t K_{\text{I}}$  and  ${}^t K_{\text{II}}$  as follows:

$$\begin{aligned} {}^t u_{1j} &= \sum_{k=1}^M N_k {}^t u_{1j}^k + {}^t K_{\text{I}} \left( f_{1j} - \sum_{k=1}^M N_k f_{1j}^k \right) + {}^t K_{\text{II}} \left( g_{1j} - \sum_{k=1}^M N_k g_{1j}^k \right), \\ {}^t u_{2j} &= \sum_{k=1}^M N_k {}^t u_{2j}^k + {}^t K_{\text{I}} \left( f_{2j} - \sum_{k=1}^M N_k f_{2j}^k \right) + {}^t K_{\text{II}} \left( g_{2j} - \sum_{k=1}^M N_k g_{2j}^k \right), \end{aligned} \quad (4.57)$$

where  $M$  and  $N_k$  are the number of nodes in the element and the interpolation functions, respectively (see Appendix E). The unknowns in (4.57) are the  $2M$  nodal displacements and the modes I and II stress intensity factors. For example, for a 12-noded quadrilateral

element there are 26 unknowns. This type of element is sometimes referred to as a subparametric element.

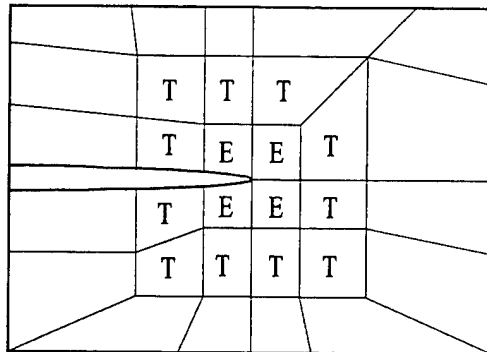


Figure 4.3 Schematic of element arrangement around a crack tip,  
E: enriched element, T: transition element.

In order to integrate the enriched element formulation with the geometrically nonlinear finite elements described in previous section, an incremental-iterative form of the governing equations for the enriched elements are required. Due to the linear kinematic relationship in the Lagrangian formulation for the linear elastic theory, the governing equations for the enriched elements may be obtained by simply replacing the "full" quantities, e.g., total nodal displacements and stress intensity factors, with the incremental or iterative quantities in the governing equations for conventional linear finite elements. One important issue in integrating the enriched nonlinear finite elements is the inter-element displacement compatibility conditions between these two types of elements. This can be overcome by introducing "transition" elements (Figure 4.3) in which the element displacement field is given by

$$\begin{aligned}
{}^t u_{1j} &= \sum_{k=1}^M N_k {}^t u_{1j}^k + Z \left[ {}^t K_I \left( f_{1j} - \sum_{k=1}^M N_k f_{1j}^k \right) + {}^t K_{II} \left( g_{1j} - \sum_{k=1}^M N_k g_{1j}^k \right) \right], \\
{}^t u_{2j} &= \sum_{k=1}^M N_k {}^t u_{2j}^k + Z \left[ {}^t K_I \left( f_{2j} - \sum_{k=1}^M N_k f_{2j}^k \right) + {}^t K_{II} \left( g_{2j} - \sum_{k=1}^M N_k g_{2j}^k \right) \right],
\end{aligned} \tag{4.58}$$

where the zeroing function  $Z$  varies from unity along the boundaries of the transition element that are in contact with crack-tip enriched elements to zero along the boundaries between the transition and the regular nonlinear elements. Although various forms of zeroing function may be used [75], in this study a linear zeroing function defined in Appendix F is chosen. Similarly, to overcome the incompatibility in the strain-displacement relations between the crack-tip and nonlinear elements we define an "artificial" strain-displacement relation as

$${}^t \epsilon_{ij} = \frac{1}{2} \left[ {}^t u_{i,j} + {}^t u_{j,i} + (1 - Z) {}^t u_{k,i} {}^t u_{k,j} \right]. \tag{4.59}$$

It may be seen that the kinematic relation (4.59) is linear along the boundaries between enriched and transition elements and is "fully" nonlinear along the boundaries between transition and nonlinear elements. It is important, however, to note that the kinematic relation (4.59) is introduced only for the purpose of obtaining better computational convergence.

Following the procedures for the nonlinear case described in previous section, we may develop the incremental governing equation for the enriched and transition elements as follows

$$\left( {}^{t+\Delta t} {}^0 \mathbf{K}_{EL}^{(n-1)} + {}^{t+\Delta t} {}^0 \mathbf{K}_{ENL}^{(n-1)} \right) \widehat{\mathbf{U}}^{(n)} = \delta_{n1} {}^{t+\Delta t} {}^0 \mathbf{F}_r + {}^{t+\Delta t} {}^0 \mathbf{E}_r^{(n-1)}, \quad n = 1, 2, \dots \tag{4.60}$$

where

$$\widehat{\mathbf{U}}^{(n)^T} = \left\{ u_1^{(n)}, u_2^{(n)}, u_1^{2(n)}, u_2^{2(n)}, \dots, u_1^{M(n)}, u_2^{M(n)}, K_I^{(n)}, K_{II}^{(n)} \right\}, \quad (4.61)$$

$${}^{t+\Delta t}{}_0 \mathbf{K}_{EL}^{(n)} = \int_{\Omega_V} {}^{t+\Delta t}{}_0 \mathbf{B}_{EL}^{(n)^T} \mathbf{C} {}^{t+\Delta t}{}_0 \mathbf{B}_{EL}^{(n)} d^0 V, \quad (4.62)$$

$${}^{t+\Delta t}{}_0 \mathbf{K}_{ENL}^{(n)} = \int_{\Omega_V} \mathbf{B}_{ENL}^T {}^{t+\Delta t}{}_0 \mathbf{S}^{(n)} \mathbf{B}_{ENL} d^0 V, \quad (4.63)$$

$${}^{t+\Delta t}{}_0 \mathbf{F}_r = {}^{t+\Delta t} \bar{\mathbf{R}}_r - {}^t \bar{\mathbf{R}}_r - \int_{\Omega_V} {}^t \mathbf{B}_{EL}^{(*)^T} {}_0 \widehat{\mathbf{S}}_T d^0 V, \quad (4.64)$$

$${}^{t+\Delta t}{}_0 \bar{\mathbf{E}}_r^{(n)} = \begin{cases} {}^{t+\Delta t} \bar{\mathbf{R}}_r - \int_{\Omega_V} {}^{t+\Delta t}{}_0 \mathbf{B}_{EL}^{(n)^T} {}^{t+\Delta t}{}_0 \widehat{\mathbf{S}}^{(n)} d^0 V, & n \neq 0, \\ {}^t \bar{\mathbf{R}}_r - \int_{\Omega_V} {}^t \mathbf{B}_{EL}^{(*)^T} {}_0 \widehat{\mathbf{S}}^{(*)} d^0 V, & n = 0, \end{cases} \quad (4.65)$$

$${}^t \bar{\mathbf{R}}_r = \begin{pmatrix} {}^t \mathbf{R}_r \\ \dots \\ {}^t \widetilde{\mathbf{R}}_r \end{pmatrix}. \quad (4.66)$$

In equations (4.61)-(4.66) the stress matrix and vectors  ${}^{t+\Delta t}{}_0 \mathbf{S}^{(n)}$ ,  ${}^{t+\Delta t}{}_0 \widehat{\mathbf{S}}^{(n)}$ , and  ${}_0 \widehat{\mathbf{S}}_T$  are defined the same as those in the nonlinear formulation,  ${}^t \mathbf{R}_r$  is given by (4.47), and  ${}^t \widetilde{\mathbf{R}}_r$  is the "singular" load vector corresponding to the unknown stress intensity factors and is a null vector if no enriched or transition elements are on a loaded boundary. The strain-displacement transformation matrices  ${}^{t+\Delta t}{}_0 \mathbf{B}_{EL}^{(n)}$  and  $\mathbf{B}_{ENL}$  are given in Appendix F.

Similar to the nonlinear formulation, the integrals in Equations (4.62)-(4.66) are evaluated by using Gaussian quadratures. However, a higher order integration is required for the enriched elements because the embedded analytical solution contains a strain singularity at the crack tip.

#### 4.5 Direction of Crack Growth

Due to the lack of symmetry with respect to the interface in the FGM coating/homogeneous substrate material system, a mixed-mode condition exists regardless

of whether the loading is mode I or mixed mode. From the viewpoint of crack driving forces, it is apparent that the crack will not advance along the interface under the mixed-mode conditions, unless the plane of the crack is a weak cleavage plane. To determine the direction of crack growth, one may examine the stress state near the crack tip. It had been observed in [65] that for the problem of crack along the nominal interface of inhomogeneous/homogeneous medium with continuous material properties the stress state around the crack tip has the same asymptotic behavior as that in a homogeneous medium. Therefore, the asymptotic stress state in the immediate neighborhood of the crack tip may be written in polar coordinates as follows [80]:

$$\begin{aligned}\sigma_{rr}(r, \theta) &= \frac{1}{\sqrt{2\pi r}} \cos \frac{\theta}{2} \left[ K_I \left( 1 + \sin^2 \frac{\theta}{2} \right) + K_{II} \left( \frac{3}{2} \sin \theta - 2 \tan \frac{\theta}{2} \right) \right] + O(r^{1/2}), \\ \sigma_{\theta\theta}(r, \theta) &= \frac{1}{\sqrt{2\pi r}} \cos \frac{\theta}{2} \left( K_I \cos^2 \frac{\theta}{2} - \frac{3}{2} K_{II} \sin \theta \right) + O(r^{1/2}), \\ \sigma_{r\theta}(r, \theta) &= \frac{1}{2\sqrt{2\pi r}} \cos \frac{\theta}{2} \left[ K_I \sin \theta - K_{II} (3 \cos \theta - 1) \right] + O(r^{1/2}),\end{aligned}\quad (4.67)$$

where  $r$  is the distance to the crack tip and  $\theta$  is measured counterclockwise from the interface. Following [81], we may estimate the direction of crack propagation by the plane of the maximum cleavage stress  $\sigma_{\theta\theta}$  around the crack tip. The crack growth (or kinking) angle  $\theta_0$  may be obtained by solving

$$\frac{\partial}{\partial \theta} \sigma_{\theta\theta}(r, \theta_0) = 0, \quad \sigma_{\theta\theta}(r, \theta_0) > 0. \quad (4.68)$$

It may be seen that (4.68) is equivalent to finding the direction of the principal stress and is the same as solving  $\sigma_{r\theta}(r, \theta_0) = 0$ . Whichever case is used, we obtain

$$\cos \frac{\theta_0}{2} \left[ K_I \sin \theta_0 - K_{II} (3 \cos \theta_0 - 1) \right] = 0. \quad (4.69)$$

From (4.69) it may be seen that  $\cos \frac{\theta_0}{2} = 0$  gives  $\theta = \pm \pi$ , which corresponds to the plane of crack. The second term in (4.69) provides the non-trivial solution and may be expressed in the following form

$$\tan^2 \frac{\theta_0}{2} - \frac{K_I}{2K_{II}} \tan \frac{\theta_0}{2} - \frac{1}{2} = 0, \quad \sigma_{\theta\theta}(r, \theta_0) > 0. \quad (4.70)$$

#### 4.6 On the Material Inhomogeneity of FGMs and Direction of Crack

From the derivation for the geometrically nonlinear finite elements we may see that material inhomogeneity would not change the form of the system of linear equations (4.40). The material property functions are involved only in evaluating the Gaussian integrations and in computing stresses from strains at the Gaussian points. Therefore, the material inhomogeneity can be considered simply by evaluating the material properties at the Gaussian quadrature points from the global material property variation functions.

A limitation of the enriched finite element procedure is that the enriched crack-tip elements are based on the asymptotic displacement fields for homogeneous materials. Thus, the size of the enriched element should be small enough such that the material property variation in the enriched element is negligible.

#### 4.7 Convergence Criterion and Summary of the Finite Element Procedure

In performing the incremental-iterative procedure, it is clear that a convergence criterion is required to terminate the iteration in each incremental step. A straightforward criterion would be to require the out-of-balance load vector  $\mathbf{E}_r$  or  $\overline{\mathbf{E}}_r$  within a preset tolerance of the original load increment. However, a difficulty with this criterion is that the displacement solution does not enter the termination criterion. In order to provide some indication of when both the displacements and forces are near their equilibrium values, we use a convergence criterion in which the increment in internal energy (i.e., the work done

by the out-of-balance loads through the displacement increments) is compared to the initial internal energy increment. Convergence is assumed to be reached when the following relations are satisfied [82]:

$$\widehat{U}^{(n)} \left\{ \begin{array}{l} {}^t_0 \mathbf{E}_r^{(n-1)} \\ {}^t_0 \overline{\mathbf{E}}_r^{(n-1)} \end{array} \right\} \leq \epsilon_E \widehat{U}^{(1)} \left\{ \begin{array}{l} {}^t_0 \mathbf{F}_r + {}^t_0 \mathbf{E}_r^{(0)} \\ {}^t_0 \overline{\mathbf{F}}_r + {}^t_0 \overline{\mathbf{E}}_r^{(0)} \end{array} \right\}, \quad (4.71)$$

where in this study the tolerance is chosen as

$$\epsilon_E = 1 \times 10^{-9}. \quad (4.72)$$

Following the discussion in previous sections, the incremental-iterative finite element procedure may be summarized as follows:

- (i) The total external loading and temperature change of the medium are divided into certain number of increments.
- (ii) For a certain incremental step, set up the matrices and vectors  $\mathbf{K}_L^{(0)}, \mathbf{K}_{NL}^{(0)}, \mathbf{F}_r, \mathbf{E}_r^{(0)}$  (Equations (4.42)-(4.45)) for nonlinear elements and  $\mathbf{K}_{EL}^{(0)}, \mathbf{K}_{ENL}^{(0)}, \overline{\mathbf{F}}_r, \overline{\mathbf{E}}_r^{(0)}$  (Equations (4.62)-(4.65)) for enriched elements.
- (iii) Construct the global stiffness matrix and forcing vector for the system of equations based on (4.40) and (4.60), solve for the incremental nodal displacements and stress intensity factors, and compute the total displacements.
- (iv) The incremental strains are obtained by using (4.48) and the total strains and stresses are then computed.
- (v) A new set of matrices and vectors  $\mathbf{K}_L^{(1)}, \mathbf{K}_{NL}^{(1)}, \mathbf{E}_r^{(1)}, \mathbf{K}_{EL}^{(1)}, \mathbf{K}_{ENL}^{(1)}, \overline{\mathbf{E}}_r^{(1)}$  are set up with the updated quantities.
- (vi) Solving incremental and total displacements, strains, stresses, and stress intensity factors by following the same procedures described in (iii) and (iv).
- (vii) Repeat steps (v) and (vi) until the convergence criterion (4.71) is satisfied.
- (viii) Proceed to the next incremental step and repeat steps (ii) through (vii).

---

The finite element code based on the solution procedure described above was developed. The elements used in this analysis are 12-noded quadrilateral and 10-noded triangular cubic isoparametric elements. Details on the formulation of the elements can be found in [83]. To test the implementation of the code, two problems with analytical solutions are examined in Appendix G. Because of the lack of analytical solutions involving finite deformation, material inhomogeneity, and crack problems we could not examine the implementation of all these aspects together. However, from the excellent agreement between the finite element results with analytical solutions (Appendix G), it is safe to assume that the code implementation is working properly and that the finite element solutions for problems with unknown analytical solutions may be considered as being accurate.

## Chapter 5

### Results and Discussion

#### 5.1 The Instability Analysis

By following the numerical procedure described in Chapter 3, we can solve the isothermal nonlinear elasticity problem as shown in Figure 2.1. The results of interest are the critical or instability strain, the crack opening displacement, and the phase angle. The critical strain represents the bifurcation point at which buckling of the coating occurs. The crack opening displacement shows the shape of the crack. The phase angle shows the propensity of direction for the crack to grow.

In the stability analysis, some hypothetical material combinations are used for comparison purpose. These combinations are:

- (1).  $\mu_2(h)/\mu_1 = 20.09, \gamma h = 3.0,$
- (2).  $\mu_2(h)/\mu_1 = 10, \gamma h = 2.3026,$
- (3).  $\mu_2(h)/\mu_1 = 0.1, \gamma h = -2.3026,$
- (4).  $\mu_2(h)/\mu_1 = 0.04979, \gamma h = -3.0,$

where  $\gamma h$  is the measure of material inhomogeneity ( $\mu_2(y) = \mu_1 \exp(\gamma y)$ ,  $\gamma h = \ln[\mu_2(h)/\mu_1]$ ). Also we consider the case  $\gamma h = 0.0001$  which represents extremely closely to a homogeneous half space containing a crack parallel to the surface. Note that it is not possible to let  $\gamma h$  identically equal to zero in this model due to numerical difficulties. It was previously shown that in crack problems for FGMs the effect of the Poisson's ratio on the fracture mechanics parameters is not very significant [72]. Therefore, in the stability analysis we assume that the Poisson's ratio is the same for all materials ( $\nu_1 = \nu_2 = 0.3$ ).

In order to validate the formulation in Chapter 2 and 3, we first examine the case of  $\gamma h = 0.0001$  and compare the results obtained for the case of  $\gamma h = 0$  for which an independent formulation is given in Appendix H. The critical strain  $(\epsilon_0)_{cr}$  and phase angle

$\psi$  for both  $\gamma h = 0.0001$  and  $\gamma h = 0$  are given in Table 5.1. Comparison of these results shows that they agree with each other. Therefore, we may assume that the formulation is correct and the results can be considered to be accurate.

The calculated critical value of the external load  $\epsilon_0$  as a function of the dimensionless length parameter  $h/a$  for  $\gamma h = 2.3026, 0.0001$ , and  $-2.3026$  are shown in Figure 5.1. It can be seen that the critical strain  $(\epsilon_0)_{\text{cr}}$  increases monotonically as  $h/a$  increases, which could also be seen from the classical plate theory. The figure also shows that regardless of the nature of coating inhomogeneity, for a given  $h/a$  the homogeneous medium always requires a greater instability load to initiate buckling. Intuitively one would expect that the critical loads for  $\gamma h > 0$  and  $\gamma h < 0$  would bracket  $(\epsilon_0)_{\text{cr}}$  for  $\gamma h = 0$ . The fact that this argument could be very misleading may be seen from Figure 5.2 which shows the influence of material inhomogeneity on the buckling strain  $(\epsilon_0)_{\text{cr}}$  for  $h/a = 0.05, 0.1$ , and  $0.15$ . Also shown in Figure 5.2 is the critical strain obtained from the plate theory as described in Appendix I. It may be seen that the critical strain given by the plate theory is symmetric in  $\gamma h$  and becomes maximum for the homogeneous medium,  $\gamma h = 0$ . The critical strain obtained from the continuum theory shows the same trend except that the maximum is slightly shifted toward negative  $\gamma h$ . Note that for very small values of  $h/a$  as expected the results obtained from plate and continuum theories are indistinguishable, whereas for larger values of  $h/a$  the difference between the critical strains given by the two theories could be very significant. This can also be seen from Figure 5.3 which shows the difference between the critical strains computed from continuum and plate models as a function of  $h/a$ . The difference may be attributed to the fact that at  $x = \mp a$  the plate is assumed to have built-in ends, whereas the continuum theory imposes no such artificial constraints. Furthermore, due to higher constraints at the ends, the plate model predicts higher values for the critical or instability load compared with those computed by

continuum model. This can also be observed from the results shown in Figures 5.2 and 5.3.

Figures 5.4-5.7 show the crack opening displacements for some fixed values of coating inhomogeneity  $\gamma h$  and the dimensionless length parameter  $h/a$ . Note that in these figures the opening and shearing components ( $v_2(x, +0) - v_1(x, -0)$  and  $u_2(x, +0) - u_1(x, -0)$ , respectively) are given normalized with respect to the crack opening at  $x = 0$ , i.e.,  $v_2(0, +0) - v_1(0, -0)$ . As mentioned in Chapter 3 because of the eigenvalue-problem nature of the perturbation analysis, only the shape but not the exact displacement of the crack opening may be obtained. It can be seen from Figures 5.4 and 5.5 that for larger coating thickness or shorter crack length the slope of the crack opening is higher. Also given in Figure 5.4 is the crack opening displacement predicted by plate theory which is not a function of  $h/a$  (see Appendix I). As expected, the crack opening displacement obtained from plate model is very close to the one for the case of small  $h/a$  by using continuum model. Nevertheless, as the value of  $h/a$  increases, the difference between the crack opening displacements around the crack tip given by continuum and plate models is becoming larger and larger. Again, this is due to the "fixed-end" boundary condition used in the plate model. Figures 5.6 and 5.7 show the influence of material inhomogeneity on the crack opening shapes at the inception of buckling instability.

Figure 5.8 shows the phase angle  $\psi$  as a function of  $h/a$  for  $\gamma h = 2.3026, 0.0001$ , and  $-2.3026$ . It is observed that generally the phase angles are negative, which suggests that the mode II stress intensity factors are negative. It can further be seen that the phase angle  $\psi$  is more negative at the instability point for the case of smaller  $\gamma h$  except for small  $h/a$  ( $h/a < 0.1$ ). This can also be seen from Figure 5.9 which shows the phase angle  $\psi$  vs. coating inhomogeneity  $\gamma h$  for  $h/a = 0.3$ .

Table 5.1 Critical strain and phase angle for a homogeneous half-space containing a crack parallel to the surface subjected to fixed-grip compression as described in Figure 2.1 with  $\gamma h = 0$  and  $\gamma h = 0.0001$ .

$h/a$	Critical strain $(\epsilon_0)_{\text{cr}}$		Phase angle $\psi$ (degree)	
	$\gamma h = 0.0001$	$\gamma h = 0$	$\gamma h = 0.0001$	$\gamma h = 0$
0.05	0.001921	0.001921	-39.1	-39.1
0.1	0.007103	0.007103	-39.8	-39.8
0.15	0.01467	0.01467	-40.3	-40.3
0.2	0.02381	0.02381	-40.6	-40.6
0.25	0.03388	0.03388	-40.7	-40.7
0.3	0.04439	0.04439	-40.8	-40.8
0.35	0.05498	0.05498	-40.7	-40.7
0.4	0.06540	0.06540	-40.6	-40.6
0.45	0.07551	0.07551	-40.5	-40.5
0.5	0.08520	0.08520	-40.3	-40.3

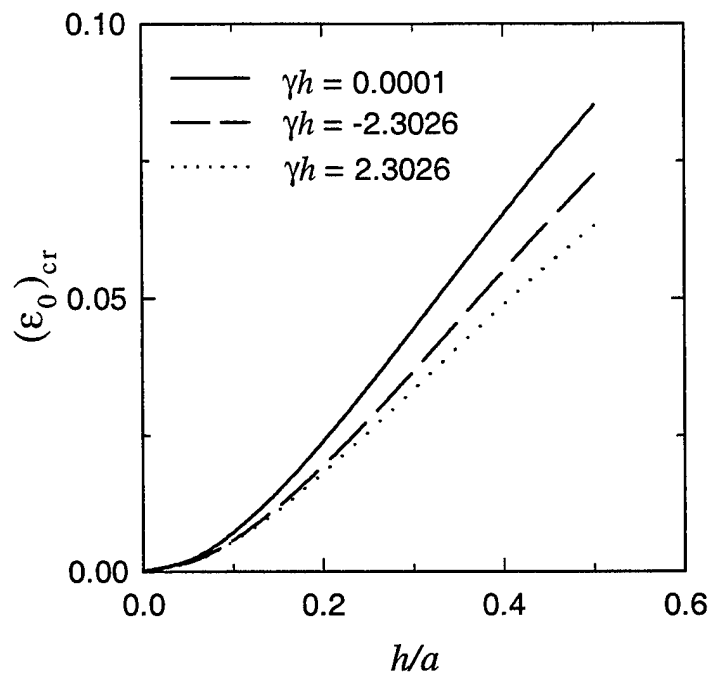


Figure 5.1 Instability strain  $(\epsilon_0)_{\text{cr}}$  as a function of  $h/a$ .

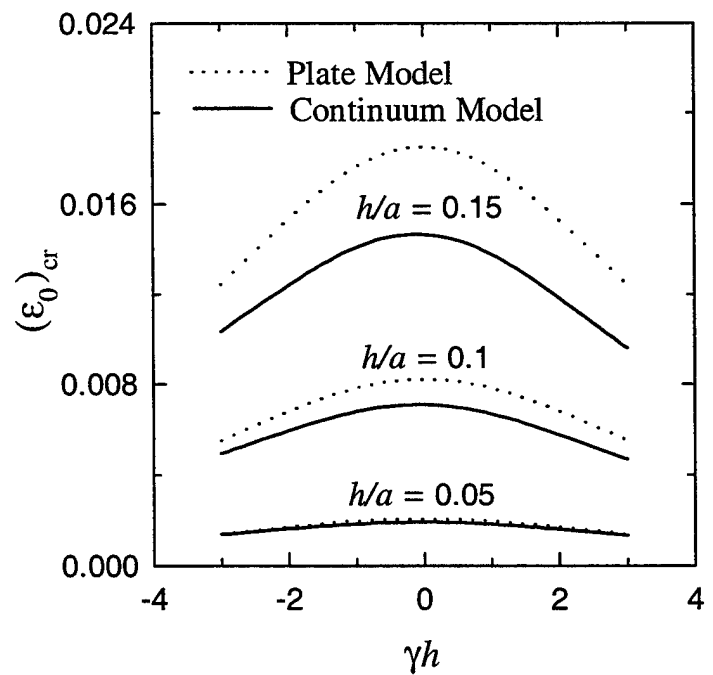


Figure 5.2 Instability strain  $(\epsilon_0)_{\text{cr}}$  as a function of coating inhomogeneity  $\gamma h$ .

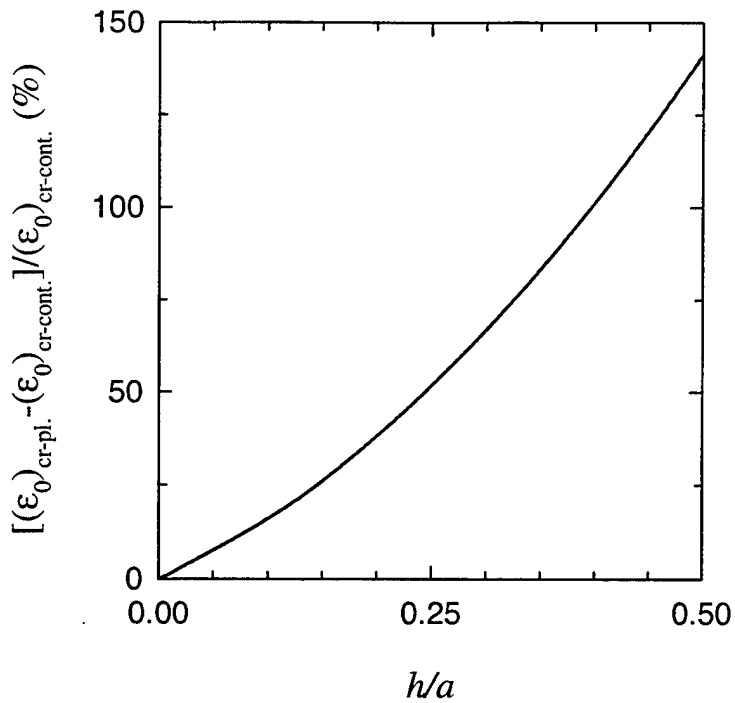


Figure 5.3 The difference between the instability strain predicted by plate approximation  $(\epsilon_0)_{\text{cr-pl.}}$  and that by continuum model  $(\epsilon_0)_{\text{cr-cont.}}$  as a function of  $h/a$ .

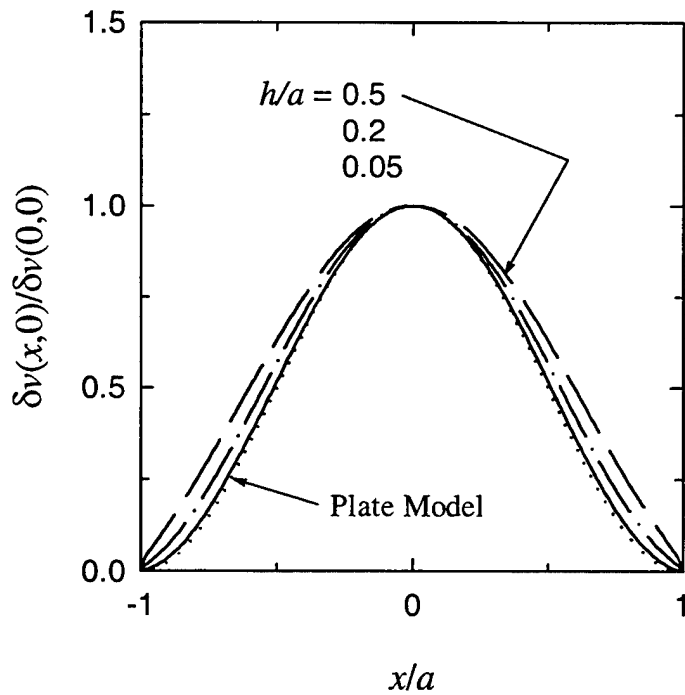


Figure 5.4 Normalized crack opening displacements for  $\gamma h = -2.3026$ ,  $\delta v(x, 0) = v_2(x, +0) - v_1(x, -0)$ .

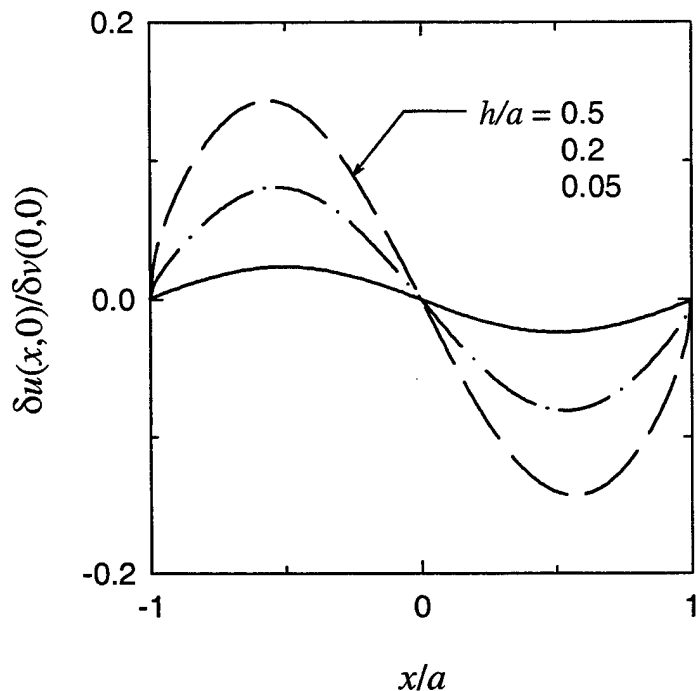


Figure 5.5 Normalized crack opening displacements for  $\gamma h = -2.3026$ ,  $\delta u(x, 0) = u_2(x, +0) - u_1(x, -0)$ .

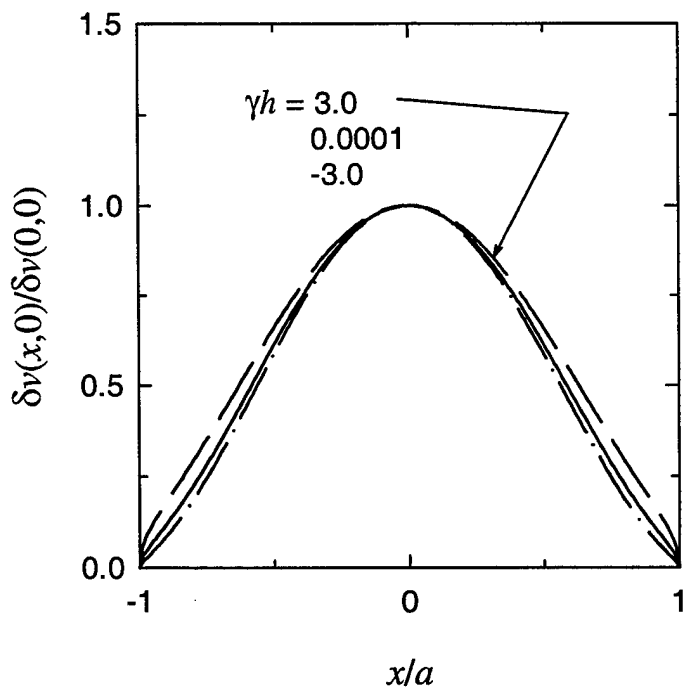


Figure 5.6 Normalized crack opening displacements for  $h/a = 0.3$ ,  $\delta v(x, 0) = v_2(x, +0) - v_1(x, -0)$ .

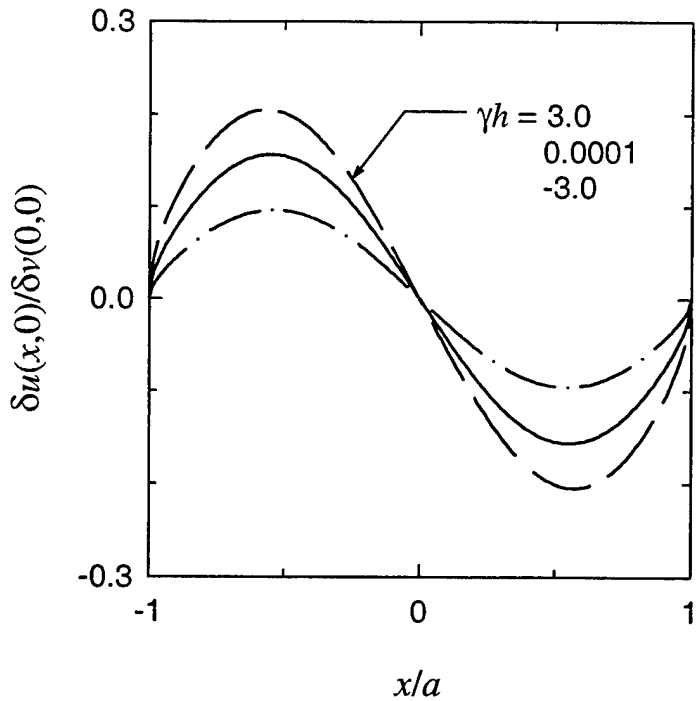


Figure 5.7 Normalized crack opening displacements for  $h/a = 0.3$ ,  $\delta u(x, 0) = u_2(x, +0) - u_1(x, -0)$ .

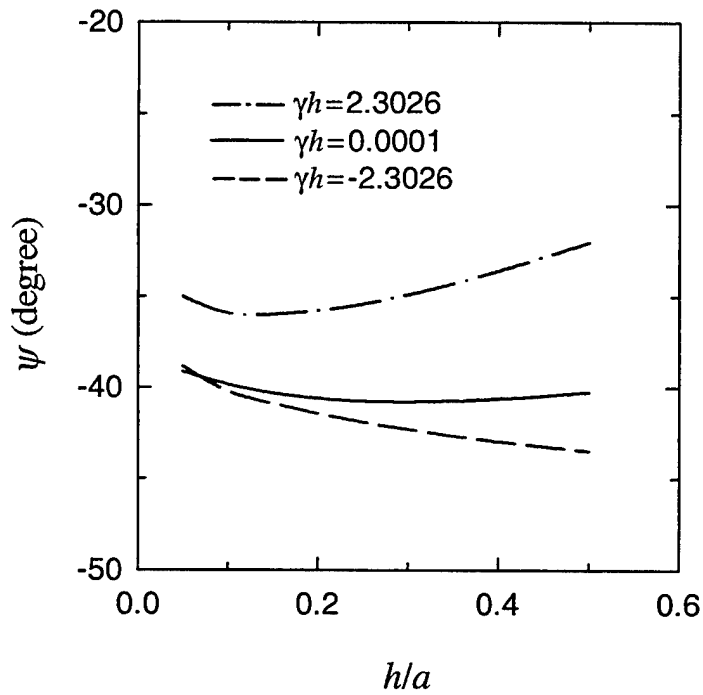


Figure 5.8 Phase angle  $\psi$  for the interface crack at buckling instability as a function of  $h/a$ .

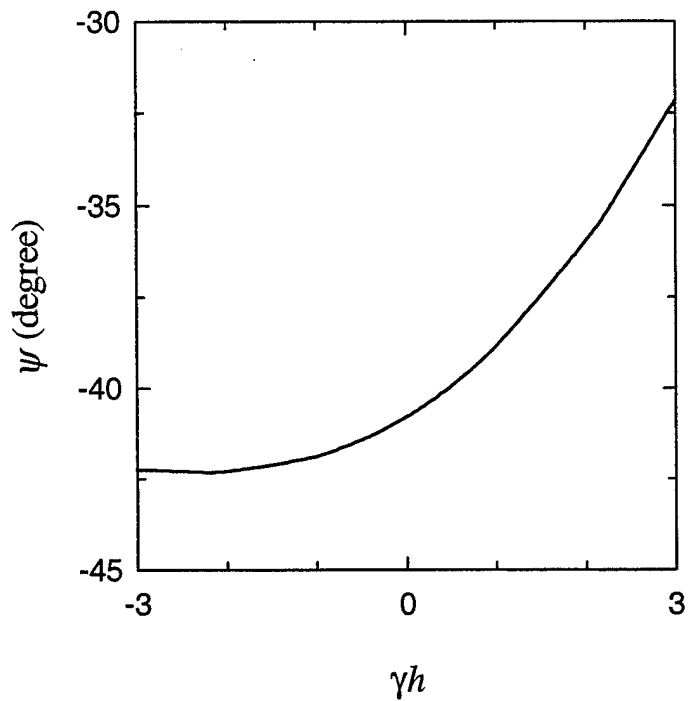


Figure 5.9 The influence of coating inhomogeneity  $\gamma h$  on the phase angle  $\psi$  for the interface crack at buckling instability,  $h/a = 0.3$ .

## 5.2 The Weakened Interface Model

In the instability analysis of plane-strain weakened interface problem described in Figure 2.2, two real material combinations [84] are used. They are:

- (1). Zirconia on Rene-41 ( $\mu_2(h)/\mu_1 = 0.6873$ ,  $\gamma h = -0.3750$ ),
- (2). Zirconia on Ti-6Al-4V ( $\mu_2(h)/\mu_1 = 1.294$ ,  $\gamma h = 0.2577$ ),

where the mechanical properties of the ceramics and metal constituents are given in Table 5.2.

Table 5.2 Material properties used in the numerical calculations in Section 5.2 [84].

Material	$E$ (GPa)	$\nu$
Rene-41	219.7	0.3
Ti-6Al-4V	116.7	0.3
Zirconia	151	0.3

The instability strains which are calculated by using the numerical procedure described in Chapter 3 are given in Figures 5.10-5.15. In these results it is assumed that the opening and shearing components of the bridging spring constants described in Figure 2.2(b) are the same, i.e.,  $s_1 = s_2 = s$ . Figure 5.10 shows the instability strain  $(\epsilon_0)_{cr}$  as a function of dimensionless length parameter  $h/a$  for the cases of homogeneous half space containing a "weakened interface" zone parallel to the surface. The instability strain  $(\epsilon_0)_{cr}$  vs.  $h/a$  plots for the weakened interface problem in a zirconia/Ti-6Al-4V FGM coating on Ti-6Al-4V substrate, and a zirconia/Rene-41 FGM coating on Rene-41 substrate are given in Figures 5.11, and 5.12, respectively. The normalized spring constant associated with the unbroken but weak ligaments in the weakened interface region are assumed to be  $as/\mu_1 = 0.001$ . The results for  $as/\mu_1 = 0$  which corresponds to fully separated crack (as shown in Figure 2.1) are also presented in Figures 5.10-5.12 for comparison. It may be seen from these

figures that the weakened interface model gives higher instability loads compared with the case of fully separated case.

The influence of the spring constant on the instability loads for the weakened interface problem may be seen in Figures 5.13 and 5.14 which shows the instability strains for the case of  $\gamma h = 0.2577$  and  $\gamma h = -0.3750$ , respectively. In these figures one may see that the instability strains remain rather unchanged when  $as/\mu_1 < 0.001$ ; and  $(\epsilon_0)_{cr}$  increases sharply as the value of  $as/\mu_1$  exceeds 0.01. The influence of  $as/\mu_1$  on instability loads can also be seen in Figure 5.15 which shows the instability strain as a function of coating inhomogeneity for several fixed values of  $as/\mu_1$  and  $h/a$ . It may be seen that as the value of  $as/\mu_1$  increases much higher instability strains are observed for the case of negative  $\gamma h$ , and that the symmetry of the instability strain in coating inhomogeneity gradually disappears as  $\gamma h$  increases. The higher instability strains for the case of negative  $\gamma h$  may be attributed to the lower nominal bending stiffness of the FGM coating compared with that of positive  $\gamma h$ . Intuitively, one may see that the coating with softening profile (negative  $\gamma h$ ) but the same bridging spring constant  $as/\mu_1$  requires greater driving force than that for stiffening profile (positive  $\gamma h$ ) to induce the instability and buckling. Also observed in Figure 5.15 is that the increase of  $(\epsilon_0)_{cr}$  for the cases of negative  $\gamma h$  is more significant for smaller value of  $h/a$ .

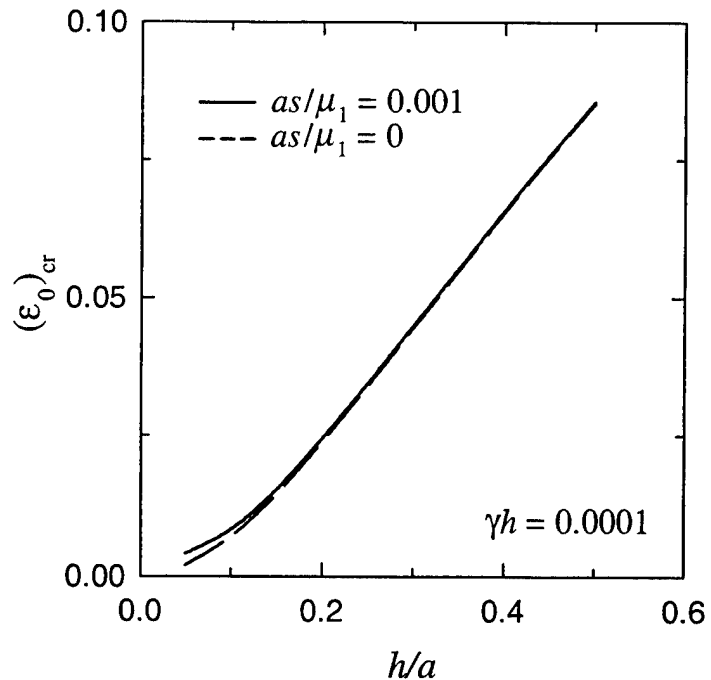


Figure 5.10 The instability strain  $(\epsilon_0)_{\text{cr}}$  as a function of  $h/a$  for a coating bonded to a homogeneous half-space containing a weakened interface region.

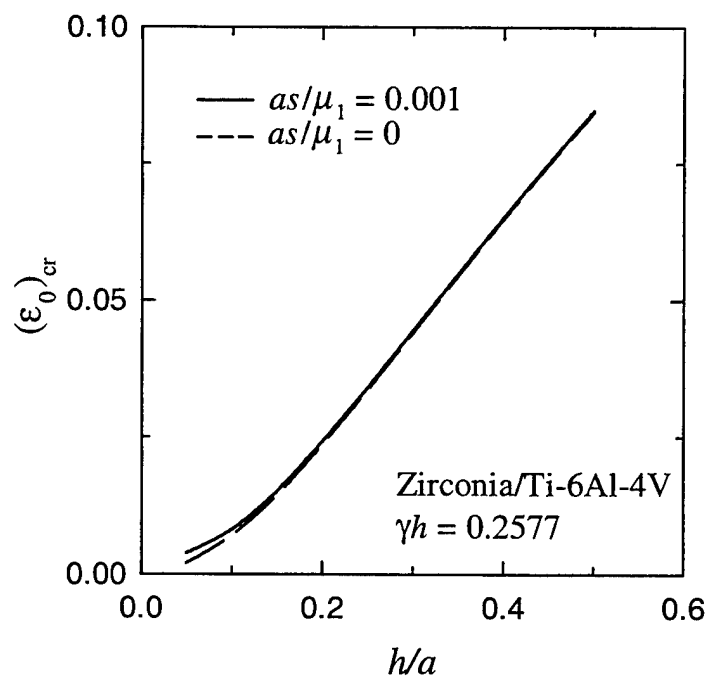


Figure 5.11 The instability strain  $(\epsilon_0)_{\text{cr}}$  as a function of  $h/a$  for a  $\text{ZrO}_2/\text{Ti-6Al-4V}$  FGM coating bonded to a  $\text{Ti-6Al-4V}$  substrate containing a weakened interface region.

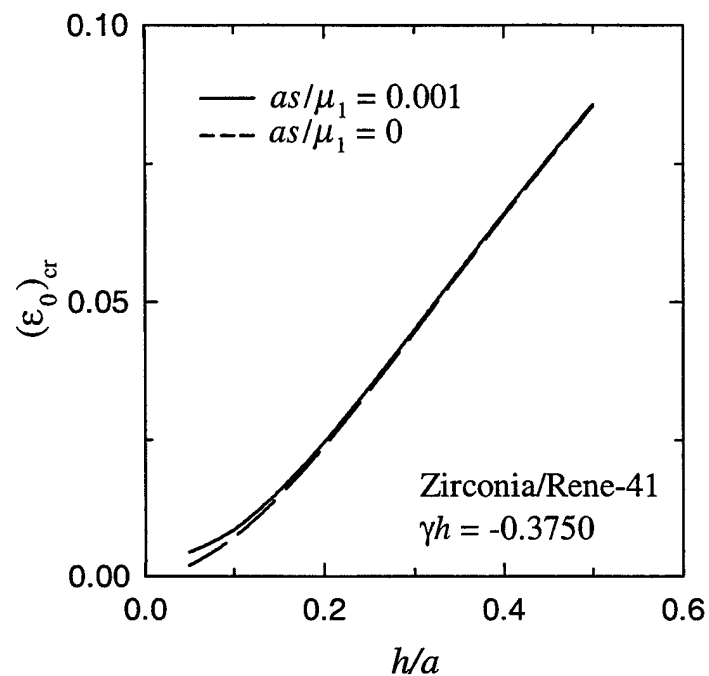


Figure 5.12 The instability strain  $(\epsilon_0)_{\text{cr}}$  as a function of  $h/a$  for a  $\text{ZrO}_2/\text{Rene-41}$  FGM coating bonded to a Rene-41 substrate containing a weakened interface region.

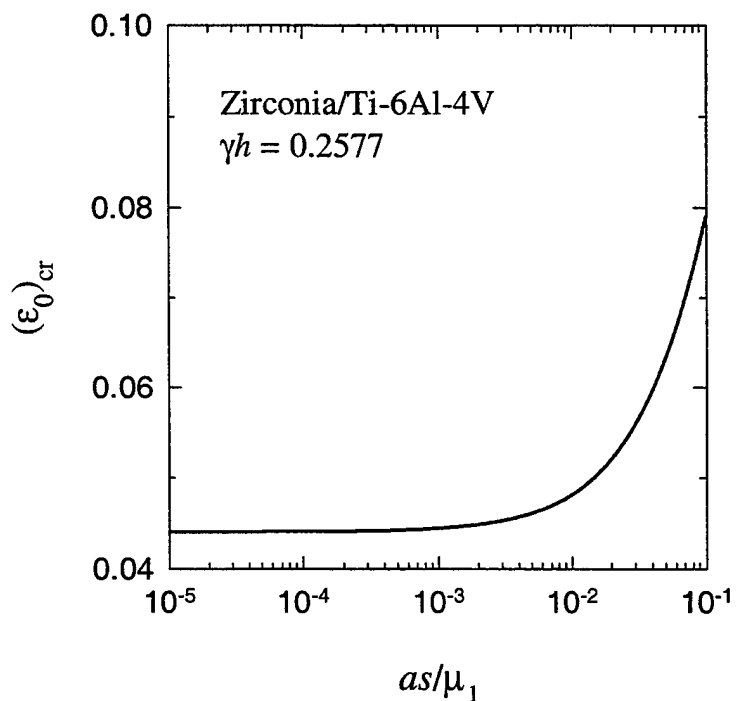


Figure 5.13 The influence of the normalized bridging constant  $as/\mu_1$  on the instability strain  $(\epsilon_0)_{\text{cr}}$  for the weakened interface,  $\gamma h = 0.2577$ ,  $h/a = 0.3$ .

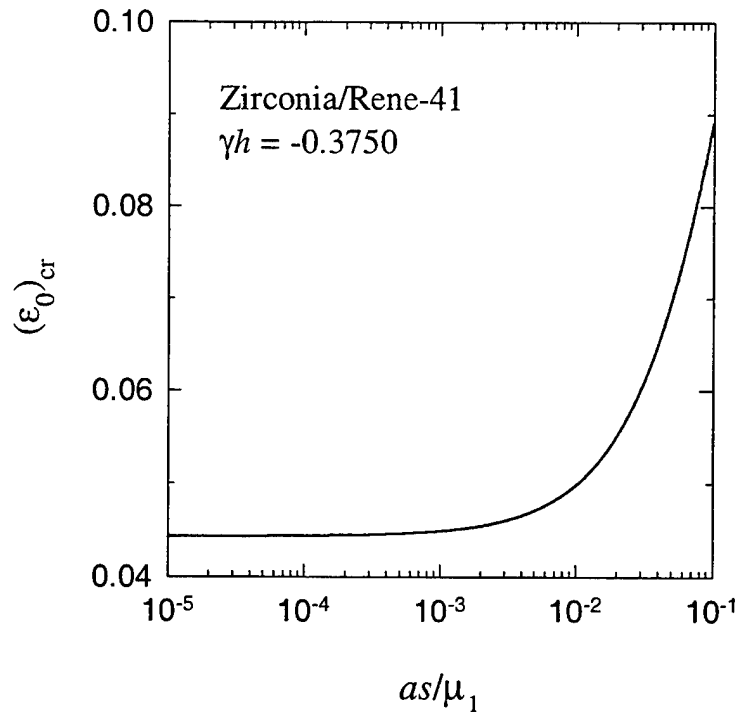


Figure 5.14 The influence of the normalized bridging constant  $as/\mu_1$  on the instability strain  $(\epsilon_0)_{\text{cr}}$  for the weakened interface,  $\gamma h = -0.3750$ ,  $h/a = 0.3$ .

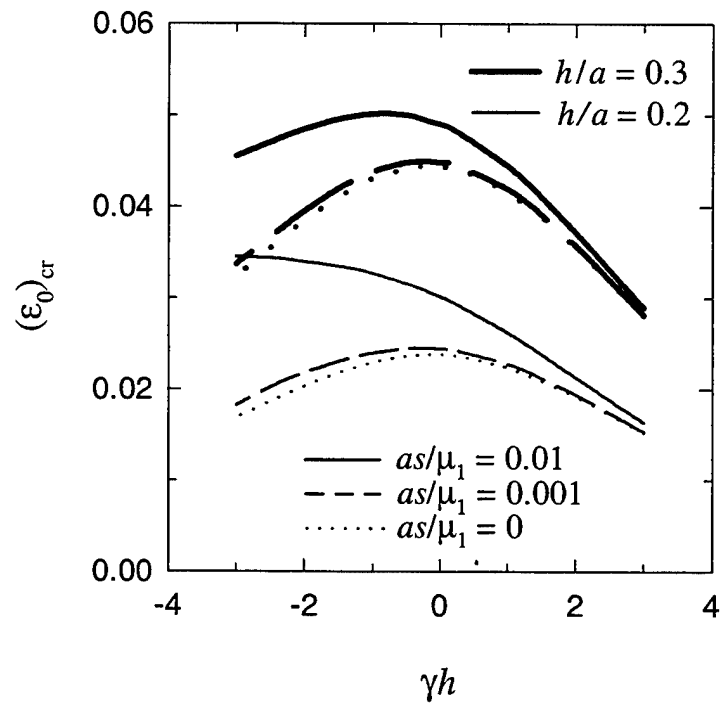


Figure 5.15 Instability strain  $(\epsilon_0)_{\text{cr}}$  as a function of coating inhomogeneity  $\gamma h$  for the FGM coating/homogeneous substrate containing a weakened interface under fixed-grip compression.

### 5.3 Postbuckling Analysis

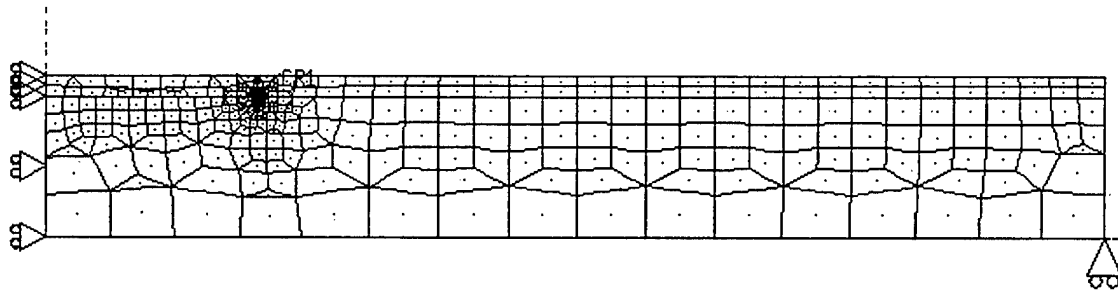
The postbuckling problem of the debonded coating is investigated by using the geometrically nonlinear finite element procedure described in Chapter 4. The top coat of the specimen under consideration may be either a homogeneous ceramic layer or a smoothly graded metal/ceramic composite. It is assumed that the specimen is under either plane strain or axisymmetric condition. Figure 5.16(a) shows a typical finite element mesh and the boundary conditions (without mechanical loading) for a two-layered coating/substrate system. Note that by taking advantage of the symmetry of the geometry and loading conditions, only the right half of the specimen is modeled (for plane strain problem). A vertical displacement constraint is given at the outside lower corner to prevent rigid body motion of the specimen. As shown in Figure 5.16(b), mesh refinement is done around the crack tip. The size of the enriched and transition crack-tip elements are chosen to be around 1/20 of the layer thickness of the coating above the interface crack.

#### 5.3.1 *Fixed-grip Loading*

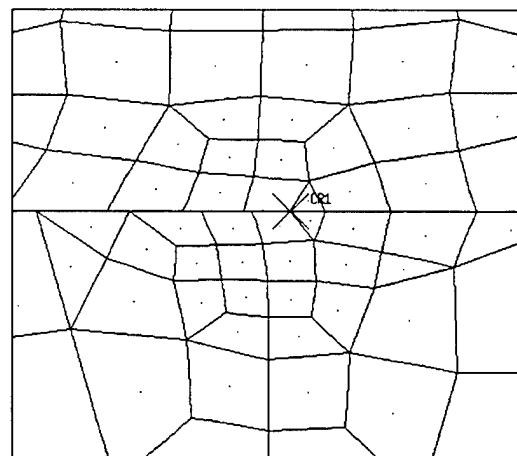
In order to obtain the fracture mechanics parameters, e.g., strain energy release rate and stress intensity factors, and to compare the results of the finite element analysis with the analytical benchmark solutions from the stability analysis, the problem considered here is the fixed-grip compression problem as shown in Figure 2.1. The results are given in Figures 5.17-5.20. In the numerical analysis the following relative dimensions are used:  $h_s/h_c = 30$ ,  $2a/h_c = 40$ ,  $2l/h_c = 200$ , where  $h_s$ ,  $h_c$ ,  $2a$  and  $2l$  are the substrate thickness, coating thickness, crack length, and the length of the specimen, respectively. The results obtained by varying  $h_s/h_c$  and  $2l/h_c$  showed that the dimensions used were sufficiently large to properly simulate the semi-infinite medium. Note that due to the geometry of the medium and the nature of the loading, the "preferred" load-displacement path, i.e., the one corresponding to buckling and crack opening, cannot be obtained in a

straightforward manner from the incremental-iterative technique which starts from zero external load. Similar to the procedure followed for the elastica problem described in Appendix G, first a transverse load disturbance is introduced at  $(x, y) = (0, 0)$  on the coating to induce initial crack opening, which is then removed at a later stage of the incremental-loading history to obtain an equilibrium point in the postbuckling regime for the original problem (without the transverse load disturbance). After that the load-displacement path is constructed by using the incremental-iterative method which starts from this computed equilibrium point. Figure 5.17 shows the crack opening displacement at  $x = 0$  (denoted by  $\delta$ ). The analytical results obtained from the stability solution are indicated by small circles on the  $\epsilon_0$  axis. The figure also shows the result for the homogeneous medium  $\gamma h_c = 0$  obtained from the plate theory (Appendix I) for comparison. The critical or instability strains  $(\epsilon_0)_{cr}$  obtained from the postbuckling analysis are the intersection points of the postbuckling curves with the  $\epsilon_0$  axis. The agreement between the critical loads obtained from the analytical and numerical methods appears to be quite good. Again note that for a given crack opening the plate theory requires a greater compressive strain  $\epsilon_0$  than the continuum theory, which is consistent with the results given in Figure 5.2. The normalized strain energy release rate and stress intensity factors are given in Figures 5.18 and 5.19. The normalizing quantities are given by  $K_0 = E_s \epsilon_1 \sqrt{\pi h_c}$  and  $G_0 = (1 - \nu_s^2) K_0^2 / E_s$  where  $\epsilon_1 = 0.002$ . From Figure 5.18 it may be seen that  $G = 0$  for  $\epsilon_0 < (\epsilon_0)_{cr}$ , for a given  $\epsilon_0 > (\epsilon_0)_{cr}$  the material inhomogeneity has a significant influence on the strain energy release rate, and by and large the relative trends conform to intuitively expected results, namely  $G$  corresponding to  $\gamma h_c = 0$  is bracketed by that obtained from  $\gamma h_c < 0$  and  $\gamma h_c > 0$  and  $G$  increases with decreasing  $\gamma h_c$ . By examining the results for  $\gamma h_c = 0$  in Figures 5.17 and 5.18 it may be seen that the crack opening displacement and strain energy release rate predicted by plate theory are consistently smaller than that obtained from the continuum theory. This may again be

attributed to a higher degree of constraint in the plate model resulting from the assumption of "built-in" ends. From Figure 5.19 it may be seen that generally the magnitudes of the mode II stress intensity factors  $K_{II}$  are greater than that of  $K_I$ . The dominance of  $K_{II}$  can also be seen from Figure 5.20 which shows the phase angle  $\psi$  as a function of compressive strain for the postbuckling regime. The stronger  $K_{II}$  implies the tendency for the crack kinking into the coating and spalling the coating off. However, perhaps a more practical approach to studying the spallation process would be either comparing the calculated strain energy release rates  $G$  with the mode mixity-dependent fracture toughness  $G_c$  or analyzing the buckled part of the coating by using a maximum stress-based rupture theory.



(a)



(b)

Figure 5.16 A typical finite element mesh and boundary conditions for a coating/substrate system containing an interface crack, (a) FE mesh for the right half of the medium, (b) Enlarged crack tip region, CR1 denotes the crack tip.

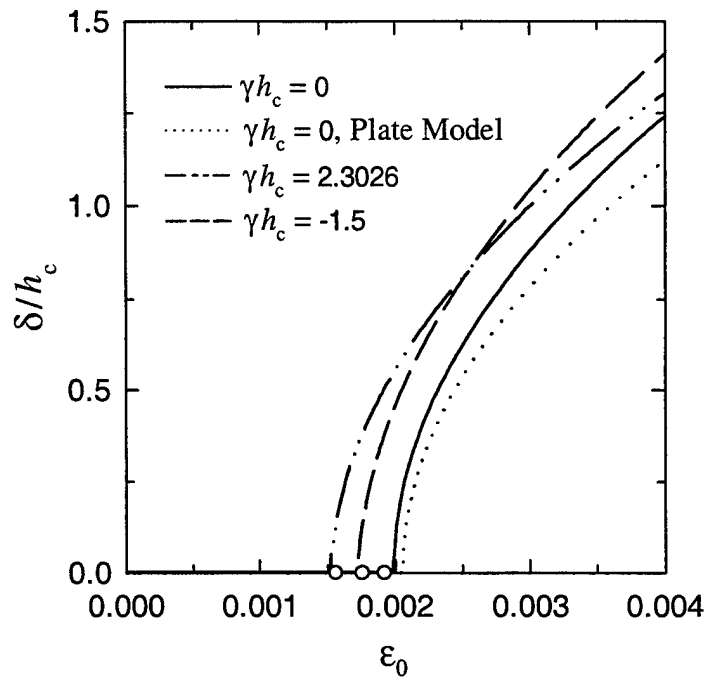


Figure 5.17 Crack opening displacement  $\delta/h_c$  at the center of crack as a function of compressive strain  $\epsilon_0$ , the circles on the  $\epsilon_0$  axis are the instability strains  $(\epsilon_0)_{cr}$  calculated from the analytical stability solution.

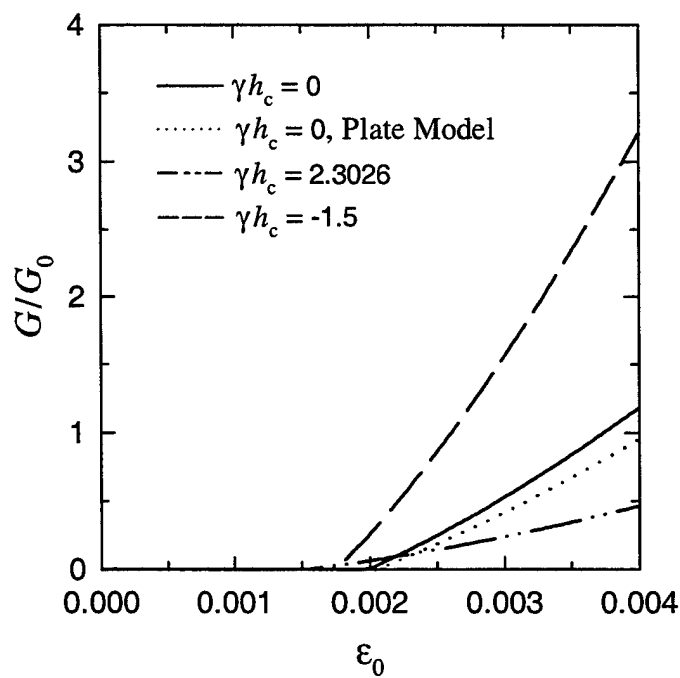


Figure 5.18 Strain energy release rate  $G/G_0$  as a function of compressive strain  $\epsilon_0$ ,  $G_0 = (1 - \nu_s^2)K_0^2/E_s$ ,  $K_0 = E_s \epsilon_1 \sqrt{\pi h_c}$ ,  $\epsilon_1 = 0.002$ .

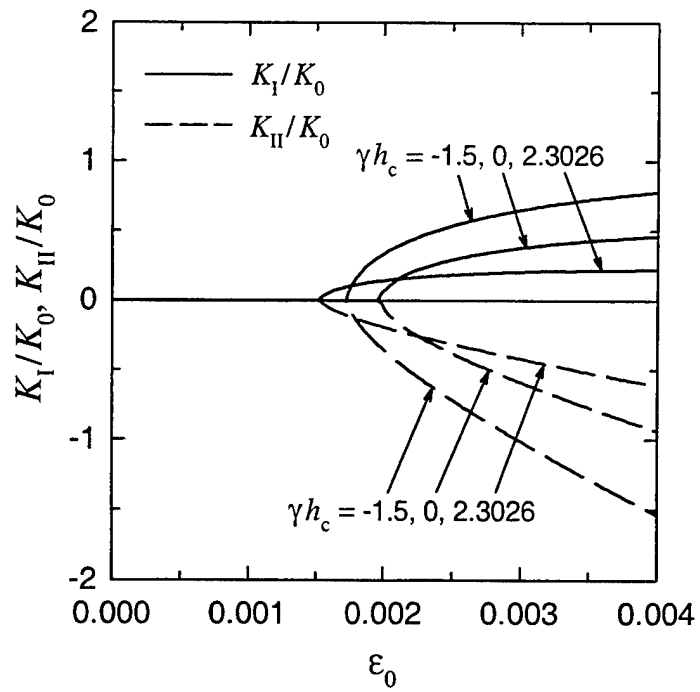


Figure 5.19 Modes I and II stress intensity factors  $K_I$  and  $K_{II}$  as functions of compressive strain  $\epsilon_0$ ,  $K_0 = E_s \epsilon_1 \sqrt{\pi h_c}$ ,  $\epsilon_1 = 0.002$ .

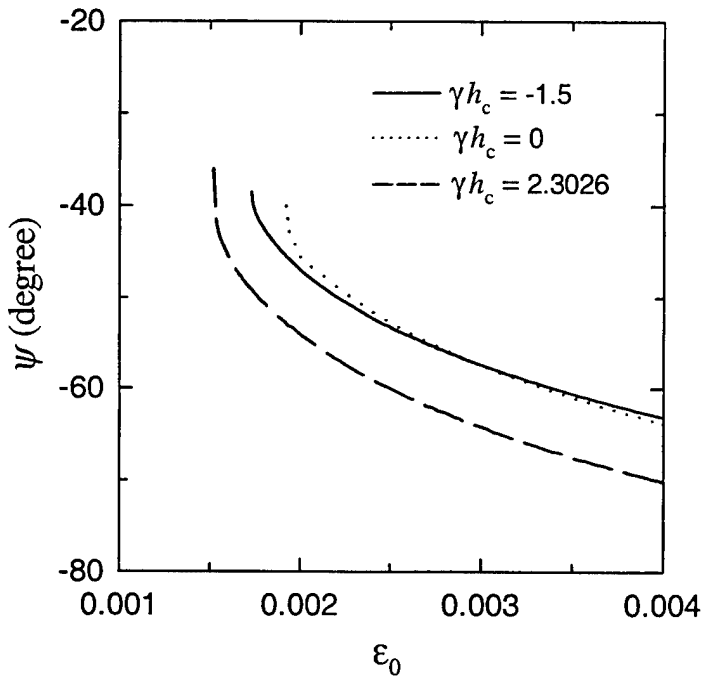


Figure 5.20 Phase angle as a function of compressive strain  $\epsilon_0$ .

### 5.3.2 Thermal Loading

The problem considered here is the temperature change induced coating blister in the metal substrate/ceramic (or FGM) coating containing an interface crack. Due to the mismatch in coefficients of thermal expansion between the coating and substrate, compressive residual stress is developed in the ceramic coating (which usually has a smaller thermal expansion coefficient compared with metallic substrate) during the cool-down stage of the thermal cycling process. As a result the coating buckles as the temperature change reaches a critical value. In this part of the study we consider a layered composite specimen subjected to a uniform negative temperature change. It is assumed that the specimen is stress-free before cooling down and that the deformation is elastic.

#### 5.3.2.1 The Plane Strain Problem

As an example the plane strain problem for a nickel-based Rene-41 substrate coated with zirconia, containing an interface crack and subjected to a uniform temperature drop  $\Delta T$  is considered. The dimensions of the specimen given in Figure 5.21 [6] are  $h_c = 2$  mm,  $h_s = 12.5$  mm, and  $l = 100$  mm. The relevant thermomechanical properties of the substrate and the coating for this specific example are given in Table 5.3. Also considered here is the uniform cool-down problem for the medium described in Figure 5.21 in which the homogeneous zirconia coating is replaced by an inhomogeneous FGM coating. A linear variation of the thermomechanical properties in the FGM coating is assumed, i.e.,

$$E(y) = \begin{cases} E_c + (E_s - E_c) \left( \frac{h_s + h_c - y}{h_c} \right), & h_s < y < h_s + h_c, \\ E_s, & 0 < y < h_s, \end{cases} \quad (5.1)$$

$$\alpha(y) = \begin{cases} \alpha_c + (\alpha_s - \alpha_c) \frac{h_s + h_c - y}{h_c}, & h_s < y < h_s + h_c, \\ \alpha_s, & 0 < y < h_s. \end{cases} \quad (5.2)$$

where  $(E_c, \alpha_c)$  and  $(E_s, \alpha_s)$  are the elastic moduli and coefficients of thermal expansion of the pure ceramics and metallic substrate, respectively, and are given in Table 5.3.

Table 5.3 Material properties of the plane-strain specimen described in Figure 5.21 [84].

	Material	$E$ (GPa)	$\nu$	$\alpha$ ( $10^{-6} \text{ }^\circ\text{C}^{-1}$ )
Substrate	Rene-41	219.7	0.3	16.7
Ceramics	Zirconia	151	0.3	10.0

Figures 5.22-5.30 show the results of the postbuckling analysis for the homogeneous zirconia coating. The constants used for normalization in these figures are  $T_0 = 100 \text{ K}$ ,  $K_0 = E_s \alpha_s T_0 \sqrt{\pi h_c}$ ,  $G_0 = (1 - \nu_s^2) K_0^2 / E_s$ . It may be seen from Figures 5.22, which shows the normalized crack opening displacement  $\delta/h_c$  at  $x = 0$  as a function of  $\Delta T/T_0$  for some fixed values of  $a/h_c$ , that instead of having an explicit buckling point, the "crack opening" is a smooth function of  $\Delta T/T_0$ . Figure 5.23 shows the normalized energy release rate  $G/G_0$  versus temperature drop for various values of  $a/h_c$ . Also shown in Figures 5.22 and 5.23 are the results obtained by using plate theory with the assumption that the buckled coating has "built-in" ends. By comparing the results from continuum and plate theories in these figures it may be seen that, again because of the higher degree of constraint at the ends, the plate model underestimates the buckling deflection and strain energy release rate. Note that the smooth transition, rather than an explicit buckling point in the crack opening displacement and strain energy release rate vs.  $\Delta T/T_0$  plots may be explained by observing that the temperature change induced residual stresses would result in a slightly bending of the specimen, and this bending curvature serves as the imperfection

that triggers the opening of the crack. Also, because of the bending of the specimen, the solution technique (adding and removing a transverse load disturbance) used for the fixed-grip loading problem (Section 5.3.1) is not necessary for the thermal loading problem, unless the substrate/coating thickness ratio is very large such that the radius of the bending curvature is extremely high.  $\hat{K}_I$  and  $\hat{K}_{II}$  shown in Figure 5.24 are the real and imaginary parts of the complex stress intensity factor obtained from the continuum analysis of the related bimaterial interface crack problem. The phase angle as a function of  $\Delta T/T_0$  is given in Figure 5.25. It may be seen from the sign of  $\hat{K}_{II}$  or the phase angle that, again it favors the crack kinking into the coating unless, as in most cases, the interface is the weak fracture plane. Note that the calculated stress intensity factors  $K_I$  and  $K_{II}$  have the dimension of  $\text{Pa}\cdot\text{m}^{1/2-i\epsilon}$ , where the bimaterial constant  $\epsilon$  is defined by (4.53). In order to recast these quantities in a form with conventional units (e.g.,  $\text{Pa}\cdot\text{m}^{1/2}$ ) and to have the result scalable, we use the following "rotated" complex stress intensity factor [85]

$$\hat{K} = \hat{K}_I + i\hat{K}_{II} = KL^{i\epsilon} = (K_I + iK_{II})L^{i\epsilon}, \quad (5.3)$$

where  $L$  is an arbitrary length quantity which, in this study, is selected to be equal to the coating thickness, i.e.,  $L = h_c$ . The new phase angle  $\hat{\psi}$  as shown in Figure 5.25 can be related to the computed phase angle  $\psi$  through the expression

$$\hat{\psi} = \psi + \epsilon \ln L. \quad (5.4)$$

The stresses  $\sigma_{xx}$ ,  $\sigma_{yy}$ , and  $\sigma_{xy}$  alone  $y/h_c = 6.25$  for the case of  $a/h_c = 20$  and  $\Delta T = 1000^\circ\text{C}$  are plotted in Figures 5.26-5.28, respectively. Note that  $y/h_c = 6.25$  corresponds to the interface when  $a < x < l$  and to the bottom surface of the debonded coating for  $0 < x < a$ . The stress  $\sigma_{xx}$  on the top surface of the coating ( $y/h_c = 7.25$ ) is also given in Figure 5.26. From Figures 5.26-5.28 it is observed that the thermal residual bending stress  $\sigma_{xx}$  is the dominant stress components except for around the crack tip and where the interface intersecting free surface. It may also be seen from Figure 5.26 that on

the top surface of the coating high  $\sigma_{xx}$  appears around  $x = 0$ . This high  $\sigma_{xx}$  may induce surface crack and fracture of the coating. The stresses  $\sigma_{xx}$  along  $x = 0$  and  $x = a$  for  $a/h_c = 20$  are given in Figures 5.29 and 5.30, respectively. The nature of these stresses is mainly associated with the global thermal bending except for the crack tip where the singular behavior dominants.

Figures 5.31-5.38 show the results for the FGM coating described in (5.1) and (5.2). For comparison the results for the homogeneous zirconia coating given in Figures 5.22 and 5.23 are also included in Figures 5.31 and 5.32. Figure 5.33 shows the normalized stress intensity factors as a function of  $\Delta T/T_0$  for several values of  $a/h_c$ . Basically the results for FGM coating show the same trend as those for homogeneous coatings. It is, however, observed that for the same temperature drop  $\Delta T$  both the crack opening displacement at the center of crack and the strain energy release rate for the FGM coating are considerably smaller than that for the homogeneous coating. This may be attributed to the decrease in thermal residual stresses because of the smooth transition of thermomechanical properties in FGM and the increase in the effective bending stiffness of the coating. As a result the FGM coating is expected to be more resistant to buckling and spallation resulting from cool-down.

Figures 5.34-5.36 give the stresses  $\sigma_{xx}$ ,  $\sigma_{yy}$ , and  $\sigma_{xy}$ , respectively, along  $y/h_c = 6.25$  for the case of  $a/h_c = 20$  and  $\Delta T = 1000^\circ\text{C}$ . The stress  $\sigma_{xx}$  on the top surface of the coating ( $y/h_c = 7.25$ ) is also given in Figure 5.34. The stresses  $\sigma_{xx}$  along  $x = 0$  and  $x = a$  for  $a/h_c = 20$  are given in Figures 5.37 and 5.38, respectively. Basically the stress variations for the FGM coating show the same trend as that for the homogeneous ceramic coating (Figures 5.26-5.30). However, one important feature of the FGM coating is that the positive  $\sigma_{xx}$  observed in the ceramic coating top surface (Figure 5.26) does not appear in the FGM coating (Figure 5.34); instead, the FGM coating surface is under compression which may prevent the initiation of surface cracks.

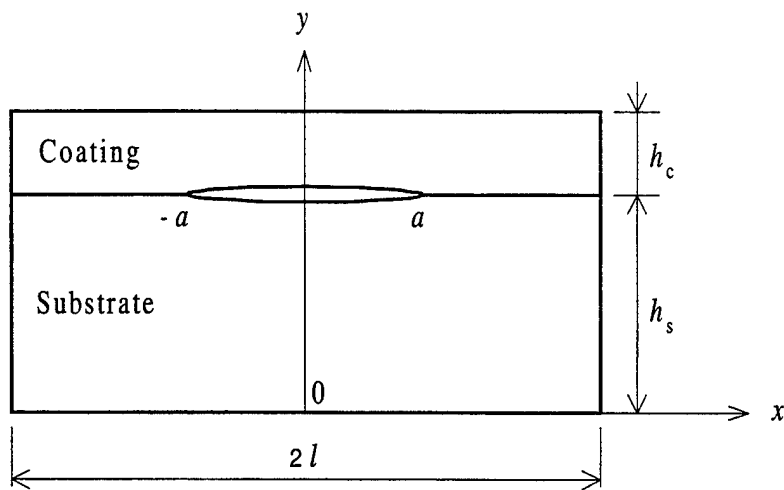


Figure 5.21 Specimen configuration for the plane strain thermal buckling problem.

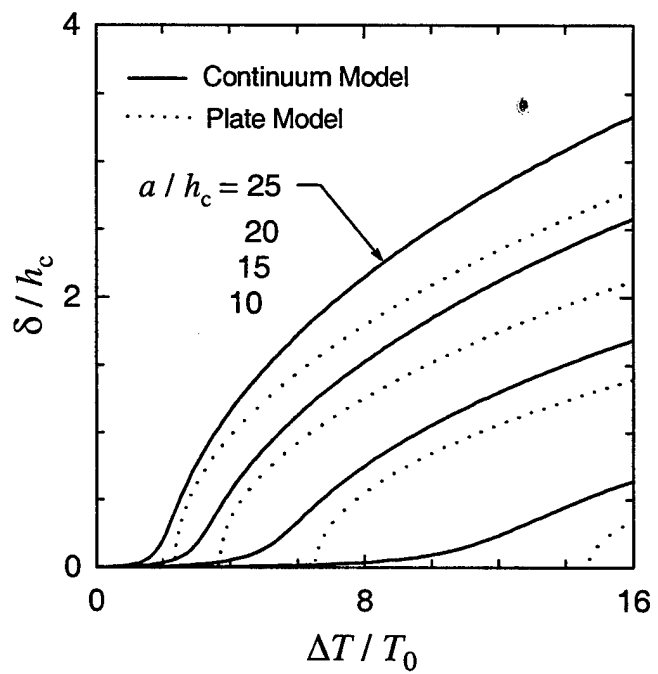


Figure 5.22 Crack opening displacement  $\delta/h_c$  at the center of the crack as a function of temperature drop  $\Delta T/T_0$  for homogeneous zirconia coating,  $T_0 = 100$  K.

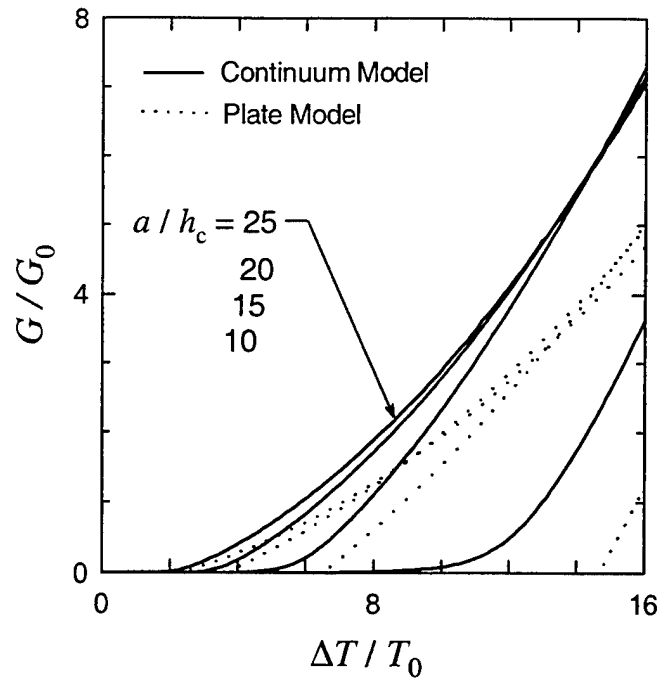


Figure 5.23 Strain energy release rate for homogeneous zirconia coating under uniform temperature drop,  $T_0 = 100$  K,  $K_0 = E_s \alpha_s T_0 \sqrt{\pi h_c}$ ,  $G_0 = (1 - \nu_s^2) K_0^2 / E_s$ .

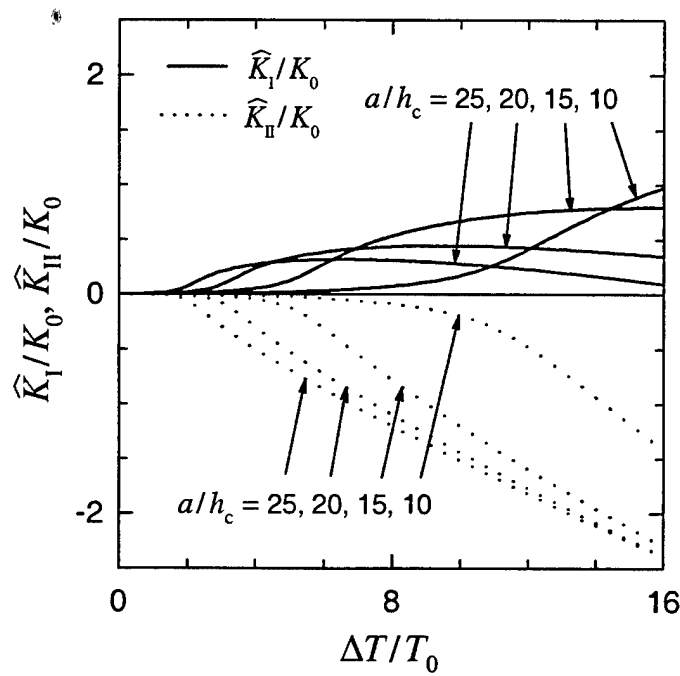


Figure 5.24 Normalized stress intensity factors for homogeneous zirconia coating as a function of temperature drop,  $T_0 = 100$  K,  $K_0 = E_s \alpha_s T_0 \sqrt{\pi h_c}$ ,  $G_0 = (1 - \nu_s^2) K_0^2 / E_s$ ,  $\hat{K}_I + i\hat{K}_{II} = (K_I + iK_{II})h_c^{ie}$ .

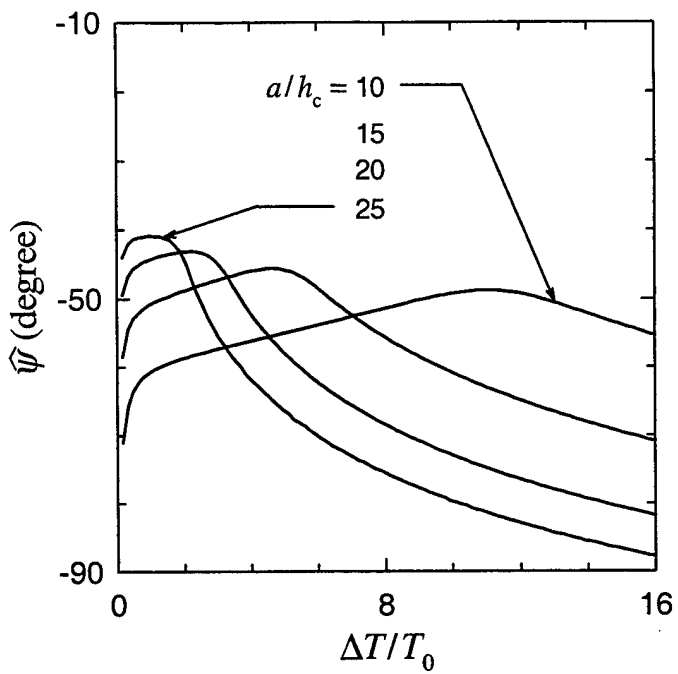


Figure 5.25 Phase angle  $\hat{\psi}$  as a function of temperature drop for homogeneous zirconia coating,  $\hat{\psi} = \psi + \epsilon \ln h_c$ ,  $T_0 = 100$  K.

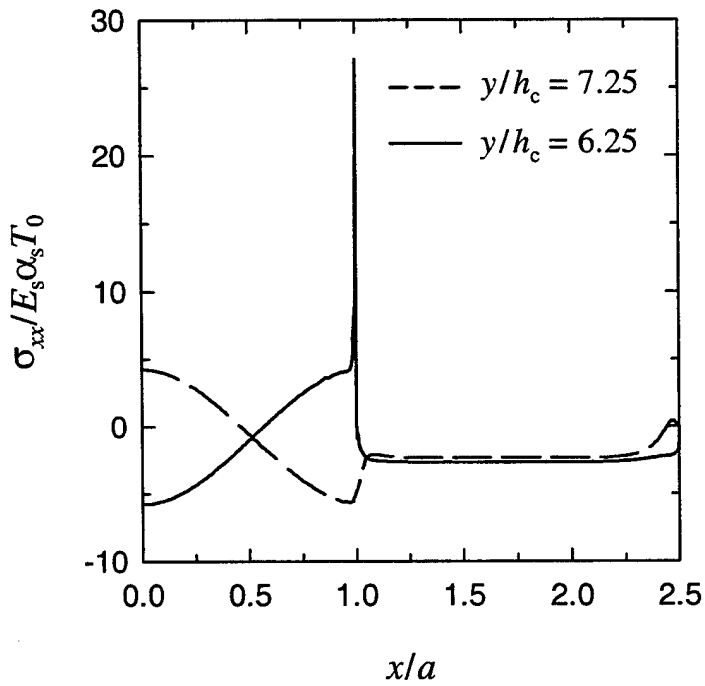


Figure 5.26 Variation of normalized  $\sigma_{xx}(x, y_0)$  along (i) the crack surface and the interface ( $y_0/h_c = 6.25$ ) and (ii) the top surface ( $y_0/h_c = 7.25$ ) of the homogeneous TBC described in Figure 5.21 under 1000 °C temperature drop,  $a/h_c = 20$ ,  $T_0 = 100$  K.

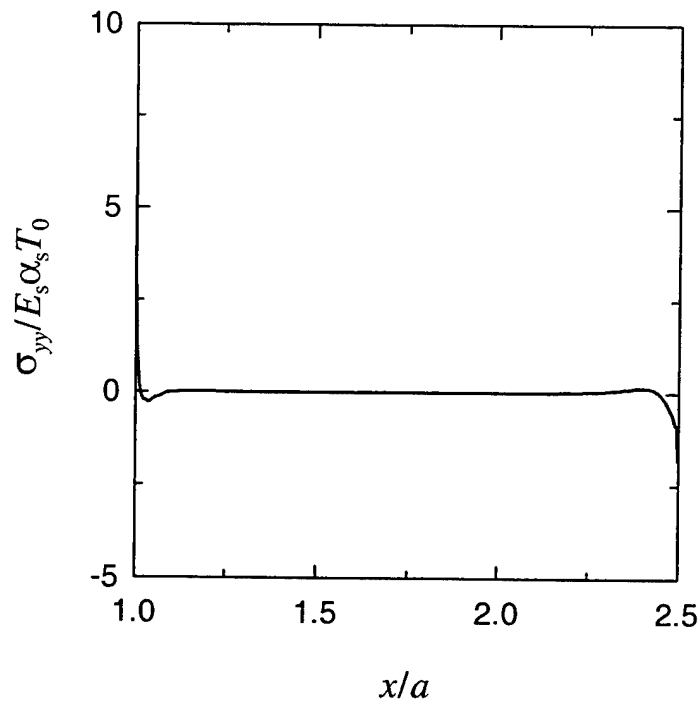


Figure 5.27 Variation of normalized  $\sigma_{yy}(x, y_0)$  along the interface of the homogeneous TBC described in Figure 5.21 under 1000 °C temperature drop,  $y_0/h_c = 6.25$ ,  $a/h_c = 20$ ,  $T_0 = 100$  K.

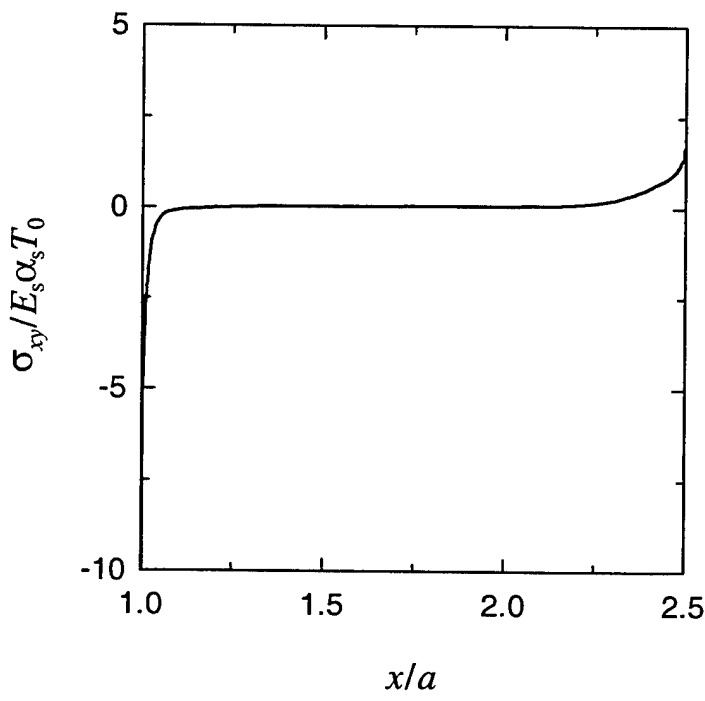


Figure 5.28 Variation of normalized  $\sigma_{xy}(x, y_0)$  along the interface of the homogeneous TBC described in Figure 5.21 under 1000 °C temperature drop,  $y_0/h_c = 6.25$ ,  $a/h_c = 20$ ,  $T_0 = 100$  K.

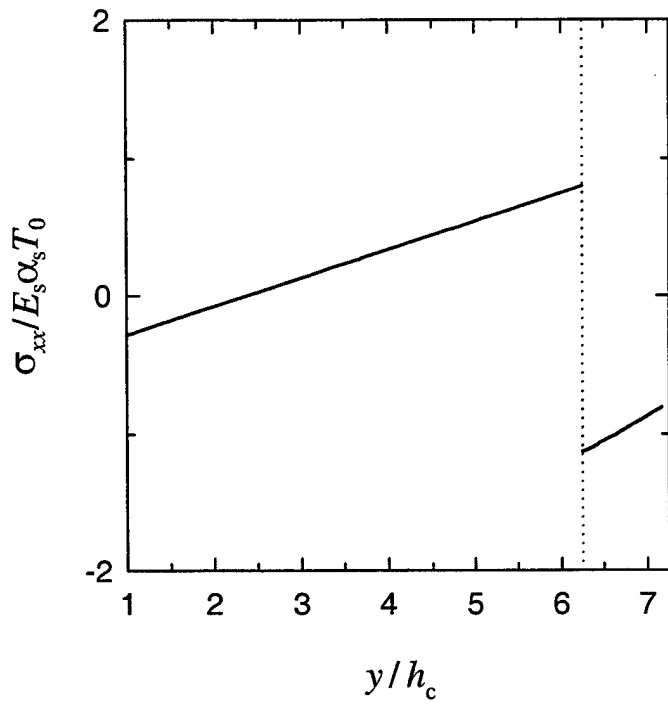


Figure 5.29 Variation of normalized  $\sigma_{xx}$  along  $x = 0$  for the homogeneous TBC described in Figure 5.21 under 1000 °C temperature drop,  $a/h_c = 20$ ,  $T_0 = 100$  K.

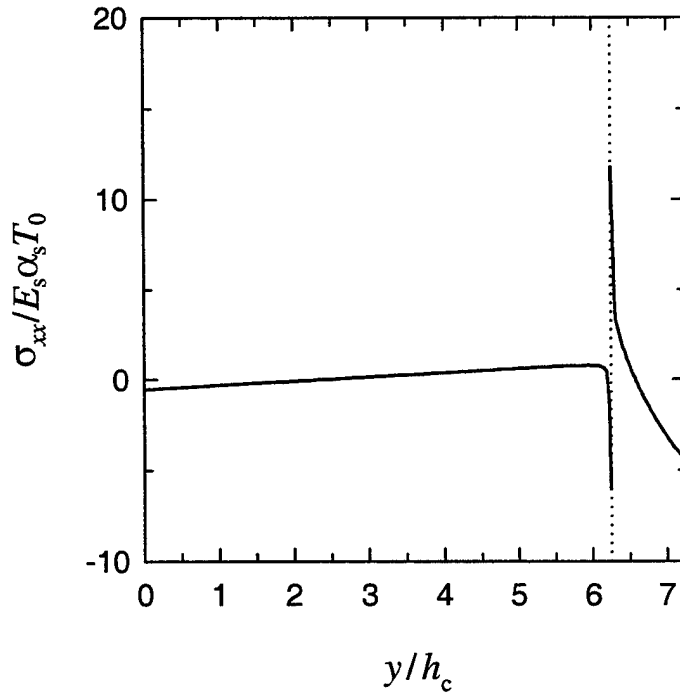


Figure 5.30 Variation of normalized  $\sigma_{xx}$  along  $x/a = 1$  for the homogeneous TBC described in Figure 5.21 under 1000 °C temperature drop,  $a/h_c = 20$ ,  $T_0 = 100$  K.

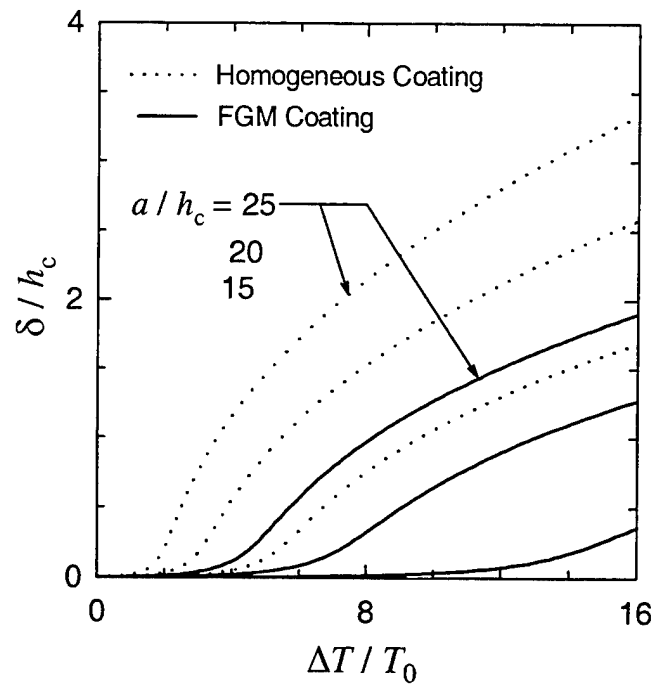


Figure 5.31 Crack opening displacement at the center of the crack vs. temperature drop in FGM and homogeneous coatings,  $T_0 = 100$  K.

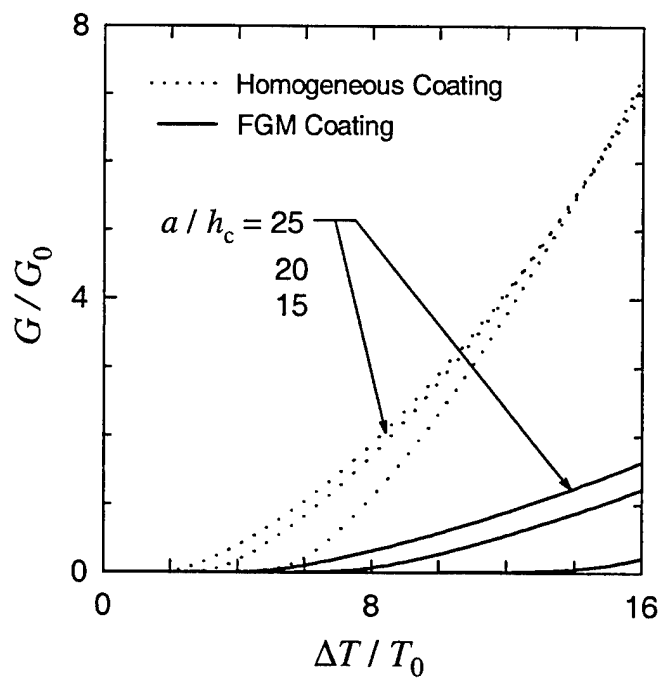


Figure 5.32 Strain energy release rate for homogeneous and FGM coatings under uniform temperature drop,  $T_0 = 100$  K,  $K_0 = E_s \alpha_s T_0 \sqrt{\pi h_c}$ ,  $G_0 = (1 - \nu_s^2) K_0^2 / E_s$ .

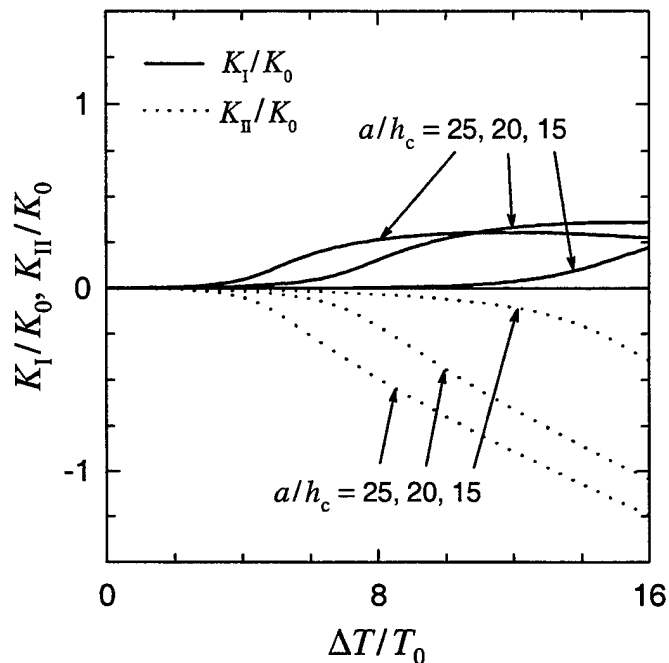


Figure 5.33 Stress intensity factors for FGM coating as a function of temperature drop,  $T_0 = 100\text{ K}$ ,  $K_0 = E_s \alpha_s T_0 \sqrt{\pi h_c}$ ,  $G_0 = (1 - \nu_s^2) K_0^2 / E_s$ .

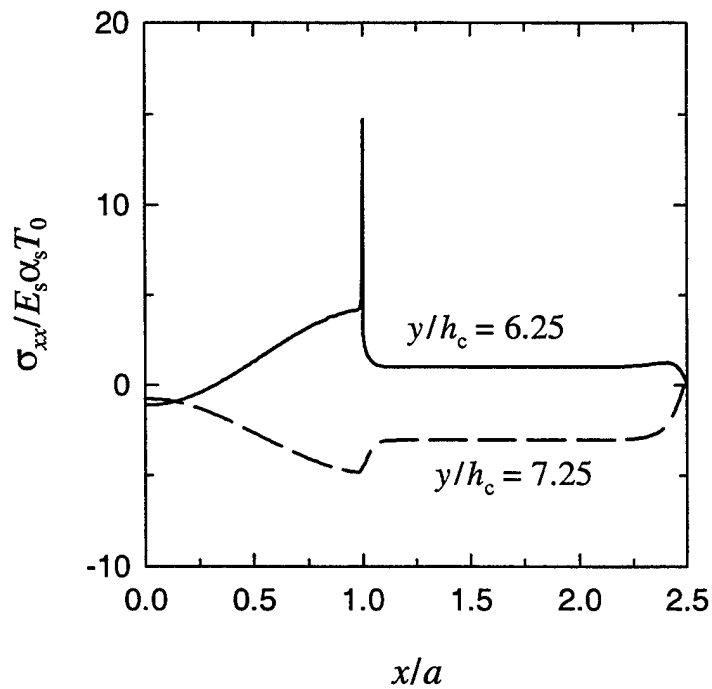


Figure 5.34 Variation of normalized  $\sigma_{xx}(x, y_0)$  along (i) the crack surface and the interface ( $y_0/h_c = 6.25$ ) and (ii) the top surface ( $y_0/h_c = 7.25$ ) of the FGM coating described in Figure 5.21 under  $1000^\circ\text{C}$  temperature drop,  $a/h_c = 20$ ,  $T_0 = 100\text{ K}$ .

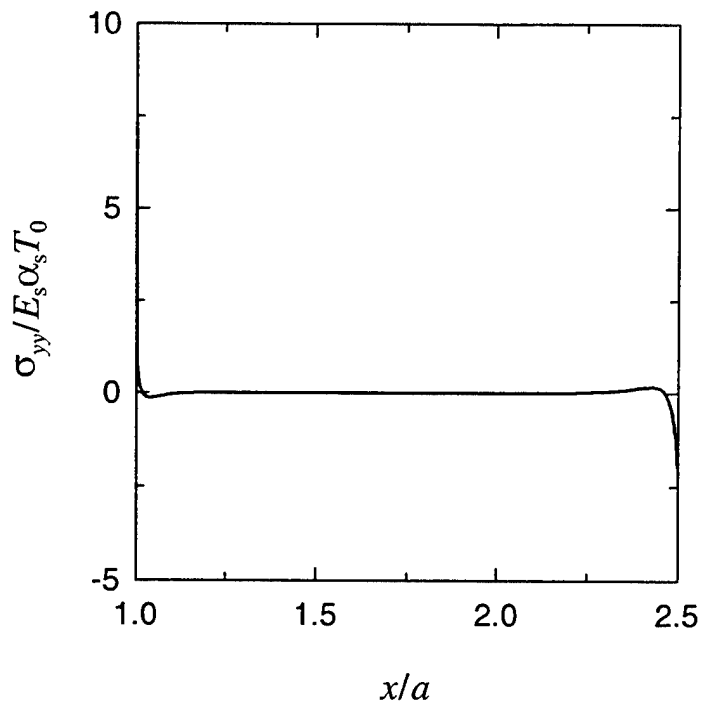


Figure 5.35 Variation of normalized  $\sigma_{yy}(x, y_0)$  along the interface of the FGM coating described in Figure 5.21 under 1000 °C temperature drop,  $y_0/h_c = 6.25$ ,  $a/h_c = 20$ ,  $T_0 = 100$  K.

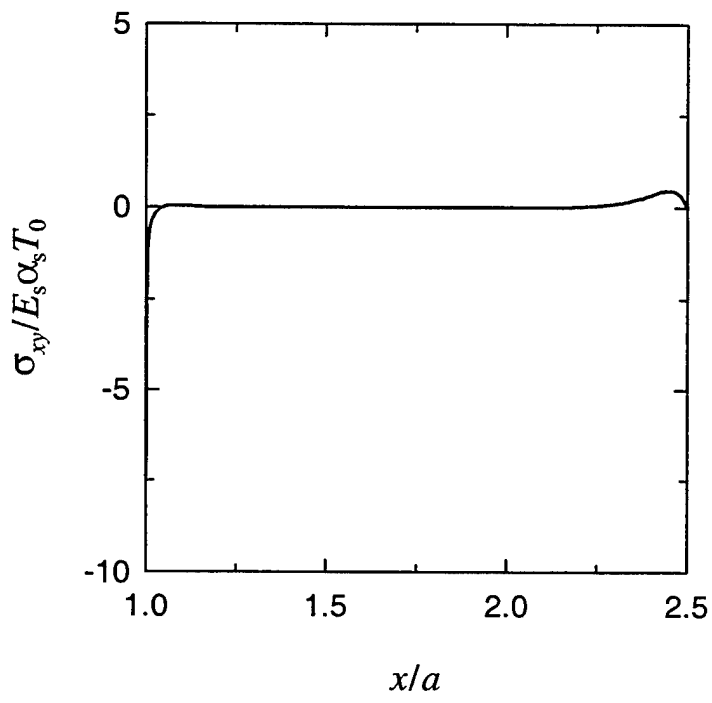


Figure 5.36 Variation of normalized  $\sigma_{xy}(x, y_0)$  along the interface of the FGM coating described in Figure 5.21,  $y_0/h_c = 6.25$ ,  $a/h_c = 20$ ,  $T_0 = 100$  K.

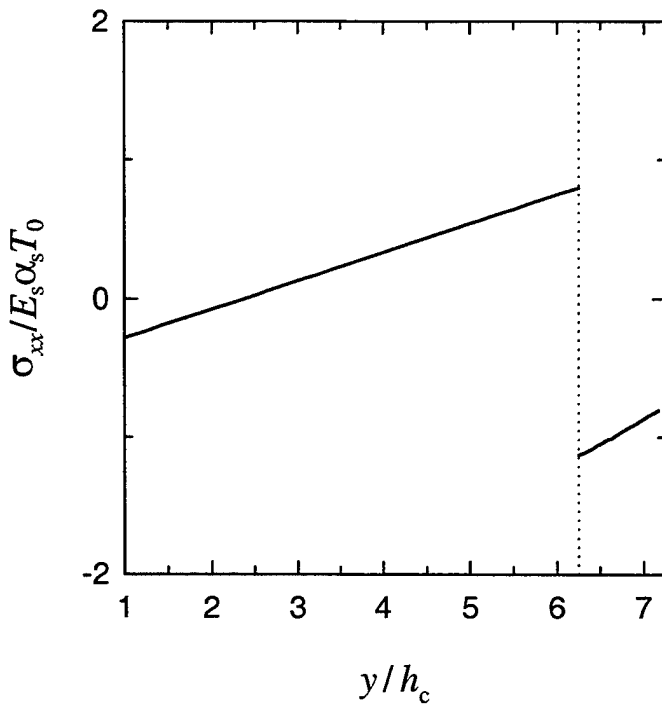


Figure 5.37 Variation of normalized  $\sigma_{xx}$  along  $x = 0$  for the FGM coating described in Figure 5.21 under 1000 °C temperature drop,  $a/h_c = 20$ ,  $T_0 = 100$  K.

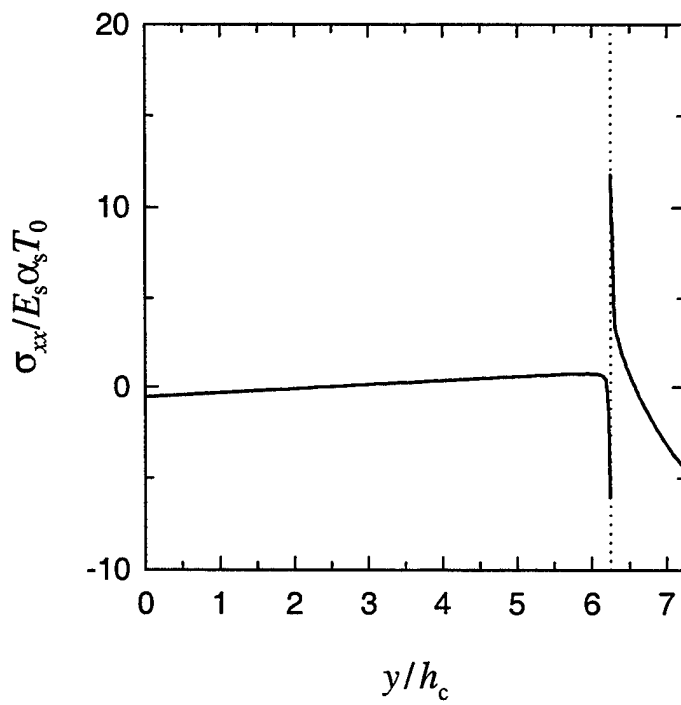


Figure 5.38 Variation of normalized  $\sigma_{xx}$  along  $x/a = 1$  for the FGM coating described in Figure 5.21 under 1000 °C temperature drop,  $a/h_c = 20$ ,  $T_0 = 100$  K.

### 5.3.2.2 The Axisymmetric Problem

The first axisymmetric example considered here is described in Figure 5.39 [86]. The disk-shaped specimen with dimensions  $h_c = 0.556$  mm,  $h_b = 0.184$  mm,  $h_s = 9.26$  mm, and  $R = 40$  mm is subjected to negative temperature changes. The relevant thermomechanical properties of the specific specimen are given in Table 5.4. Figures 5.40 and 5.41 show crack opening displacement at  $r = 0$  and strain energy release rate, respectively, obtained from both continuum and plate models for several values of  $a/h_c$ . The normalization factors used in the axisymmetric problems are given as follows:

$$T_0 = 100 \text{ K}, \quad K_0 = E_s \alpha_s T_0 \sqrt{\pi h_c}, \quad G_0 = (1 - \nu_s) K_0^2 / E_s. \quad (5.5)$$

It may be seen from these figures that basically the continuum and plate models agree with each other very well except in the case of  $a/h_c = 40$ . For the case of  $a/h_c = 40$  it is not only that significant discrepancy is observed between results from continuum and plate models, but also that the results from continuum theory for  $a/h_c = 40$  do not follow the trend observed in other cases ( $a/h_c = 20$  and  $30$ ). The rationale for the discrepancy between the case of  $a/h_c = 40$  and others can be seen by examining Figures 5.42 and 5.43. Figure 5.42 shows, for the case  $a/h_c = 40$ , the evolution of the deformed shapes of the specimen as temperature changes. It may be seen from this figure that around the inception of crack opening ( $\Delta T \sim 200^\circ\text{C}$ ) the deflection of the separated part of the coating exhibits the shape of first buckling mode. As temperature drops more, the shape of the deflection gradually changes from first buckling mode to third buckling mode. Figure 5.43 shows the deformed shapes of the specimen under  $1000^\circ\text{C}$  temperature drop for  $a/h_c = 30$  and  $40$ . It is observed that unlike the case of  $a/h_c = 40$ , the deflections for the case of  $a/h_c = 30$  remains the shape of first buckling mode. It is important to note that because of the inability of the plate model described in Appendix I to dictate higher buckling modes, the results based on the first buckling mode (as shown in Figure 5.40 and 5.41 for  $a/h_c = 40$ ) cannot correctly predict the postbuckling behavior. Figure 5.44

shows the normalized stress intensity factors as functions of temperature drop. Again, relaxation in stress intensity factors due to higher buckling mode for the case of  $a/h_c = 40$  is observed.

By comparing the strain energy release rates  $G$  obtained from plate and continuum models for the cases of  $a/h_c = 30$  in Figure 5.41, one may see that the strain energy release rate predicted by plate model is higher than that given by the continuum model. This observation does not agree with the one made in the plane strain case and seems to contradict the "higher constraint in plate model" explanation. The reason for the difference between results for plane and axisymmetric geometry is that in the postbuckling analysis the deformed shape is asymptotically obtained for the initial postbuckling regime. As a consequence, the plate model would overpredict the crack opening displacement and strain energy release rate (Appendix I). Apparently in the case of  $a/h_c = 30$  the effect of the higher constraining "fixed end" assumption in plate model (e.g., observed in the case of  $a/h_c = 20$ ) is out weighted by the approximation errors of the asymptotic analysis and thus the plate model overpredicts the results.

Table 5.4 Material properties of the disk-shaped specimen described in Figure 5.39 [86].

	Material	$E$ (GPa)	$\nu$	$\alpha (10^{-6} \text{ }^{\circ}\text{C}^{-1})$
Substrate	Ni-based Superalloy	175.8	0.25	13.91
Bond Coat	NiCrAlZr	137.9	0.27	15.16
Top Coat	$\text{ZrO}_2$ -8wt% $\text{Y}_2\text{O}_3$	27.6	0.25	10.01

To examining the influence of substrate thickness on the crack opening and fracture mechanics parameters, we fix the crack radius/coating thickness ratio as  $a/h_c = 20$  and vary the substrate thickness from the specimen's original  $h_s/h_c = 16.8$  to  $h_s/h_c = 8.4$  and 4.2. The results are given in Figures 5.45-5.47. Basically, it may be seen from these figures that the crack opening displacement at the center of the crack, the strain energy

release rate, and the magnitude of stress intensity factors decrease slightly as  $h_s/h_c$  decreases. Nevertheless, the results obtained from plate model varies significantly as  $h_s/h_c$  changes and the difference between plate and continuum models increases as the substrate thickness decreases. Therefore, it may be concluded that plate model would give better approximation for greater value of substrate thickness.

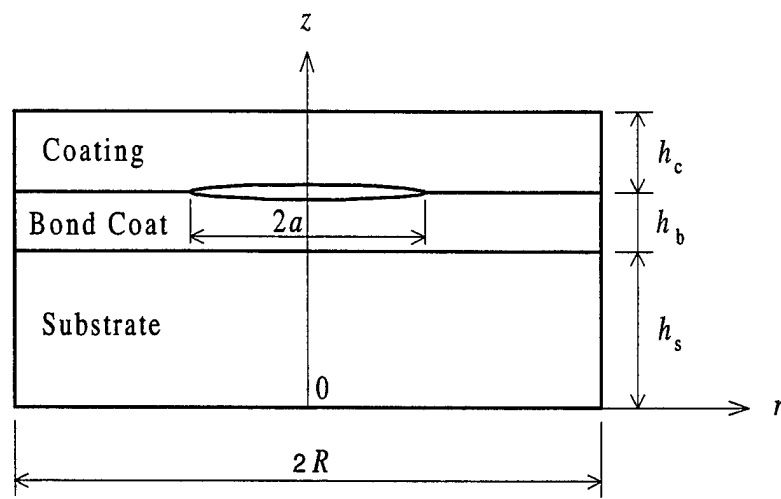


Figure 5.39 Specimen configuration for the first axisymmetric thermal buckling problem.

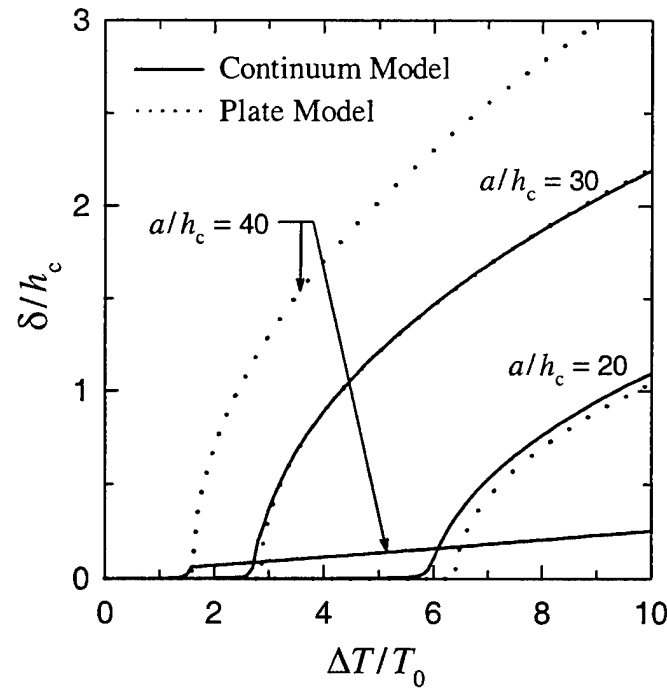


Figure 5.40 Crack opening displacement at the center of the crack for the homogeneous PSZ coating under uniform temperature drop  $\Delta T$ ,  $T_0 = 100$  K.

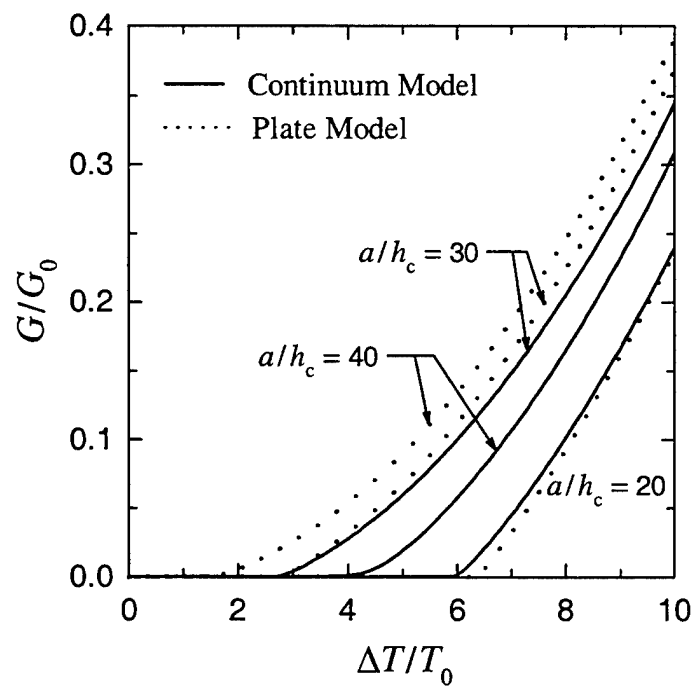
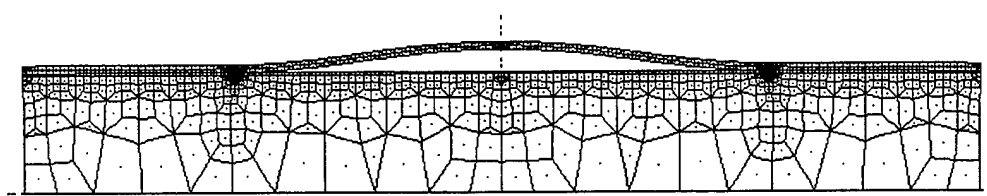
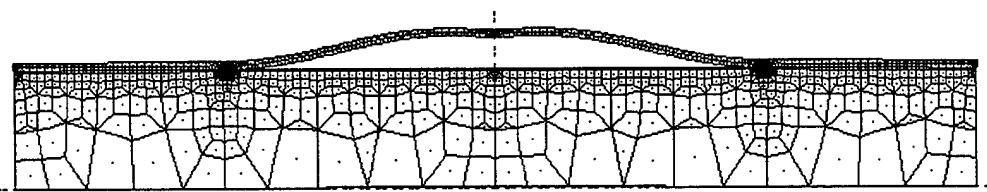


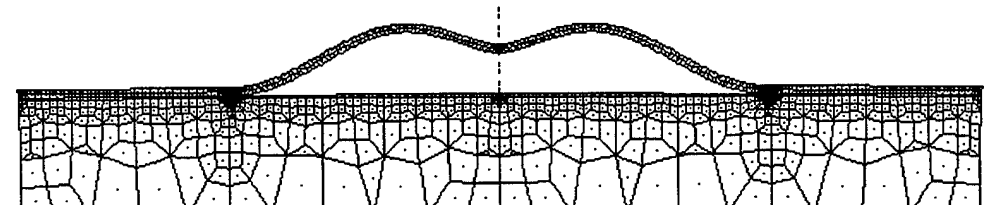
Figure 5.41 Strain energy release rate as a function of temperature drop  $\Delta T$  for the homogeneous PSZ coating,  $T_0 = 100$  K.



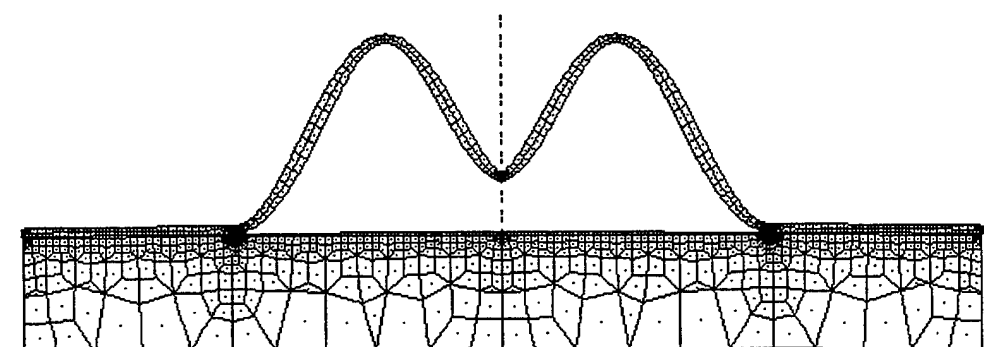
(a)  $\Delta T/T_0 = 2$



(b)  $\Delta T/T_0 = 3$

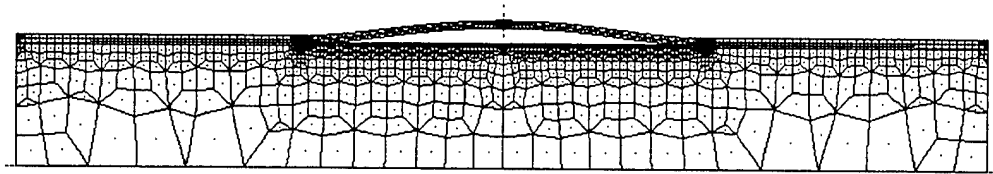


(c)  $\Delta T/T_0 = 4$

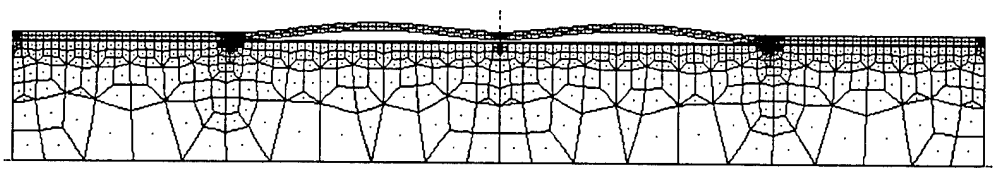


(d)  $\Delta T/T_0 = 5$

Figure 5.42 Evolution of the displacement of homogeneous ceramic coating under uniform temperature change, (a)  $\Delta T/T_0 = 2$ , (b)  $\Delta T/T_0 = 3$ , (c)  $\Delta T/T_0 = 4$ , (d)  $\Delta T/T_0 = 5$ ,  $T_0 = 100$  K,  $a/h_c = 40$ , Scale factor = 40.



(a)  $a/h_c = 30$



(b)  $a/h_c = 40$

Figure 5.43 Deformed shape of the homogeneous ceramic coating under uniform temperature change, (a)  $a/h_c = 30$ , (b)  $a/h_c = 40$ ,  $\Delta T/T_0 = 10$ .

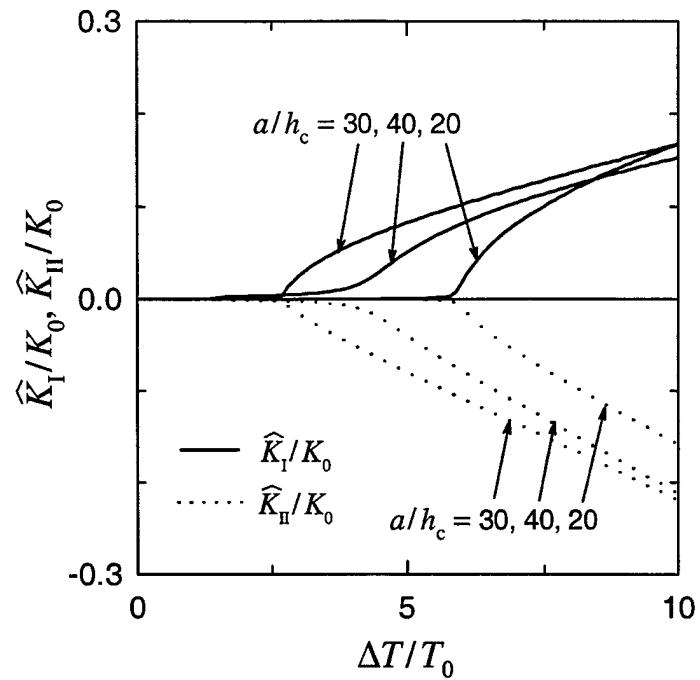


Figure 5.44 Normalized stress intensity factors for homogeneous zirconia coating under uniform temperature drop,  $T_0 = 100$  K,  $K_0 = E_s \alpha_s T_0 \sqrt{\pi h_c}$ ,  $G_0 = (1 - \nu_s) K_0^2 / E_s$ ,  $\hat{K}_I + i\hat{K}_{II} = (K_I + iK_{II})h_c^{i\epsilon}$ .

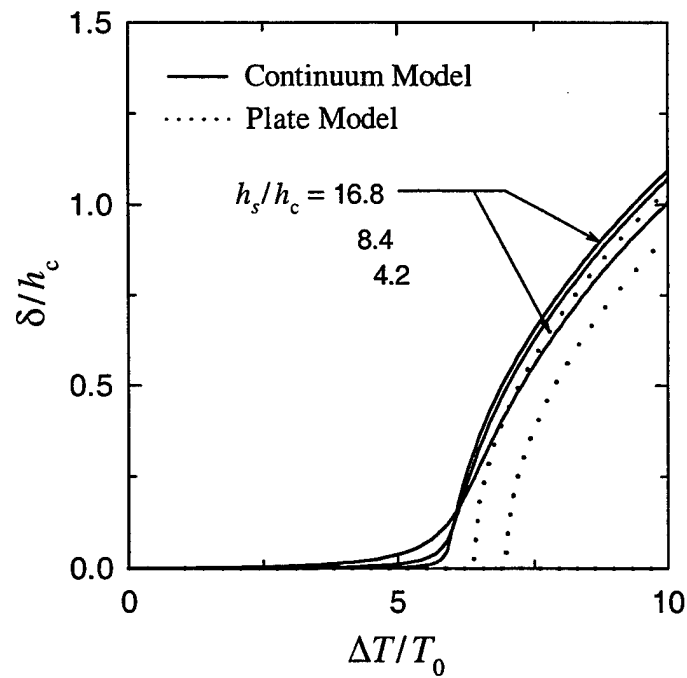


Figure 5.45 Crack opening displacement at the center of the crack for the homogeneous PSZ coating under uniform temperature drop,  $T_0 = 100$  K.

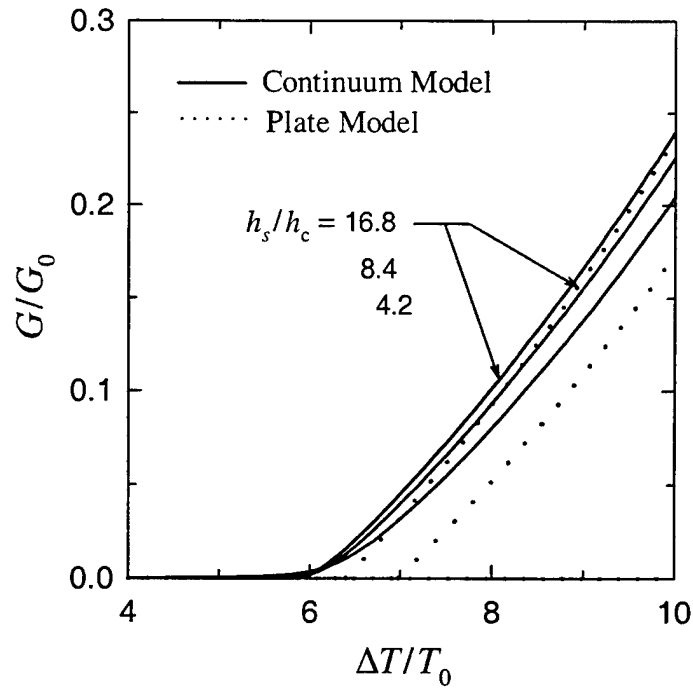


Figure 5.46 Strain energy release rate as a function of temperature drop for the homogeneous PSZ coating,  $T_0 = 100$  K.

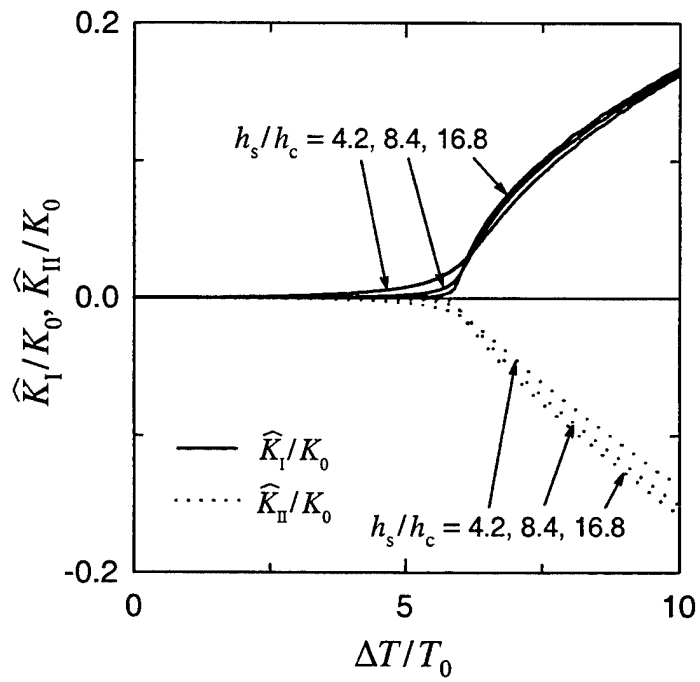


Figure 5.47 Normalized stress intensity factors for homogeneous zirconia coating under uniform temperature drop,  $T_0 = 100$  K,  $K_0 = E_s \alpha_s T_0 \sqrt{\pi h_c}$ ,  $G_0 = (1 - \nu_s) K_0^2 / E_s$ ,  $\hat{K}_I + i\hat{K}_{II} = (K_I + iK_{II})h_c^{ie}$ .

The second axisymmetric specimen we examined is shown in Figure 5.48 [63]. The dimensions of the specimen are given as follows [63]:  $h_c = 127 \mu\text{m}$ ,  $h_t = 10 \mu\text{m}$ ,  $h_b = 48.2 \mu\text{m}$ ,  $h_s = 3.175 \text{ mm}$ , and  $2R = 25.4 \text{ mm}$ . The specimen under consideration originally consists of only three layers: superalloy substrate, metallic bond coat, and top coat that is either a homogeneous ceramic coating or a metal/ceramics FGM coating. A thin layer of thermally grown oxide (TGO) which consists of mainly aluminum oxide is grown at the bond coat-top coat interface after an extended exposure to high temperature oxidative environment. The material property gradation of the FGM is assumed such that the FGM has the same material properties as the bond coat at the bond coat-top coat interface, the same properties as the pure ceramics at the TBC surface, and the property variations in between are given as

$$\begin{aligned}
 E(z) &= E_c + (E_b - E_c) \left( \frac{h_c + h_t + h_b + h_s - z}{h_c} \right)^{p_1}, \\
 \nu(z) &= \nu_c + (\nu_b - \nu_c) \left( \frac{h_c + h_t + h_b + h_s - z}{h_c} \right)^{p_2}, \\
 \alpha(z) &= \alpha_c + (\alpha_b - \alpha_c) \left( \frac{h_c + h_t + h_b + h_s - z}{h_c} \right)^{p_3}, \\
 h_t + h_b + h_s &< z < h_c + h_t + h_b + h_s,
 \end{aligned} \tag{5.6}$$

where  $(E_b, \nu_b, \alpha_b)$  and  $(E_c, \nu_c, \alpha_c)$  are the thermomechanical properties of the metallic bond coat and ceramics, respectively,  $p_1$ ,  $p_2$ , and  $p_3$  are the measures of inhomogeneity of the FGM, and  $(p_1, p_2, p_3) \geq 0$ . The power-law variations for the thermomechanical properties are defined such that the FGM is metal-rich for  $0 < (p_1, p_2, p_3) < 1$ ; a linear variation from 100% metal to 100% ceramics when  $p_1 = p_2 = p_3 = 1$ ; and ceramic-rich for the case of  $1 < (p_1, p_2, p_3) < \infty$ . Two limiting cases of the material gradation are that the coating consists of 100% metallic bond coat material if  $p_1$ ,  $p_2$ , and  $p_3$  equal to zero; and that as  $p_1$ ,  $p_2$ , and  $p_3$  approach infinity, the coating becomes pure ceramics. As an

example, the profile of elastic modulus described in (5.6) is plotted for various values  $p_1$  in Figure 5.49. The relevant thermomechanical properties for the specimen described in Figure 5.48 are given in Table 5.5.

Table 5.5\* Material properties of the disk-shaped specimen described in Figure 5.48.

	Material	$E$ (GPa)	$\nu$	$\alpha$ ( $10^{-6} \text{ }^{\circ}\text{C}^{-1}$ )
Substrate	Ni-based Superalloy	151.4	0.26	15.38
Bond Coat	NiCrAlZr	122.9	0.27	15.49
TGO	$\text{Al}_2\text{O}_3$	320	0.21	8.8
Ceramics	$\text{ZrO}_2\text{-}8\text{wt\%Y}_2\text{O}_3$ (PSZ)	11.54	0.25	10.91

The results for the specimen described in Figure 5.48 under uniform temperature drop are given in Figures 5.50-5.77. The normalizing quantities used here are defined in (5.5), in which the quantities with a subscript s correspond to the properties of the substrate given in Table 5.5. The normalization of the complex stress intensity factors associated with crack between dissimilar material interface is done by following the method described in the plane strain cases (Equation (5.3)) and  $L = h_c$  is used as the length parameter for the "rotation". It is assumed that the TBC system is stress free before the temperature changes. Figures 5.50 and 5.51 show the results for the "original" specimen which does not contain TGO layer (i.e.,  $h_t = 0$ ). The FGM top coat examined here is assumed to have linear material property variations, i.e.,  $p_1 = p_2 = p_3 = 1$  in (5.6). It can be seen that FGM coating gives smaller crack opening (Figure 5.50) and strain energy release rate (Figure 5.51) compared with the homogeneous PSZ coating. The results which is consistent with the plane strain results given in Section 5.3.2.1 can, again, be explained by the lower thermal residual stresses and higher bending stiffness of the FGM coating. The

\* The material data in this table are the mean values computed from the temperature-dependent properties given in Table 1.1 while the data given in Table 5.4 are the same as the material properties at  $22^{\circ}\text{C}$  shown in Table 1.1.

results for the oxidized TBCs that consist of four layers are given in Figures 5.52-5.54. It is observed that the FGM coating with linearly varying thermomechanical properties gives smaller driving forces for interface crack propagation than homogeneous coating. The "rotated" stress intensity factors, as shown in Figure 5.54, indicate the stronger mode II contribution, which is also observed in the plane strain case. It is assumed in this study that the intrinsic residual stresses associated with TGO growth are negligible because of the expected stress relaxation due to the extended exposure to elevated temperatures. Note that because of the insertion of the TGO layer, the continuity of the material properties across the bond coat-top coat interface is lost and consequently the stress intensity factors are complex rather than real. Also note that as observed in experiments [27], the metallic particles in the graded coating would be oxidized after a sustained exposure to high temperature and, thus, a change of material property profile in the FGM is expected. Nevertheless, it was also been observed in the FGM coating system that the location of interface crack is right below the region which consists mainly oxidized metallic particles. Therefore a simplified layered system, i.e., FGM layer defined by (5.6) above the TGO layer is used in this study to approximate the more complicated real material system.

Figures 5.55-5.57 show the effect of TGO layer on the crack opening and crack-extension driving forces for the TBC system with FGM ( $p_1 = p_2 = p_3 = 1$  in (5.6)) top coat. It may be seen that the crack opens at a much smaller temperature drop when TGO layer exists. Also the crack driving forces for the case with TGO are much higher than that without TGO for the same temperature change. The huge differences in the results shown in Figures 5.55-5.57 induced by the thin layer of TGO may be attributed to the highest elastic modulus and lowest coefficient of thermal expansion among the materials in the TBC system (Table 5.5). This combination would increase the level of residual compressive stress significantly and thus gives higher strain energy release rate and larger crack opening. Therefore, it is very important to take the TGO layer into consideration in

evaluating the crack problems in TBCs when the surface temperature reaches beyond 800°C.

The strain energy release rates for the oxidized TBCs (Figure 5.48) with either homogeneous or FGM ( $p_1 = p_2 = p_3 = 1$  in (5.6)) top coat are given as functions of normalized crack length in Figures 5.58 and 5.59. It is observed that under a uniform temperature change the strain energy release rate first increases rapidly but then gradually levels off as  $a/h_c$  increases. An important application of the result of strain energy release rate as a function of crack length is to determine the service life of the coating under low cycle fatigue. It is well known that under cyclic loading such as the cyclic thermal stresses in the TBCs during service, subcritical crack propagation can be characterized as

$$\frac{da}{dN} = f_k(\Delta K), \quad (5.7)$$

where  $a$  and  $N$  denote the crack length and number of loading cycles,  $\Delta K = K_{\max} - K_{\min}$  is the range of the stress intensity factor and the function  $f_k$  is determined experimentally. For the mixed-moded interface crack problem discussed in this study, instead of (5.7), we may write

$$\frac{da}{dN} = f_G(G), \quad (5.8)$$

where  $f_G$  is determined experimentally and  $G$  may be expressed as  $G(a)$  (e.g., Figures 5.58 and 5.59). By substituting the relation of  $G$  and  $a$ , exchanging  $dN$  and  $f_G$ , and integrating both sides of (5.8), we may obtain crack length  $a$  as a function of number of loading cycles  $N$ . From this we may determine the number of fatigue cycles before  $a$  reaches the critical crack length at which brittle fracture occurs.

Figures 5.60-5.65 show the normalized stresses for a homogeneous coating with TGO layer containing an interface crack of length  $a/h_c = 30$  (Figure 5.48) under 1000 °C uniform temperature drop. The normalized stresses for the specimen (Figure 5.48,

$a/h_c = 30$ ) with FGM top coat ( $p_1 = p_2 = p_3 = 1$  in (5.6)) under  $1000^\circ\text{C}$  uniform temperature drop are given in Figures 5.66-5.71. By examining the normalized stresses  $\sigma_{rr}$ ,  $\sigma_{zz}$ , and  $\sigma_{rz}$  along the crack surface ( $0 < r < a$ ) and the TGO-bond coat interface ( $a < r < R$ ) for the cases of homogeneous top coat (Figures 5.60-5.62) and FGM top coat (Figures 5.66-5.68), it may be seen that, except for around the crack tip and the point of materials interface intersecting free surface, the residual bending stress  $\sigma_{rr}$  resulting from temperature drop is the dominant stress. It is also observed that the bottom surface of the debonded FGM coating is under higher compressive  $\sigma_{rr}$  than that for homogeneous top coat. The normalized stress  $\sigma_{rr}$  on the top surface of the homogeneous and FGM coatings are given in Figure 5.63 and 5.69, respectively. Compared to the stress  $\sigma_{rr}$  on the top surface of the debonded FGM coating  $\sigma_{rr}$  for the homogeneous top coat appears to be higher and, thus, is more prone to the growth of surface crack. The normalized stress  $\sigma_{rr}$  along  $r = 0$  and  $r = a$  for the TBC are given in Figure 5.64 and 5.65 for homogeneous coating and in Figure 5.70 and 5.71 for FGM coating. It may be seen that in both cases the TGO layer is under very high compression.

The influence of material inhomogeneity on the crack opening at  $r = 0$ , strain energy release rate, and stress intensity factors are shown in Figures 5.72, 5.73, and 5.74, respectively, for the 4-layered TBC system described in Figure 5.48 ( $a/h_c = 30$ ). Here we assume that for the FGM top coat the inhomogeneity parameters for the elastic modulus, Poisson's ratio, and coefficient of thermal expansion have the same value, i.e.,  $p_1 = p_2 = p_3 = p$ . Figures 5.75, 5.76, and 5.77 also plot the crack opening, strain energy release rate, and stress intensity factors as a function of inhomogeneity parameter  $p$  for several fixed values of temperature change. It can be seen from Figures 5.72-5.77 that the crack driving forces and opening are smaller for the metal-rich ( $p < 1$ ) FGM than those for ceramic-rich ( $p > 1$ ). Again, this is due to the better thermomechanical properties match, especially in the coefficient of thermal expansion, across the thickness direction in

the TBC system, and thus smaller residual stresses for the metal-rich case. Thus, by increasing the metal content in the FGM coating one may reduce the driving force for interface crack growth and consequently extend the service life of the TBC system. It is interesting to note that however, from the thermal insulation point of view, metal-rich FGM is less desirable because of its higher thermal conductivity. It is then important to take all relevant factors into consideration in order to obtain the optimal design of the FGM coating.

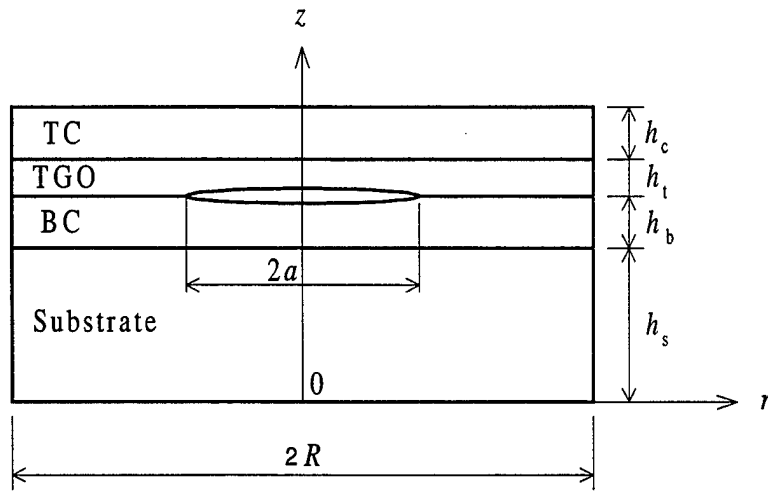


Figure 5.48 Specimen configuration for the second axisymmetric thermal buckling problem.

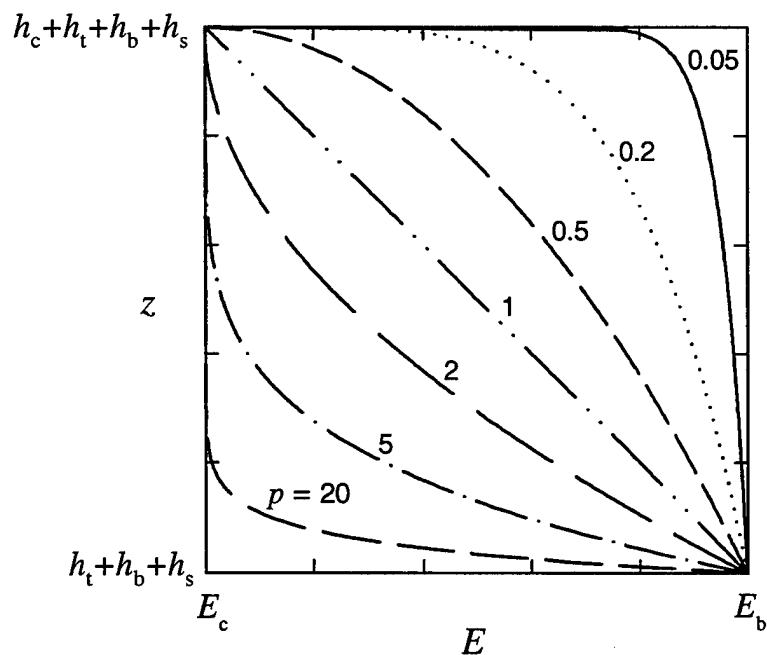


Figure 5.49 The thickness variation of the Young's modulus in the FGM coating given in Figure 5.48,  $E_b$  and  $E_c$  are the elastic modulus of bond coat and ceramics, respectively.

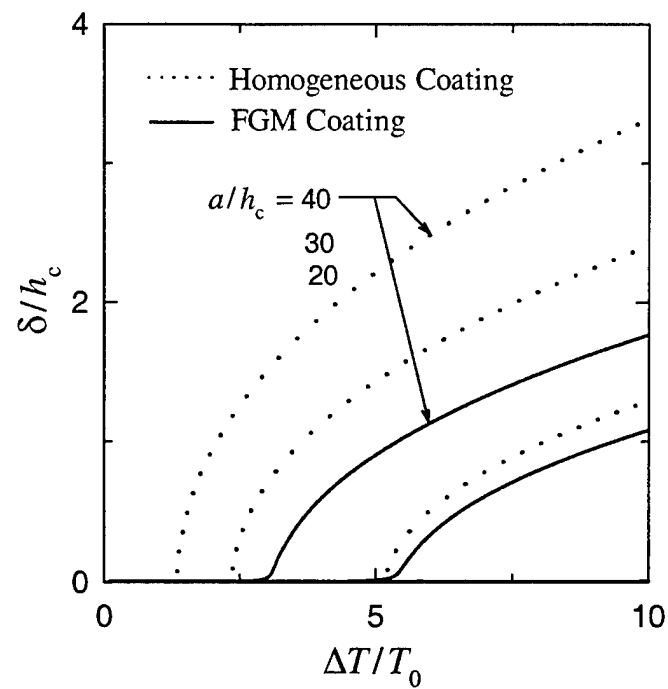


Figure 5.50 Crack opening displacements at the center of crack for homogeneous and FGM top coats without TGO under uniform temperature drop,  $T_0 = 100$  K.

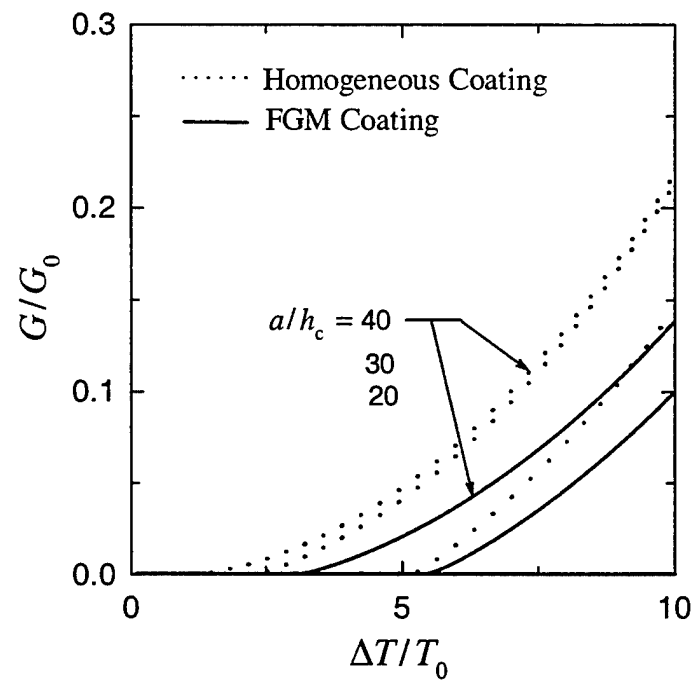


Figure 5.51 Strain energy release rate as a function of temperature drop for the homogeneous and FGM coatings without TGO,  $T_0 = 100$  K.

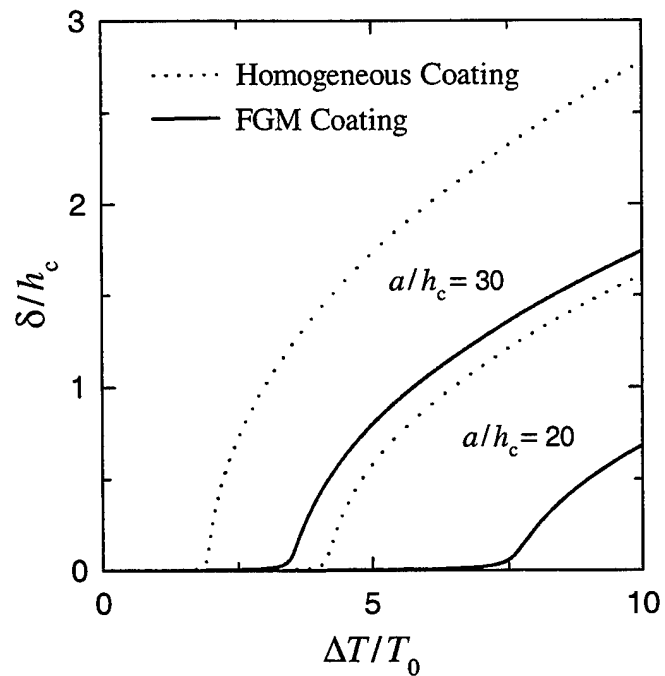


Figure 5.52 Crack opening displacements at the center of crack for homogeneous and FGM top coats with TGO under uniform temperature drop,  $T_0 = 100$  K.

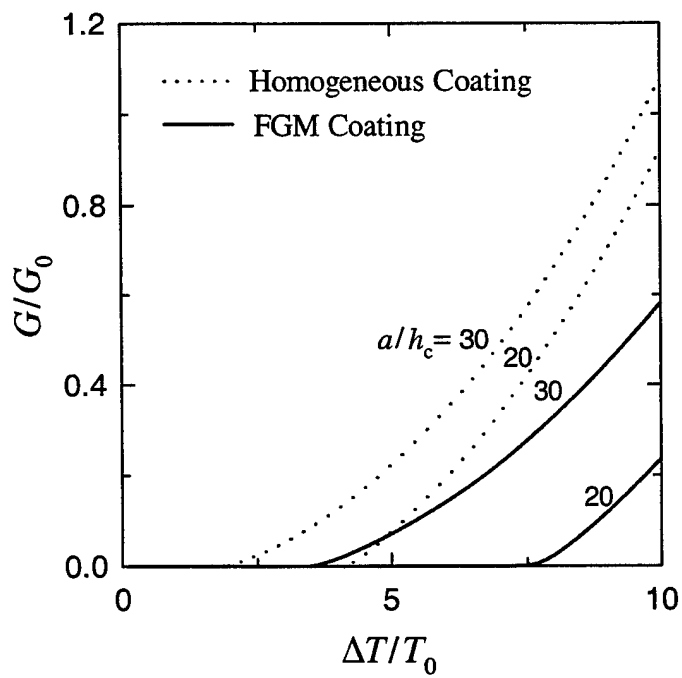


Figure 5.53 Strain energy release rate as a function of temperature drop for the homogeneous and FGM coatings with TGO,  $T_0 = 100$  K.

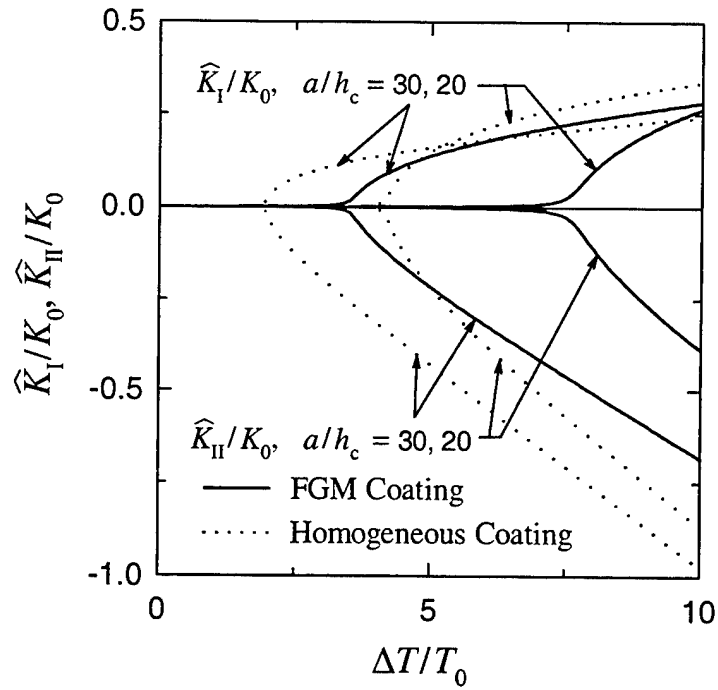


Figure 5.54 Normalized stress intensity factors for homogeneous and FGM coatings with TGO under uniform temperature drop,  $T_0 = 100\text{ K}$ ,  $K_0 = E_s \alpha_s T_0 \sqrt{\pi h_c}$ ,  $G_0 = (1 - \nu_s) K_0^2 / E_s$ ,  $\hat{K}_I + i\hat{K}_{II} = (K_I + iK_{II})h_c^{i\epsilon}$ .

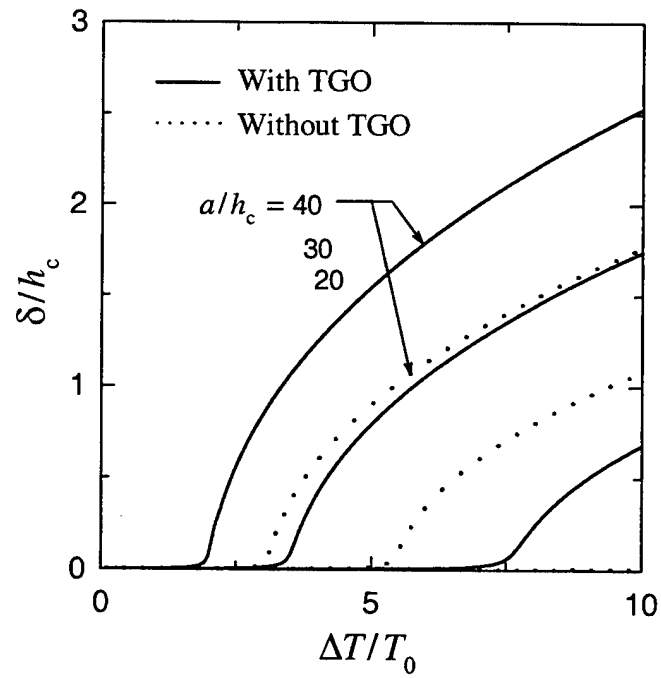


Figure 5.55 Crack opening displacement at the center of crack for FGM top coat under uniform temperature drop,  $T_0 = 100\text{ K}$ .

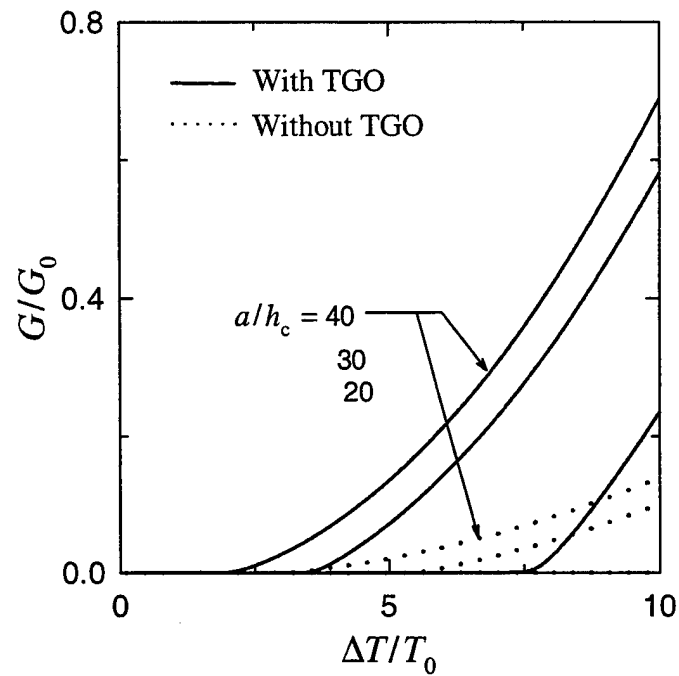


Figure 5.56 Strain energy release rate as a function of temperature drop for the FGM coating,  $T_0 = 100$  K.

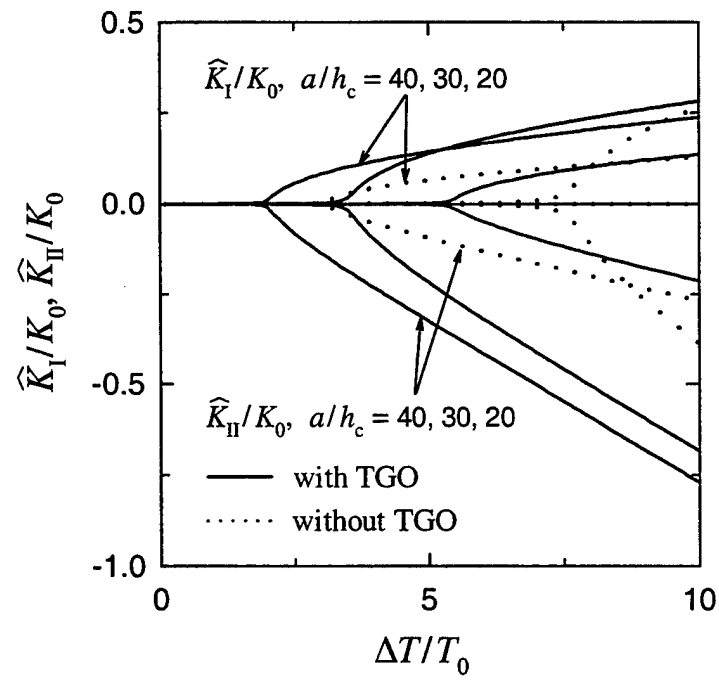


Figure 5.57 Normalized stress intensity factors for FGM coating under uniform temperature drop,  $T_0 = 100$  K,  $K_0 = E_s \alpha_s T_0 \sqrt{\pi h_c}$ ,  $G_0 = (1 - \nu_s) K_0^2 / E_s$ ,  $\hat{K}_I + i\hat{K}_{II} = (K_I + iK_{II})h_c^{ie}$ .

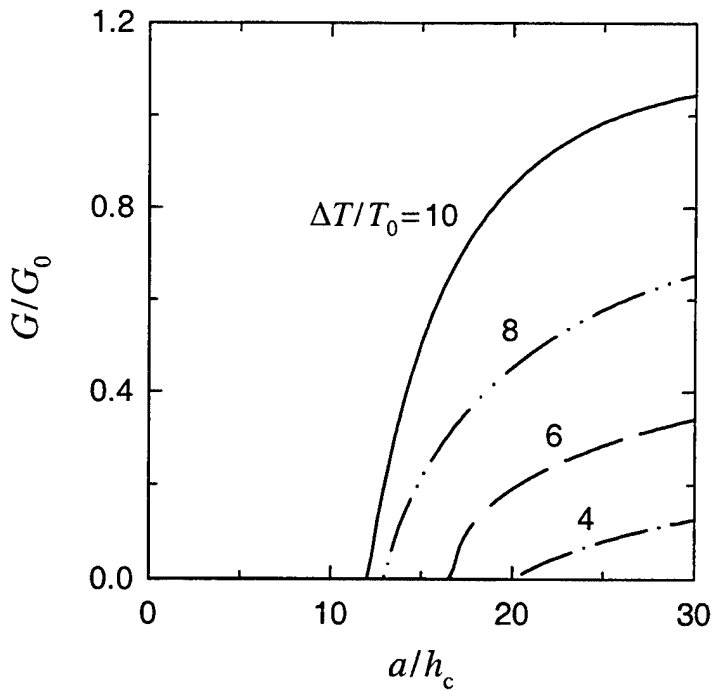


Figure 5.58 Strain energy release rate as a function of normalized crack length for the homogeneous coating with TGO layer,  $T_0 = 100$  K,  $K_0 = E_s \alpha_s T_0 \sqrt{\pi h_c}$ ,  $G_0 = (1 - \nu_s) K_0^2 / E_s$ .

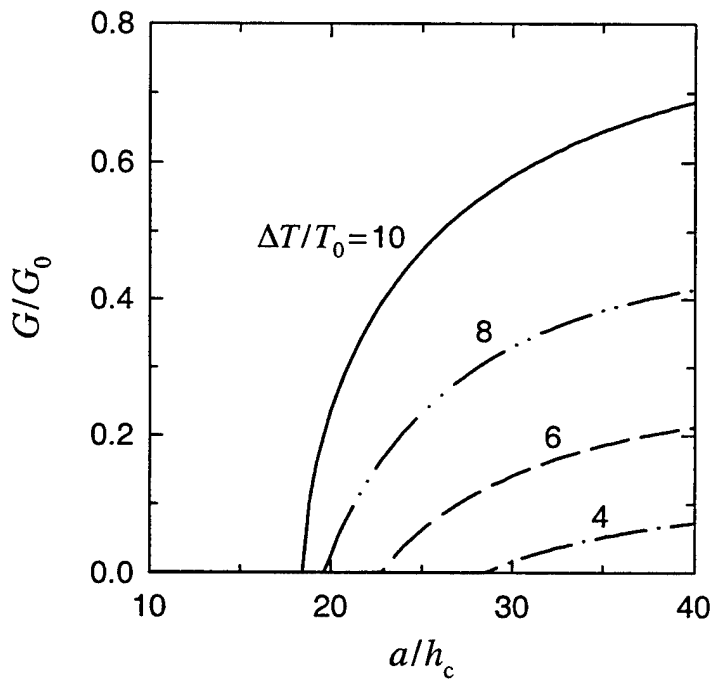


Figure 5.59 Strain energy release rate as a function of normalized crack length for the FGM coating with TGO layer,  $T_0 = 100$  K,  $K_0 = E_s \alpha_s T_0 \sqrt{\pi h_c}$ ,  $G_0 = (1 - \nu_s) K_0^2 / E_s$ .

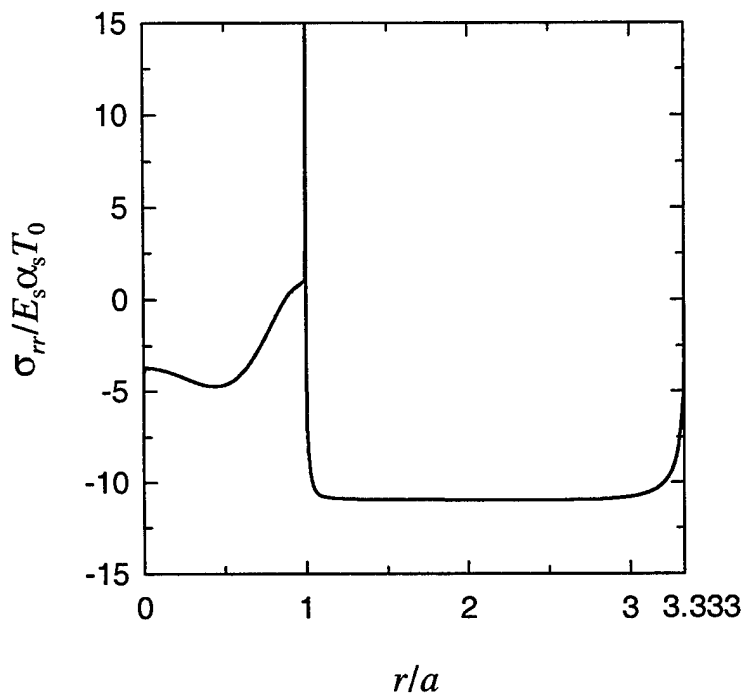


Figure 5.60 Variation of normalized  $\sigma_{rr}(r, z_0)$  along the crack surface ( $0 < r < a$ ) and the BC-TGO interface ( $r > a$ ) of the homogeneous TBC described in Figure 5.48,  $z_0/h_c = 25.36$ ,  $a/h_c = 30$ ,  $T_0 = 100$  K.

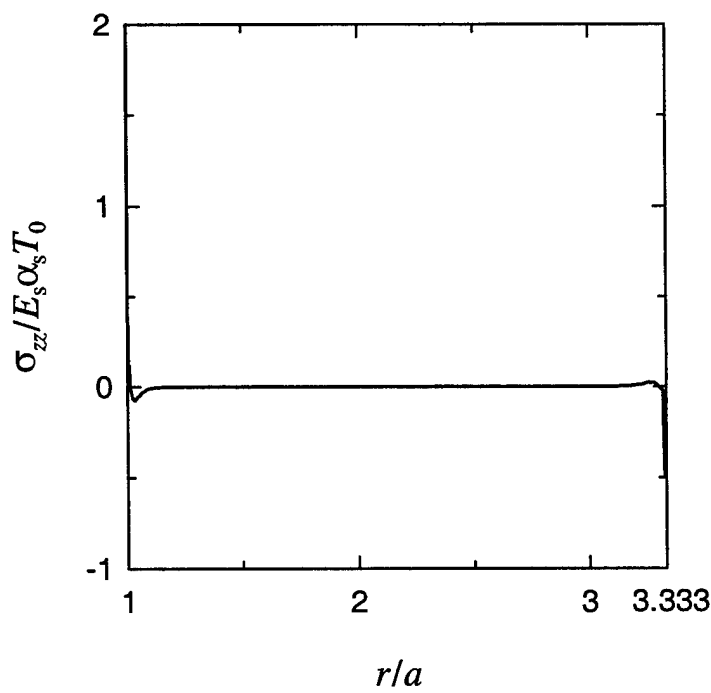


Figure 5.61 Variation of normalized  $\sigma_{zz}(r, z_0)$  along the BC-TGO interface of the homogeneous TBC described in Figure 5.48,  $z_0/h_c = 25.36$ ,  $a/h_c = 30$ ,  $T_0 = 100$  K.

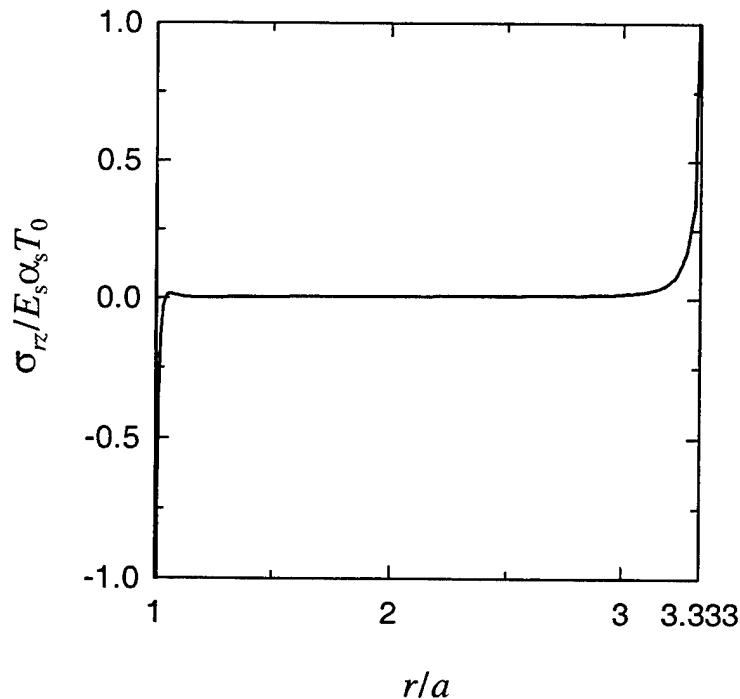


Figure 5.62 Variation of normalized  $\sigma_{rz}(r, z_0)$  along the BC-TGO interface of the homogeneous TBC described in Figure 5.48,  $z_0/h_c = 25.36$ ,  $a/h_c = 30$ ,  $T_0 = 100$  K.

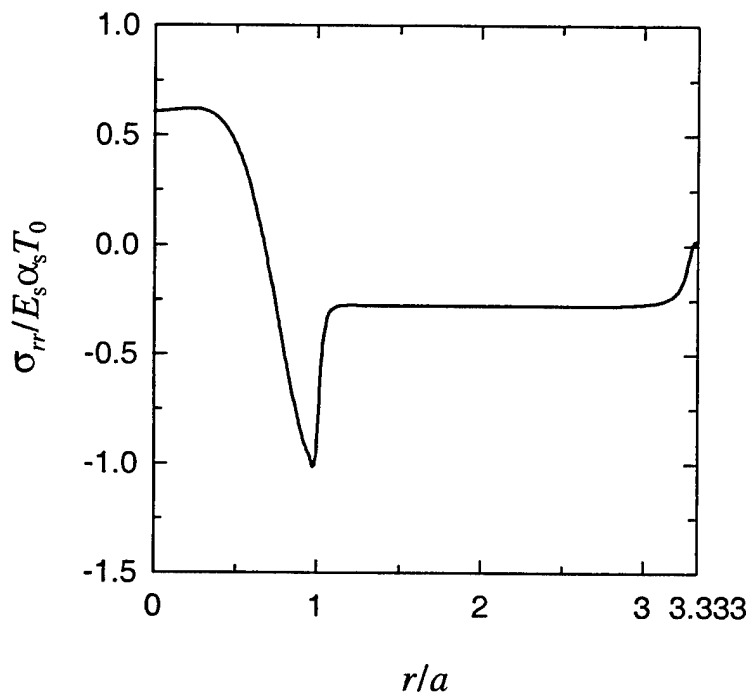


Figure 5.63 Variation of normalized  $\sigma_{rr}(r, z_0)$  along the coating surface of the homogeneous TBC described in Figure 5.48,  $z_0/h_c = 26.42$ ,  $a/h_c = 30$ ,  $T_0 = 100$  K.

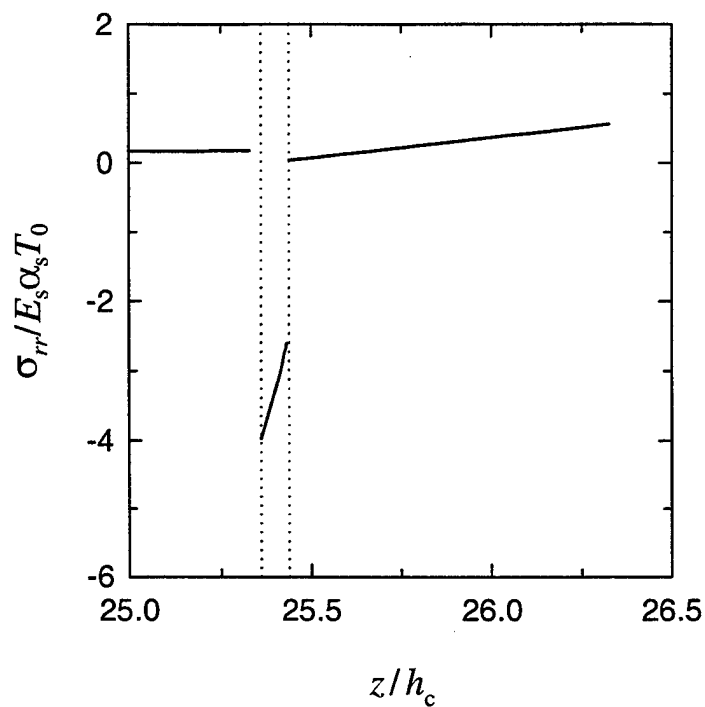


Figure 5.64 Variation of normalized  $\sigma_{rr}$  along  $r = 0$  in the homogeneous TBC described in Figure 5.48,  $a/h_c = 30$ ,  $T_0 = 100$  K.

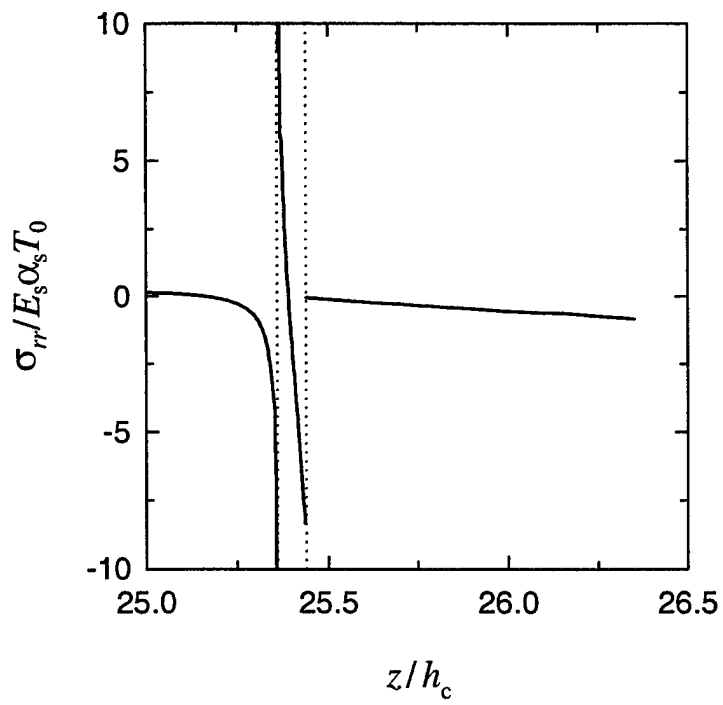


Figure 5.65 Variation of normalized  $\sigma_{rr}$  along  $r/a = 1$  in the homogeneous TBC described in Figure 5.48,  $a/h_c = 30$ ,  $T_0 = 100$  K.

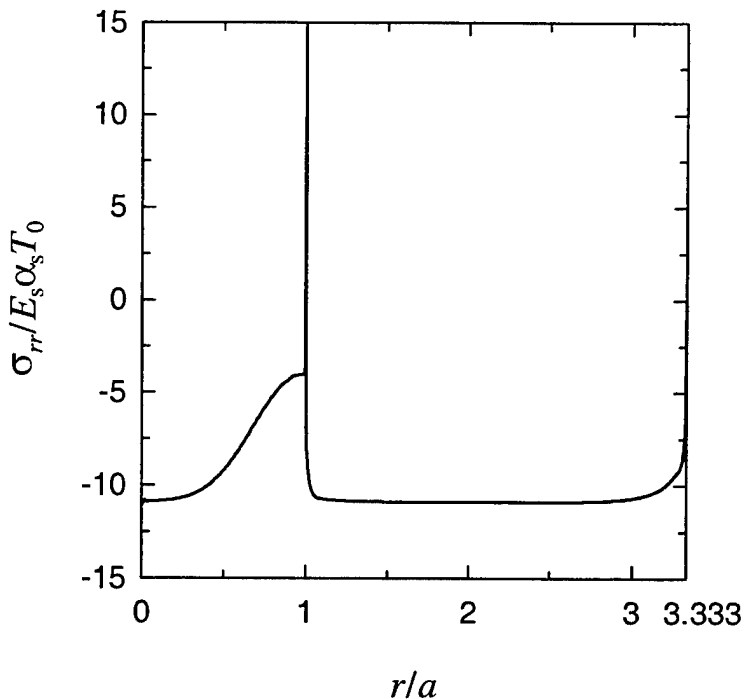


Figure 5.66 Variation of normalized  $\sigma_{rr}(r, z_0)$  along the crack surface ( $0 < r < a$ ) and the BC-TGO interface ( $r > a$ ) of the FGM coating described in Figure 5.48,  $z_0/h_c = 25.36$ ,  $a/h_c = 30$ ,  $T_0 = 100$  K.

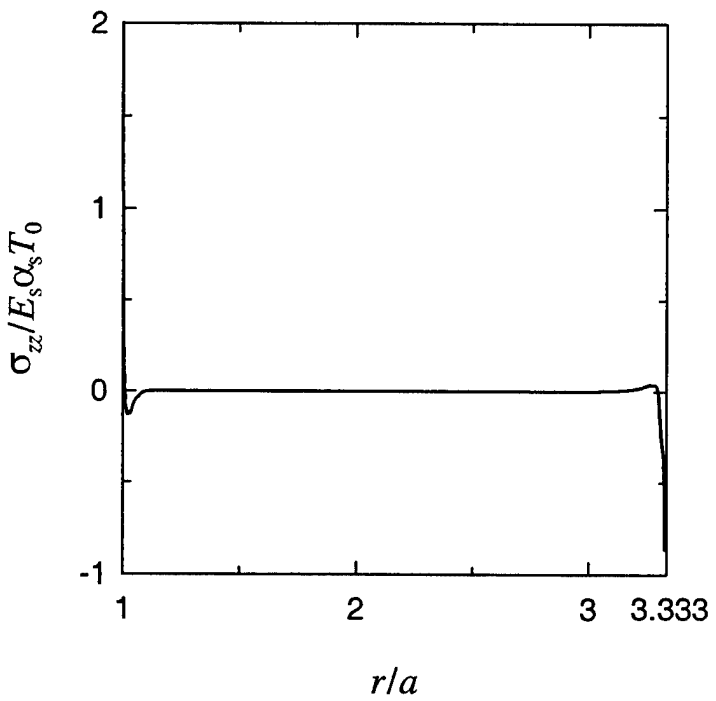


Figure 5.67 Variation of normalized  $\sigma_{zz}(r, z_0)$  along the BC-TGO interface of the FGM coating described in Figure 5.48,  $z_0/h_c = 25.36$ ,  $a/h_c = 30$ ,  $T_0 = 100$  K.

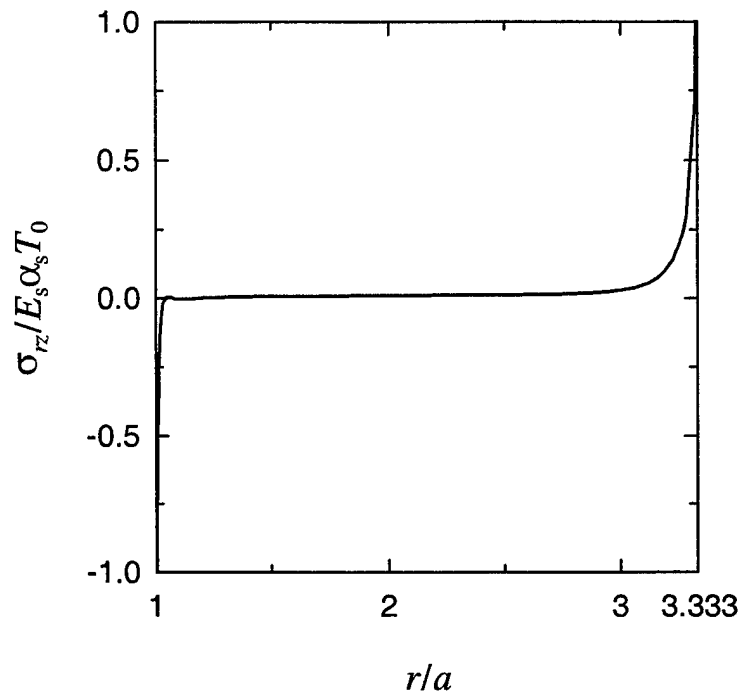


Figure 5.68 Variation of normalized  $\sigma_{rz}(r, z_0)$  along the BC-TGO interface of the FGM coating described in Figure 5.48,  $z_0/h_c = 25.36$ ,  $a/h_c = 30$ ,  $T_0 = 100$  K.

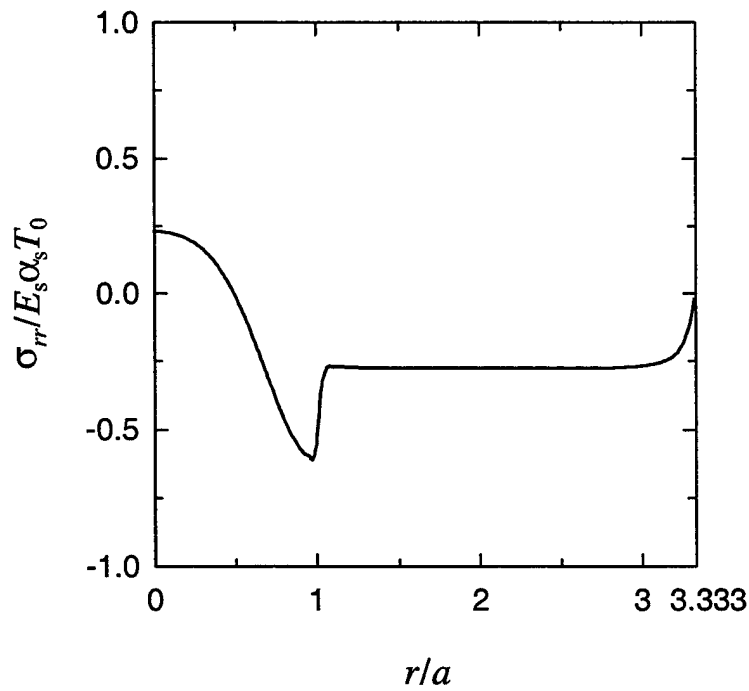


Figure 5.69 Variation of normalized  $\sigma_{rr}(r, z_0)$  along the surface of the FGM coating described in Figure 5.48,  $z_0/h_c = 26.42$ ,  $a/h_c = 30$ ,  $T_0 = 100$  K.

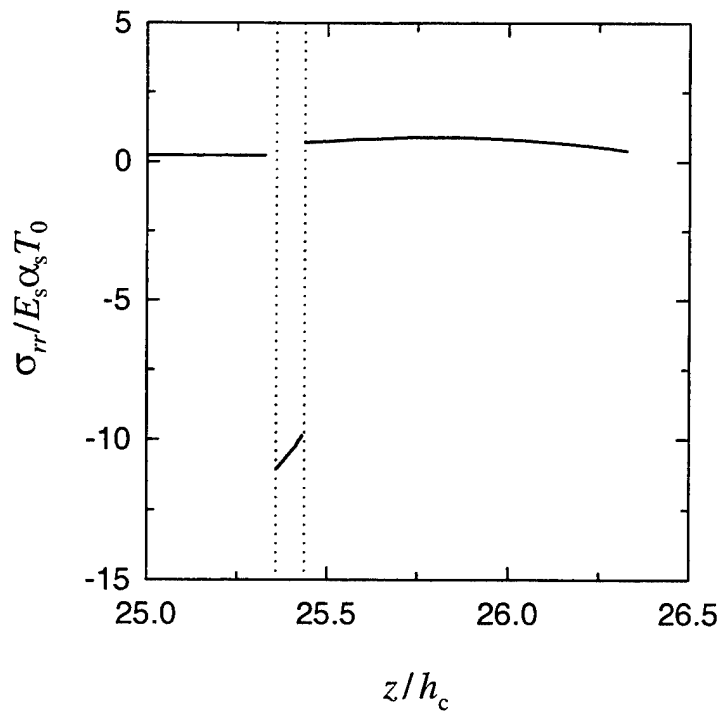


Figure 5.70 Variation of normalized  $\sigma_{rr}$  along  $r = 0$  in the FGM coating described in Figure 5.48,  $a/h_c = 30$ ,  $T_0 = 100$  K.

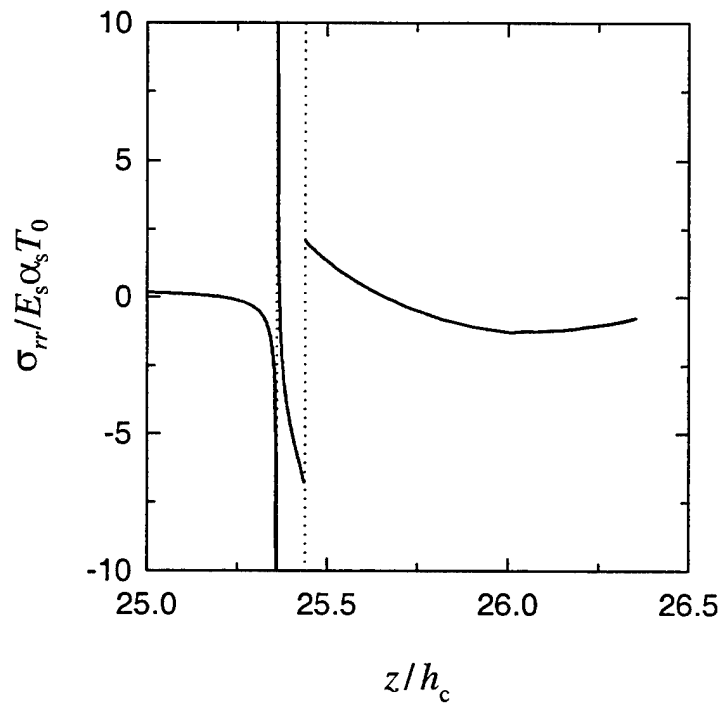


Figure 5.71 Variation of normalized  $\sigma_{rr}$  along  $r/a = 1$  in the FGM coating described in Figure 5.48,  $a/h_c = 30$ ,  $T_0 = 100$  K.

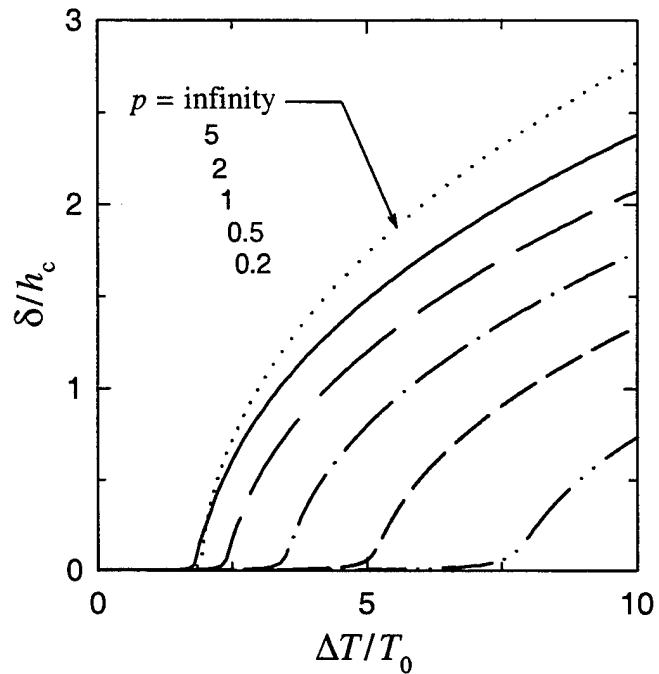


Figure 5.72 The influence of inhomogeneity parameter  $p$  on the crack opening displacement at the center of crack for FGM top coat with TGO under uniform temperature drop,  $T_0 = 100$  K,  $a/h_c = 30$ .

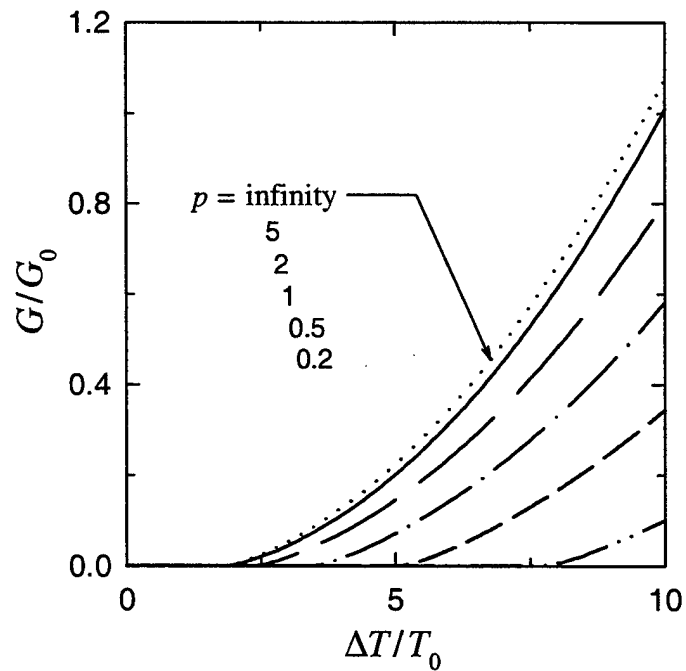


Figure 5.73 The influence of inhomogeneity parameter  $p$  on the strain energy release rate for FGM coating with TGO under uniform temperature drop,  $T_0 = 100$  K,  $a/h_c = 30$ .

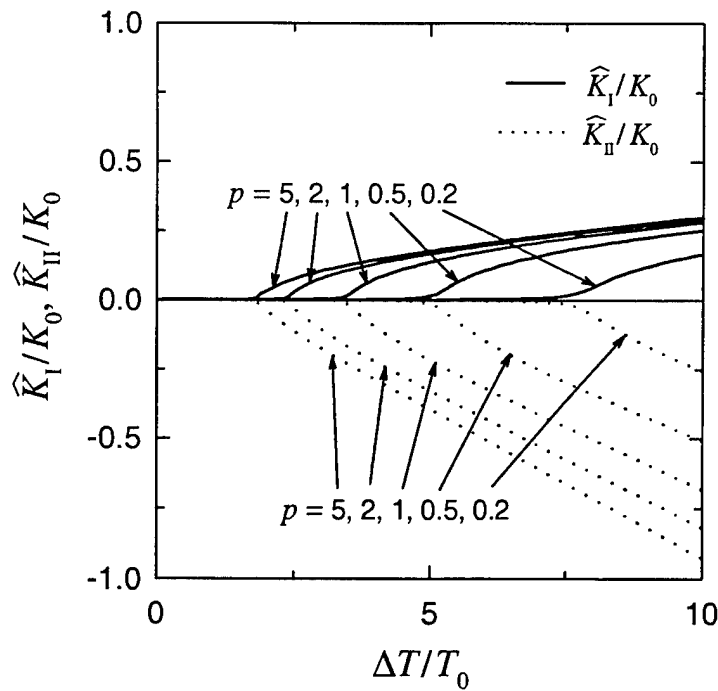


Figure 5.74 The influence of inhomogeneity parameter  $p$  on the stress intensity factors for the FGM coating with TGO under uniform temperature drop,  $T_0 = 100$  K,  $a/h_c = 30$ ,  $K_0 = E_s \alpha_s T_0 \sqrt{\pi h_c}$ ,  $G_0 = (1 - \nu_s) K_0^2 / E_s$ ,  $\hat{K}_I + i\hat{K}_{II} = (K_I + iK_{II})h_c^{ie}$ .

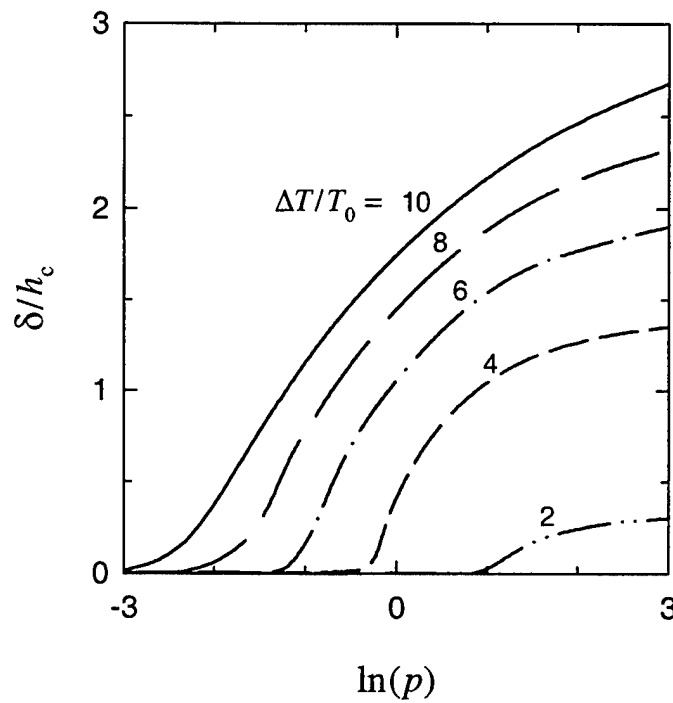


Figure 5.75 Crack opening displacement at the center of crack as a function of inhomogeneity parameter  $p$  for FGM top coat with TGO under uniform temperature drop,  $T_0 = 100$  K,  $a/h_c = 30$ .

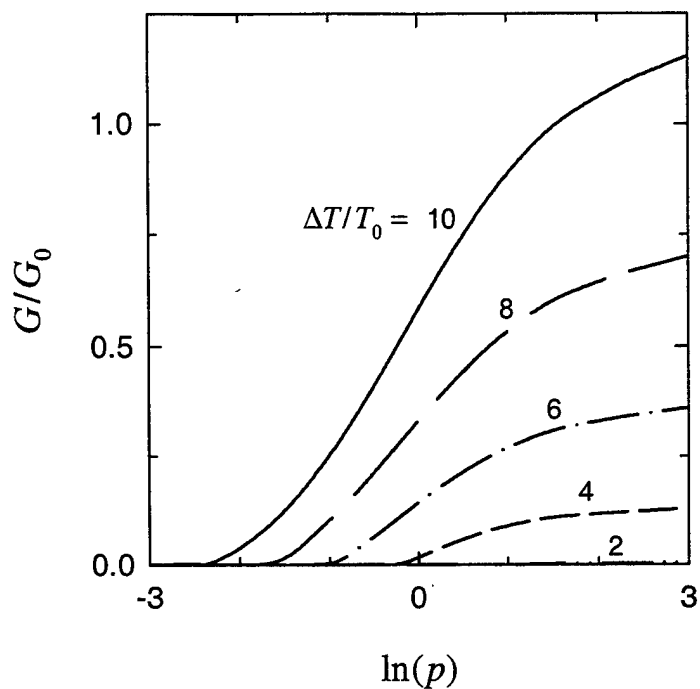


Figure 5.76 Strain energy release rate as a function of inhomogeneity parameter  $p$  for FGM top coat with TGO under uniform temperature drop,  $T_0 = 100$  K,  $a/h_c = 30$ .

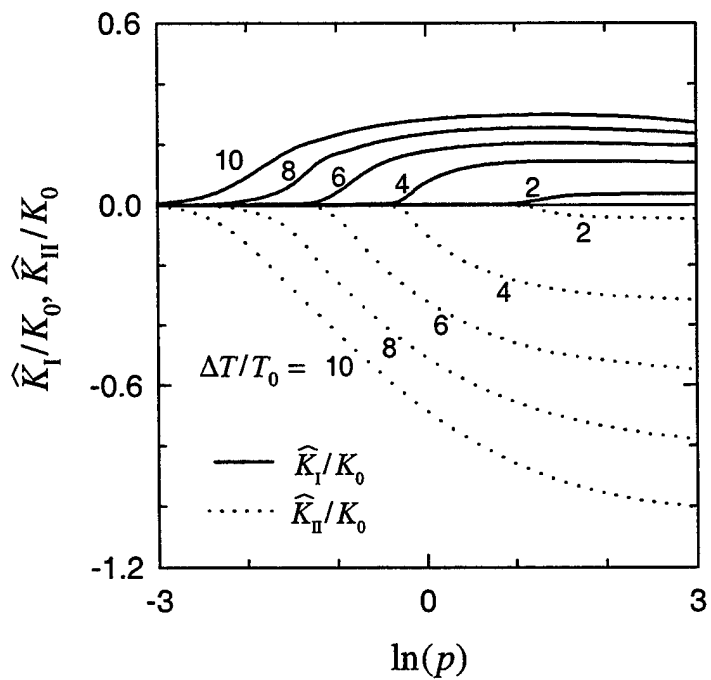


Figure 5.77 Stress intensity factors as functions of inhomogeneity parameter  $p$  for FGM coating with TGO under uniform temperature drop,  $T_0 = 100$  K,  $a/h_c = 30$ ,  $K_0 = E_s \alpha_s T_0 \sqrt{\pi h_c}$ ,  $G_0 = (1 - \nu_s) K_0^2 / E_s$ ,  $\hat{K}_I + i\hat{K}_{II} = (K_I + iK_{II})h_c^{ie}$ .

As discussed above and in Chapter 1, the oxidation process occurring at elevated temperature replaces the fabricated continuity with a distinct jump in material properties, introduces a weak interface, and therefore, accelerate the failure process of the TBC system. A more pragmatic approach to the design of TBC system for high temperature environment is to incorporate additional layers in the coating structure to satisfy the functionality required for more oxidation resistance. One example of such an approach would be to replace the original thermal insulation ceramics/metal grading by a multi-layered grading that consists of a thermal insulation ceramics/oxygen barrier ceramics FGM and an oxygen barrier ceramics/metal FGM. To study the blister and spallation problem for such TBC system, an axisymmetric specimen as shown in Figure 5.78 is considered. In this example,  $\text{Al}_2\text{O}_3$  is used as the oxygen barrier material and the same materials in previous example as described in Table 5.5 are used for the alternative TBC system. It is assumed that a thin layer of TGO would grow between the two FGM layers via the inward diffusion of oxygen through the PSZ/ $\text{Al}_2\text{O}_3$  FGM and the outward diffusion of cation toward the surface of the  $\text{Al}_2\text{O}_3$ /bond coat FGM. The dimensions of the specimen described in Figure 5.78 are given as:  $h_c = 130 \mu\text{m}$ ,  $h_g = 10 \mu\text{m}$ ,  $h_b = 50 \mu\text{m}$ ,  $h_s = 3 \text{ mm}$ ,  $2R = 25.4 \text{ mm}$ . A crack of radius  $a/h_c = 30$  is assumed to be along the TGO- $\text{Al}_2\text{O}_3$ /bond coat FGM interface. The temperature drop induced buckling problems are investigated for the "virgin" specimen (i.e.,  $h_t = 0$  in Figure 5.78) and the specimen under extended exposure to high temperature environment ( $h_t = 5 \mu\text{m}$ ). The thermomechanical properties of the PSZ/ $\text{Al}_2\text{O}_3$  and  $\text{Al}_2\text{O}_3$ /bond coat FGMs are defined as

$$\begin{aligned}
E(z) &= E_c + (E_t - E_c) \left( \frac{h_c + h_t + h_g + h_b + h_s - z}{h_c} \right)^4, \\
\nu(z) &= \nu_c + (\nu_t - \nu_c) \left( \frac{h_c + h_t + h_g + h_b + h_s - z}{h_c} \right)^4, \\
\alpha(z) &= \alpha_c + (\alpha_t - \alpha_c) \left( \frac{h_c + h_t + h_g + h_b + h_s - z}{h_c} \right)^4, \\
h_t + h_g + h_b + h_s &< z < h_c + h_t + h_g + h_b + h_s,
\end{aligned} \tag{5.9a}$$

and

$$\begin{aligned}
E(z) &= E_t + (E_b - E_t) \left( \frac{h_g + h_b + h_s - z}{h_g} \right)^{1/4}, \\
\nu(z) &= \nu_t + (\nu_b - \nu_t) \left( \frac{h_g + h_b + h_s - z}{h_g} \right)^{1/4}, \\
\alpha(z) &= \alpha_t + (\alpha_b - \alpha_t) \left( \frac{h_g + h_b + h_s - z}{h_g} \right)^{1/4}, \\
h_b + h_s &< z < h_g + h_b + h_s,
\end{aligned} \tag{5.9b}$$

respectively. In Equations (5.9a) and (5.9b)  $(E_c, \nu_c, \alpha_c)$ ,  $(E_t, \nu_t, \alpha_t)$  and  $(E_b, \nu_b, \alpha_b)$  are the thermomechanical properties of PSZ,  $\text{Al}_2\text{O}_3$ , and the metallic bond coat, respectively, and are given in Table 5.5. Note that the power 4 in (5.9a) is used for a PSZ-rich top coat; and the power 1/4 in (5.9b) indicates a metal-rich FGM. The results are given in Figures 5.79-5.81. For the purpose of comparison, Figures 5.79-5.81 also plot the results for a 4-layered material system with ceramics/metal FGM top coat described in Figure 5.48 with dimensions given as:  $h_c = 130 \mu\text{m}$ ,  $h_t = 5 \mu\text{m}$ ,  $h_b = 50 \mu\text{m}$ ,  $h_s = 3 \text{ mm}$ ,  $2R = 25.4 \text{ mm}$ ,  $a/h_c = 30$ . The material inhomogeneity for the FGM top coat in the 4-layered system is defined in (5.6) with that  $p_1 = p_2 = p_3 = p = 4$ . It may be seen from these results that the crack opening at  $z = 0$  and the strain energy release rate are much higher for the TBC

system with two graded layers than the original one with only FGM top coat. This is due to higher degree of mismatch in the coefficient of thermal expansion caused by higher content of aluminum oxide. Therefore, from the viewpoint of crack driving forces, one may expect that the multiple layered TBC system containing  $\text{Al}_2\text{O}_3$  would not provide better protection against coating blister and spallation. However, such coating system possesses other advantages against coating fracture. One such advantage is that the multi-layer arrangement eliminates the unfavorable material property discontinuity and consequently, removes the stress concentration and reduce the possibility of crack initiation at the locations where the interface intersects the free end [6]. Also because of the higher density of the fabricated  $\text{Al}_2\text{O}_3$  oxygen barrier than that of thermally grown oxide, it provides better insulation against oxygen diffusion. This, in turn, reduces the growth speed of TGO and retards the weakening process of the "interface" (initiation and growth of microcracks) and, as a result, prolongs the service life of the coating [19]. It is then important to consider from both the viewpoints of increasing the material toughness and reducing the fracture driving forces when evaluating a coating system such as the TBC system with multiple graded layers described above.

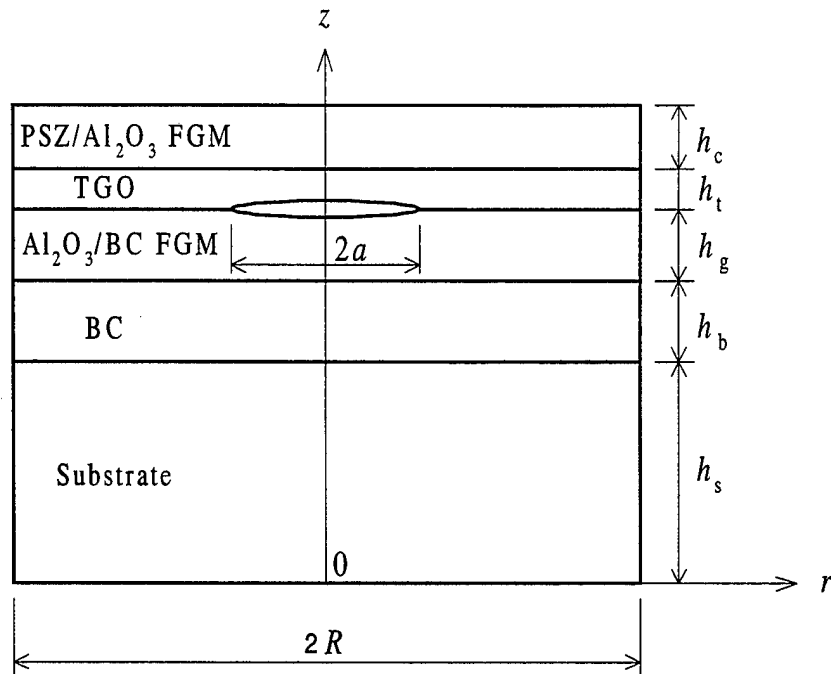


Figure 5.78 Specimen configuration for the TBC with multiple graded layers under thermal buckling.

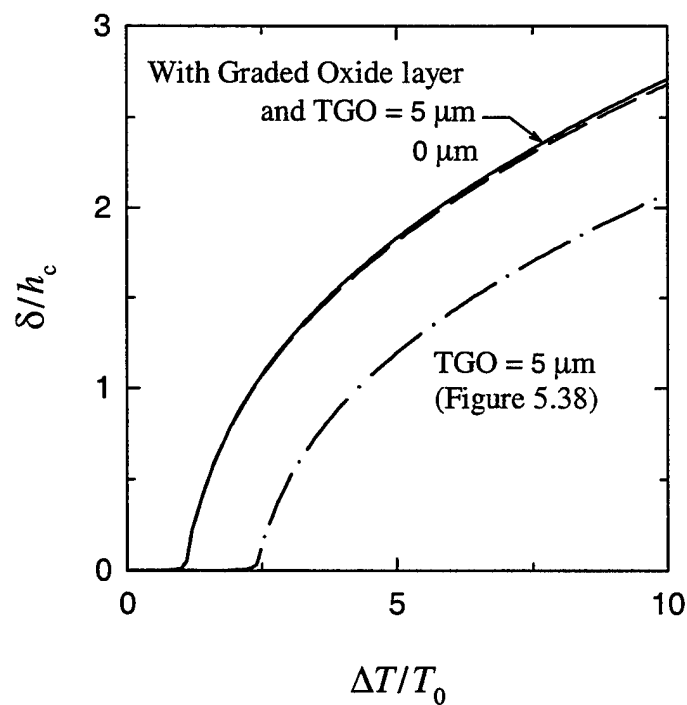


Figure 5.79 Comparison of the crack opening displacement at the center of crack for the TBC systems described in Figures 5.48 and 5.78 under uniform temperature drop,  $T_0 = 100$  K.

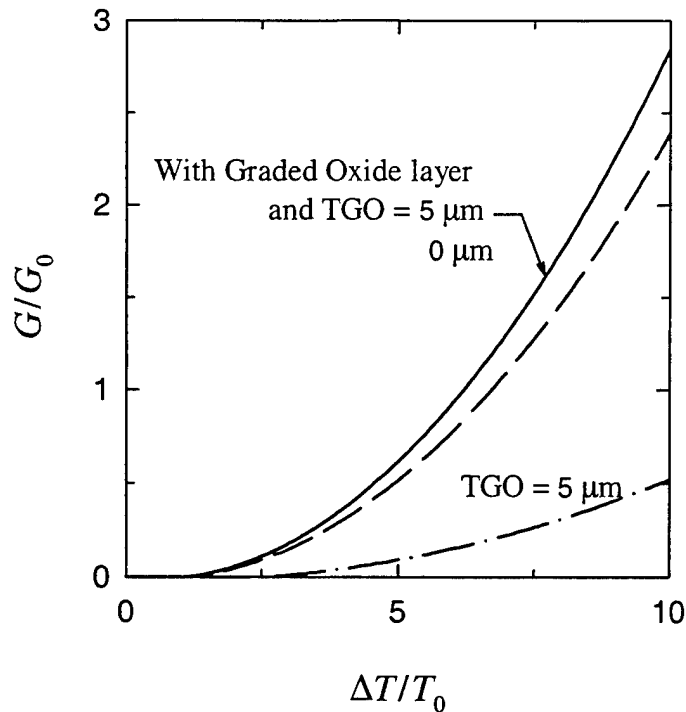


Figure 5.80 Comparison of the strain energy release rates for the TBC systems described in Figures 5.48 and 5.78 under uniform temperature drop,  $T_0 = 100$  K.

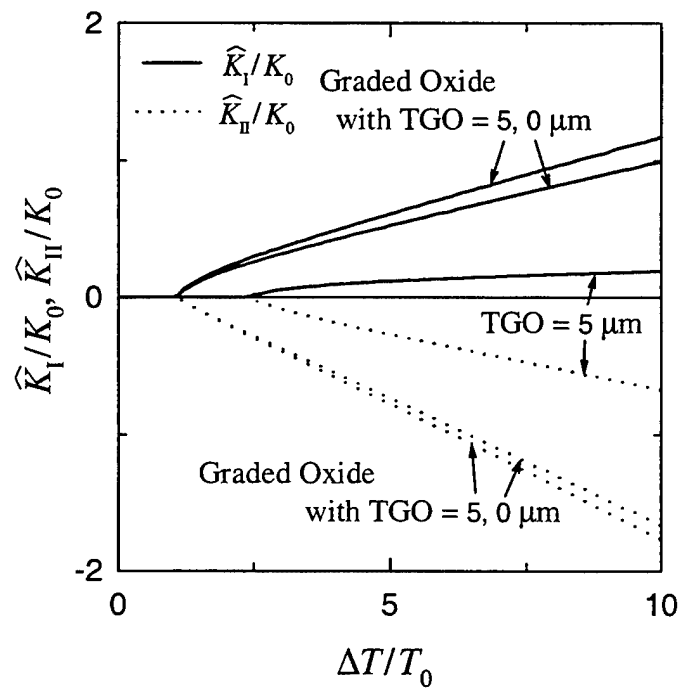


Figure 5.81 Comparison of the stress intensity factors for the TBC systems described in Figures 5.48 and 5.78 under uniform temperature drop,  $T_0 = 100$  K,  $K_0 = E_s \alpha_s T_0 \sqrt{\pi h_c}$ ,  $G_0 = (1 - \nu_s) K_0^2 / E_s$ ,  $\hat{K}_I + i\hat{K}_{II} = (K_I + iK_{II})h_c^{ie}$ .

## 5.4 The Influence of Initial Curvature

Thermal barrier coatings are often used to protect structural components such as turbine blades in high performance engines and wing-tips for aerospace plane from high temperature environment. In these applications usually the coatings are applied to surfaces with curvature rather than flat. In this section we examine the effect of the initial curvature of the specimen on the blister of interface crack by considering a simplified model using the geometrically nonlinear finite element method. As an example, the plane strain problem of a ceramic-rich FGM coating bonded to a cylindrical metallic substrate containing an interface crack as shown in Figure 5.82 is considered. Thickness of the coating and substrate and the crack length are given as:  $h_c = 130 \mu\text{m}$ ,  $h_s = 3.05 \text{ mm}$ , and  $2a = 5.2 \text{ mm}$  ( $a/h_c = 20$ ), respectively. The thermomechanical properties of the ceramic-rich FGM are defined as follows:

$$\begin{aligned} E(z) &= E_c + (E_m - E_c) \left( \frac{h_c + R - r}{h_c} \right)^4, \\ \nu(z) &= \nu_c + (\nu_m - \nu_c) \left( \frac{h_c + R - r}{h_c} \right)^4, \quad R < r < h_c + R, \\ \alpha(z) &= \alpha_c + (\alpha_m - \alpha_c) \left( \frac{h_c + R - r}{h_c} \right)^4, \end{aligned} \quad (5.10)$$

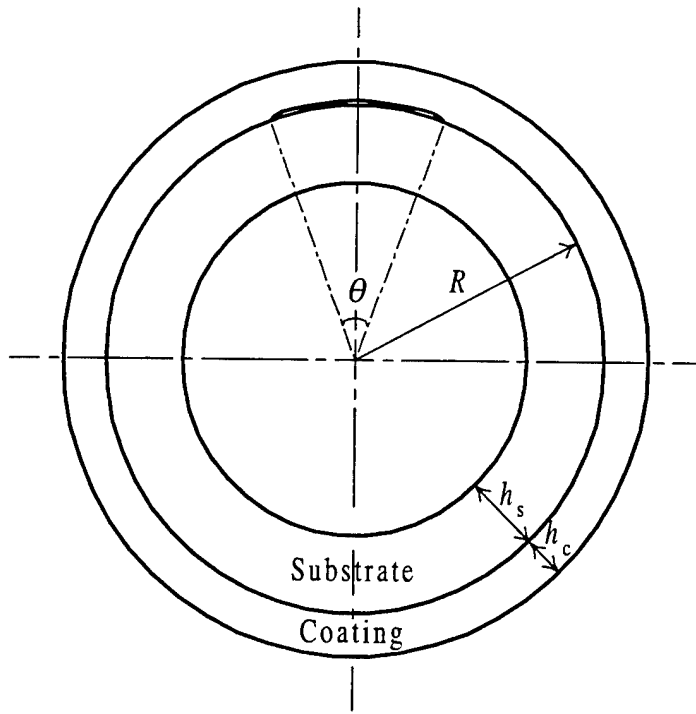
where the subscript c and m denote the ceramics and metal, respectively, and the material properties of the metal and ceramics are given in Table 5.6. The influence of curvature is studied by varying the radius of curvature of the cylindrical specimen. By taking advantage of the symmetry, only the right half of the cylinder is modeled. Since the purpose of the study is to examine the effect of the curvature, for simplicity, the bond coat and the oxide layers are not included in the analysis.

Table 5.6 Material properties of the cylindrical specimen described in Figure 5.82.

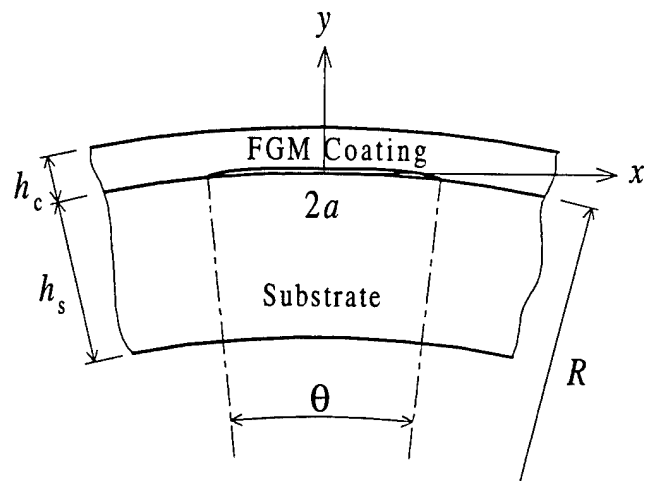
	Material	$E$ (GPa)	$\nu$	$\alpha (10^{-6} \text{ }^{\circ}\text{C}^{-1})$
Metal (Substrate)	Ni-based Superalloy	151.4	0.26	15.38
Ceramics	$\text{ZrO}_2$ -8wt% $\text{Y}_2\text{O}_3$ (PSZ)	11.54	0.25	10.91

Figures 5.83-5.85 show the results for the specimen described in Figure 5.82 under uniform temperature drop. The constants used for normalization in these figures are  $T_0 = 100 \text{ K}$ ,  $K_0 = E_s \alpha_s T_0 \sqrt{\pi h_c}$ ,  $G_0 = (1 - \nu_s^2) K_0^2 / E_s$ . It is assumed that the cylinder is stress-free before the temperature change. The crack opening at  $x = 0$  is shown in Figure 5.83 in which the case of  $R = \text{infinity}$  is approximated by a finite specimen as shown in Figure 5.21 with  $l/a = 20$ . It may be seen from Figure 5.83 that, for the cases of finite radius of curvature  $R$ , instead of remaining closed until certain critical temperature change, the crack opens as soon as temperature starts to drop. Figure 5.83 also shows the results based on small deformation (linear) theory. As expected, the results for the linear model are simply straight lines in the plot of crack opening vs. temperature drop. By comparing the results based on linear theory with the one based on nonlinear theory, one may see that the results are similar for small radius of curvature; and that for large values of  $R$  the linear model predicts only the portion corresponding to initial temperature drop. The same observation can be made from Figure 5.84 in which the strain energy release rate is given as a function of temperature drop. It may also be seen that the results for the case of  $R = 2000$  shown in Figures 5.83 and 5.84 behave basically the same way as the imperfection problems in buckling analysis. From this example we may conclude that for the problem of crack at a curved interface under in-plane compressive loading, the deformation is governed by nonlinear kinematic relationship when the curvature of the interface is very small; and that as the curvature increases (or  $R$  decreases), the deformation changes gradually from the one associated with buckling mechanism to the one governed by linear kinematic relationship.

Figure 5.85 shows the stress intensity factors as a function of temperature drop for several radii of curvature. It may be seen from this figure that the negative mode II stress intensity factor  $K_{II}$  is the predominant stress intensity factor and increases (in magnitude) as the radius of curvature  $R$  decreases. Also observed in Figure 5.85 is that the mode I stress intensity factor decreases as  $R$  decreases. Furthermore, as the value of  $R$  drops below one hundred (results not shown here),  $K_I$  becomes negative and the crack surface contact near the crack tips is observed as soon as the temperature drops. To further examine the crack problems with such  $R$  values, a finite element procedure with contact algorithm is required. The crack problems with surface contact, however, will not be discussed in this study.



(a) The cross-section of the cylinder with an interface crack



(b) Enlarged crack region

Figure 5.82 Configuration of the cylindrical specimen for the temperature loading problem, (a) the cross-section of the cylinder, (b) enlarged crack region,  $2a = R\theta$ .

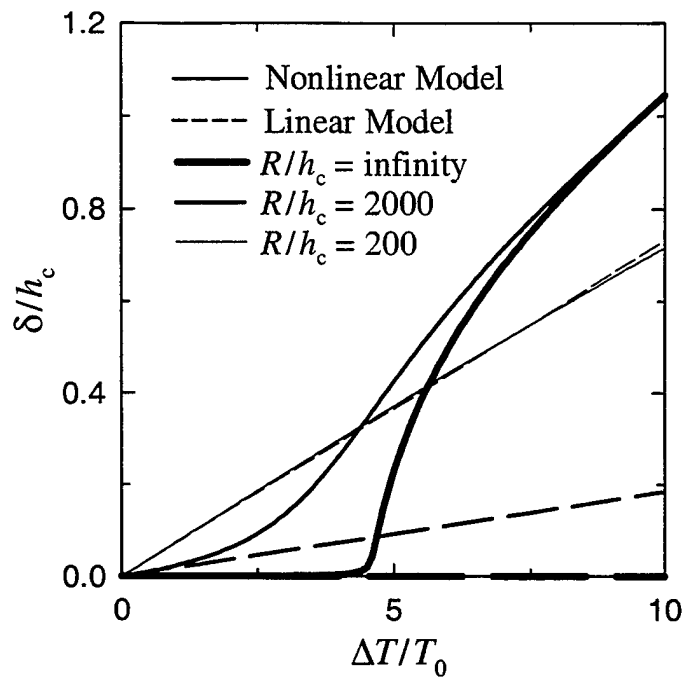


Figure 5.83 Crack opening displacement at the center of crack for FGM coating under uniform temperature drop,  $T_0 = 100$  K.

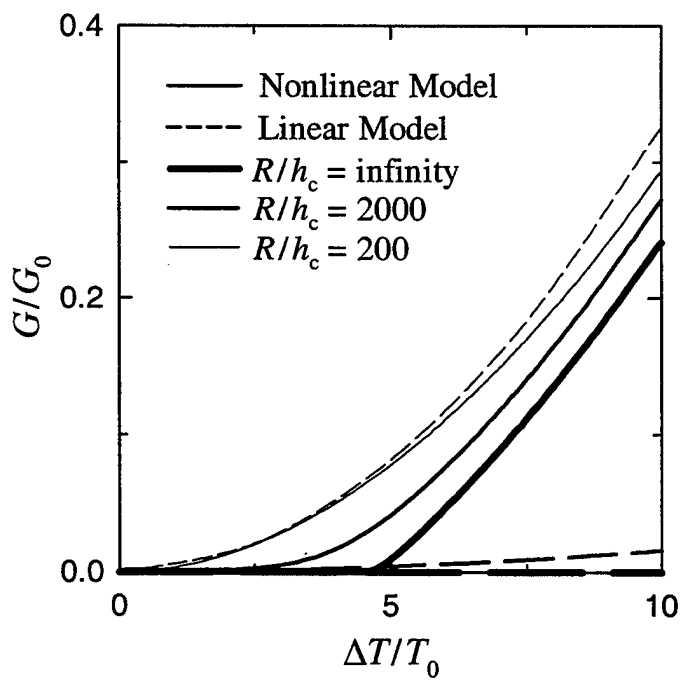


Figure 5.84 Strain energy release rate as a function of temperature drop for FGM coating,  $T_0 = 100$  K.

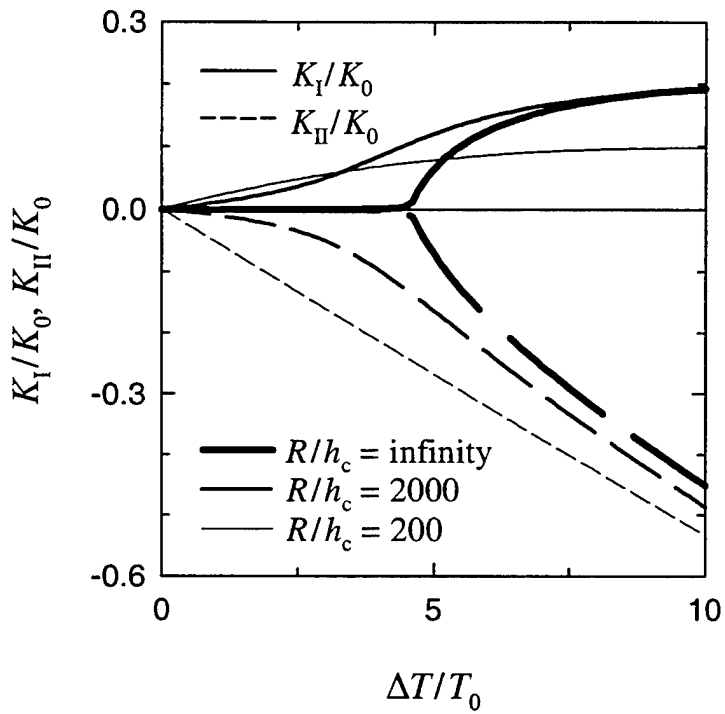


Figure 5.85 Stress intensity factors for FGM coating as a function of temperature drop,  $T_0 = 100$  K.

## Chapter 6

### Conclusions and Future Work

#### 6.1 Conclusions

In this study, the interface crack problem of TBC systems with functionally graded coatings under thermal or mechanical compressive stress is examined. The failure mode is characterized by the buckling instability induced coating blister which provides the driving force for the interface crack to extend and lead to the spallation of the coating. The instability problem for a FGM coating subjected to a far-field fixed-grip compression is investigated first by reducing the nonlinear governing equation to a linear eigenvalue problem using a perturbation method. The problem is solved under the mixed-boundary conditions by using the integral transformation technique. The analytical solution is then used to investigate the influence of coating inhomogeneity upon the instability load for the coating with either an interface crack or a highly weakened interface region and serves as a benchmark for the subsequent numerical study.

The postbuckling problem is examined by using a geometrical nonlinear finite element method with enriched crack-tip elements for extracting the postbuckling fracture mechanics parameters such as strain energy release rate and stress intensity factors. The finite element procedure is used to investigate both plane strain and axisymmetric problems with various layered structure subjected to in-plane residual compression induced by uniform temperature drop. Solutions based on plate theory are also given to compare with the results based on the continuum theory.

From the results obtained in this work, we may summarize the conclusions as follows:

- (1). For a FGM coating under in-plane fixed-grip compression as described in Figure 2.1, the instability strain is the highest when the coating has approximately the same modulus

as the substrate, and the value of the instability strain decreases for the case of stiffening ( $\gamma h > 0$ ) as well as softening ( $\gamma h < 0$ ) FGM coatings.

(2). The instability strain for the graded coating with weakened interface zone is higher than that for the coating with a fully separated crack of the same size. The increase in instability strain is more significant for higher weakened interface length/coating thickness ratio. It is also observed that due to a relatively lower bending stiffness but the same bridging spring constant, the FGM coating with negative  $\gamma h$  requires much higher compressive strain to induce instability compared with that for the coating with positive  $\gamma h$ .

(3). From the postbuckling analysis it is observed that the mode II stress intensity factor is negative and is the dominant stress intensity factor for the interface crack problem under in-plane thermal or mechanical compressive loads. From the viewpoint of crack driving forces, this means that the interface crack tends to kink into the coating rather than substrate and could result in the spallation of the coating. However, initiation of the crack growth requires that the crack driving force exceeds the mode mixity-dependent fracture toughness around the crack tip. Therefore, it is possible that the crack will extend along the rather weak (in toughness) interface until it reaches the free edge or until the mode II driving force is strong enough to cause the crack kinking.

(4). Compared with solutions based on continuum theory, the plate theory based analysis overestimates the instability strain and underestimates the strain energy release rate due to the boundary conditions with higher constraints. One may conclude that the plate approximation gives nonconservative results. The difference between results from the plate and continuum models lessens as the crack length/coating thickness ratio increases. Nevertheless, as observed in one of the examples, the postbuckling solution obtained by using plate model is limited to the first buckling mode, while under the continuum mechanics approach higher buckling modes are permitted.

(5). Because of the better match in the thermomechanical properties in the FGM coating/metallic bond coat/substrate system compared with that for homogeneous ceramic coating/bond coat/substrate system, in the FGM coating the in-plane thermal residual compressive stresses is lower. Also the FGM coating possesses higher bending stiffness than pure ceramic coating. As a result the FGM coatings have certain advantages over homogeneous coatings from the viewpoint of crack driving force.

(6). Higher metal content in the FGM coating further improves the thermomechanical property match and increases the bending stiffness of the coating and consequently, further reduces the crack driving force. Nevertheless, higher metal content compromises the thermal insulation function of the coating. Therefore, the optimal design of the FGM coating would be to design the composition such that the coating provides the best fracture resistance while it satisfies the thermal insulation requirement.

(7). The TGO layer, with it's low coefficient of thermal expansion, is considered as the unfavorable composition in the TBC system because it increases the level of residual stresses and introduces a distinctive interface to the originally tailored FGM coating system. Besides, the oxide layer often served as the weak cleavage plane for the crack to initiate and grow.

(8). The problem of compression induced interface crack growth for FGM coatings on non-flat structural components is investigated. It is observed that for the case of small curvature the deformation of the coating is governed by the imperfection-buckling like mechanism and requires nonlinear analysis. On the other hand, for higher substrate curvature the problem may be characterized by linear small deformation theory.

## **6.2 Remarks on Future Work**

The spallation of TBCs is basically a thermal-chemical-mechanical process. While the compression induced coating blister that leads to spallation has been investigated in this

work, there are still several ambiguous points in the whole picture of the spallation failure of the coating that need to be investigated. The first one would be, as briefly discussed in Chapter 1, the growth of TGO at the bond coat/top coat interface and its influence on the initiation of cracks along the interface and on the weakening of the fracture toughness of the interface. It has been observed that the spallation of the coating is strongly linked to the growth of oxide. The growth of TGO would result in the change of stress state near the oxide layer due to the volume change associated with the chemical reaction. Also the growth of TGO may introduce interface asperities at which cracks would initiate under local tensile stresses. Besides, the change in the constituents and microstructures of the TGO seems to have strong influence on the weakening of the fracture toughness of the bond coat/top coat interface. Therefore, the following problems are to be considered: (i) a model for the growth process of TGO and the associated residual stresses, (ii) a stress analysis and the associated crack problem for the interface asperities considering the effect of oxide growth, and (iii) a quantitative assessment of the interface fracture toughness as a function of oxide growth.

One important problem to be investigated is to examine the influence of crack surface contact. It is observed that when the in-plane compressive load reaches a certain level in the postbuckling regime, crack surface contact occurs in front of the crack tip. It is also possible that the coating might deform into higher buckling mode which may cause crack surface contact. To correctly interpret the postbuckling results it is necessary to implement the contact algorithm and a special enriched crack-tip element which contains the correct asymptotic displacement fields considering crack surface contact. The crack surface contact also plays an important role in the more realistic three-dimensional coating blister problem, which can be an extension of this work. As observed in the delamination problem of composite laminates, a circular blister would gradually transform first to an elliptical shape and further into more complicated configurations [55,56,62] as the in-plane

compressive load increases. This feature, which cannot be detected by using a two-dimensional or axisymmetric analysis, is due to the crack surface contact near the crack front. Therefore, the contact algorithm and special enriched elements are required in the three-dimensional analysis to obtain the correct results.

In this work we assume that the material behaves linearly elastically during the cool down period and that initially at high temperature the residual stresses are relaxed for the fracture characterization. In reality, because of the complexities in environmental and loading conditions during the processing and service of the TBC system, it is expected that the nonlinear material behavior would play an important role in the stress analysis and fracture characterization. In this work, as a first step, the fracture mode characterization provided an insight into the crack problem through the associated parametric study under the elastic assumption. However, to further examine the more realistic problems it is required to take into account nonlinear material properties. Those to be considered include the creep behavior of the materials during the period subjected to sustained exposure to high temperature, the sintering of ceramic top coat and the accompanying material property change, and the plastic deformation at the highly strained locations.

Another problem to be considered as an extension of this work is to take into account the heat transfer in the thermal stress and crack problem. During the service stage, the temperature gradient and local hot spots in the material system are observed due to the heating and cooling boundary conditions and the local thermal insulation associated with cracks. The thermal stresses associated with the multidimensional temperature profile might be the driving force for the growth of interface crack. Also the non-uniform temperature change in the medium during the cool down process would result in different thermal residual stress profile than that for uniform temperature change. It is then important to consider the heat transfer in order to more accurately quantify the fracture driving forces.

## References

1. Yamanouchi, M., Koizumi, M., Hirai, T., and Shiota, I., Eds., 1990, *FGM '90*, Proceedings of the 1st International Symposium on Functionally Gradient Materials, FGM Forum, Tokyo, Japan.
2. Holt, J. B., Koizumi, M., Hirai, T., and Munir, Z. A., Eds., 1993, *Ceramic Transactions - Functionally Gradient Materials*, Vol. 34, American Ceramic Society, Westerville, Ohio.
3. Ilschner, B., and Cherradi, N., Eds., 1995, Proceedings of the 3rd International Symposium on Structural and Functionally Gradient Materials, Presses Polytechniques et Universitaires Romandes, Lausanne, Switzerland.
4. Shiota, I., and Miyamoto, Y., Eds., 1997, *FGM '96*, Proceedings of the 4th International Symposium on Functionally Graded Materials, Elsevier, Amsterdam.
5. Kaysser, W. A., Ed., 1999, *Materials Science Forum - Functionally Graded Materials*, Vol. 308-311, Trans Tech Publications.
6. Lee, Y.-D., and Erdogan, F., 1995, "Residual/thermal stresses in FGM and laminated thermal barrier coatings," *International Journal of Fracture*, Vol. 69, pp. 145-165.
7. Kurihara, K., Sasaki, K., and Kawarada, M., 1990, "Adhesion improvement of diamond films," *FGM '90*, Proceedings of the 1st International Symposium on Functionally Gradient Materials, Yamanouchi, M., Koizumi, M., Hirai, T., and Shiota, I., Eds., FGM Forum, Tokyo, Japan, pp. 65-69.
8. Hirano, T., Teraki, J., and Yamada, T., 1990, "On the design of functionally gradient materials," *FGM '90*, Proceedings of the 1st International Symposium on Functionally Gradient Materials, Yamanouchi, M., Koizumi, M., Hirai, T., and Shiota, I., Eds., FGM Forum, Tokyo, Japan, pp. 5-10.

9. Hirai, T., and Sasaki, M., 1991, "Vapor-deposited functionally gradient materials," JSME International Journal, Series I, Vol. 34, No. 2, pp. 123-129.
10. Fukui, Y., 1991, "Fundamental investigation of functionally gradient material manufacturing system using centrifugal force," JSME International Journal, Series III, Vol. 34, No. 1, pp. 144-148.
11. Miyamoto, Y., 1990, "New ceramic processing approaches using combustion synthesis under gas pressure," The American Ceramics Society Bulletin, Vol. 69, No. 4, pp. 686-690.
12. Erdogan, F., and Chiu, T.-C., 1999, "On the spallation of FGM coatings," *Materials Science Forum - Functionally Graded Materials*, Kaysser, W. A., Ed., Vols. 308-311, pp. 917-922.
13. Evans, A. G., Crumley, G. B., and Demaray, R. E., 1983, "On the mechanical behavior of brittle coatings and layers," Oxidation of Metals, Vol. 20, No. 5/6, pp. 193-216.
14. Evans, A. G., He, M. Y., and Hutchinson, J. W., 1997, "Effect of interface undulations on the thermal fatigue of thin films and scales on metal substrates," Acta Materialia, Vol. 45, No. 9, pp. 3543-3554.
15. Gell, M., Vaidyanathan, K., Barber, B., Cheng, J., and Jordan, E., 1999, "Mechanism of spallation in platinum aluminide/electron beam physical vapor-deposited thermal barrier coatings," Metallurgical and Materials Transactions A, Vol. 30A, pp. 427-435.
16. Hsueh, C. H., and Evans, A. G., 1983, "Oxidation induced stresses and some effects on the behavior of oxide films," Journal of Applied Physics, Vol. 54, No. 11, pp. 6672-6686.
17. Stecura, S., 1989, "Two-layer thermal barrier coatings I: effects of composition and temperature on oxidation behavior and failure," Thin Solid Films, Vol. 182, pp. 121-139.

18. Lih, W., Chang, E., Chao, C. H., and Tsai, M. L., 1992, "Effect of pre-aluminization on the properties of  $ZrO_2$ -8wt.%  $Y_2O_3$ /Co-29Cr-6Al-1Y thermal-barrier coatings," *Oxidation of Metals*, Vol. 38, No. 1/2, pp. 99-124.
19. Sun, J. H., Chang, E., Chao, C. H., and Cheng, M. J., 1993, "The spalling and degradation mechanism of  $ZrO_2$ -8wt.%  $Y_2O_3$ /CVD- $Al_2O_3$ /Ni-22Cr-10Al-1Y thermal-barrier coatings," *Oxidation of Metals*, Vol. 40, No. 5/6, pp. 465-481.
20. Wu, B.-C., Chang, E., Chang, S.-F., and Tu, D., 1989, "Degradation mechanisms of  $ZrO_2$ -8wt.%  $Y_2O_3$ /Ni-22Cr-10Al-1Y thermal barrier coatings," *Journal of the American Ceramic Society*, Vol. 72, No. 2, pp. 212-218.
21. Brandl, W., Grabke, H. J., Toma, D., and Krüger, J., 1996, "The oxidation behaviour of sprayed MCrAlY coatings," *Surface and Coating Technology*, Vol. 86-87, pp. 41-47.
22. Leyens, C., Fritscher, K., Peters, M., and Kaysser, W. A., 1997, "Transformation and oxidation of a sputtered low-expansion Ni-Cr-Al-Ti-Si bond coating for thermal barrier systems," *Surface and Coating Technology*, Vol. 94-95, pp. 155-160.
23. Brindley, W. J., and Miller, R. A., 1990, "Thermal barrier coating life and isothermal oxidation of low-pressure plasma-sprayed bond coat alloys," *Surface and Coatings Technology*, Vol. 43/44, pp. 446-457.
24. Reed, D. J., and Wuensch, B. J., 1980, "Ion-probe measurement of oxygen self-diffusion in single-crystal  $Al_2O_3$ ," *Journal of the American Ceramic Society*, Vol. 63, No. 1/2, pp. 88-92.
25. Schütze, M., 1997, *Protective Oxide Scales and Their Breakdown*, John Wiley & Sons, New York.
26. Nusier, S. Q., and Newaz, G., 1998, "Crack initiation in thermal barrier coatings due to interface asperity," *Proceedings of the 8th Japan-US Conference on Composite Materials*, Newaz, G. M., and Gibson, R. F., Eds., pp. 417-426.

27. Lee, W. Y., Stinton, D. P., Berndt, C. C., Erdogan, F., Lee, Y.-D., and Mutasim, Z., 1996, "Concept of functionally graded materials for advanced thermal barrier coating applications," *Journal of the American Ceramic Society*, Vol. 79, No. 12, pp. 3003-3012.

28. Kachanov, L. M., 1976, "Separation failure of composite materials," *Polymer Mechanics*, Vol. 12, pp. 812-815.

29. Chai, H., Babcock, C. D., and Knauss, W. G., 1981, "One dimensional modeling of failure in laminated plates by delamination buckling," *International Journal of Solids and Structures*, Vol. 17, pp. 1069-1083.

30. Chai, H., Knauss, W. G., and Babcock, C. D., 1983, "Observation of damage growth in compressively loaded laminates," *Experimental Mechanics*, Vol. 23, pp. 329-337.

31. Bottega, W. J., and Maewal, A., 1983, "Delamination buckling and growth in laminates," *Journal of Applied Mechanics*, Vol. 50, pp. 184-189.

32. Evans, A. G., and Hutchinson, J. W., 1984, "On the mechanics of delamination and spalling in compressed films," *International Journal of Solids and Structures*, Vol. 20, pp. 455-466.

33. Yin, W.-L., and Wang, J. T. S., 1984, "The energy-release rate in the growth of a one-dimensional delamination," *Journal of Applied Mechanics*, Vol. 51, pp. 939-941.

34. Shivakumar, K. N., and Whitcomb, J. D., 1985, "Buckling of a sublamine in a quasi-isotropic composite laminate," *Journal of Composite Materials*, Vol. 19, pp. 2-18.

35. Chai, H., and Babcock, C. D., 1985, "Two-dimensional modeling of compressive failure in delaminated laminates," *Journal of Composite Materials*, Vol. 19, pp. 67-98.

36. Yin, W.-L., 1988, "The effect of laminated structure on delamination buckling and growth," *Journal of Composite Materials*, Vol. 22, pp. 502-517.

37. Peck, S. O., and Springer, G. S., 1991, "The behavior of delaminations in composite plates-analytical and experimental results," *Journal of Composite Materials*, Vol. 25, pp. 907-929.
38. Kutlu, Z., and Chang, F.-K., 1992, "Modeling compression failure of laminated composites containing multiple through-the-width delaminations," *Journal of Composite Materials*, Vol. 26, pp. 350-387.
39. Garg, A. C., 1988, "Delamination - a damage mode in composite structures," *Engineering Fracture Mechanics*, Vol. 29, No. 5, pp. 557-584.
40. Abate, S., 1991, "Impact on laminated composite materials," *Applied Mechanics Reviews*, Vol. 44, No. 4, pp. 155-190.
41. Hutchinson, J. W., and Suo, Z., 1992, "Mixed mode cracking in layered materials," *Advances in Applied Mechanics*, Hutchinson, J. W., and Wu, T. Y., Eds., Vol. 29, pp. 63-191, Academic Press, New York.
42. Keer, L. M., Nemat-Nasser, S., and Oranratnachai, A., 1982, "Surface instability and splitting in compressed brittle elastic solids containing crack arrays," *Journal of Applied Mechanics*, Vol. 49, pp. 761-767.
43. Wang, W.-X., Shen, W., Takao, Y., Shen, Z., and Chen, P.-H., 1991, "An analysis of compressive stability of elastic solids containing a crack parallel to the surface," *Engineering Fracture Mechanics*, Vol. 40, pp. 1023-1033.
44. Wang, W.-X., and Takao, Y., 1995, "Load buckling of a layer bonded to a half-space with an interface crack," *Journal of Applied Mechanics*, Vol. 62, pp. 64-70.
45. Madenci, E., and Westmann, R. A., 1991, "Local delamination buckling in layered systems," *Journal of Applied Mechanics*, Vol. 58, pp. 157-165.
46. Madenci, E., 1991, "Delamination growth and buckling in an orthotropic strip," *International Journal of Solids and Structures*, Vol. 27, No. 14, pp. 1773-1788.

47. Madenci, E., 1991, "Slightly open, penny-shaped crack in an infinite solid under biaxial compression," *Theoretical and Applied Fracture Mechanics*, Vol. 16, pp. 215-222.
48. Madenci, E., and Westmann, R. A., 1993, "Local delamination growth in layered systems under compressive load," *Journal of Applied Mechanics*, Vol. 60, pp. 895-902.
49. Madenci, E., Balkan, H., and Quan, M., 1995, "Biaxial compression of a thin layer with circular debonding over a substrate," *International Journal of Solids and Structures*, Vol. 32, No. 23, pp. 3465-3477.
50. Balkan, H., and Madenci, E., 1998, "Thermal loading of a thin layer with circular debonding over a substrate," *International Journal of Fracture*, Vol. 91 No. 3, pp. 217-231.
51. Nilsson, K.-F., and Giannakopoulos, A. E., 1990, "Finite element simulation of delamination growth," 1st International Conference on Computer Aided Assessment and Control of Localized Damage, Aliabadi, M. H., Brebbia, C. A., and Cartwright, D. J., Eds., Springer Verlag, Portsmouth, UK, Vol. 2, pp. 299-313.
52. Storåkers, B., and Andersson, B., 1988, "Nonlinear plate theory applied to delamination in composites," *Journal of the Mechanics and Physics of Solids*, Vol. 36, No. 6, pp. 689-718.
53. Nilsson, K.-F., and Storåkers, B., 1992, "On interface crack growth in composite plates," *Journal of Applied Mechanics*, Vol. 59, pp. 530-538.
54. Nilsson, K.-F., Thesken, J. C., Sindelar, P., Giannakopoulos, A. E., and Storåkers, B., 1993, "A theoretical and experimental investigation of buckling induced delamination growth," *Journal of the Mechanics and Physics of Solids*, Vol. 41, No. 4, pp. 749-782.
55. Nilsson, K.-F., and Giannakopoulos, A. E., 1995, "A finite element analysis of configurational stability and finite growth of buckling driven delamination," *Journal of the Mechanics and Physics of Solids*, Vol. 43, No. 12, pp. 1983-2021.

56. Giannakopoulos, A. E., Nilsson, K.-F., and Tsamasphyros, G., 1995, "The contact problem at delamination," *Journal of Applied Mechanics*, Vol. 62, pp. 989-996.

57. Suo, Z., and Hutchinson, J. W., 1990, "Interface crack between two elastic layers," *International Journal of Fracture*, Vol. 43, pp. 1-18.

58. Suo, Z., 1990, "Delamination specimens for orthotropic materials," *Journal of Applied Mechanics*, Vol. 57, pp. 627-634.

59. Rybicki, E. F., and Kanninen, M. F., 1977, "A finite element calculation of stress intensity factors by a modified crack closure integral," *Engineering Fracture Mechanics*, Vol. 9, pp. 931-938.

60. Whitcomb, J. D., 1989, "Three-dimensional analysis of a postbuckled embedded delamination," *Journal of Composite Materials*, Vol. 23, pp. 862-889.

61. Whitcomb, J. D., 1989, "Comparison of full 3-D, thin-film 3-D, and thin-film plate analyses of a postbuckled embedded delamination," *Journal of Composites Technology & Research*, Vol. 11, No. 4, pp. 154-157.

62. Whitcomb, J. D., 1992, "Analysis of a laminate with a postbuckled embedded delamination, including contact effects," *Journal of Composite Materials*, Vol. 26, pp. 1523-1535.

63. Nusier, S. Q., and Newaz, G. M., 1997, "Analysis of interfacial cracks in a TBC/superalloy system under thermo-mechanical loading," *American Society of Mechanical Engineers (Paper) 97-GT-391*, ASME, New York.

64. Hellen, T. K., 1975, "On the method of virtual crack extensions," *International Journal for Numerical Methods in Engineering*, Vol. 9, pp. 187-207.

65. Delale, F., and Erdogan, F., 1988, "Interface crack in a nonhomogeneous elastic medium," *International Journal of Engineering Science*, Vol. 26, No. 6, pp. 559-568.

66. Chen, Y. F., and Erdogan, F., 1996, "Interface crack problem for a nonhomogeneous coating bonded to a homogeneous substrate," *Journal of the Mechanics & Physics of Solids*, Vol. 44, No. 5, pp. 771-787.

67. Lee, Y.-D., and Erdogan, F., 1998, "Interface cracking of FGM coatings under steady-state heat flow," *Engineering Fracture Mechanics*, Vol. 59, No. 3, pp. 361-380.

68. Erdogan, F., Kaya, A. C., and Joseph, P. F., 1991, "Crack problem in bonded nonhomogeneous materials," *Journal of Applied Mechanics*, Vol. 58, No. 2, pp. 410-418.

69. Erdogan, F., Wu, B. H., 1996, "Crack problems in FGM layers under thermal stresses," *Journal of Thermal Stresses*, Vol. 19, No. 3, pp. 237-265.

70. Kasmalkar, M., 1997, "The surface crack problem for a functionally graded coating bonded to a homogeneous layer," Ph.D. Thesis, Lehigh University.

71. Bao, G., and Cai, H., 1997, "Delamination cracking in functionally graded coating/metal substrate systems," *Acta Materialia*, Vol. 45, No. 3, pp. 1055-1066.

72. Chen, Y., 1990, "Interface crack in nonhomogeneous bonded materials of finite thickness," Ph.D. Thesis, Lehigh University.

73. Muskhelishvili, N. I., 1992, *Singular Integral Equations*, Dover, New York.

74. Abramowitz, M., and Stegun, I. E., 1973, *Handbook of Mathematical Functions*, Dover, New York.

75. Nied, H. F., and Kaya, A. C., 1992, "FRAC2D - finite element based software for 2-D and axisymmetric fracture analysis," General Electric Technical Report, 92CRD028.

76. Malvern, L. E., 1969, *Introduction to the Mechanics of a Continuous Medium*, Prentice-Hall, Eaglewood Cliffs, NJ.

77. Bathe, K. J., 1996, *Finite Element Procedures*, Prentice-Hall, Eaglewood Cliffs, NJ.

78. Lee, Y.-D., and Erdogan, F., "Interface cracking of graded coatings," *International Journal of Fracture*, in press.

79. Benzley, S. E., 1974, "Representation of singularities with isoparametric finite elements," *International Journal of Numerical Methods in Engineering*, Vol. 8, No. 3, pp. 537-545.

80. Williams, M. L., 1957, "On the stress distribution at the base of a stationary crack," *Journal of Applied Mechanics*, Vol. 24, pp. 109-114.

81. Erdogan, F., and Sih, G. C., 1963, "On the crack extension in plates under plane loading and transverse shear," *Journal of Basic Engineering*, Vol. 85, pp. 519-525.

82. Bathe, K. J., and Cimento, A. P., 1980, "Some practical procedures for the solution of nonlinear finite element equations," *Computer Methods in Applied Mechanics and Engineering*, Vol. 22, pp. 59-85.

83. Yildirim, B., and Nied, H. F., "Post-buckling and interface fracture," to be published.

84. Noda, N., and Tsuji, T., 1991, "Steady thermal stresses in a plate of functionally gradient material," *Nippon Kikai Gakkai Ronbunshu, a Hen*, Vol. 57, No. 533, pp. 98-103.

85. Rice, J. R., 1988, "Elastic fracture mechanics concepts for interfacial cracks," *Journal of Applied Mechanics*, Vol. 55, pp. 98-103.

86. Nusier, S., and Newaz, G., 1998, "Analysis of interfacial cracks in a TBC/superalloy system under thermal loading," *Engineering Fracture Mechanics*, Vol. 60, No. 5-6, pp. 577-581.

87. Timoshenko, S. P., and Gere, J. M., 1961, *Theory of Elastic Stability*, McGraw-Hill, New York.

88. Beer, F. P., and Johnston, E. R. Jr., 1992, *Mechanics of Materials*, 2nd Ed., McGraw-Hill, New York.

## Appendix A

### Finite Deformation Theory of Elasticity

#### A.1 Analysis of Strain

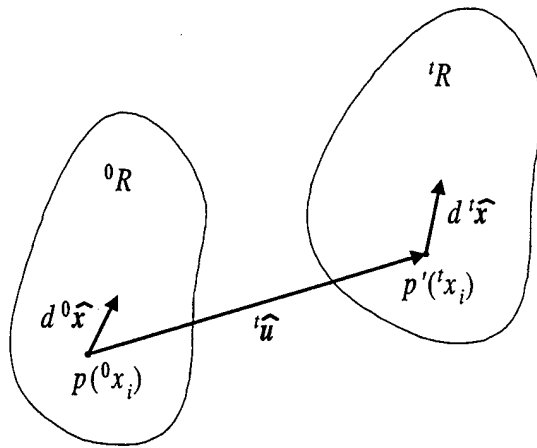


Figure A.1 Motion of a continuous medium.

In characterizing the strains in the finite deformation theory, we employ the Lagrangian approach, in which the coordinates defining a point of the medium before deformation are used for locating the point during the subsequent deformation. Figure A.1 shows at configuration  $t$  a deformed body  $tR$  which occupies the region  ${}^0R$  in the undeformed state. The coordinates of a typical material point  $p$  in the undeformed state are  $({}^0x_1, {}^0x_2, {}^0x_3)$ . The same material point occupies  $({}^t x_1, {}^t x_2, {}^t x_3)$  in the deformed state and we have

$${}^t x_i = {}^0 x_i + {}^t u_i, \quad i = 1, 2, 3. \quad (\text{A1})$$

Note that the left superscript is used to denote the configuration. To determine the strain in the Lagrangian configuration, first we define the deformation gradient [76] referred to the undeformed configuration as follows:

$${}^t_0\mathbf{F} = \{{}^t_0x_{i,j}\}_{3 \times 3} = \begin{pmatrix} \frac{\partial^t x_1}{\partial^0 x_1} & \frac{\partial^t x_1}{\partial^0 x_2} & \frac{\partial^t x_1}{\partial^0 x_3} \\ \frac{\partial^t x_2}{\partial^0 x_1} & \frac{\partial^t x_2}{\partial^0 x_2} & \frac{\partial^t x_2}{\partial^0 x_3} \\ \frac{\partial^t x_3}{\partial^0 x_1} & \frac{\partial^t x_3}{\partial^0 x_2} & \frac{\partial^t x_3}{\partial^0 x_3} \end{pmatrix}; \quad (\text{A2})$$

and define the spatial deformation gradient [76] which referred to the configuration  $t$  (Eulerian formulation) as

$${}^0_t\mathbf{F} = {}^t_0\mathbf{F}^{-1} = \{{}^0_t x_{i,j}\}_{3 \times 3}. \quad (\text{A3})$$

Note that in the notation we used while a differentiation is involved, the left subscript indicates the configuration in which the coordinate is measured, for example,  ${}^t_0x_{i,j} = \frac{\partial^t x_i}{\partial^0 x_j}$ . For an arbitrary infinitesimal material vector  $d^0\hat{\mathbf{x}}$  at undeformed configuration and the corresponding vector  $d^t\hat{\mathbf{x}}$  at deformed configuration we may write

$$d^t\hat{\mathbf{x}} = {}^t_0\mathbf{F} \bullet d^0\hat{\mathbf{x}}, \quad d^0\hat{\mathbf{x}} = {}^t_0\mathbf{F}^{-1} \bullet d^t\hat{\mathbf{x}}. \quad (\text{A4})$$

The strain tensor  ${}^t_0\mathbf{E}$  are defined such that it gives the change in the squared length of the material vector  $d^0\hat{\mathbf{x}}$  as

$$(d^t s)^2 - (d^0 s)^2 = 2(d^0\hat{\mathbf{x}}) \bullet {}^t_0\mathbf{E} \bullet (d^0\hat{\mathbf{x}}), \quad (\text{A5})$$

where

$$(d^t s)^2 = (d^t\hat{\mathbf{x}}) \bullet (d^t\hat{\mathbf{x}}), \quad (d^0 s)^2 = (d^0\hat{\mathbf{x}}) \bullet (d^0\hat{\mathbf{x}}). \quad (\text{A6})$$

From (A4)-(A6) it may be seen that

$${}^t_0\mathbf{E} = \{{}^t_0\epsilon_{i,j}\}_{3 \times 3} = \frac{1}{2}({}^t_0\mathbf{F}^T {}^t_0\mathbf{F} - \mathbf{I}), \quad (\text{A7})$$

or

$${}^t_0\epsilon_{ij} = \frac{1}{2} \left( \frac{\partial^t x_k}{\partial^0 x_i} \frac{\partial^t x_k}{\partial^0 x_j} - \delta_{ij} \right), \quad i, j = 1, 2, 3, \quad (\text{A8})$$

where  $\mathbf{I}$  is the unit tensor and  $\delta_{ij}$  is the Kronecker delta. By substituting (A1) into (A8), we may write the Lagrangian strain components as

$${}^t\epsilon_{ij} = \frac{1}{2}({}^t_0 u_{i,j} + {}^t_0 u_{j,i} + {}^t_0 u_{k,i} {}^t_0 u_{k,j}). \quad (\text{A9})$$

Note that (A9) is also called Green-Lagrange strains. Also note that if the displacement gradients are small, we may neglect the last term in (A9) and recover the components for small strains.

## A.2 Stress and Equations of Equilibrium

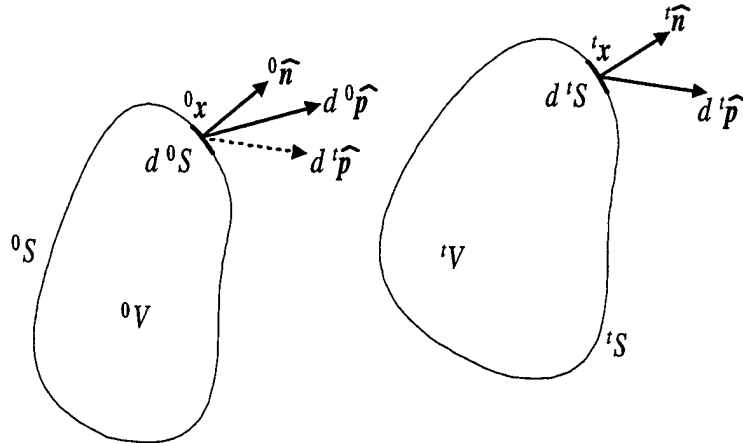


Figure A.2 Force vectors for Piola-Kirchhoff stress definition.

The stress measure to use with the Green-Lagrange strain tensor  ${}^t_0 \mathbf{E}$  is the second Piola-Kirchhoff stress tensor  ${}^t_0 \boldsymbol{\sigma}$ . The basic ideas of the second Piola-Kirchhoff stress tensor can be indicated in terms of the force vectors illustrated in Figure A.2. The second Piola-Kirchhoff stress tensor  ${}^t_0 \boldsymbol{\sigma}$  is formulated such that it gives a force  $d^0 \hat{\mathbf{p}}$  related to the force  $d^t \hat{\mathbf{p}}$  in the same way that a material vector  $d^0 \hat{\mathbf{x}}$  at  ${}^0 \hat{\mathbf{x}}$  is related by the deformation to the corresponding spatial vector  $d^t \hat{\mathbf{x}}$  at  ${}^t \hat{\mathbf{x}}$ . That is

$$({}^0\widehat{\mathbf{n}} \bullet {}^t_0\boldsymbol{\sigma}) d^0 S = d^0 \widehat{\mathbf{p}} = {}^t_0\boldsymbol{F}^{-1} \bullet d^t \widehat{\mathbf{p}} = {}^t_0\boldsymbol{F}^{-1} \bullet ({}^t\widehat{\mathbf{n}} \bullet {}^t\boldsymbol{\tau}) d^t S, \quad (\text{A10})$$

where  ${}^t\boldsymbol{\tau}$  is the Cauchy stress tensor (defined in the Eulerian configuration). To determine the relation between Cauchy stress tensor and the second Piola-Kirchhoff stress tensor, first we have the relation between the deformed and original configurations given by [76]

$$\begin{aligned} {}^t\widehat{\mathbf{n}} d^t S &= \left( \frac{d^t V}{d^0 V} \right) {}^0\widehat{\mathbf{n}} \bullet {}^t_0\boldsymbol{F}^{-1} d^0 S, \\ \frac{d^t V}{d^0 V} &= \det({}^t_0\boldsymbol{F}), \end{aligned} \quad (\text{A11})$$

giving

$${}^t\boldsymbol{\tau} = \left( \frac{d^0 V}{d^t V} \right) {}^t_0\boldsymbol{F} \bullet {}^t_0\boldsymbol{\sigma} \bullet {}^t_0\boldsymbol{F}^T, \quad (\text{A12})$$

or

$${}^t\tau_{ij} = \left( \frac{d^0 V}{d^t V} \right) {}^t_0 x_{i,m} {}^t_0 x_{j,n} {}^t_0 \sigma_{mn}. \quad (\text{A13})$$

Note that the second Piola-Kirchhoff stress tensor is work-conjugate with the Green-Lagrange strain tensor [76]. Also note that from the symmetry of  ${}^t\boldsymbol{\tau}$ , it may be seen from (A12) that the second Piola-Kirchhoff stress tensor  ${}^t_0\boldsymbol{\sigma}$  is also symmetric.

From (A10) we can also write the natural boundary condition in Lagrangian formulation as

$${}^t_0\boldsymbol{F} \bullet ({}^0\widehat{\mathbf{n}} \bullet {}^t_0\boldsymbol{\sigma}) = \frac{d^t \widehat{\mathbf{p}}}{d^0 S} = {}^t_0\widehat{\mathbf{T}}, \quad (\text{A14})$$

or

$$({}^t_0 \sigma_{ij} + {}^t_0 \sigma_{jk} {}^t_0 u_{i,k}) {}^0 n_j = {}^t_0 T_i, \quad i = 1, 2, 3, \quad (\text{A15})$$

where  ${}^t_0\widehat{\mathbf{T}}$  is the applied traction vector. Note that the left subscript in  ${}^t_0 T_i$  denotes the configuration with respect to which the quantity is measured.

From the static equilibrium of a deformed infinitesimal parallelepiped  $d^tV$ , we may write the equilibrium equation for the Eulerian configuration as

$$\frac{\partial^t \tau_{ij}}{\partial^t x_j} + {}^t P_i = 0, \quad i = 1, 2, 3, \quad (\text{A16})$$

where  ${}^t \tau_{ij}$  is the component of Cauchy stress tensor and  ${}^t P_i$  is the Eulerian component of body force vector. To transform (A16) into Lagrangian formulation, first we consider the body force part in (A16). Assuming that originally the infinitesimal parallelepiped has volume  $d^0V$  at undeformed configuration, we may write the relation between  ${}^t P_i$  and its equivalent body force component  ${}^0 P_i$  at undeformed configuration as follows:

$${}^t P_i d^t V = {}^0 P_i d^0 V. \quad (\text{A17})$$

By substituting (A13) and (A17) into (A16) and using chain rule, we may write the equilibrium equation in terms of the second Piola-Kirchhoff stresses as

$$\frac{\partial}{\partial^0 x_k} \left( {}^0 x_{i,m} {}^0 x_{j,n} {}^0 \sigma_{mn} \right) {}^0 x_{k,j} + {}^0 P_i = 0. \quad (\text{A18})$$

Providing that

$$\frac{\partial}{\partial^0 x_k} \left( \frac{\partial^t x_j}{\partial^0 x_n} \right) \frac{\partial^0 x_k}{\partial^t x_j} = 0, \quad (\text{A19})$$

$${}^0 x_{j,n} {}^0 x_{k,j} = \delta_{kn},$$

Equation (A18) may be rewritten as

$$\frac{\partial}{\partial^0 x_n} \left( {}^0 x_{i,m} {}^0 \sigma_{mn} \right) + {}^0 P_i = 0. \quad (\text{A20})$$

The equilibrium equation (A20) for the Lagrangian formulation may further be simplified as

$$\frac{\partial}{\partial^0 x_j} \left( {}^0 \sigma_{ij} + {}^0 u_{i,k} {}^0 \sigma_{jk} \right) + {}^0 P_i = 0, \quad i = 1, 2, 3. \quad (\text{A21})$$

### A.3 Stress-Strain Relations

By assuming that the material is isotropic and generalizing the linear elastic relation for small deformation, we may obtain the elastic material description for finite deformation analysis as follows:

$${}^t_0\sigma_{ij} = {}^t_0C_{ijrs} {}^t_0\epsilon_{rs} - \delta_{ij}C_T\epsilon_T, \quad i, j = 1, 2, 3, \quad (\text{A22})$$

where

$$\begin{aligned} {}^t_0C_{ijrs} &= \lambda\delta_{ij}\delta_{rs} + \mu(\delta_{ir}\delta_{js} + \delta_{is}\delta_{jr}), \\ \lambda &= \frac{E\nu}{(1+\nu)(1-2\nu)}, \quad \mu = \frac{E}{2(1+\nu)}, \\ C_T &= \frac{E}{1-2\nu}, \quad \epsilon_T = \alpha(\Delta T), \end{aligned} \quad (\text{A23})$$

$E$ ,  $\nu$ , and  $\alpha$  being the Young's modulus, Poisson's ratio, and thermal expansion coefficient, respectively,  $\Delta T$  being the temperature change in the medium.

## Appendix B

### Expressions of Various Functions in the Kernels

#### B.1 Expressions of $A_1, A_2, C_1, C_2, C_3$ , and $C_4$ in Terms of $F_1$ and $F_2$

The unknown coefficients  $A_1, A_2, C_1, \dots, C_4$  for the general solution in the stability analysis may be expressed in terms of  $F_1$  and  $F_2$ , the Fourier transform of the density functions  $f_1$  and  $f_2$ , respectively, through a system of linear equations, (2.39)-(2.44), derived from the boundary and continuity conditions. These equations are solved in such a way that at first, two unknowns,  $C_3$  and  $C_4$ , are determined in terms of the other two unknowns,  $C_1$  and  $C_2$ , from a pair of equations ((2.39), (2.40)) which contains these four unknowns only, then applying the relation obtained from the first step into another pair of homogeneous equations ((2.41), (2.42)) to determine  $C_1, \dots, C_4$  in terms of the last two unknowns,  $A_1$  and  $A_2$ , which appear in the boundary conditions ((2.45), (2.46)) that used as the integral equations. Compared with solving the six unknowns directly in terms of  $F_1$  and  $F_2$ , it can be seen later that this procedure provides a better algebraic structure for studying the asymptotic behavior of the kernels.

In order to simplify the asymptotic analysis which will be described in Appendix C, first the following quantities are defined

$$n_1^* = \frac{n_1}{|\alpha|} = -\frac{\rho\xi}{2} - \sqrt{\frac{\xi^2}{4} + 1 - \frac{8\kappa\epsilon_0}{(\kappa+1)^2} + \beta\sqrt{\frac{(8\epsilon_0)^2}{(\kappa+1)^4} - \left(\frac{3-\kappa}{\kappa+1}\right)\xi^2}}, \quad (B1)$$

$$n_2^* = \frac{n_2}{|\alpha|} = -\frac{\rho\xi}{2} - \sqrt{\frac{\xi^2}{4} + 1 - \frac{8\kappa\epsilon_0}{(\kappa+1)^2} - \beta\sqrt{\frac{(8\epsilon_0)^2}{(\kappa+1)^4} - \left(\frac{3-\kappa}{\kappa+1}\right)\xi^2}}, \quad (B2)$$

$$n_3^* = \frac{n_3}{|\alpha|} = -\frac{\rho\xi}{2} + \sqrt{\frac{\xi^2}{4} + 1 - \frac{8\kappa\epsilon_0}{(\kappa+1)^2} + \beta\sqrt{\frac{(8\epsilon_0)^2}{(\kappa+1)^4} - \left(\frac{3-\kappa}{\kappa+1}\right)\xi^2}}, \quad (B3)$$

$$n_4^* = \frac{n_4}{|\alpha|} = -\frac{\rho\xi}{2} + \sqrt{\frac{\xi^2}{4} + 1 - \frac{8\kappa\epsilon_0}{(\kappa+1)^2} - \beta\sqrt{\frac{(8\epsilon_0)^2}{(\kappa+1)^4} - \left(\frac{3-\kappa}{\kappa+1}\right)\xi^2}}, \quad (\text{B4})$$

$$\begin{aligned} m_k^* &= \frac{m_k}{i\beta} \\ &= -\frac{2n_k^* + \rho(3-\kappa)\xi}{(\kappa+1)n_k^{*2} + \rho(\kappa+1)\xi n_k^* - (\kappa-1) + 8\left(\frac{\kappa-1}{\kappa+1}\right)\epsilon_0}, \quad k = 1, \dots, 4, \end{aligned} \quad (\text{B5})$$

$$\lambda_1^* = \frac{\lambda_1}{|\alpha|} = \sqrt{1 - \frac{8\epsilon_0}{\kappa+1}}, \quad (\text{B6})$$

$$\lambda_2^* = \frac{\lambda_2}{|\alpha|} = \sqrt{1 - \frac{8(\kappa-1)\epsilon_0}{(\kappa+1)^2}}, \quad (\text{B7})$$

where  $m_j$ ,  $n_j$  and  $\lambda_j$  are defined by (2.26), (2.27), and (2.29), respectively, and

$$\xi = \frac{|\gamma|}{|\alpha|}, \quad \rho = \frac{|\gamma|}{\gamma}, \quad \beta = \frac{|\alpha|}{\alpha}. \quad (\text{B8})$$

Following the procedure described above, we may rewrite (2.39) and (2.40), respectively, as

$$\sum_{k=1}^4 \left[ \frac{3-\kappa}{\kappa-1} + m_k^* n_k^* \left( \frac{\kappa+1}{\kappa-1} \right) \right] e^{n_k^* |\gamma| h / \xi} C_k = 0, \quad (\text{B9})$$

$$\sum_{k=1}^4 (n_k^* - m_k^*) e^{n_k^* |\gamma| h / \xi} C_k = 0. \quad (\text{B10})$$

Solving (B9) and (B10) we obtain

$$C_3 = \left( \frac{a_4 b_1 - a_1 b_4}{a_3 b_4 - a_4 b_3} \right) e^{(n_1^* - n_3^*) |\gamma| h / \xi} C_1 + \left( \frac{a_4 b_2 - a_2 b_4}{a_3 b_4 - a_4 b_3} \right) e^{(n_2^* - n_3^*) |\gamma| h / \xi} C_2, \quad (\text{B11})$$

$$C_4 = \left( \frac{a_1 b_3 - a_3 b_1}{a_3 b_4 - a_4 b_3} \right) e^{(n_1^* - n_4^*) |\gamma| h / \xi} C_1 + \left( \frac{a_2 b_3 - a_3 b_2}{a_3 b_4 - a_4 b_3} \right) e^{(n_2^* - n_4^*) |\gamma| h / \xi} C_2, \quad (\text{B12})$$

where

$$a_j = \frac{3-\kappa}{\kappa-1} + m_j^* n_j^* \left( \frac{\kappa+1}{\kappa-1} \right), \quad j = 1, \dots, 4, \quad (\text{B13})$$

$$b_j = n_j^* - m_j^*, \quad j = 1, \dots, 4. \quad (\text{B14})$$

Equations (2.41) and (2.42) may be rewritten, respectively, as

$$2A_1 + \left( 1 + \lambda_1^{*2} \right) A_2 + \sum_{k=1}^4 \left[ \frac{3-\kappa}{\kappa-1} + m_k^* n_k^* \left( \frac{\kappa+1}{\kappa-1} \right) \right] C_k = 0, \quad (\text{B15})$$

$$\left( \lambda_1^* + \frac{1}{\lambda_1^*} \right) A_1 + 2\lambda_2^* A_2 - \sum_{k=1}^4 (n_k^* - m_k^*) C_k = 0. \quad (\text{B16})$$

From (B11), (B12), (B15), and (B16),  $C_1$  and  $C_2$  may be expressed as follows:

$$C_1 = - \left( \frac{2k_{22} + l_{21}k_{12}}{k_{11}k_{22} - k_{12}k_{21}} \right) A_1 + \left( \frac{l_{12}k_{22} - 2\lambda_2 k_{12}}{k_{11}k_{22} - k_{12}k_{21}} \right) A_2, \quad (\text{B17})$$

$$C_2 = \left( \frac{l_{21}k_{11} + 2k_{21}}{k_{11}k_{22} - k_{12}k_{21}} \right) A_1 + \left( \frac{2\lambda_2 k_{11} - l_{12}k_{21}}{k_{11}k_{22} - k_{12}k_{21}} \right) A_2, \quad (\text{B18})$$

where

$$l_{12} = -1 - \lambda_1^{*2}, \quad (\text{B19})$$

$$l_{21} = \lambda_1^* + \frac{1}{\lambda_1^*}, \quad (\text{B20})$$

$$k_{11} = a_1 + a_3 \left( \frac{a_4 b_1 - a_1 b_4}{a_3 b_4 - a_4 b_3} \right) e^{(n_1^* - n_3^*) |\gamma| h / \xi} + a_4 \left( \frac{a_1 b_3 - a_3 b_1}{a_3 b_4 - a_4 b_3} \right) e^{(n_1^* - n_4^*) |\gamma| h / \xi}, \quad (\text{B21})$$

$$k_{12} = a_2 + a_3 \left( \frac{a_4 b_2 - a_2 b_4}{a_3 b_4 - a_4 b_3} \right) e^{(n_2^* - n_3^*) |\gamma| h / \xi} + a_4 \left( \frac{a_2 b_3 - a_3 b_2}{a_3 b_4 - a_4 b_3} \right) e^{(n_2^* - n_4^*) |\gamma| h / \xi}, \quad (\text{B22})$$

$$k_{21} = b_1 + b_3 \left( \frac{a_4 b_1 - a_1 b_4}{a_3 b_4 - a_4 b_3} \right) e^{(n_1^* - n_3^*) |\gamma| h / \xi} + b_4 \left( \frac{a_1 b_3 - a_3 b_1}{a_3 b_4 - a_4 b_3} \right) e^{(n_1^* - n_4^*) |\gamma| h / \xi}, \quad (\text{B23})$$

$$k_{22} = b_2 + b_3 \left( \frac{a_4 b_2 - a_2 b_4}{a_3 b_4 - a_4 b_3} \right) e^{(n_2^* - n_3^*) |\gamma| h / \xi} + b_4 \left( \frac{a_2 b_3 - a_3 b_2}{a_3 b_4 - a_4 b_3} \right) e^{(n_2^* - n_4^*) |\gamma| h / \xi}. \quad (\text{B24})$$

Now, substituting (B11), (B12), (B17), and (B18) into (2.43) and (2.44), which may be rewritten as

$$-\left(\frac{1}{\lambda_1^*}\right)A_1 - \lambda_2^* A_2 - \sum_{k=1}^4 m_k^* C_k = \frac{F_1}{|\alpha|}, \quad (\text{B25})$$

$$-(A_1 + A_2 - C_1 - C_2 - C_3 - C_4) = \frac{F_2}{i\alpha}, \quad (\text{B26})$$

we obtain

$$A_1 = -\left(\frac{d_{22}}{d_{11}d_{22} - d_{21}d_{12}}\right)\frac{F_1}{|\alpha|} - \left(\frac{d_{12}}{d_{11}d_{22} - d_{21}d_{12}}\right)\frac{F_2}{i\alpha}, \quad (\text{B27})$$

$$A_2 = \left(\frac{d_{21}}{d_{11}d_{22} - d_{21}d_{12}}\right)\frac{F_1}{|\alpha|} + \left(\frac{d_{11}}{d_{11}d_{22} - d_{21}d_{12}}\right)\frac{F_2}{i\alpha}, \quad (\text{B28})$$

where

$$\begin{aligned} d_{11} = & \left[ m_1^* + m_3^* \left( \frac{a_4 b_1 - a_1 b_4}{a_3 b_4 - a_4 b_3} \right) e^{(n_1^* - n_3^*)|\gamma|h/\xi} \right. \\ & + m_4^* \left( \frac{a_1 b_3 - a_3 b_1}{a_3 b_4 - a_4 b_3} \right) e^{(n_1^* - n_4^*)|\gamma|h/\xi} \left. \right] \left( \frac{-2k_{22} - l_{21}k_{12}}{k_{11}k_{22} - k_{12}k_{21}} \right) \\ & + \left[ m_2^* + m_3^* \left( \frac{a_4 b_2 - a_2 b_4}{a_3 b_4 - a_4 b_3} \right) e^{(n_2^* - n_3^*)|\gamma|h/\xi} \right. \\ & + m_4^* \left( \frac{a_2 b_3 - a_3 b_2}{a_3 b_4 - a_4 b_3} \right) e^{(n_2^* - n_4^*)|\gamma|h/\xi} \left. \right] \left( \frac{l_{21}k_{11} + 2k_{21}}{k_{11}k_{22} - k_{12}k_{21}} \right) \\ & + \frac{1}{\lambda_1^*}, \end{aligned} \quad (\text{B29})$$

$$\begin{aligned} d_{12} = & \left[ m_1^* + m_3^* \left( \frac{a_4 b_1 - a_1 b_4}{a_3 b_4 - a_4 b_3} \right) e^{(n_1^* - n_3^*)|\gamma|h/\xi} \right. \\ & + m_4^* \left( \frac{a_1 b_3 - a_3 b_1}{a_3 b_4 - a_4 b_3} \right) e^{(n_1^* - n_4^*)|\gamma|h/\xi} \left. \right] \left( \frac{l_{12}k_{22} - 2\lambda_2^* k_{12}}{k_{11}k_{22} - k_{12}k_{21}} \right) \\ & + \left[ m_2^* + m_3^* \left( \frac{a_4 b_2 - a_2 b_4}{a_3 b_4 - a_4 b_3} \right) e^{(n_2^* - n_3^*)|\gamma|h/\xi} \right. \\ & + m_4^* \left( \frac{a_2 b_3 - a_3 b_2}{a_3 b_4 - a_4 b_3} \right) e^{(n_2^* - n_4^*)|\gamma|h/\xi} \left. \right] \left( \frac{2\lambda_2^* k_{11} - l_{12}k_{21}}{k_{11}k_{22} - k_{12}k_{21}} \right) \\ & + \lambda_2^*, \end{aligned} \quad (\text{B30})$$

$$\begin{aligned}
d_{21} = & \left[ 1 + \left( \frac{a_4 b_1 - a_1 b_4}{a_3 b_4 - a_4 b_3} \right) e^{(n_1^* - n_3^*) |\gamma| h / \xi} \right. \\
& + \left. \left( \frac{a_1 b_3 - a_3 b_1}{a_3 b_4 - a_4 b_3} \right) e^{(n_1^* - n_4^*) |\gamma| h / \xi} \right] \left( \frac{-2k_{22} - l_{21}k_{12}}{k_{11}k_{22} - k_{12}k_{21}} \right) \\
& + \left[ 1 + \left( \frac{a_4 b_2 - a_2 b_4}{a_3 b_4 - a_4 b_3} \right) e^{(n_2^* - n_3^*) |\gamma| h / \xi} \right. \\
& + \left. \left( \frac{a_2 b_3 - a_3 b_2}{a_3 b_4 - a_4 b_3} \right) e^{(n_2^* - n_4^*) |\gamma| h / \xi} \right] \left( \frac{l_{21}k_{11} + 2k_{21}}{k_{11}k_{22} - k_{12}k_{21}} \right) \\
& - 1,
\end{aligned} \tag{B31}$$

$$\begin{aligned}
d_{22} = & \left[ 1 + \left( \frac{a_4 b_1 - a_1 b_4}{a_3 b_4 - a_4 b_3} \right) e^{(n_1^* - n_3^*) |\gamma| h / \xi} \right. \\
& + \left. \left( \frac{a_1 b_3 - a_3 b_1}{a_3 b_4 - a_4 b_3} \right) e^{(n_1^* - n_4^*) |\gamma| h / \xi} \right] \left( \frac{l_{12}k_{22} - 2\lambda_2^* k_{12}}{k_{11}k_{22} - k_{12}k_{21}} \right) \\
& + \left[ 1 + \left( \frac{a_4 b_2 - a_2 b_4}{a_3 b_4 - a_4 b_3} \right) e^{(n_2^* - n_3^*) |\gamma| h / \xi} \right. \\
& + \left. \left( \frac{a_2 b_3 - a_3 b_2}{a_3 b_4 - a_4 b_3} \right) e^{(n_2^* - n_4^*) |\gamma| h / \xi} \right] \left( \frac{2\lambda_2^* k_{11} - l_{12}k_{21}}{k_{11}k_{22} - k_{12}k_{21}} \right) \\
& - 1.
\end{aligned} \tag{B32}$$

By substituting (B27) and (B28) into (B17) and (B18) and then into (B11) and (B12),  $C_1, \dots, C_4$  may be expressed explicitly in terms of  $F_1$  and  $F_2$ .

## B.2 Expressions of $D_{ijk}$ in the Kernels (2.48)-(2.51)

In terms of the quantities defined in Appendix B.1 we may rewrite (2.45) and (2.46) as follows:

$$\lim_{y \rightarrow -0} \frac{\mu_1}{2\pi} \int_{-\infty}^{\infty} \left( -2A_1 e^{\lambda_1 y} + l_{12} A_2 e^{\lambda_2 y} \right) i\alpha e^{i\alpha x} d\alpha = 0, \quad -a < x < a, \tag{B33}$$

$$\lim_{y \rightarrow -0} \frac{\mu_1}{2\pi} \int_{-\infty}^{\infty} \left( l_{21} A_1 e^{\lambda_1 y} + 2\lambda_2^* A_2 e^{\lambda_2 y} \right) |\alpha| e^{i\alpha x} d\alpha = 0, \quad -a < x < a. \tag{B34}$$

By substituting (B27) and (B28) into (B33) and (B34) the functions  $D_{ijk}$ ,  $i, j, k = 1, 2$ , in the kernels (2.48)-(2.51) are given by

$$D_{111}(\alpha) = \frac{2d_{22}}{d_{11}d_{22} - d_{21}d_{12}}, \quad (\text{B35})$$

$$D_{112}(\alpha) = \frac{l_{12}d_{21}}{d_{11}d_{22} - d_{21}d_{12}}, \quad (\text{B36})$$

$$D_{121}(\alpha) = \frac{2d_{12}}{d_{11}d_{22} - d_{21}d_{12}}, \quad (\text{B37})$$

$$D_{122}(\alpha) = \frac{l_{12}d_{11}}{d_{11}d_{22} - d_{21}d_{12}}, \quad (\text{B38})$$

$$D_{211}(\alpha) = -\frac{l_{21}d_{22}}{d_{11}d_{22} - d_{21}d_{12}}, \quad (\text{B39})$$

$$D_{212}(\alpha) = \frac{2\lambda_2^*d_{21}}{d_{11}d_{22} - d_{21}d_{12}}, \quad (\text{B40})$$

$$D_{221}(\alpha) = \frac{l_{21}d_{12}}{d_{11}d_{22} - d_{21}d_{12}}, \quad (\text{B41})$$

$$D_{222}(\alpha) = -\frac{2\lambda_2^*d_{11}}{d_{11}d_{22} - d_{21}d_{12}}. \quad (\text{B42})$$

Note that from (B1)-(B5), (B13), (B14), (B21)-(B24), and (B29)-(B32) it may be seen that

$$n_1^*(\alpha) = n_2^*(-\alpha), \quad n_3^*(\alpha) = n_4^*(-\alpha), \quad (\text{B43})$$

$$m_1^*(\alpha) = m_2^*(-\alpha), \quad m_3^*(\alpha) = m_4^*(-\alpha), \quad (\text{B44})$$

$$a_1(\alpha) = a_2(-\alpha), \quad a_3(\alpha) = a_4(-\alpha), \quad (\text{B45})$$

$$b_1(\alpha) = b_2(-\alpha), \quad b_3(\alpha) = b_4(-\alpha), \quad (\text{B46})$$

$$k_{11}(\alpha) = k_{12}(-\alpha), \quad k_{21}(\alpha) = k_{22}(-\alpha), \quad (\text{B47})$$

$$d_{ij}(\alpha) = d_{ij}(-\alpha), \quad i, j = 1, 2. \quad (\text{B48})$$

Thus, from (B35)-(B42) we may see that

$$D_{ijk}(\alpha) = D_{ijk}(-\alpha), \quad |\alpha| < \infty, \quad i, j, k = 1, 2. \quad (\text{B49})$$

Furthermore, it may be seen that when  $|\alpha/\gamma| < [(3 - \kappa)(1 + \kappa)^3]^{1/2}/8\epsilon_0$  and  $\epsilon_0 < 0.5$ ,  $n_j^*$  ( $j = 1, \dots, 4$ ) are complex. From (B1)-(B5), (B13), (B14), (B21)-(B24), and (B29)-(B32) we have

$$\begin{aligned} n_j^*(\alpha) &= \overline{n_j^*(-\alpha)}, \quad m_j^*(\alpha) = \overline{m_j^*(-\alpha)}, \\ a_j(\alpha) &= \overline{a_j}(-\alpha), \quad b_j(\alpha) = \overline{b_j}(-\alpha), \quad i, j = 1, 2, \\ k_{ij}(\alpha) &= \overline{k_{ij}}(-\alpha), \quad d_{ij}(\alpha) = \overline{d_{ij}}(-\alpha), \end{aligned} \quad (\text{B50})$$

when  $|\alpha/\gamma| < [(3 - \kappa)(1 + \kappa)^3]^{1/2}/8\epsilon_0$ . By applying (B50) to (B35)-(B42), we obtain

$$D_{ijk}(\alpha) = \overline{D_{ijk}}(-\alpha), \quad \left| \frac{\alpha}{\gamma} \right| < \frac{[(3 - \kappa)(1 + \kappa)^3]^{1/2}}{8\epsilon_0}, \quad i, j, k = 1, 2. \quad (\text{B51})$$

It may be seen from (B51) that the real part of  $D_{ijk}$ 's are even in  $\alpha$ , which agrees with (B49). However, according to (B51) the imaginary part of  $D_{ijk}$ 's are odd functions of  $\alpha$  when  $|\alpha/\gamma| < [(3 - \kappa)(1 + \kappa)^3]^{1/2}/8\epsilon_0$ , but (B49) gives that  $\text{Im}(D_{ijk})$  is even in  $\alpha$ . Therefore, we may conclude that  $D_{ijk}$ 's are real functions and are even in  $\alpha$ .

## Appendix C

### Asymptotic Expressions for the Integrands in the Kernels

To asymptotically expand the integrands  $B_{ij}$ ,  $i, j = 1, 2$ , (Equation (3.10)) in the kernels for large  $\eta$ , we follow the approach for determine the closed form ((B35)-(B42)) of these integrands described in Appendix B. Beginning with the characteristic roots (B1)-(B4), we determine the asymptotic expansions, substitute them into the expressions for the successive algebraic functions, and repeat the asymptotic expansion-substitution process until the asymptotic series for (B35)-(B42) are obtained.

In order to simplify the asymptotic analysis, we first carry out the first-term asymptotic approximation for some functions. As  $\alpha$  approaches infinity, from (3.5) and (B8) we have

$$\eta \rightarrow \infty, \quad \xi \rightarrow 0, \quad \beta = 1. \quad (C1)$$

Thus, from (B1)-(B5), (B13), and (B14), we have, as  $\alpha$  or  $\eta$  goes to infinity,

$$n_1^* = -\lambda_2^* + O(\xi), \quad (C2)$$

$$n_2^* = -\lambda_1^* + O(\xi), \quad (C3)$$

$$n_3^* = \lambda_2^* + O(\xi), \quad (C4)$$

$$n_4^* = \lambda_1^* + O(\xi), \quad (C5)$$

$$m_1^* = \lambda_2^* + O(\xi), \quad (C6)$$

$$m_2^* = \frac{1}{\lambda_1^*} + O(\xi), \quad (C7)$$

$$m_3^* = -\lambda_2^* + O(\xi), \quad (C8)$$

$$m_4^* = -\frac{1}{\lambda_1^*} + O(\xi), \quad (C9)$$

$$a_1 = -1 - \lambda_1^{*2} + O(\xi), \quad (C10)$$

$$a_2 = -2 + O(\xi), \quad (C11)$$

$$a_3 = -1 - \lambda_1^{*2} + O(\xi), \quad (C12)$$

$$a_4 = -2 + O(\xi), \quad (C13)$$

$$b_1 = -2\lambda_2^* + O(\xi), \quad (C14)$$

$$b_2 = -\lambda_1^* - \frac{1}{\lambda_1^*} + O(\xi), \quad (C15)$$

$$b_3 = 2\lambda_2^* + O(\xi), \quad (C16)$$

$$b_4 = \lambda_1^* + \frac{1}{\lambda_1^*} + O(\xi), \quad (C17)$$

where  $\lambda_1^*$  and  $\lambda_2^*$  are given in (B6) and (B7), respectively. It may be seen that for  $1 < \kappa < 3$  and  $\epsilon_0 < 0.228$ , we have  $a_i b_j - a_j b_i = O(1)$  ( $i, j = 1, 2, 3, 4$ ). Also it can be seen that the leading term for  $n_{1,2}^* - n_{3,4}^*$  is negative and of order one. Therefore, from (B21)-(B24), we may write  $k_{ij}$  as

$$k_{11} = a_1 + O(0), \quad (C18)$$

$$k_{12} = a_2 + O(0), \quad (C19)$$

$$k_{21} = b_1 + O(0), \quad (C20)$$

$$k_{22} = b_2 + O(0). \quad (C21)$$

Furthermore, from (B29)-(B32), the asymptotic expression for  $d_{ij}$  ( $i, j = 1, 2$ ) may be expressed as follows:

$$d_{11} = m_1^* \left( \frac{-2b_2 - l_{21}a_2}{a_1b_2 - a_2b_1} \right) + m_2^* \left( \frac{l_{21}a_1 + 2b_1}{a_1b_2 - a_2b_1} \right) + \frac{1}{\lambda_1^*} + O(0), \quad (C22)$$

$$d_{12} = m_1^* \left( \frac{l_{12}b_2 - 2\lambda_2^* a_2}{a_1 b_2 - a_2 b_1} \right) + m_2^* \left( \frac{2\lambda_2^* a_1 - l_{12}b_1}{a_1 b_2 - a_2 b_1} \right) + \lambda_2^* + O(0), \quad (C23)$$

$$d_{21} = \left( \frac{-2b_2 - l_{21}a_2}{a_1 b_2 - a_2 b_1} \right) + \left( \frac{l_{21}a_1 + 2b_1}{a_1 b_2 - a_2 b_1} \right) - 1 + O(0), \quad (C24)$$

$$d_{22} = \left( \frac{l_{12}b_2 - 2\lambda_2^* a_2}{a_1 b_2 - a_2 b_1} \right) + \left( \frac{2\lambda_2^* a_1 - l_{12}b_1}{a_1 b_2 - a_2 b_1} \right) - 1 + O(0). \quad (C25)$$

It is clear to see that instead of performing the asymptotic expansion for the extremely complicated (B29)-(B32), we may simply expand (C22)-(C25) to obtain the asymptotic expressions for  $d_{ij}$ .

In this analysis, the 11-term asymptotic expression for  $D_{ijk}$  and  $B_{ij}$ , defined by (B35)-(B42) and (3.10), respectively, for  $\eta \rightarrow \infty$  or  $\xi \rightarrow 0$  are desired. The procedure used for the analysis is, first, obtaining the 11-term asymptotic expansions for  $n_1^*$  and  $n_2^*$ , substituting them into (B5) to compute the 11-term asymptotic expansions for  $m_1^*$  and  $m_2^*$ , obtaining the 11-term asymptotic expressions for  $a_1$ ,  $a_2$ ,  $b_1$ , and  $b_2$  by substituting the expansions of  $n_1^*$ ,  $n_2^*$ ,  $m_1^*$ , and  $m_2^*$  into (B13) and (B14), then substituting the results into (C22)-(C25) to determine the 11-term asymptotic expansions for  $d_{ij}$ , and finally substituting these series into (B35)-(B42) and then (3.10) to obtain the 10-term asymptotic expressions for  $D_{ijk}$  and  $B_{ij}$ . It may be seen that the asymptotic analysis described above involves only simple algebraic manipulation of polynomials once the asymptotic expansions for  $n_1^*$  and  $n_2^*$  are obtained.

The asymptotic analysis is performed by using symbolic manipulating software MAPLE. Because of the lengthy expression for the coefficients for higher order terms, only the expression for first 2 terms are given for  $D_{ijk}$ 's and  $B_{ij}$ 's, which are given by

$$D_{111} = \frac{2\lambda_1^*}{1 - \lambda_1^{*2}} + \frac{3\lambda_2^{*2} + \lambda_1^*\lambda_2^*(1 + \lambda_1^*\lambda_2^* - \lambda_1^{*2}) - (1 + \lambda_1^{*2})^2}{2\lambda_2^*(\lambda_1^* + \lambda_2^*)(1 - \lambda_1^{*2})^2} \left( \frac{\rho}{\eta} \right) + O\left(\frac{1}{\eta^2}\right), \quad (C26)$$

$$\begin{aligned}
D_{112} = & -\frac{(1+\lambda_1^{*2})^2}{2\lambda_2^*(1-\lambda_1^{*2})} \\
& + \frac{(\lambda_1^{*5} + \lambda_1^{*4}\lambda_2^* + 4\lambda_1^{*3} + 3\lambda_1^* - 8\lambda_1^*\lambda_2^{*2} - \lambda_2^*)(1+\lambda_1^{*2})}{8\lambda_2^{*2}(\lambda_1^* + \lambda_2^*)(1-\lambda_1^{*2})^2} \left(\frac{\rho}{\eta}\right) \quad (C27) \\
& + O\left(\frac{1}{\eta^2}\right),
\end{aligned}$$

$$D_{121} = -\frac{1+\lambda_1^{*2}}{1-\lambda_1^{*2}} + \frac{3\lambda_2^* - \lambda_1^* - \lambda_1^{*2}\lambda_2^* - \lambda_1^{*3}}{4\lambda_1^*(\lambda_1^* + \lambda_2^*)(1-\lambda_1^{*2})} \left(\frac{\rho}{\eta}\right) + O\left(\frac{1}{\eta^2}\right), \quad (C28)$$

$$D_{122} = \frac{1+\lambda_1^{*2}}{1-\lambda_1^{*2}} - \frac{(1+\lambda_1^{*2})(1-\lambda_1^*\lambda_2^*)}{4\lambda_1^*\lambda_2^*(\lambda_1^* + \lambda_2^*)(1-\lambda_1^{*2})} \left(\frac{\rho}{\eta}\right) + O\left(\frac{1}{\eta^2}\right), \quad (C29)$$

$$\begin{aligned}
D_{211} = & -\frac{1+\lambda_1^{*2}}{1-\lambda_1^{*2}} \\
& + \frac{(\lambda_1^{*4} + \lambda_1^{*3}\lambda_2^* + 2\lambda_1^{*2} - \lambda_1^{*2}\lambda_2^{*2} - \lambda_1^*\lambda_2^* - 3\lambda_2^{*2} + 1)(1+\lambda_1^{*2})}{4\lambda_1^*\lambda_2^*(\lambda_1^* + \lambda_2^*)(1-\lambda_1^{*2})^2} \left(\frac{\rho}{\eta}\right) \quad (C30) \\
& + O\left(\frac{1}{\eta^2}\right),
\end{aligned}$$

$$\begin{aligned}
D_{212} = & \frac{1+\lambda_1^{*2}}{1-\lambda_1^{*2}} \\
& - \frac{(\lambda_1^{*5} + \lambda_1^{*4}\lambda_2^* + 4\lambda_1^{*3} + 3\lambda_1^* - 8\lambda_1^*\lambda_2^{*2} - \lambda_2^*)(1+\lambda_1^{*2})}{4\lambda_2^*(\lambda_1^* + \lambda_2^*)(1-\lambda_1^{*2})^2} \left(\frac{\rho}{\eta}\right) + O\left(\frac{1}{\eta^2}\right), \quad (C31)
\end{aligned}$$

$$\begin{aligned}
D_{221} = & -\frac{(1+\lambda_1^{*2})^2}{2\lambda_1^*(1-\lambda_1^{*2})} \\
& + \frac{(3\lambda_2^* - \lambda_1^* - \lambda_1^{*2}\lambda_2^* - \lambda_1^{*3})(1+\lambda_1^{*2})}{8\lambda_1^{*2}(\lambda_1^* + \lambda_2^*)(1-\lambda_1^{*2})} \left(\frac{\rho}{\eta}\right) + O\left(\frac{1}{\eta^2}\right), \quad (C32)
\end{aligned}$$

$$D_{222} = \frac{2\lambda_2^*}{1-\lambda_1^{*2}} - \frac{(1-\lambda_1^*\lambda_2^*)}{2\lambda_1^*(\lambda_1^* + \lambda_2^*)(1-\lambda_1^{*2})} \left(\frac{\rho}{\eta}\right) + O\left(\frac{1}{\eta^2}\right), \quad (C33)$$

$$B_{ij} = B_{ij1} \left(\frac{1}{\eta}\right) + B_{ij2} \left(\frac{1}{\eta^2}\right) + O\left(\frac{1}{\eta^3}\right), \quad i, j = 1, 2, \quad (C34)$$

where

$$B_{111} = \rho \left( \lambda_1^{*7} + \lambda_1^{*6}\lambda_2^* + 5\lambda_1^{*5} - 3\lambda_1^{*4}\lambda_2^* + 7\lambda_1^{*3} - 12\lambda_1^{*3}\lambda_2^{*2} + 4\lambda_1^{*2}\lambda_2^{*3} - 9\lambda_1^{*2}\lambda_2^* + 3\lambda_1^* - 4\lambda_1^*\lambda_2^{*2} - 5\lambda_2^* + 12\lambda_2^{*3} \right) / \left[ 8\lambda_2^{*2}(\lambda_1^* + \lambda_2^*)(1 - \lambda_1^{*2})^2 \right], \quad (\text{C35})$$

$$B_{112} = \frac{[4\lambda_1^*\lambda_2^* - (1 + \lambda_1^{*2})^2](\lambda_1^{*2} - 2\lambda_1^*\lambda_2^* + 1)(\lambda_1^{*2} - 2\lambda_2^{*2} + 1)}{8\lambda_1^*\lambda_2^{*3}(\lambda_1^* + \lambda_2^*)(1 - \lambda_1^{*2})^3}, \quad (\text{C36})$$

$$B_{121} = - \frac{\rho(\lambda_1^{*2} + \lambda_1^{*2}\lambda_2^{*2} - 3\lambda_2^{*2} + 1)}{4\lambda_1^*\lambda_2^*(\lambda_1^* + \lambda_2^*)(1 - \lambda_1^{*2})}, \quad (\text{C37})$$

$$B_{122} = \frac{[4\lambda_1^*\lambda_2^* - (1 + \lambda_1^{*2})^2](\lambda_1^{*2} - 2\lambda_1^*\lambda_2^* + 1)}{16\lambda_1^{*2}\lambda_2^{*2}(1 - \lambda_1^{*2})^2}, \quad (\text{C38})$$

$$B_{211} = \frac{\rho(\lambda_1^{*2} + \lambda_1^{*2}\lambda_2^{*2} - 3\lambda_2^{*2} + 1)}{4\lambda_1^*\lambda_2^*(\lambda_1^* + \lambda_2^*)(1 - \lambda_1^{*2})}, \quad (\text{C39})$$

$$B_{212} = - \frac{[4\lambda_1^*\lambda_2^* - (1 + \lambda_1^{*2})^2](\lambda_1^{*2} - 2\lambda_1^*\lambda_2^* + 1)}{16\lambda_1^{*2}\lambda_2^{*2}(1 - \lambda_1^{*2})^2}, \quad (\text{C40})$$

$$B_{221} = - \frac{\rho(\lambda_1^{*5} + \lambda_1^{*4}\lambda_2^* + 2\lambda_1^{*3} - 6\lambda_1^{*2}\lambda_2^* + 5\lambda_1^* - 3\lambda_2^*)}{8\lambda_1^{*2}(\lambda_1^* + \lambda_2^*)(1 - \lambda_1^{*2})}, \quad (\text{C41})$$

$$B_{222} = \frac{[4\lambda_1^*\lambda_2^* - (1 + \lambda_1^{*2})^2](\lambda_1^{*2} - 2\lambda_1^*\lambda_2^* + 1)}{8\lambda_1^{*3}\lambda_2^*(\lambda_1^* + \lambda_2^*)(1 - \lambda_1^{*2})^2}. \quad (\text{C42})$$

Note that the relation  $B_{12k} = -B_{21k}$ ,  $k = 1, 2, \dots$ , is observed in the asymptotic analysis.

## Appendix D

### Formula for Evaluating the Asymptotic Kernels

It may be seen that the integrals involving the asymptotic series in the Fredholm kernels (3.16), (3.17), (3.22), and (3.23) have the following two general forms:

$$C_k(\omega) = \int_A^\infty \frac{\cos \omega \eta}{\eta^k} d\eta, \quad k = 1, 2, \dots, \quad (D1)$$

$$S_k(\omega) = \int_A^\infty \frac{\sin \omega \eta}{\eta^k} d\eta, \quad k = 1, 2, \dots, \quad (D2)$$

To determine  $C_k$  and  $S_k$ , first we make a change of variable as follows:

$$t = |\omega| \eta, \quad (D3)$$

and  $C_k$  and  $S_k$  can be rewritten as

$$C_k(\omega) = |\omega|^{k-1} \int_{|\omega|A}^\infty \frac{\cos t}{t^k} dt, \quad (D4)$$

$$S_k(\omega) = \frac{|\omega|^k}{\omega} \int_{|\omega|A}^\infty \frac{\sin t}{t^k} dt. \quad (D5)$$

Now consider the integrals in (D4) and (D5). For the case of  $k = 1$  we have

$$\int_{|\omega|A}^\infty \frac{\cos t}{t} dt = -\text{Ci}(|\omega|A), \quad (D6)$$

$$\begin{aligned} \int_{|\omega|A}^\infty \frac{\sin t}{t} dt &= \int_0^\infty \frac{\sin t}{t} dt - \text{Si}(|\omega|A) \\ &= \frac{\pi}{2} - \text{Si}(|\omega|A), \end{aligned} \quad (D7)$$

where

$$\text{Ci}(x) = \gamma_0 + \ln(x) + \int_0^x \frac{\cos t - 1}{t} dt, \quad x > 0, \quad (D8)$$

$$\text{Si}(x) = \int_0^x \frac{\sin t}{t} dt, \quad x > 0. \quad (\text{D9})$$

Integrating by parts, we may express the integrals in (D4) and (D5) for  $k > 1$  as follows:

$$\begin{aligned} \int_{|\omega|A}^{\infty} \frac{\cos t}{t^k} dt &= - \frac{\cos t}{(k-1)t^{k-1}} \Big|_{t=|\omega|A}^{\infty} - \frac{1}{k-1} \int_{|\omega|A}^{\infty} \frac{\sin t}{t^{k-1}} dt \\ &= \frac{1}{k-1} \left[ \frac{\cos(|\omega|A)}{(|\omega|A)^{k-1}} - \int_{|\omega|A}^{\infty} \frac{\sin t}{t^{k-1}} dt \right], \end{aligned} \quad (\text{D10})$$

$$\begin{aligned} \int_{|\omega|A}^{\infty} \frac{\sin t}{t^k} dt &= - \frac{\sin t}{(k-1)t^{k-1}} \Big|_{t=|\omega|A}^{\infty} + \frac{1}{k-1} \int_{|\omega|A}^{\infty} \frac{\cos t}{t^{k-1}} dt \\ &= \frac{1}{k-1} \left[ \frac{\sin(|\omega|A)}{(|\omega|A)^{k-1}} + \int_{|\omega|A}^{\infty} \frac{\cos t}{t^{k-1}} dt \right]. \end{aligned} \quad (\text{D11})$$

By substituting (D6)-(D11) into (D4) and (D5),  $C_k$ 's and  $S_k$ 's may be expressed as follows:

$$C_1(\omega) = -\text{Ci}(|\omega|A), \quad (\text{D12})$$

$$S_1(\omega) = \frac{|\omega|}{\omega} \left[ \frac{\pi}{2} - \text{Si}(|\omega|A) \right], \quad (\text{D13})$$

$$C_k(\omega) = \frac{1}{k-1} \left[ \frac{\cos(|\omega|A)}{A^{k-1}} + \omega S_{k-1}(\omega) \right], \quad k > 1, \quad (\text{D14})$$

$$S_k(\omega) = \frac{1}{k-1} \left[ \left( \frac{|\omega|}{\omega} \right) \frac{\sin(|\omega|A)}{A^{k-1}} + \omega C_{k-1}(\omega) \right], \quad k > 1, \quad (\text{D15})$$

## Appendix E

### Matrices and Vectors Used in the Two-dimensional Element Formulation

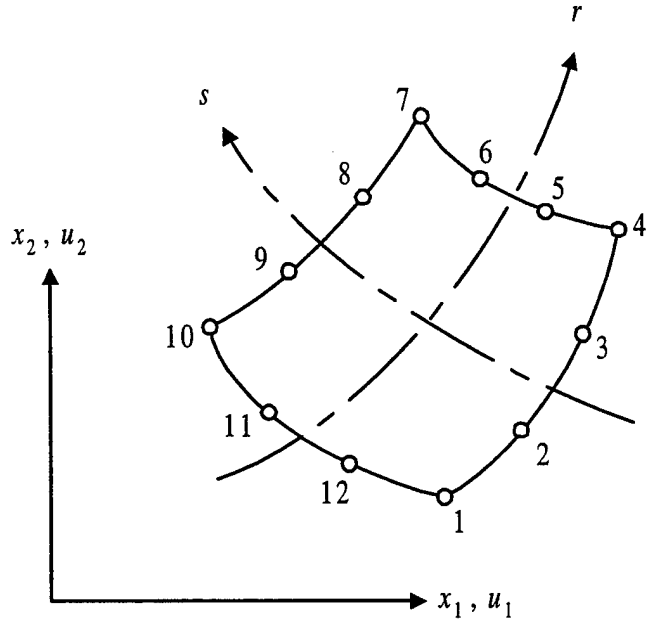


Figure E.1 Two-dimensional 12-noded isoparametric element.

For the derivation of the matrices and vectors, we consider a typical two-dimensional element at time  $t$  as shown in Figure E.1. For isoparametric element formulation, we write the element coordinates and displacements as

$${}^0x_1 = \sum_{k=1}^M N_k {}^0x_1^k; \quad {}^0x_2 = \sum_{k=1}^M N_k {}^0x_2^k, \quad (E1)$$

$${}^t u_1 = \sum_{k=1}^M N_k {}^t u_1^k; \quad {}^t u_2 = \sum_{k=1}^M N_k {}^t u_2^k, \quad (E2)$$

where  $M$  is the number of nodes in the element,  $N_k$  is the interpolation function,  ${}^0x_1^k$  and  ${}^0x_2^k$  are the global coordinates of the nodal points at time 0, and  ${}^t u_1^k$  and  ${}^t u_2^k$  are the

displacements of the nodal points at time  $t$ . Similarly, the incremental displacements  $u_1$  and  $u_2$  in terms of incremental nodal displacements  $u_1^k$  and  $u_2^k$  are given by

$$u_1 = \sum_{k=1}^M N_k u_1^k; \quad u_2 = \sum_{k=1}^M N_k u_2^k. \quad (\text{E3})$$

Note that the superscript  $(n)$  which refers to the values of displacements, strains, and stresses computed in the  $n$ -th iteration for certain increment is omitted in this Appendix. However, it is important to note that the values computed from  $(n-1)$ -th iteration are used for evaluating the matrices and vectors with a superscript  $(n)$ .

First we consider the axisymmetric problem in which the coordinate  $(^0x_1, ^0x_2)$  refers to  $(r, z)$ . To determine the linear strain-displacement transformation matrix  ${}_0\mathbf{B}_L^{(n)}$ , the following incremental linear strain and incremental displacement vectors are defined

$${}_0\widehat{\mathbf{e}}^{(n)T} = \left\{ {}_0e_{11}, {}_0e_{22}, 2{}_0e_{12}, {}_0e_{33} \right\}, \quad (\text{E4})$$

$$\widehat{\mathbf{U}}^{(n)T} = \left\{ u_1^1, u_2^1, u_1^2, u_2^2, \dots, u_1^M, u_2^M \right\}, \quad (\text{E5})$$

giving

$${}_0\widehat{\mathbf{e}}^{(n)} = {}_0^t\mathbf{B}_L^{(n)} \widehat{\mathbf{U}}^{(n)}, \quad (\text{E6})$$

where

$${}^t_0\mathbf{B}_L^{(n)} = \begin{pmatrix}
(1+l_{11})_0N_{1,1} & l_{21}{}_0N_{1,1} & \dots \\
l_{12}{}_0N_{1,2} & (1+l_{22})_0N_{1,2} & \dots \\
(1+l_{11})_0N_{1,2} + l_{12}{}_0N_{1,1} & (1+l_{22})_0N_{1,1} + l_{21}{}_0N_{1,2} & \dots \\
(1+l_{33})\frac{N_1}{{}^0\bar{x}_1} & 0 & \dots \\
\vdots & (1+l_{11})_0N_{i,1} & l_{21}{}_0N_{i,1} \\
\vdots & l_{12}{}_0N_{i,2} & (1+l_{22})_0N_{i,2} \\
\vdots & (1+l_{11})_0N_{i,2} + l_{12}{}_0N_{i,1} & (1+l_{22})_0N_{i,1} + l_{21}{}_0N_{i,2} \\
\vdots & (1+l_{33})\frac{N_i}{{}^0\bar{x}_1} & 0 \\
\vdots & (1+l_{11})_0N_{M,1} & l_{21}{}_0N_{M,1} \\
\vdots & l_{12}{}_0N_{M,2} & (1+l_{22})_0N_{M,2} \\
\vdots & (1+l_{11})_0N_{M,2} + l_{12}{}_0N_{M,1} & (1+l_{22})_0N_{M,1} + l_{21}{}_0N_{M,2} \\
\vdots & (1+l_{33})\frac{N_M}{{}^0\bar{x}_1} & 0
\end{pmatrix}, \quad 1 < i < M,$$

in which  ${}^0\bar{x}_1$  denotes the  ${}^0x_1$  value of the Gaussian point where  ${}^t_0\mathbf{B}^{(n)}$  is evaluated,  ${}_0N_{k,j}$  is given by

$${}_0N_{k,j} = \frac{\partial N_k}{\partial {}^0x_j}, \quad (E8)$$

and  $l_{ij}$  are defined as

$$l_{ij} = \sum_{k=1}^M {}_0N_{k,j} {}^t u_i^k, \quad i, j = 1, 2; \quad l_{33} = \frac{\sum_{k=1}^M N_k {}^t u_1^k}{{}^0\bar{x}_1}. \quad (E9)$$

Similarly, the nonlinear strain-displacement transformation matrix  $\mathbf{B}_{NL}$  related to  ${}_0\eta_{ij}$  in (4.36) is given by

$$\mathbf{B}_{NL} = \begin{pmatrix} {}_0N_{1,1} & 0 & {}_0N_{2,1} & 0 & \dots & {}_0N_{M,1} & 0 \\ {}_0N_{1,2} & 0 & {}_0N_{2,2} & 0 & \dots & {}_0N_{M,2} & 0 \\ 0 & {}_0N_{1,1} & 0 & {}_0N_{2,1} & \dots & 0 & {}_0N_{M,1} \\ 0 & {}_0N_{1,2} & 0 & {}_0N_{2,2} & \dots & 0 & {}_0N_{M,2} \\ \frac{N_1}{{}^0\bar{x}_1} & 0 & \frac{N_2}{{}^0\bar{x}_1} & 0 & \dots & \frac{N_M}{{}^0\bar{x}_1} & 0 \end{pmatrix}. \quad (\text{E10})$$

The stress matrix corresponding to  $\mathbf{B}_{NL}$  in (4.43) and the stress vector corresponding to  ${}^t_0\mathbf{B}_L^{(n)}$  in (4.45) may then be expressed, respectively, as

$${}^t_0\mathbf{S}^{(n)} = \begin{pmatrix} {}^t_0\sigma_{11} & {}^t_0\sigma_{12} & 0 & 0 & 0 \\ {}^t_0\sigma_{12} & {}^t_0\sigma_{22} & 0 & 0 & 0 \\ 0 & 0 & {}^t_0\sigma_{11} & {}^t_0\sigma_{12} & 0 \\ 0 & 0 & {}^t_0\sigma_{12} & {}^t_0\sigma_{22} & 0 \\ 0 & 0 & 0 & 0 & {}^t_0\sigma_{33} \end{pmatrix}, \quad (\text{E11})$$

$${}^t\widehat{\mathbf{S}}^{(n)\top} = \left\{ {}^t_0\sigma_{11}, {}^t_0\sigma_{22}, {}^t_0\sigma_{12}, {}^t_0\sigma_{33} \right\}. \quad (\text{E12})$$

For the linear elastic, isotropic, and inhomogeneous medium investigated in this study, we may write the constitutive equation for the asymmetric problem as

$${}^t_0\widehat{\mathbf{S}} = \mathbf{C} {}^t_0\widehat{\boldsymbol{\epsilon}} + {}^t_0\widehat{\mathbf{S}}_T, \quad (\text{E13})$$

where  ${}^t_0\widehat{\mathbf{S}}$  is given in (E12) and

$$\mathbf{C} = \frac{E}{(1+\nu)(1-2\nu)} \begin{pmatrix} 1-\nu & \nu & 0 & \nu \\ \nu & 1-\nu & 0 & \nu \\ 0 & 0 & \frac{1-2\nu}{2} & 0 \\ \nu & \nu & 0 & 1-\nu \end{pmatrix}, \quad (\text{E14})$$

$${}^t_0\widehat{\boldsymbol{\epsilon}}^\top = \left\{ {}^t_0\epsilon_{11}, {}^t_0\epsilon_{22}, 2{}^t_0\epsilon_{12}, {}^t_0\epsilon_{33} \right\}, \quad (\text{E15})$$

$${}^t_0\widehat{\mathbf{S}}_T^\top = -\frac{E\alpha T}{(1-2\nu)} \left\{ 1, 1, 0, 1 \right\}, \quad (\text{E16})$$

$T$  being the temperature change between "time  $t$ " and "time 0". Similarly, we may write the incremental thermal stress  ${}^t_0\widehat{\mathbf{S}}_T$  as

$${}_0\widehat{\mathbf{S}}_T^T = -\frac{E\alpha(\Delta T)}{(1-2\nu)} \{ 1, 1, 0, 1 \}, \quad (E17)$$

$\Delta T$  being the temperature change between "time  $t + \Delta t$ " and "time  $t$ ".

For plane strain problem in which  $({}^0x_1, {}^0x_2)$  refers to  $(x, y)$ , it may be seen that the matrices and vectors are very similar to the ones used for axisymmetric problems and only minor modifications on (E4)-(E17) are needed: for  ${}_0\widehat{\mathbf{e}}^{(n)}$ ,  ${}_0\widehat{\mathbf{S}}^{(n)}$ ,  ${}_0\widehat{\boldsymbol{\epsilon}}$ ,  ${}_0\widehat{\mathbf{S}}_T$ , and  ${}_0\widehat{\mathbf{S}}_T^T$ , we remove the last entry in the vectors in (E4), (E12), (E15), (E16), and (E17), respectively; for  ${}_0^t\mathbf{B}_L^{(n)}$  and  $\mathbf{B}_{NL}$ , the last rows in (E7) and (E10), respectively, are removed; for  ${}_0^t\mathbf{S}^{(n)}$  and  $\mathbf{C}$ , the last columns and last rows in (E11) and (E14) are removed.

The matrices and vectors used for the plane stress problem are the same as the ones used for the plane strain problem except the following constitutive law related matrix and vectors:

$$\mathbf{C} = \frac{E}{1-\nu^2} \begin{pmatrix} 1 & \nu & 0 \\ \nu & 1 & 0 \\ 0 & 0 & \frac{1-\nu}{2} \end{pmatrix} \quad (\text{plane stress}), \quad (E18)$$

$${}_0^t\widehat{\mathbf{S}}_T^T = -\frac{E\alpha T}{(1-\nu)} \{ 1, 1, 0 \} \quad (\text{plane stress}), \quad (E19)$$

$${}_0\widehat{\mathbf{S}}_T^T = -\frac{E\alpha(\Delta T)}{(1-\nu)} \{ 1, 1, 0 \} \quad (\text{plane stress}). \quad (E20)$$

## Appendix F

### Functions and Matrices Used in the Enriched Finite Elements

The functions used in the asymptotic displacement expressions (4.51) for an interface crack between two distinct isotropic materials (Figure 4.2) are given by

$$\begin{aligned} f_{1j} &= F_{1j} \cos \phi - G_{1j} \sin \phi, & g_{1j} &= F_{2j} \cos \phi - G_{2j} \sin \phi, \\ f_{2j} &= F_{1j} \sin \phi + G_{1j} \cos \phi, & g_{2j} &= F_{2j} \sin \phi + G_{2j} \cos \phi, \end{aligned} \quad (\text{F1})$$

where

$$\begin{aligned} F_{1j} &= \frac{1}{4\mu_j \cosh(\pi\epsilon)} \sqrt{\frac{r}{2\pi}} (D_j + 2\delta \sin \theta \sin \Theta), \\ F_{2j} &= -\frac{1}{4\mu_j \cosh(\pi\epsilon)} \sqrt{\frac{r}{2\pi}} (E_j - 2\delta \sin \theta \cos \Theta), \\ G_{1j} &= -\frac{1}{4\mu_j \cosh(\pi\epsilon)} \sqrt{\frac{r}{2\pi}} (E_j + 2\delta \sin \theta \cos \Theta), \\ G_{2j} &= -\frac{1}{4\mu_j \cosh(\pi\epsilon)} \sqrt{\frac{r}{2\pi}} (D_j - 2\delta \sin \theta \sin \Theta), \end{aligned} \quad (\text{F2})$$

$$\epsilon = \frac{1}{2\pi} \ln \left[ \left( \frac{\kappa_1}{\mu_1} + \frac{1}{\mu_2} \right) / \left( \frac{\kappa_2}{\mu_2} + \frac{1}{\mu_1} \right) \right], \quad (\text{F3})$$

$$\delta_1 = e^{-(\pi-\theta)\epsilon}, \quad \delta_2 = e^{(\pi+\theta)\epsilon}, \quad (\text{F4})$$

$$\Theta = \epsilon \ln r + \frac{\theta}{2}, \quad (\text{F5})$$

$$D_j = \beta \gamma_j \cos \frac{\theta}{2} + \beta' \gamma'_j \sin \frac{\theta}{2}, \quad E_j = \beta' \gamma_j \cos \frac{\theta}{2} - \beta \gamma'_j \sin \frac{\theta}{2}, \quad (\text{F6})$$

$$\beta = \frac{0.5 \cos(\epsilon \ln r) + \epsilon \sin(\epsilon \ln r)}{0.25 + \epsilon^2}, \quad \beta' = \frac{0.5 \sin(\epsilon \ln r) - \epsilon \cos(\epsilon \ln r)}{0.25 + \epsilon^2}, \quad (\text{F7})$$

$$\gamma_j = \kappa_j \delta_j - \frac{1}{\delta_j}, \quad \gamma'_j = \kappa_j \delta_j + \frac{1}{\delta_j}. \quad (\text{F8})$$

By following the same terminology used in Appendix E, the linear and nonlinear strain-displacement transformation matrices for the enriched elements are given as follows:

$$\begin{aligned} {}_0^t \mathbf{B}_{EL}^{(n)} = & \begin{pmatrix} (1 + l_{11}^*)_0 N_{1,1} & l_{21}^* {}_0 N_{1,1} \\ l_{12}^* {}_0 N_{1,2} & (1 + l_{22}^*)_0 N_{1,2} \\ (1 + l_{11}^*)_0 N_{1,2} + l_{12}^* {}_0 N_{1,1} & (1 + l_{22}^*)_0 N_{1,1} + l_{21}^* {}_0 N_{1,2} \\ (1 + l_{33}^*) \frac{N_1}{{}_0 \bar{x}_1} & 0 \end{pmatrix} \\ & \begin{pmatrix} (1 + l_{11}^*)_0 N_{i,1} & l_{21}^* {}_0 N_{i,1} & \dots \\ l_{12}^* {}_0 N_{i,2} & (1 + l_{22}^*)_0 N_{i,2} & \dots \\ (1 + l_{11}^*)_0 N_{i,2} + l_{12}^* {}_0 N_{i,1} & (1 + l_{22}^*)_0 N_{i,1} + l_{21}^* {}_0 N_{i,2} & \dots \\ (1 + l_{33}^*) \frac{N_i}{{}_0 \bar{x}_1} & 0 & \dots \end{pmatrix} \\ & \begin{pmatrix} \dots & (1 + l_{11}^*)_0 N_{M,1} & l_{21}^* {}_0 N_{M,1} \\ \dots & l_{12}^* {}_0 N_{M,2} & (1 + l_{22}^*)_0 N_{M,2} \\ \dots & (1 + l_{11}^*)_0 N_{M,2} + l_{12}^* {}_0 N_{M,1} & (1 + l_{22}^*)_0 N_{M,1} + l_{21}^* {}_0 N_{M,2} \\ \dots & (1 + l_{33}^*) \frac{N_M}{{}_0 \bar{x}_1} & 0 \end{pmatrix} \\ & \begin{pmatrix} B_{1(M+1)} & B_{1(M+2)} \\ B_{2(M+1)} & B_{2(M+2)} \\ B_{3(M+1)} & B_{3(M+2)} \\ B_{4(M+1)} & B_{4(M+2)} \end{pmatrix}, \end{aligned} \quad (\text{F9})$$

$$\mathbf{B}_{ENL} = (1 - Z) \begin{pmatrix} {}_0N_{1,1} & 0 & {}_0N_{2,1} & 0 & \dots \\ {}_0N_{1,2} & 0 & {}_0N_{2,2} & 0 & \dots \\ 0 & {}_0N_{1,1} & 0 & {}_0N_{2,1} & \dots \\ 0 & {}_0N_{1,2} & 0 & {}_0N_{2,2} & \dots \\ \frac{N_1}{{}^0\bar{x}_1} & 0 & \frac{N_2}{{}^0\bar{x}_1} & 0 & \dots \\ \dots & {}_0N_{M,1} & 0 & 0 & 0 \\ \dots & {}_0N_{M,2} & 0 & 0 & 0 \\ \dots & 0 & {}_0N_{M,1} & 0 & 0 \\ \dots & 0 & {}_0N_{M,2} & 0 & 0 \\ \dots & \frac{N_M}{{}^0\bar{x}_1} & 0 & 0 & 0 \end{pmatrix}, \quad (F10)$$

where

$$l_{ij}^* = (1 - Z)l_{ij}, \quad (\text{F11})$$

$$B_{1(M+1)} = Z \left( \frac{\partial f_{1j}}{\partial^0 x_1} - \sum_{k=1}^M \frac{\partial N_k}{\partial^0 x_1} f_{1j}^k \right) + \frac{\partial Z}{\partial^0 x_1} \left( f_{1j} - \sum_{k=1}^M N_k f_{1j}^k \right), \quad (\text{F12})$$

$$B_{1(M+2)} = Z \left( \frac{\partial g_{1j}}{\partial^0 x_1} - \sum_{k=1}^M \frac{\partial N_k}{\partial^0 x_1} g_{1j}^k \right) + \frac{\partial Z}{\partial^0 x_1} \left( g_{1j} - \sum_{k=1}^M N_k g_{1j}^k \right), \quad (\text{F13})$$

$$B_{2(M+1)} = Z \left( \frac{\partial f_{2j}}{\partial^0 x_2} - \sum_{k=1}^M \frac{\partial N_k}{\partial^0 x_2} f_{2j}^k \right) + \frac{\partial Z}{\partial^0 x_2} \left( f_{2j} - \sum_{k=1}^M N_k f_{2j}^k \right), \quad (\text{F14})$$

$$B_{2(M+2)} = Z \left( \frac{\partial g_{2j}}{\partial^0 x_2} - \sum_{k=1}^M \frac{\partial N_k}{\partial^0 x_2} g_{2j}^k \right) + \frac{\partial Z}{\partial^0 x_2} \left( g_{2j} - \sum_{k=1}^M N_k g_{2j}^k \right), \quad (\text{F15})$$

$$\begin{aligned}
B_{3(M+1)} = & Z \left( \frac{\partial f_{1j}}{\partial^0 x_2} - \sum_{k=1}^M \frac{\partial N_k}{\partial^0 x_2} f_{1j}^k + \frac{\partial f_{2j}}{\partial^0 x_1} - \sum_{k=1}^M \frac{\partial N_k}{\partial^0 x_1} f_{2j}^k \right) \\
& + \frac{\partial Z}{\partial^0 x_2} \left( f_{1j} - \sum_{k=1}^M N_k f_{1j}^k \right) + \frac{\partial Z}{\partial^0 x_1} \left( f_{2j} - \sum_{k=1}^M N_k f_{2j}^k \right), \tag{F16}
\end{aligned}$$

$$\begin{aligned}
B_{3(M+2)} = & Z \left( \frac{\partial g_{1j}}{\partial^0 x_2} - \sum_{k=1}^M \frac{\partial N_k}{\partial^0 x_2} g_{1j}^k + \frac{\partial g_{2j}}{\partial^0 x_1} - \sum_{k=1}^M \frac{\partial N_k}{\partial^0 x_1} g_{2j}^k \right) \\
& + \frac{\partial Z}{\partial^0 x_2} \left( g_{1j} - \sum_{k=1}^M N_k g_{1j}^k \right) + \frac{\partial Z}{\partial^0 x_1} \left( g_{2j} - \sum_{k=1}^M N_k g_{2j}^k \right), \tag{F17}
\end{aligned}$$

$$B_{4(M+1)} = \left( f_{1j} - \sum_{k=1}^M N_k f_{1j}^k \right) \Big/ {}^0 \bar{x}_1, \tag{F18}$$

$$B_{4(M+2)} = \left( g_{1j} - \sum_{k=1}^M N_k g_{1j}^k \right) \Big/ {}^0 \bar{x}_1. \tag{F19}$$

Note that the matrices (F9) and (F10) are given for axisymmetric problem. The linear and nonlinear transformation matrices for plane problem may be obtained by simply removing the last row in (F9) and (F10). The zeroing function  $Z$  has a value of unity for the enriched crack-tip elements; and for transition elements  $Z$  varies from one at the edges in contact with crack-tip elements to zero at the boundaries with regular nonlinear elements.

A linear zeroing function  $Z$  in terms of local coordinate  $(r, s)$  is given by

$$Z(r, s) = \begin{cases} \frac{1}{4}(1 \pm r)(1 \pm s), & \text{for zeroing from corner node,} \\ \frac{1}{2}(1 \pm r), & \text{for zeroing from element edge,} \\ \frac{1}{2}(1 \pm s), & \text{for zeroing from element edge.} \end{cases} \tag{F20}$$

## Appendix G

### Test Examples of the Finite Element Implementation

#### G.1 The Elastica Problem

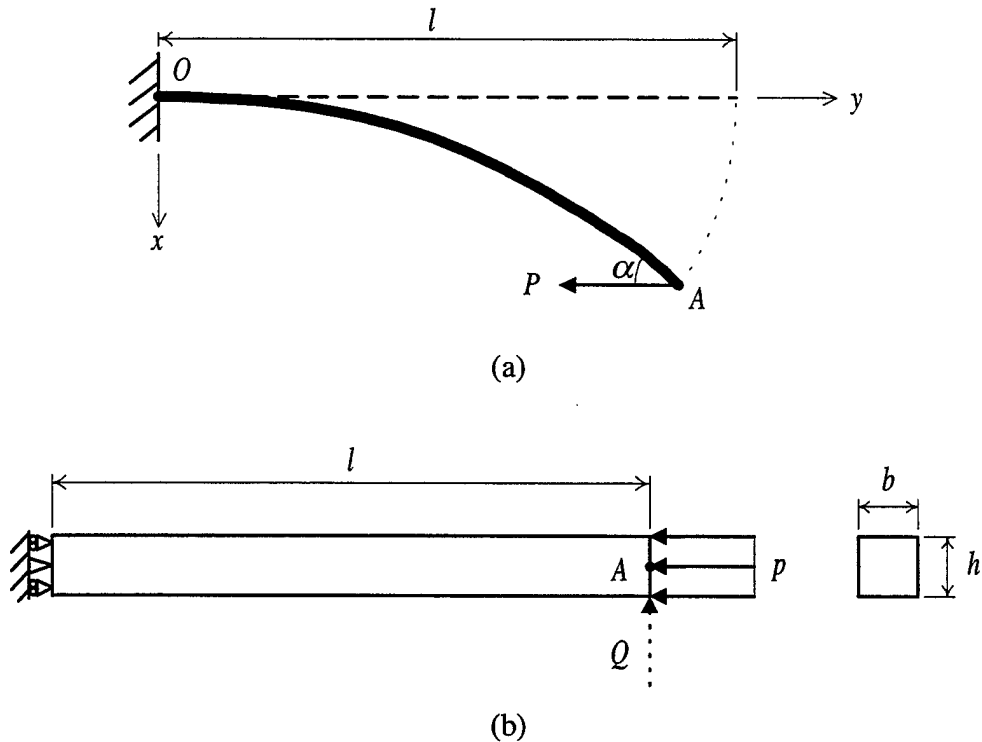


Figure G.1 (a) The elastica problem, (b) Finite element model used for simulating the elastica problem.

The problem of large deflection of a buckled column (the elastica) [87] described in Figure G.1(a) is used to test the finite deformation implementation in the finite element code. In the elastica [87] it is assumed that the cantilever column under consideration is inextensible and the load  $P$  remains in the direction parallel to  $y$ -axis. The displacements at point  $A$  is given by [87]

$$u_a = \frac{2}{k} E(\beta) - 2l, \quad v_a = \frac{2\beta}{k}, \quad \text{for } P \geq P_{\text{cr}}, \quad (\text{G1})$$

where

$$k = \sqrt{P/EI}, \quad \beta = \sin(\alpha/2), \quad kl = K(\beta), \quad P_{\text{cr}} = \frac{\pi^2 EI}{4l^2}, \quad (\text{G2})$$

$$K(\beta) = \int_0^{\pi/2} \frac{d\phi}{\sqrt{1 - \beta^2 \sin^2 \phi}}, \quad E(\beta) = \int_0^{\pi/2} \sqrt{1 - \beta^2 \sin^2 \phi} d\phi,$$

$P_{\text{cr}}$  being the Euler buckling load,  $K(\beta)$  and  $E(\beta)$  being known as the complete elliptic integral of the first and second kind, respectively. Note that the solution (G1) is given in such a way that the unknown displacements ( $u_a$ ,  $v_a$ ) and the input load  $P$  are expressed in terms of the deflection angle  $\alpha$  at point  $A$ .

Using finite element program, the model in Figure G.1(b) is used to study the elastica problem. To simulate the slender column the relative dimensions are used:  $l/h = 50$ ,  $b/h = 1$ , where  $l$ ,  $b$ , and  $h$  are the length, thickness, and width of the bar. By gradually increasing the uniform compressive pressure  $p$  ( $= P/bh$ ), the displacements at point  $A$  are obtained as a function of  $P$  from the incremental-iterative finite element procedure described in Chapter 4. Intuitively it may be seen that under axial compressive loading condition as shown in Figure G.1(b) ( $Q = 0$ ), the column would simply "shrink" rather than buckle no matter how large the compressive pressure is. Therefore, initially a transverse force  $Q$  acting as a disturbance to introduce transverse displacement of point  $A$  is applied to point  $A$ ; a reverse loading  $-Q$  is applied at a later stage after the main loading  $P$  exceeded the critical load  $P_{\text{cr}}$ . By doing this we can obtain an equilibrium configuration for the column at certain value of  $P > P_{\text{cr}}$  on the preferred branch (nontrivial solution) in the displacement vs. loading bifurcation diagram. We may then start from this equilibrium configuration and gradually either increase  $P$  or decrease  $P$  to

recover the displacement/loading relation for the elastica problem. This solution procedure can be seen from Figure G.2 which gives the  $x$ - displacement of point  $A$  vs. loading  $P$ . In this particular case we choose the loading parameters  $P^* = 1.063P_{\text{cr}}$  and  $Q^* = P^*/20$ . The axial and transverse loadings  $P, Q$  are incrementally applied in such a way that at first (i) increase  $P$  and  $Q$  from zero to  $P^*/2$  and  $Q^*$ , respectively, then (ii)  $P = P^*/2 \rightarrow P^*$ ,  $Q = Q^* \rightarrow 0$ , after that (iii) increase or decrease  $P$  from  $P^*$  and  $Q = 0$ . The stages (i) and (ii) are shown in Figure G.2 as dotted and dashed line, respectively.

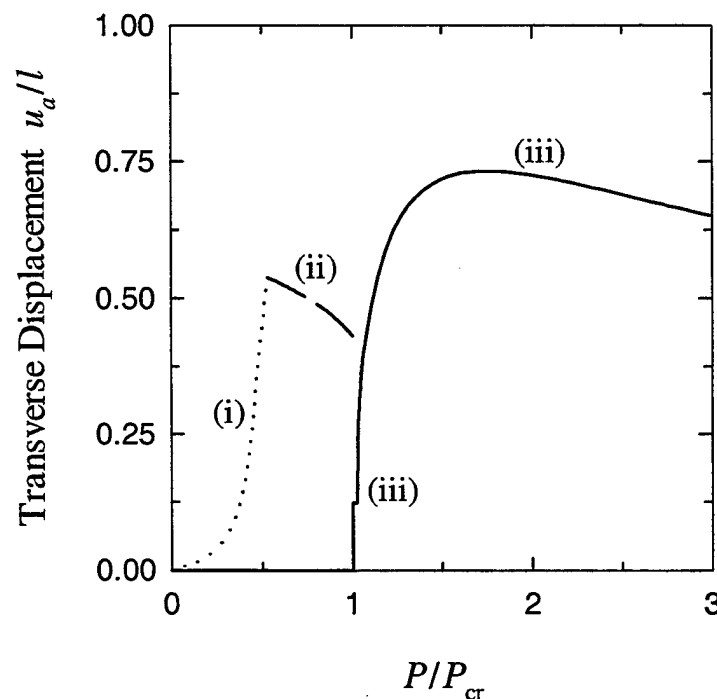


Figure G.2 Transverse displacement of point  $A$  for the problem described in Figure G.1(b), the applied loadings: (i)  $P = 0 \rightarrow P^*/2$ ,  $Q = 0 \rightarrow Q^*$ , (ii)  $P = P^*/2 \rightarrow P^*$ ,  $Q = Q^* \rightarrow 0$ , (iii)  $P = P^* \rightarrow 3P_{\text{cr}}$  or  $P = P^* \rightarrow 0$ ,  $Q^* = 0$  ( $P = bhp$ ,  $P^* = 1.063P_{\text{cr}}$ ,  $Q^* = P^*/20$ ).

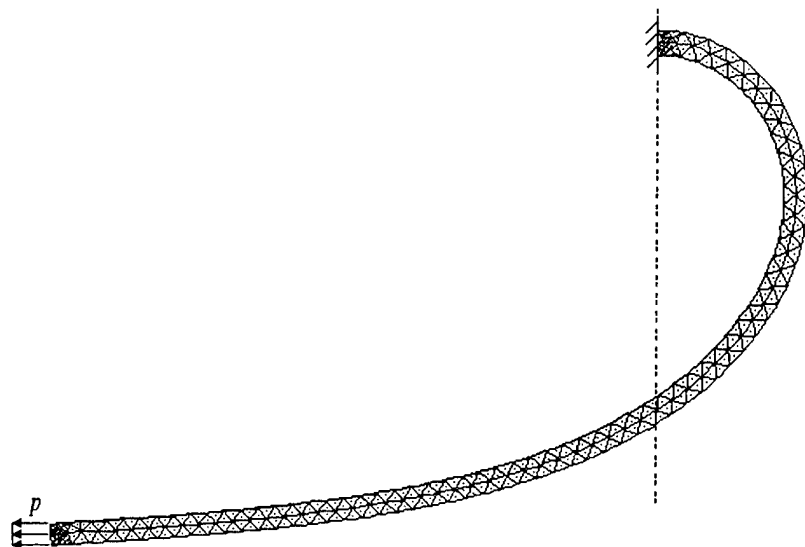


Figure G.3 The deformed shape of slender bar at  $P = bhp = 9P_{\text{cr}}$ .

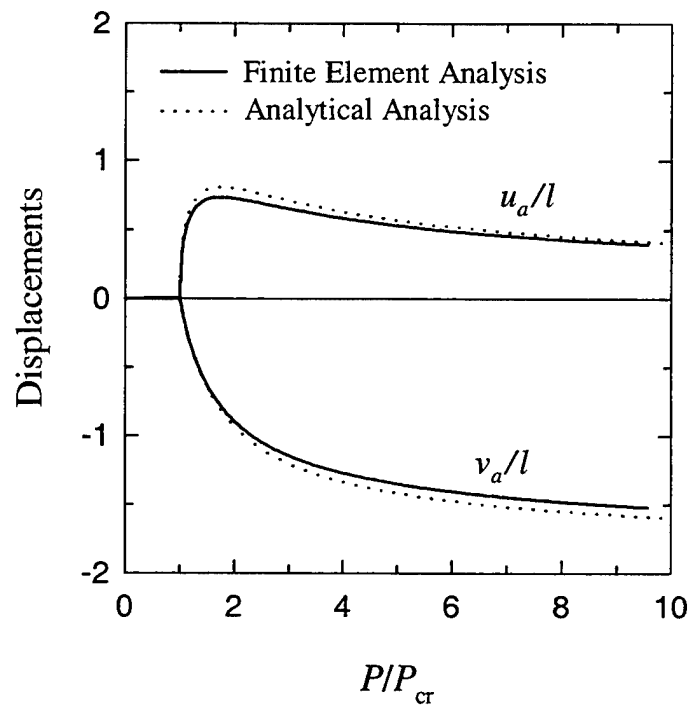


Figure G.4 Displacement components of point  $A$  in the elastica problem described in Figure G.1.

The deflected shape of the column at  $P/P_{cr} = 9$  is shown in Figure G.3. Figure G.4 shows the displacements of point  $A$  as a function of compressive load  $P$  from both analytical and finite element methods. As can be seen in Figure G.4, the results match quite well for  $1 < P/P_{cr} < 1.5$  and the difference between analytical and finite element results is less than 7% difference for  $1.5 < P/P_{cr} < 9.5$ . This difference may be attributed to the assumption used in the analytical formulation that the column is inextensible, and as expected, the difference becomes more significant at higher load.

## G.2 Interface Crack in FGM coating/Homogeneous Substrate

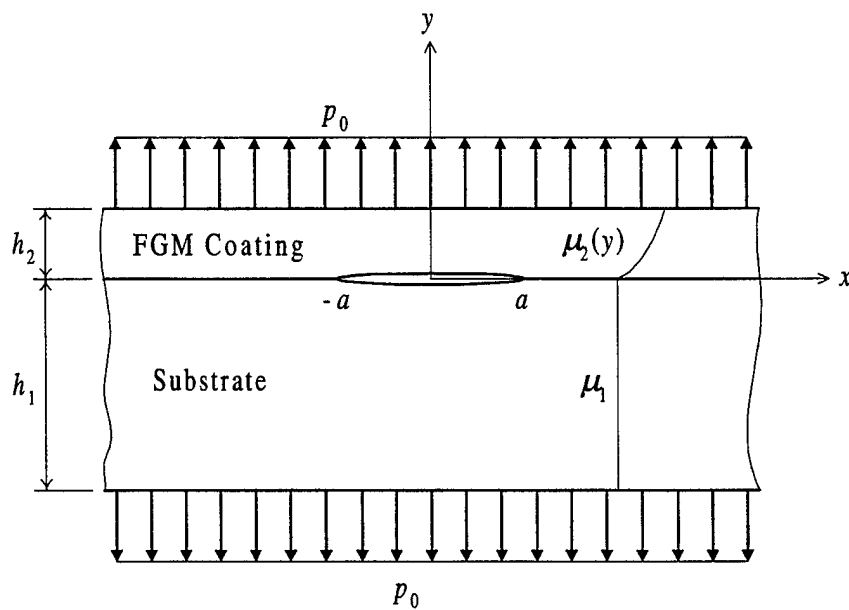


Figure G.5 Functionally graded coating bonded to homogeneous substrate with an interface crack subjected to uniform tensile stress normal to the surfaces, shear modulus of the coating:  $\mu_2(y) = \mu_1 \exp(\gamma y)$ .

To test the inhomogeneous and enriched element implementation, we consider the problem of a FGM coating bonded to a homogeneous substrate containing an interface

crack subjected to uniform normal surface loading as described in Figure G.5 [72] where the Poisson's ratio  $\nu = 0.3$  and the relative dimensions are given as:  $h_1 = 4a$ ,  $h_2 = a$ . It is assumed that the strain measures follow the small deformation theory and that the material is linear elastic. The strain energy release rates and stress intensity factors for various inhomogeneous parameters obtained analytically from singular integral equations [72] and computed by using inhomogeneous enriched finite elements are shown in Table D.1. Note that in the finite element analysis the specimen is finite in  $x$  direction and that to eliminate the end effect the length  $l = 40a$  is used. Again, excellent agreement between the analytical and finite element results are observed.

From the results of the test examples in G.1 and G.2, it is safe to assume that the inhomogeneous enriched finite element code with large displacement formulation is working correctly and that the finite element solutions for problems with unknown analytical solutions can be considered to be accurate results.

Table G.1 Normalized stress intensity factors and strain energy release rate for the problem described in Figure G.5.

$\gamma$	$G/G_0$		$k_1(a)/p_0 a^{1/2}$		$k_2(a)/p_0 a^{1/2}$	
	Analytical	FEA	Analytical	FEA	Analytical	FEA
3.0	1.132	1.136	1.062	1.064	0.068	0.067
2.5	1.244	1.249	1.115	1.117	0.039	0.038
2.0	1.382	1.388	1.175	1.178	0.006	0.005
1.5	1.550	1.557	1.245	1.247	-0.032	-0.033
1.0	1.758	1.766	1.342	1.327	-0.076	-0.076
0.75	1.880	1.889	1.367	1.371	-0.100	-0.101
0.5	2.014	2.024	1.414	1.417	-0.126	-0.127
0.25	2.164	2.175	1.463	1.467	-0.153	-0.154
0.1	2.262	2.273	1.494	1.498	-0.171	-0.171
-0.01	2.337	2.349	1.518	1.521	-0.184	-0.185
-0.1	2.401	2.414	1.537	1.541	-0.195	-0.196
-0.25	2.514	2.527	1.571	1.575	-0.214	-0.215
-0.5	2.717	2.732	1.630	1.634	-0.247	-0.248
-0.75	2.942	2.958	1.692	1.696	-0.282	-0.283
-1.0	3.191	3.208	1.758	1.762	-0.319	-0.320
-1.25	3.464	3.483	1.826	1.831	-0.358	-0.360
-1.5	3.765	3.786	1.899	1.904	-0.400	-0.402
-2.0	4.456	4.482	2.053	2.059	-0.490	-0.492
-2.5	5.281	5.312	2.221	2.228	-0.589	-0.591
-3.0	6.257	6.295	2.402	2.409	-0.697	-0.700

## Appendix H

### Formulation for the Problem of a Homogeneous Half Space Containing a Crack parallel to the Surface

The plane strain problem under consideration here is shown in Figure 2.1 with  $\mu_2 = \mu_1$  ( $\gamma = 0$ ). Because of the numerical difficulty arising from the formulation described in Chapter 2 when the inhomogeneity parameter  $\gamma$  equals exactly to zero, an independent formulation is required for the stability problem of a homogeneous half space containing a crack parallel to the surface.

Substituting  $\gamma = 0$  into (2.26)-(2.28), we can write the displacement perturbations  $u_2^*$  and  $v_2^*$  as

$$u_2^*(x, y) = \frac{1}{2\pi} \int_{-\infty}^{\infty} \sum_{k=1}^4 C_k(\alpha) e^{n_k y} e^{i\alpha x} d\alpha, \quad 0 < y < h, \quad (H1)$$

$$v_2^*(x, y) = \frac{1}{2\pi} \int_{-\infty}^{\infty} \sum_{k=1}^4 m_k(\alpha) C_k(\alpha) e^{n_k y} e^{i\alpha x} d\alpha,$$

where  $C_1, \dots, C_4$  are unknown functions of  $\alpha$ ,  $n_i$  and  $m_i$ ,  $i = 1, \dots, 4$ , are

$$n_1 = -\lambda_2^* |\alpha|, \quad n_2 = -\lambda_1^* |\alpha|, \quad n_3 = \lambda_2^* |\alpha|, \quad n_4 = \lambda_1^* |\alpha|,$$

$$m_1 = i\beta \lambda_2^*, \quad m_2 = \frac{i\beta}{\lambda_1^*}, \quad m_3 = -i\beta \lambda_2^*, \quad m_4 = -\frac{i\beta}{\lambda_1^*}, \quad (H2)$$

$$\lambda_1^* = \frac{\lambda_1}{|\alpha|}, \quad \lambda_2^* = \frac{\lambda_2}{|\alpha|}, \quad \beta = \frac{\alpha}{|\alpha|},$$

and  $\lambda_1$  and  $\lambda_2$  are defined by (2.29). The stress perturbations can be obtained by substituting (H2) into (2.32) giving

$$\begin{aligned}\sigma_{2yy}^*(x, y) = & -\frac{\mu_2}{2\pi} \int_{-\infty}^{\infty} \left[ (1 + \lambda_1^{*2}) \left( C_1 e^{-\lambda_2^* |\alpha| y} + C_3 e^{\lambda_2^* |\alpha| y} \right) \right. \\ & \left. + 2 \left( C_2 e^{-\lambda_1^* |\alpha| y} + C_4 e^{\lambda_1^* |\alpha| y} \right) \right] i\alpha e^{i\alpha x} d\alpha,\end{aligned}\quad (H3)$$

$$\begin{aligned}\sigma_{2xy}^*(x, y) = & -\frac{\mu_2}{2\pi} \int_{-\infty}^{\infty} \left[ 2\lambda_2^* \left( C_1 e^{-\lambda_2^* |\alpha| y} - C_3 e^{\lambda_2^* |\alpha| y} \right) \right. \\ & \left. + \left( \lambda_1^* + \frac{1}{\lambda_1^*} \right) \left( C_2 e^{-\lambda_1^* |\alpha| y} - C_4 e^{\lambda_1^* |\alpha| y} \right) \right] |\alpha| e^{i\alpha x} d\alpha.\end{aligned}\quad (H4)$$

To solve the unknowns functions  $A_1$ ,  $A_2$  (in the displacement perturbations for the part  $y < 0$ ) and  $C_1, \dots, C_4$ , first we define the density functions (same as in Chapter 2) as

$$\begin{aligned}\frac{\partial}{\partial x} [v_2^*(x, +0) - v_1^*(x, -0)] &= f_1(x), \\ -\infty < x < \infty. \quad (H5a,b) \\ \frac{\partial}{\partial x} [u_2^*(x, +0) - u_1^*(x, -0)] &= f_2(x),\end{aligned}$$

Now, by substituting (2.22), (2.28), (2.33) and (H2)-(H4) into (H5) and the following boundary and continuity conditions:

$$\sigma_{2yy}^*(x, h) = 0, \quad \sigma_{2xy}^*(x, h) = 0, \quad -\infty < x < \infty, \quad (H6a,b)$$

$$\sigma_{1yy}^*(x, -0) = \sigma_{2yy}^*(x, +0), \quad \sigma_{1xy}^*(x, -0) = \sigma_{2xy}^*(x, +0), \quad -\infty < x < \infty, \quad (H7a,b)$$

we can express the six unknown functions  $A_1$ ,  $A_2$  and  $C_1, \dots, C_4$  in terms of the density functions  $f_1$  and  $f_2$ . From (H5) and the displacement continuity along  $y = 0$ , i.e.,

$$u_1^*(x, -0) = u_2^*(x, +0), \quad v_1^*(x, -0) = v_2^*(x, +0), \quad |x| > a, \quad (H8a,b)$$

we can write the single-valuedness condition as

$$f_i(x) = 0, \quad |x| > a; \quad \int_{-a}^a f_i(t) dt = 0, \quad i = 1, 2. \quad (H9)$$

Also, from boundary condition on the crack surface we may write

$$\begin{aligned}\sigma_{1yy}^*(x, -0) &= \frac{\mu_1}{2\pi} \left[ \int_{-a}^a f_1(t) dt \int_{-\infty}^{\infty} B_{11}(\alpha) i\beta e^{i\alpha(x-t)} d\alpha \right. \\ &\quad \left. + \int_{-a}^a f_2(t) dt \int_{-\infty}^{\infty} B_{12}(\alpha) e^{i\alpha(x-t)} d\alpha \right] \\ &= 0, \quad -a < x < a,\end{aligned}\quad (\text{H10})$$

$$\begin{aligned}\sigma_{1xy}^*(x, -0) &= \frac{\mu_1}{2\pi} \left[ \int_{-a}^a f_1(t) dt \int_{-\infty}^{\infty} B_{21}(\alpha) e^{i\alpha(x-t)} d\alpha \right. \\ &\quad \left. + \int_{-a}^a f_2(t) dt \int_{-\infty}^{\infty} B_{22}(\alpha) i\beta e^{i\alpha(x-t)} d\alpha \right] \\ &= 0, \quad -a < x < a,\end{aligned}\quad (\text{H11})$$

where

$$B_{ij}(\alpha) = B_{ij0} \delta_{ij} + B_{ij1} e^{-2\lambda_1^* |\alpha| h} + B_{ij2} e^{-2\lambda_2^* |\alpha| h} + B_{ij3} e^{-(\lambda_1^* + \lambda_2^*) |\alpha| h}, \quad (\text{H12})$$

$$i, j = 1, 2,$$

$$B_{110} = \frac{4\lambda_1^* \lambda_2^* - (1 + \lambda_1^{*2})^2}{2\lambda_2^*(1 - \lambda_1^{*2})}, \quad (\text{H13})$$

$$B_{111} = - \frac{2\lambda_1^* [4\lambda_1^* \lambda_2^* + (1 + \lambda_1^{*2})^2]}{(1 - \lambda_1^{*2}) [4\lambda_1^* \lambda_2^* - (1 + \lambda_1^{*2})^2]}, \quad (\text{H14})$$

$$B_{112} = - \frac{(1 + \lambda_1^{*2})^2 [4\lambda_1^* \lambda_2^* + (1 + \lambda_1^{*2})^2]}{2\lambda_2^*(1 - \lambda_1^{*2}) [4\lambda_1^* \lambda_2^* - (1 + \lambda_1^{*2})^2]}, \quad (\text{H15})$$

$$B_{113} = \frac{8\lambda_1^* (1 + \lambda_1^{*2})^2}{(1 - \lambda_1^{*2}) [4\lambda_1^* \lambda_2^* - (1 + \lambda_1^{*2})^2]}, \quad (\text{H16})$$

$$B_{121} = - \frac{(1 + \lambda_1^{*2}) [4\lambda_1^* \lambda_2^* + (1 + \lambda_1^{*2})^2]}{(1 - \lambda_1^{*2}) [4\lambda_1^* \lambda_2^* - (1 + \lambda_1^{*2})^2]}, \quad (\text{H17})$$

$$B_{122} = B_{121}, \quad (\text{H18})$$

$$B_{123} = -2B_{121}, \quad (H19)$$

$$B_{211} = -B_{121}, \quad (H20)$$

$$B_{212} = -B_{122}, \quad (H21)$$

$$B_{213} = -B_{123}, \quad (H22)$$

$$B_{220} = \frac{4\lambda_1^*\lambda_2^* - (1 + \lambda_1^{*2})^2}{2\lambda_1^*(1 - \lambda_1^{*2})}, \quad (H23)$$

$$B_{221} = -\frac{(1 + \lambda_1^{*2})^2 \left[ 4\lambda_1^*\lambda_2^* + (1 + \lambda_1^{*2})^2 \right]}{2\lambda_1^*(1 - \lambda_1^{*2}) \left[ 4\lambda_1^*\lambda_2^* - (1 + \lambda_1^{*2})^2 \right]}, \quad (H24)$$

$$B_{222} = -\frac{2\lambda_2^* \left[ 4\lambda_1^*\lambda_2^* + (1 + \lambda_1^{*2})^2 \right]}{(1 - \lambda_1^{*2}) \left[ 4\lambda_1^*\lambda_2^* - (1 + \lambda_1^{*2})^2 \right]}, \quad (H25)$$

$$B_{223} = \frac{8\lambda_2^*(1 + \lambda_1^{*2})^2}{(1 - \lambda_1^{*2}) \left[ 4\lambda_1^*\lambda_2^* - (1 + \lambda_1^{*2})^2 \right]}. \quad (H26)$$

The integral equations (H10) and (H11) can further be simplified as follows:

$$\frac{\mu_1}{\pi} \int_{-a}^a \sum_{j=1}^2 \left[ B_{ij0} \left( \frac{\delta_{ij}}{t-x} \right) + k_{ij}(x, t) \right] f_j(t) dt = 0, \quad (H27)$$

$$i = 1, 2, \quad -a < x < a.$$

where

$$k_{ij}(x, t) = \frac{B_{ij1}(t-x)}{4\lambda_1^{*2}h^2 + (t-x)^2} + \frac{B_{ij2}(t-x)}{4\lambda_2^{*2}h^2 + (t-x)^2} + \frac{B_{ij3}(t-x)}{(\lambda_1^* + \lambda_2^*)^2h^2 + (t-x)^2}, \quad i, j = 1, 2. \quad (H28)$$

It can be seen that the singular integral equations (H27) have the same form as (2.66). It can further be shown that the coefficients for the Cauchy kernels are the same as in (H27)

and (2.26). Also we have  $k_{21}(x, t) = -k_{12}(x, t)$  which is the same as in the case of inhomogeneous coating bonded to homogeneous substrate. To solve the integral equations (H9) and (H27) we follow the procedure described in Chapter 3. Following Section 3.3.2, a pilot case for the problem of homogeneous half space containing a crack parallel to the surface is analyzed to examine the convergence. The computed instability strain  $(\epsilon_0)_{\text{cr}}$  as a function of approximation terms  $n$  is given in Table H.1. Again, it is observed that the calculated results by using 8 approximation terms agree very well with higher order approximations and therefore,  $n = 8$  is used in this study. Note that because the Fredholm kernels in this case have closed-form expressions (i.e., (H28)), the numerical computation is greatly simplified.

Table H.1 Effect of the number of approximation terms on the instability point and phase angle for the problem described in Figure 2.1 with  $\gamma h = 0$ ,  $\nu = 0.3$ , and  $h/a = 0.05$ .

Approximation terms $n$	Instability load $(\epsilon_0)_{\text{cr}}$	Phase angle $\psi$ (degree)
2	0.001916	-25.52
4	0.001906	-37.30
8	0.001921	-39.12
16	0.001921	-39.07
32	0.001921	-39.07

## Appendix I

### The Plate Model Analysis

#### I.1 Stability Analysis

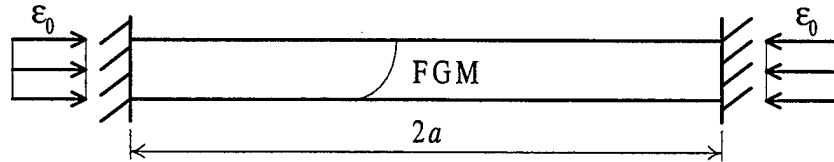


Figure I.1 Schematic of the plate model for the problem described in Figure 2.1.

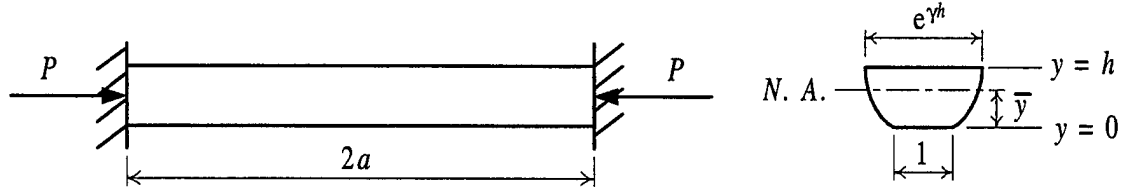


Figure I.2 Configuration of the column with transformed cross-section.

To study the buckling instability problem described in Figure 2.1, we may approximate the delaminated coating as a plate with built-in ends under fixed-grip compressive strain  $\epsilon_0$  as shown in Figure I.1. The plane strain problem can further be reduced to a FGM column of unit width with built-in ends. The elastic modulus of the column can be expressed as

$$E^*(y) = E_1^* e^{\gamma y}, \quad E_1^* = \frac{E_1}{1 - \nu^2}, \quad (I1)$$

where  $E_1$  is the elastic modulus of the substrate and  $E_1 = 2(1 + \nu)\mu_1$ . The problem may then be solved by using the Euler column approach. The material inhomogeneity described in Equation (I1) is considered by using the transformed-section method [88], that is

replacing the inhomogeneous column with rectangular cross-section by a homogeneous column with stretched width in the cross-section as shown in Figure I.2. Instead of unit width, the transformed cross-section has a width of  $E^*(y)/E_1^*$  ( $= e^{\gamma y}$ ). The position of the neutral axis for the transformed section for the case of  $\gamma \neq 0$  can be obtained as

$$\bar{y} = \frac{\int y dA}{A} = \frac{\int_0^h y e^{\gamma y} dy}{\int_0^h e^{\gamma y} dy} = \frac{\gamma h e^{\gamma h} - e^{\gamma h} + 1}{\gamma(e^{\gamma h} - 1)}, \quad (I2)$$

and the moment of inertia for the transformed section is given by

$$I_t = \int_0^h (y - \bar{y})^2 dA = \int_0^h (y - \bar{y})^2 e^{\gamma y} dy = \frac{(e^{\gamma h} - 1)^2 - (\gamma h)^2 e^{\gamma h}}{\gamma^3 (e^{\gamma h} - 1)}. \quad (I3)$$

The axial compressive load for the column corresponding to the fixed-grip compressive strain  $\epsilon_0$  can be expressed as

$$P = \int E^* \epsilon_0 dA = \int_0^h E_1^* e^{\gamma y} \epsilon_0 dy = \frac{E_1^* \epsilon_0 (e^{\gamma h} - 1)}{\gamma}. \quad (I4)$$

The Euler's buckling load for the column described in Figure I.2 is given by [87]

$$P_{cr} = \frac{4\pi^2 E_1^* I_t}{(2a)^2}. \quad (I5)$$

Substituting (I3) and (I4) into (I5), we have

$$\frac{E_1^* (e^{\gamma h} - 1)}{\gamma} (\epsilon_0)_{cr} = \frac{4\pi^2 E_1^* [(e^{\gamma h} - 1)^2 - (\gamma h)^2 e^{\gamma h}]}{4a^2 \gamma^3 (e^{\gamma h} - 1)}, \quad (I6)$$

or

$$(\epsilon_0)_{cr} = \pi^2 \left( \frac{h}{a} \right)^2 \left[ \frac{1}{(\gamma h)^2} - \frac{1}{(e^{\gamma h} + e^{-\gamma h} - 2)} \right], \quad \gamma \neq 0. \quad (I7)$$

It can be seen that the critical strain  $(\epsilon_0)_{cr}$  corresponding to the buckling instability is an even function of the inhomogeneity parameter  $\gamma h$ .

For the case of  $\gamma = 0$  which corresponding to a homogeneous coating, one may repeat the procedure and obtain the counterpart of (I6) as

$$E_1^* h(\epsilon_0)_{\text{cr}} = \frac{4\pi^2 E_1^*}{4a^2} \left( \frac{h^3}{12} \right). \quad (\text{I8})$$

The critical strain for  $\gamma = 0$  can be reduce from (I8) and is given by

$$(\epsilon_0)_{\text{cr}} = \frac{\pi^2}{12} \left( \frac{h}{a} \right)^2, \quad \gamma = 0. \quad (\text{I9})$$

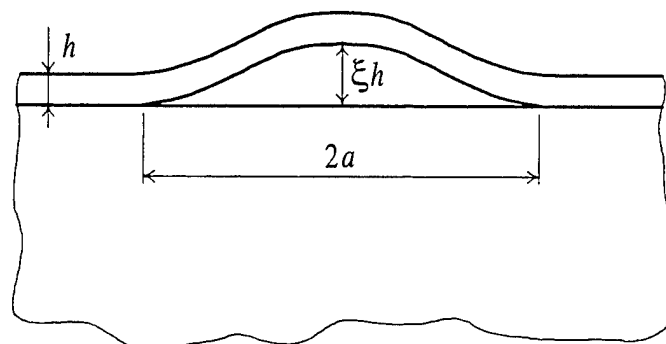
Note that (I9) may be recovered by taking limits ( $\gamma \rightarrow 0$ ) of (I7). Also it may be seen from (I7) and (I9) that for a fixed value of  $h/a$  the maximum of  $(\epsilon_0)_{\text{cr}}$  occurs at  $\gamma = 0$ .

## I.2 Postbuckling Analysis

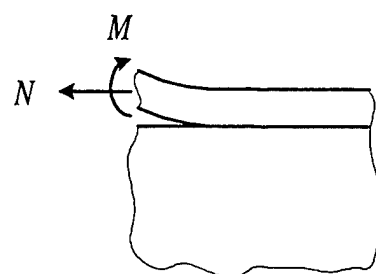
By following Hutchinson and Suo [41], the crack problem associated with the postbuckling of coating is obtained by coupling the von Karman plate solution and the split-beam approach for the fracture mechanics parameters. It is assumed that the ratio of crack length (or radius) over coating thickness is very large and the coating thickness is much smaller than the one of the substrate. The multi-layered TBC system containing an interface crack subjected to thermal or mechanical compressive stress is approximated by a coating bonded to a half-space with an interface crack as shown in Figure I.3(a). The loading  $N$  and bending moment  $M$  on the buckled coating as shown in Figure I.3(b) is then calculated by using the von Karman nonlinear plate formulation. The plane strain problem and axisymmetric problem will be discussed separately.

### I.2.1 The Plane Strain Problem

Again, the inhomogeneity of the coating is considered by using the transformed-section method as described in Appendix I.1. The thermomechanical properties  $E$ ,  $\nu$ , and  $\alpha$  are functions of  $y$ . The position of the neutral axis and the bending stiffness are given by



(a)



(b)

Figure I.3 Geometry of the one dimensional blister, (a) the buckled coating, (b) local loading of interface crack.

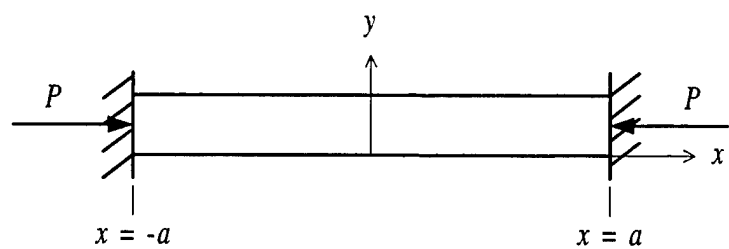


Figure I.4 Configuration of the plate for the postbuckling analysis.

$$\bar{y} = \frac{\int_0^h y E^*(y) dy}{\int_0^h E^*(y) dy}, \quad E^*(y) = \frac{E(y)}{1 - \nu^2(y)}, \quad (I10)$$

$$D = \int_0^h E^*(y)(y - \bar{y})^2 dy. \quad (I11)$$

The one-dimensional deformation of the plate in Figure I.4 is characterized by the  $y$ -displacements,  $v(x)$ , which is zero in the unbuckled state with pre-stress corresponding to the compressive load. From the moment equilibrium of the column, we may write the governing equation as

$$D \frac{d^4 v}{dx^4} + \Delta N \frac{d^2 v}{dx^2} = 0, \quad \Delta N = P - N, \quad (I12)$$

where  $\Delta N$  is the net  $x$ -direction resultant compressive force for the buckled column. Solving (I12) with the following boundary condition:

$$v|_{x=\mp a} = 0, \quad \frac{dv}{dx} \Big|_{x=\mp a} = 0, \quad (I13)$$

we obtain the deflection and the corresponding buckling load (lowest eigenvalue) as

$$v(x) = \frac{1}{2} \xi h \left( 1 + \cos \frac{\pi x}{a} \right), \quad (I14)$$

$$\Delta N = P_{cr} = \frac{\pi^2 D}{a^2},$$

respectively, where  $\xi = v(0)/h$  is the unknown "amplitude". The amplitude  $\xi$  is determined by the condition that the membrane stress in the buckled coating is the same as the buckling stress. This condition leads to

$$\int_{-a}^a \epsilon_{xx} dx = 2a \left( \frac{P - P_{cr}}{\lambda} \right), \quad \lambda = \int_0^h E^*(y) dy, \quad (I15)$$

where the nonlinear strain  $\epsilon_x$  is given by

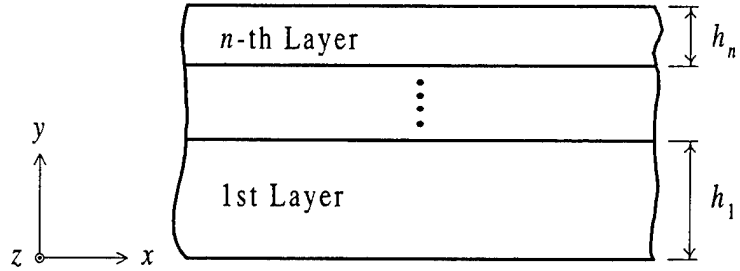


Figure I.5 Geometry of the multi-layered infinite plate.

$$\epsilon_{xx} = \frac{1}{2} \left( \frac{dv}{dx} \right)^2. \quad (\text{I16})$$

By substituting (I14) and (I16) into (I15) we obtain

$$\xi = \frac{v(0)}{h} = \frac{4}{h} \left[ \frac{D}{\lambda} \left( \frac{P}{P_{\text{cr}}} - 1 \right) \right]^{1/2}. \quad (\text{I17})$$

The bending moment at  $x = a$  and the change in resultant force in  $x$ -direction can be expressed as

$$M = D \frac{d^2 v}{dx^2} \Big|_{x=a} = \frac{\pi^2 D h}{2a^2} \xi, \quad N = P - P_{\text{cr}}. \quad (\text{I18})$$

By substituting (I18) into the general split-beam solution given by Hutchinson and Suo [41] we can obtain the strain energy release rate as

$$G = \frac{P^2}{2\lambda} \left( 1 - \frac{P_{\text{cr}}}{P} \right) \left( 1 + 3 \frac{P_{\text{cr}}}{P} \right). \quad (\text{I19})$$

The only undetermined quantity in (I17) and (I19) is the initial in-plane compressive load  $P$ . To calculate  $P$ , we assumed that initially the crack is closed and there is no shear stress in the medium. Then  $P$  is approximated by the in-plane compressive load in the coating of a multi-layered medium without interface crack as shown in Figure I.5. It may

be seen from Figure I.5 that for the medium we have  $\frac{\partial}{\partial x}(\ ) = \frac{\partial}{\partial z}(\ ) = 0$ , and that from the compatibility equations, we have

$$\frac{\partial^2 \epsilon_{xx}}{\partial y^2} = \frac{\partial^2 \epsilon_{zz}}{\partial y^2} = 0. \quad (I20)$$

Also it may be seen that the out-of-plane stress

$$\sigma_{yy} = 0. \quad (I21)$$

Solving (I20), we obtain

$$\begin{aligned} \epsilon_{xx} &= A_1 y + A_2, \\ \epsilon_{zz} &= B_1 y + B_2, \end{aligned} \quad (I22)$$

where  $A_1$ ,  $A_2$ ,  $B_1$ , and  $B_2$  are constants and we have

$$B_1 = B_2 = 0, \quad \text{for plane strain condition.} \quad (I23)$$

The remaining unknown constants  $A_1$  and  $A_2$  are determined from the boundary conditions associated with the following loading conditions:

(i) Fixed-grip Loading

For the case of fixed-grip loading shown in Figure 2.1, we simply have

$$A_1 = 0, \quad A_2 = -\epsilon_0, \quad \text{for fixed-grip loading.} \quad (I24)$$

By substituting (I21)-(I24) into the generalized Hooke's law, we obtain the stress for the coating as

$$\sigma_{xx} = -\frac{E(y)}{1 - \nu^2(y)}\epsilon_0. \quad (I25)$$

The compressive resultant force may be expressed as

$$P = - \int_0^h \sigma_{xx} dy = \lambda\epsilon_0. \quad (I26)$$

By substituting (I26) into (I17) and (I19) we may then obtain the crack opening and strain energy release rate.

### (ii) Temperature Loading

By substituting (I21)-(I23) into the generalized Hooke's law containing temperature effects, we can obtain the thermal residual stress for the layered system shown in Figure I.5 as

$$\sigma_{ixx} = \frac{E_i(y)}{1 - \nu_i^2(y)} (A_1 y + A_2) - \frac{E_i(y)}{1 - \nu_i(y)} \alpha_i(y) \Delta T, \quad y_{i-1} < y < y_i, \quad (I27)$$

where the subscript  $i$  denotes the  $i$ -th layer and

$$y_0 = 0, \quad y_i = \sum_{i=1}^n h_i. \quad (I28)$$

From the force and moment equilibrium on each cross-section, i.e.,

$$\begin{aligned} \sum_{i=1}^n \int_{y_{i-1}}^{y_i} \sigma_{ixx} dy &= 0, \\ \sum_{i=1}^n \int_{y_{i-1}}^{y_i} \sigma_{ixx} y dy &= 0, \end{aligned} \quad (I29)$$

we can calculate the unknown constants  $A_1$  and  $A_2$  and, in turn, determine the stresses  $\sigma_{ixx}$ . Assuming that there are  $m$  layers above the interface crack, the resultant compressive load can be expressed as

$$P = \sum_{i=n-m}^n \int_{y_{i-1}}^{y_i} \sigma_{ixx} dy. \quad (I30)$$

The results for the postbuckling regime can be then obtained by substituting (I30) into (I17) and (I19).

### I.2.2 The Axisymmetric Problem

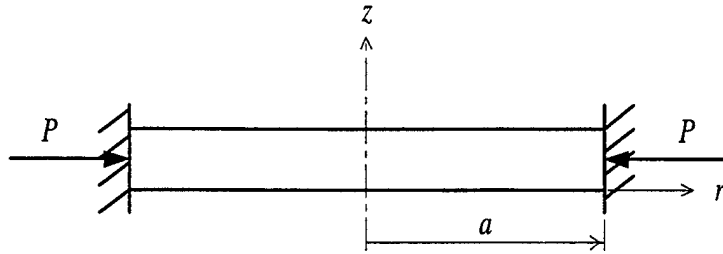


Figure I.6 Configuration of the circular plate for the postbuckling analysis.

The problem of an axisymmetric blister is investigated by following the same procedure used in the plane strain case. In this study only the interface crack problem for a homogeneous coating is discussed. From the moment and force equilibrium of the circular plate described in Figure I.6 we have

$$D\left(\frac{d^3w}{dr^3} + \frac{1}{r}\frac{d^2w}{dr^2} - \frac{1}{r^2}\frac{dw}{dr}\right) + \Delta N_r \frac{dw}{dr} = 0, \quad \Delta N_r = P - N_r, \quad (I31)$$

$$\frac{d}{dr}\left(r^3 \frac{dN_r}{dr}\right) + \frac{Ehr}{2} \left(\frac{dw}{dr}\right)^2 = 0. \quad (I32)$$

The boundary and symmetric conditions are given as follows:

$$\left.\frac{dw}{dr}\right|_{r=0} = 0, \quad w(a) = 0, \quad \left.\frac{dw}{dr}\right|_{r=a} = 0, \quad (I33a)$$

$$u(a) = r\epsilon_t|_{r=a} = \left.\frac{r}{E} \left[\frac{d}{dr}(rN_r) - \nu N_r\right]\right|_{r=a} = 0, \quad \left.\frac{dN_r}{dr}\right|_{r=0} = 0, \quad (I33b)$$

For nontrivial solution for Equation (I31) under the boundary conditions (I33a), we have

$$(\Delta N_r)_{cr} = P_{cr} = \frac{\mu^2 D}{a^2 h^2}, \quad (I34)$$

where  $\mu = 3.8317$  is the first nontrivial zero of  $J_1(x)$ , which is the Bessel function of the first kind of order one. The associated buckling mode is

$$w_1(r) = \left[ \frac{J_0(\mu r/a) - J_0(\mu)}{1 - J_0(\mu)} \right] h, \quad (I35)$$

where  $J_0$  is the Bessel function of the first kind of order zero. Note that the buckling mode is normalized such that  $w_1(0) = h$ . To examine the initial postbuckling behavior a perturbation analysis is performed. It is assumed that

$$w(r) = \xi w_1(r) + \xi^2 w_2(r) + \xi^3 w_3(r) + O(\xi^4), \quad (I36)$$

$$N_r = \xi N_{r1} + \xi^2 N_{r2} + O(\xi^3). \quad (I37)$$

Substituting (I36) and (I37) into (I31) and (I32) and writing them as power series in  $\xi$  we can equate the coefficients to zero to generate an ordered series of equilibrium equations and boundary conditions. Solving these equations we obtain [41]

$$N_{r1} = 0, \quad N_{r2} = c_1 P_{cr}, \quad (I38)$$

where  $c_1 = 0.2473(1 + \nu) + 0.2231(1 - \nu)^2$ . From (I37) and (I38) we may write

$$\xi = \frac{\delta}{h} = \left[ \frac{1}{c_1} \left( \frac{\sigma}{\sigma_{cr}} - 1 \right) \right]^{1/2}. \quad (I39)$$

Again, substituting the following quantities into split-beam solution [41]

$$M = D \frac{d^2 w}{dr^2} \Big|_{r=a}, \quad N = N_r \Big|_{r=a}, \quad (I40)$$

we obtain the asymptotic strain energy release rate for initial postbuckling as

$$\frac{G}{G_0} = c_2 \left[ 1 - \left( \frac{P_{cr}}{P} \right)^2 \right], \quad c_2 = \frac{1}{1 + 0.9021(1 - \nu)}, \quad (I41)$$

where  $G_0 = (1 - \nu)P^2/Eh$ .

In the axisymmetric problem, only the compressive stress induced by temperature change will be discussed here. To determine the initial in-plane compressive load, we follow the procedure described in previous section. First we calculate the stresses in

Cartesian coordinate and transform them into cylindrical coordinate to obtain  $\sigma_{rr}$ . For the medium described in Figure I.5 under "axisymmetric" condition, we may write

$$\sigma_{yy} = 0, \quad \epsilon_{xx} = \epsilon_{zz} = A_1 y + A_2, \quad (I42)$$

where  $A_1$  and  $A_2$  are the unknown constants. Substituting (I42) into the generalized Hooke's law, we obtain

$$\sigma_{ixx} = \sigma_{izz} = \frac{E_i(y)}{1 - \nu_i(y)} (A_1 y + A_2) - \frac{E_i(y)}{1 - \nu_i(y)} \alpha_i(y) \Delta T, \quad y_{i-1} < y < y_i, \quad (I43)$$

where  $y_i$  is defined in (I28). The unknowns  $A_1$  and  $A_2$  can be obtained by substituting (I43) into (I29) and solving the system of equations. Under the stress state described by (I42) and (I43) we can simply write

$$\sigma_{irr} = \sigma_{ixx}, \quad i = 1, \dots, n, \quad (I44)$$

The resultant compressive load for the homogeneous coating above the crack (layer  $n$ ) can then be simply expressed as

$$P = \sigma_{nxx} h. \quad (I45)$$

The results for the postbuckling regime can then be obtained by substituting (I45) into (I39) and (I41).